

Modeling the Viscoelastic Material Behavior of the Midpalatal Suture in Finite Element Simulations for the Purpose of Better Understanding the Role of Soft Tissue Sutures in Orthodontic Maxillary Expansion Procedures

by

Russel Shawn Albert Donald Fuhrer

A thesis submitted in partial fulfillment of the requirements for the degree of

Master of Science

Department of Mechanical Engineering  
University of Alberta

## Abstract

Finite element analysis can help increase understanding of how the material behavior of the midpalatal suture affects maxillary expansion in adolescents with unfused sutures. Mathematical material models describing the non-linear viscoelastic behavior of the midpalatal suture were previously developed. Adapting these tissue-specific models for use in a finite element program (ANSYS Mechanical R.14.5) may allow the extent of the suture's influence on the expansion process to be understood.

Initial work endeavored to adapt the 1-D creep and relaxation models for use in the 3D finite element environment. The materials were assumed isotropic. Both models describe a bone-suture interface region and were developed based on a 9.72mm width. Improvements to the models are highlighted by a correction factor,  $\gamma$ , that enables them to describe a thinner, more clinically appropriate, initial region width. The variable  $\gamma$  was derived to modify both 1D models for a region width of 1.72mm. Adapted models underwent verification testing using a test mesh based on the geometry from which the models were developed. Time and stress derivatives of the  $\gamma$ -modified 1D creep model were encoded into ANSYS' USERCREEP.f subroutine and compiled with the Intel 11.1 FORTRAN compiler. Creep simulations were loaded with constant expansion forces for simulated 6-week periods and evaluated against the expected results of the 1-D model. It was found that the creep strain curve could be closely replicated; however, the expansion of the suture region experienced tertiary creep expansion. This indicated that the creep model was not accurately adapted for ANSYS. Additional training of the constitutive model may be required to account for ANSYS calculating expansion based on the volume dimensions at the end of the previous solution iteration. The  $\gamma$ -modified relaxation model was approximated using a Prony expansion series to define the time dependent behavior of a generalized Maxwell model. A 7-term Prony series was curve fit to a time shifted dataset generated from the  $\gamma$ -modified relaxation equation. The model was assigned to the suture region of the test mesh. The test mesh was expanded by stepwise applications of clinically relevant (0.25mm) displacements, mimicking expansion appliance activations. 1<sup>st</sup> principal stresses within the simulated suture at the midsagittal plane peaked at 2.23 MPa for the initial appliance activation and relaxed to negligible levels in the two minutes following, thereby verifying the time-dependent behavior of the Prony approximation. Subsequent ( $n>1$ ) stress peaks diminished in magnitude as equal applied displacements caused reduced strains per activation.

The Prony relaxation model needed to be simulated as part of a skull geometry to investigate what effect, if any, the suture has on the expansion process. Cranial geometry was created from patient CT images using a semi-manual masking procedure. After smoothing and rotating the masked geometry to align the midsagittal plane with the yz-plane, the model was halved and segmented to define craniofacial suture volumes. After meshing the geometry for FEA, the partial skull was constrained at boundaries where it would connect to the remainder of the skull. Material models for the craniofacial sutures were varied between linear elastic properties of bone and soft tissue and the material model of the midpalatal/intermaxillary suture was varied between being neglected, a linear soft tissue, and the non-linear relaxation model. Multiple simulation cases were loaded identically with 29 consecutive appliance activations. Activations displacements were each 0.125mm, spaced 12 hours apart. The stress relaxation properties of the midpalatal/intermaxillary suture volume had a noticeable effect on the reaction force at the appliance in the two minutes following the activation, but negligible effect on the final displacement of the dentition. Results also indicated craniofacial suture properties could significantly change final dentition position and reaction force.

Based upon the suture and partial skull simulations, it was concluded that the Prony approximation accurately replicates the expected relaxation behavior and has a noticeable effect on the system immediately post-activation. The adapted creep model is not suitable for further tests without modification to utilize the state of the previous iteration instead of initial conditions. Future work in developing a predictive finite element model of maxillary expansion may involve characterizing and incorporating into ANSYS the viscoelastic behavior of cranial bone and the craniofacial sutures. This may result in displacements and appliance reaction forces that are more reflective of clinical results.

## **Preface**

This thesis is an original work by Russel Shawn Albert Donald Fuhrer. Patient data, in the form of computed tomography scans, were provided by Manuel Lagraverre under the research ethics approval number PRO-00013379 from the University of Alberta Research Ethics Board. No part of this thesis has been previously published.

*“The storm had now definitely abated,  
and what thunder there was now grumbled over more distant hills,  
like a man saying “And another thing...”  
twenty minutes after admitting he’s lost the argument”*

~Douglas Adams, from Chapter 3 of *“So Long and Thanks for All the Fish”*

*“Let us think the unthinkable,  
Let us do the undoable,  
Let us prepare to grapple with the ineffable itself,  
And see if we may not eff it after all.”*

~Douglas Adams, from *“Dirk Gently’s Holistic Detective Agency”*

*To my wife Shannon, my best friend and soulmate, who  
helped drag me through the last of it...*

*To my parents who supported me throughout the entirety  
of my life and all the paths I've taken...*

*To my family and friends for bringing me smiles during  
the hardships and doubts...*

*...I dedicate my thesis to all of you.*

## Acknowledgements

Although this thesis only has one name on the cover, it could not have been completed without the community of people in my life. The individuals mentioned below have played a significant role in setting me up for success in my pursuit of this degree.

First and foremost, I feel I must acknowledge the mentorship and guidance I've received from my supervisor Dr. Jason Carey. Without your encouragement I would not have embarked on this journey, nor do I think I could have completed it. I must also thank Dr. Paul Major for welcoming me into the Orthodontic Biomechanics Testing & Development Research Group and indulging my research in the engineering and computer modelling of orthodontics. Thanks must be given to Dr. Dan Romanyk, without your initial mathematical models of the midpalatal suture my research would not have had a foundation upon which to build. Dr. Manuel Lagravère for providing the CT image sets I needed to build the partial skull FEA geometry for this study.

The financial support provided by the Ormco Donation Fund, the Department of Mechanical Engineering, the Faculty of Graduate Studies and Research, the Graduate Students Association, and the University of Alberta has allowed me to be fiscally capable to pursue the goal of completing this degree and cannot be understated.

As my topic of study has involved massive amounts of computer use, I would be remiss if I did not thank the MecE IT staff. Without their help my research would have been over before it began, and it would have definitely been finished after my 1st and 2nd hard drive failures had it not been for David Dubyk.

My life as a graduate student would have been a much lonelier one without the comradery and friendship of my lab mates. Between the coffee breaks, the B.S. sessions, and beers you've all made helped make it an experience I won't easily forget.

Love and support from my family has been unending. My parents, Russel and Cheryl Fuhrer, have had faith in me and have kept me pointed in the right direction even when I felt overwhelmed and lost my direction. Without you both, I could not have become the man I am today nor accomplished all I have.

I admit that my degree has been characterized at times by frustration and stress. However, all of the hardship has been made worth it for meeting the most wonderful, intelligent, driven, compassionate, and beautiful woman I have ever had the pleasure of knowing, my lovely wife Shannon. Without you, my life would have significantly fewer smiles and fewer laughs. I don't know if I could have done this without you. You feel like home, and I look forward to the start of our post-thesis lives together

# Table of Contents

<b>1</b>	<b>Introduction and Project Background</b>	<b>1</b>
1.1	<i>Defining Maxillary Expansion</i> .....	1
1.2	<i>Aims and Motivation</i> .....	3
1.2.1	Pre-2013 FEA Research in Modelling the MPS and ME	3
1.2.2	Post-2013 FEA Research in Modelling the MPS and ME	4
1.2.3	Recent Microstructure Modelling of Sutures	6
1.3	<i>Creep</i> .....	7
1.3.1	Overview of MPS Specific 1-D Creep Model	9
1.4	<i>Viscoelastic Relaxation</i> .....	10
1.4.1	Overview of the MPS Specific 1-D Viscoelastic Relaxation Model	12
1.5	<i>Additional Craniofacial Sutures</i> .....	12
1.6	<i>Outline of Overall Method of Thesis Research</i> .....	13
1.7	<i>References</i> .....	16
<b>3</b>	<b>Implementation and Evaluation of the Relaxation Model Using a 3-D Partial Skull Geometry</b>	<b>84</b>
3.1	<i>Introduction</i> .....	84
3.2	<i>Materials and Methods</i> .....	85
3.2.1	Geometry Creation Considerations	86
3.2.2	Selection of Patient DICOM Images	88
3.2.3	Masking Techniques Utilized in Simpleware	89
3.2.4	Preparing the Partial Cranium FEA Model	99
3.2.5	FEA Trials and Loading Conditions	107
3.3	<i>Results and Discussion</i> .....	115
3.3.1	Geometry Trimming and Natural Boundary Conditions Verification	115
3.3.2	Maxillary Expansion Simulations with Various Material Models and Sutures	119
3.4	<i>Conclusions and Future Work</i> .....	137
3.4.1	Simplifications and Assumptions Identified in this Study	141
3.5	<i>References</i> .....	142

<b>4</b>	<b>Summary, Conclusions, Recommendations</b>	<b>144</b>
4.1	<i>Modification of the 1-D Constitutive Equations</i> .....	145
4.2	<i>Adaptation of 1-D Creep Model for Finite Element Analysis</i> .....	145
4.3	<i>Adaptation of 1-D Relaxation Model for Finite Element Analysis</i> .....	146
4.4	<i>Partial Cranium Modelling Utilizing Relaxation Model</i> .....	147
4.5	<i>Overall Conclusions</i> .....	148
4.6	<i>Future Work</i> .....	149
4.7	<i>References</i> .....	151
	<b>Bibliography</b>	<b>152</b>
	<b>Appendix A - APDL Code for Meshing and Testing RTG Models</b>	<b>160</b>
A.1	<i>Code for the RTG Model with a 2-Node Bar Element Suture – Creep Testing</i> .....	160
A.2	<i>Code for the RTG Model with a Brick Element Suture – Creep Testing</i> .....	163
A.3	<i>Code for the RTG Model with a Brick Element Suture – Relaxation Testing (Single Load Step)</i> .....	170
A.4	<i>Parameterized Solve Block Code for the RTG Model with a Brick Element Suture – Relaxation Testing</i> .....	174
	<b>Appendix B - Attempt to Incorporate Strain Dependency into Prony Relaxation Model Using ANSYS</b>	
	<b>Hyperelasticity Material Model</b>	<b>179</b>
B.1	<i>Method, Results, and Conclusions</i> .....	179
B.2	<i>Future Work</i> .....	182
B.3	<i>References</i> .....	182
	<b>Appendix C - APDL Code For Partial Skull Model Finite Element Trials</b>	<b>184</b>
C.1	<i>Loading Partial Skull Mesh and Creating Nodal Component Blocks</i> .....	184
	<b>Appendix D - Iterate Partial Skull Meshing Method Using NURBS and HyperMesh</b>	<b>200</b>
D.1	<i>Methods and Observations</i> .....	200
D.2	<i>Future Work</i> .....	204

## List of Tables

Table 1-1: MST Model Coefficients.....	23
Table 1-2: RTG Mesh Configurations .....	27
Table 1-3: Summary Element Types Used in ANSYS FEA Simulations .....	28
Table 1-4: Time Variations of Relaxation Data for Prony Series Curve Fitting .....	45
Table 1-5: Creep Model FEA Case Configuration Summary.....	48
Table 1-6: FEA Cases for Relaxation Model Tests .....	50
Table 1-7: Comparison of Spring Model and $\gamma$ -modified Elastic Moduli Over Time for an Assumed Bone Width of 4mm.....	52
Table 1-8: Sensitivity of $\gamma$ -modified and Simplified Spring Models to Changes in Assumed Bone Width .	53
Table 1-9: Peak Relative Error of Creep Model Simulations for 0.49N, 0.98N, and 1.96N Cases.....	56
Table 1-10: Summary of Shear Modulus Prony Curve Fit Regression Errors for Different Fit Orders.....	67
Table 1-11: Prony Coefficients for Shear Moduli ( $G$ ) for 3 Time Fit Cases .....	68
Table 3-1: Ages of Craniofacial Suture Fusion .....	87
Table 3-2: Patient DICOM Image Set Summary .....	88
Table 3-3: FE model Masks .....	100
Table 3-4: Prony 7-term Approximation Coefficients.....	112
Table 3-5: Summary of Partial Skull Simulation Cases.....	113
Table 3-6: Comparison of Averaged Displacements of Selected Node Sets Representing Pulp Chambers .....	118
Table 3-7: Completion Summary of Simulations .....	119
Table 3-8: Comparison of X-Component of Displacement of the 1 <sup>st</sup> Molar in Cranial Simulations; Simulations with Soft Linear Elastic Properties for the CFS are highlighted in green .....	124
Table 3-9: Comparison of Completed Simulation Expansion x-Component to Clinical T2-T3 Measurements for Patient.....	132
Table B-1: Strain Ranges and Approximate Curve Fit Residuals .....	180

## List of Figures

Fig. 1-1: Depiction of Outward Application of Expansion Forces or Displacement on a Picture of a 3-D Printed Cranium .....	2
Fig. 1-2: A Bone-Borne Appliance in a Patient’s Mouth.....	2
Fig. 1-3: Depiction of the Tensile Deformation of a Material Over Time Highlighting the Three Phases of Creep.....	8
Fig. 1-4: Depiction of the Stress Relaxation of a Viscoelastic Model Subjected to Sequentially Applied Displacements.....	10
Fig. 1-5: Simple Viscoelastic Models Represented Using Linear Springs and Dampers.....	11
Fig. 1-6: Flowchart Outlining Overall Thesis Structure .....	14
Fig. 1-7: MSS Geometry Approximation Utilized by Romanyk et al.....	22
Fig. 1-8: Stress (A) and Elastic Modulus (B) Response of the Relaxation Model Over Time to Variation in Applied Strain.....	24
Fig. 1-9: Depiction of RTG with Applied and Natural Boundary Conditions .....	26
Fig. 1-10: Figure of FEA model with 2-Node Bar and 8-Node Brick Elements .....	29
Fig. 1-11: Figure of FEA model with 8-Node Brick Elements .....	30
Fig. 1-12: Anticipated Deformation of Initially Cubic (A) and Flattened (B) Elements Under 0%, 50%, and 200% Tensile Strain.....	31
Fig. 1-13: Suture Strain and System Expansion Comparison of 1-D Creep Model Formulations .....	34
Fig. 1-14: Stress and Strain Comparison of the 1-D Relaxation Model Formulations .....	35
Fig. 1-15: Simplified Spring-Model Approximation of RTG Geometry.....	36
Fig. 1-16: USERCREEP.f Subroutine Flowchart.....	42
Fig. 1-17: Generalized Maxwell Spring-Damper Model Diagram .....	43
Fig. 1-18: Flowchart Detailing Solution Sub-Step Do-Loop Code for Relaxation Simulations .....	51
Fig. 1-19: Peak Elastic Modulus for Relaxation Models at t=5s for Varied Bone Widths; 0.25mm System Expansion .....	53
Fig. 1-20: 100g (0.98N) Unmodified Creep Model Strain ( $\epsilon$ ) Results.....	55

Fig. 1-21: 200g (1.96N) Unmodified Creep Model Strain ( $\epsilon$ ) Abs. Relative Error .....	55
Fig. 1-22: Comparison of Strain ( $\epsilon$ ) Results for 200g (1.96N) Static and Dynamic Simulations .....	58
Fig. 1-23: Comparison of Abs. Relative Error for 200g (1.96N) Static and Dynamic Simulations .....	58
Fig. 1-24: 0.49N (50g) Load – $\gamma$ -modified Model Strain .....	60
Fig. 1-25: 0.98N (100g) Load – $\gamma$ -modified Model Strain .....	60
Fig. 1-26: 1.96N (200g) Load – $\gamma$ -modified Model Strain .....	61
Fig. 1-27: 0.49N (50g) Load Test Strain – $\gamma$ -modified Expansion .....	61
Fig. 1-28: 0.98N (100g) Load – $\gamma$ -modified Expansion .....	62
Fig. 1-29: 1.96N (200g) Load – $\gamma$ -modified Expansion .....	62
Fig. 1-30: Deformed Geometry of SOLID185 $\gamma$ -term Creep Simulation – 1 <sup>st</sup> Principal Strain for Last Resolved Time Step .....	63
Fig. 1-31: Stress and Strain vs. Time for SOLID185 $\gamma$ -term Creep Simulation, 50g Simulation .....	64
Fig. 1-32: 1 <sup>st</sup> Principal Stress in Center of Sagittal Plane of RTG for Prony Fit Time Variations .....	69
Fig. 1-33: 1 <sup>st</sup> Principal Strain Results at Appliance Activation Using Linear and Non-Linear Geometry Options .....	70
Fig. 1-34: 1 <sup>st</sup> Principal Stress Results at Appliance Activation Using Linear and Non-Linear Geometry Options .....	71
Fig. 1-35: Comparing the Maximum Stress of Relaxation Simulations Using Static and Dynamic Solvers .....	72
Fig. 1-36: Maximum Displacement, Strain, and Stress Results of 29 Activation Relaxation Simulation .....	73
Fig. 1-37: 1 <sup>st</sup> Principal Stress Plots of RTG Following 1 <sup>st</sup> Appliance Activation .....	74
Fig. 1-38: 1 <sup>st</sup> Principal Stress Plots of RTG Following 29 <sup>th</sup> Appliance Activation .....	75
Fig. 3-1: ScanIP Workflow .....	89
Fig. 3-2: Comparison of Full (A) and Windowed (B) Binned Background Data .....	90
Fig. 3-3: Comparison of Raw (A) and Smoothed (B) Background Data .....	91
Fig. 3-4: Comparison of Pre-Smoothed (A) and Post-Smoothed (B) Cranial Mask .....	92
Fig. 3-5: Workflow of the Rotation and Crop Procedure .....	93

Fig. 3-6: ROI Positioning Landmarks On a Partial Mask (Deleted Right Hand Half of Mask Shown Greyed Out) .....	94
Fig. 3-7: Angle Measurements (A) XY-Plane View (B) XZ-View .....	95
Fig. 3-8: Workflow of the Suture Masking Procedure .....	97
Fig. 3-9: Model Masks; (A) Bone Masks, (B) Isolated Suture Masks, (C) Assembled Masks.....	98
Fig. 3-10: FEA Model Preparation Workflow .....	99
Fig. 3-11: Fixed Cantilever Beam Under(A) Directly Applied Displacement (B) Remotely Applied Displacement .....	102
Fig. 3-12: Comparison of CT and FE Appliance Loading Point .....	104
Fig. 3-13: Natural Boundary Conditions for Partial Skull Model .....	106
Fig. 3-14: Partial Cranium Models (A) Untrimmed Geometry (B) Trimmed Geometry .....	108
Fig. 3-15: Strain Contour Plot Comparison of Back Removed and Partial Skull Models.....	116
Fig. 3-16: Nodal Selection on Central Incisor .....	117
Fig. 3-17: Nodal Selection on 1 <sup>st</sup> Molar (Nodes Shown as Black Points).....	117
Fig. 3-18: Cumulative Displacement of the Case 6 model .....	120
Fig. 3-19: Average X- Component Displacement of Central Incisor Nodes over the Course of the Simulation .....	121
Fig. 3-20: Average X- Component Displacement of 1 <sup>st</sup> Molar Nodes over the Course of the Simulation	121
Fig. 3-21: Bone-Suture Volume Interface; Close-up of the Zygomaticotemporal Suture in the Trimmed Model.....	123
Fig. 3-22: Post Activation 1 <sup>st</sup> Principal Stress Contour Plots Following 1 <sup>st</sup> Appliance Activation.....	125
Fig. 3-23: Post Activation 1 <sup>st</sup> Principal Stress Contour Plots Following 29 <sup>th</sup> Appliance Activation .....	126
Fig. 3-24: Selected Nodes with the MPS/IMS Structure; Selected Nodes Circled for Ease of Identification .....	127
Fig. 3-25: Averaged 1 <sup>st</sup> Principal Stress of the Selected MPS/IMS Nodes for Partial Skull Simulation Cases 5, 6, and 7.....	128

Fig. 3-26: Averaged 1 <sup>st</sup> Principal Stress of the Selected MPS/IMS Nodes for Partial Skull Simulation Cases 5, 6, and 7; Only Looking at the 4-minutes following the 1 <sup>st</sup> Activation.....	128
Fig. 3-27: 1 <sup>st</sup> Principal Stress of the 18 MPS/IMS Nodes (See Fig. 3-24) for Partial Skull Simulation Case 6; Only Showing First Activation .....	129
Fig. 3-28: 1 <sup>st</sup> Principal Stress of the 18 MPS/IMS Nodes for Partial Skull Simulation Case 6 Compared to The Predicted Stress Based on the 1-D Relaxation Model and the reported 1 <sup>st</sup> Principal Strain for the Nodes at 5 seconds .....	130
Fig. 3-29: Simulation Load Point Reaction Forces versus Time.....	130
Fig. 3-30: Simulation Load Point Reaction Forces versus Time; First Four Appliance Activations .....	131
Fig. 3-31: Case 3 Partial Skull Model - MPS Neglected; 29 <sup>th</sup> Activation.....	134
Fig. 3-32: Case 6 Partial Skull Model – MPS/IMS Relaxation Model; 29 <sup>th</sup> Activation .....	135
Fig. 3-33: Case 8 Partial Skull Model - MPS Relaxation Model, IMS Stiff Linear Elastic Model; 29 <sup>th</sup> Activation .....	136
Fig. B-1: Specimen Geometry with Dimensions in mm; Thickness of 2mm .....	181
Fig. B-2: ANSYS Mooney-Rivlin and Response Function Results; 1 <sup>st</sup> Principal Stress versus 1 <sup>st</sup> Principal Strain .....	181
Fig. D-1: Specimen Geometry with Dimensions in mm; Thickness of 2mm .....	200
Fig. D-2: NURBS Half Skull in SolidWorks .....	201
Fig. D-3: HyperMesh Model .....	202
Fig. D-4: Partially Meshed Geometry in HyperMesh .....	203

## List of Common Symbols and Variables

$A$	-	Cross sectional area in mm <sup>2</sup>
$C_1, C_2, C_3$	-	Experimentally derived coefficients utilized by the 1-D creep equation
$dx$	-	Applied displacement from an appliance, measured in mm
$E$	-	Young's modulus in MPa
$E_B, E_S, E_{eff}$	-	Young's modulus for bone, suture, and total system
$E_\gamma, E_{SS}$	-	$\gamma$ -modified and spring suture model elastic modulus for stress relaxation behavior
$F$	-	Force in Newtons
$G(t)$	-	Shear moduli
$k$	-	spring constant in N/m
$K(t)$	-	Bulk moduli
$k_B, k_S, k_{eff}$	-	Spring constant of bone, suture, and total system
$t_0$	-	Time at appliance activation
$t_s$	-	Time from appliance activation, measured in units of seconds
$t_w$	-	Time from appliance activation, measured in units of weeks
$X_0$	-	Initial distance between the mini-screw implants
$x_B, x_S, x_{eff}$	-	Change in length of bone, suture, and total system
$X_B, X_S, X_{eff}$	-	Original length of bone, suture, and total system
$x_F$	-	Initial width of the suture volume in FEA simulations, measured in mm
$X_i$	-	Distance between mini-screw implants after appliance activation
$x_R$	-	Initial width of suture volume as estimated from the initial Romanyk et al. creep paper, measured in mm
$\alpha_i^{K,G}$	-	Prony series fractional coefficient
$\beta$	-	Analytically derived coefficient used to determine the Young's modulus at $t_0$ for Prony series input
$\gamma$	-	Geometrically derived coefficient used to modify $\varepsilon_R$ , unitless
$\varepsilon$	-	Resultant strain calculated from the 1-D creep equation, measured in mm/mm
$\varepsilon_0$	-	Applied strain from a screw-type appliance, measured in mm/mm
$\varepsilon_R$	-	Applied strain determined by appliance induced displacement divided by the original width between Mini-Screw Implants, measured in mm/mm
$\nu$	-	Poisson's Ratio
$\sigma$	-	Resultant stress calculated from the 1-D relaxation equation, units of MPa
$\sigma_0$	-	Stress from applied force from a constant force spring-type appliance, measured in units of MPa
$\sigma_c$	-	Cauchy stress
$\tau_i^{K,G}$	-	Prony series time coefficients

## Glossary of Common Terms

- +FE - A software module for ScanIP for generating FE meshes
- +NURBS - A software module for ScanIP for generating NURBS Surfaces
- ANSYS - Referring to the ANSYS Academic Teaching Advanced Mechanical APDL, R. 14.5.7
- CFS - Craniofacial Sutures
- FE - Finite Element
- FEA - Finite Element Analysis
- FEM - Finite Element Modelling
- FORTRAN - FORMula TRANslation; A high-level computer programming language suited to numerical analysis.
- FZS - Frontozygomatic Suture
- Hexahedral - A 6-sided cube shaped finite element, often with 8 or 20 nodes
- HyperMesh - A software package by Altair HyperWorks that can be used to mesh geometries for use in FEA
- IMS - Intermaxillary Suture
- LINK180 - 2-node bar-type element in ANSYS suitable for use in 3-D space
- MATLAB® - Numerical Analysis software package
- Mesh - A 3-D structure composed of simple polygonal elements used to define a more complex geometry
- MPS - Midpalatal Suture
- MSI - Mini-screw Implants
- MSS - Midsagittal suture (New Zealand White Rabbits)
- MST - Multiple Superposition Theory
- NURBS - Non-Uniform Rational B-Spline Surfaces
- Prony Series - A mathematical approximation function
- RTG - Rectilinear Testing Geometry
- ScanIP - Software package from Simpleware used for image processing
- Simpleware - Referring to software company Simpleware Ltd. Based in Exeter, UK
- SOLID185 - A 3-D 8-node structural solid element in ANSYS; Can be configured as a hexahedral or tetrahedral shape
- SOLID186 - A 3-D 20-node structural solid element in ANSYS; Can be configured as a hexahedral or tetrahedral shape
- SOLID187 - A 3-D tetrahedral 10-node structural solid element in ANSYS
- Tetrahedral - A 4-sided finite element, often with 4 or ten nodes
- Viscoelastic - Non-linear material model characterized by creep and stress relaxation behaviors
- ZMS - Zygomaticomaxillary Suture
- ZTS - Zygomaticotemporal Suture

# 1 Introduction and Project Background

The relevant background information and motivations for using Finite Element Analysis (FEA) for studying how the non-linear material properties of the Midpalatal Suture (MPS) affect the process of Maxillary Expansion (ME) are detailed in the following chapter.

## 1.1 Defining Maxillary Expansion

What is the process of ME? Why is this procedure performed? How is it enacted in patients? These questions are key to understanding the background and motivation of this study.

ME is an orthodontic procedure that utilizes a mechanical appliance to effect widening of the upper dental arch by use of outward mechanical force. This process widens the MPS along the midsagittal plane (Fig. 1-1). Commonly used by clinicians, it helps align the upper and lower dental arches, reducing malocclusion. It is also used to help in cases where adolescent patients suffer from sleep apnea or nasal respiratory issues as it may serve to expand airflow passages within the sinuses[1]. Fig. 1-2 shows an example of a bone-borne expander in-situ.

Patients who undergo this procedure are adolescents as the MPS must be unfused. As the patient ages through their teenage/puberty years, the palatal bone of the maxilla on either side of the MPS will become more inter-digitized. Even though the MPS may not fully fuse until mid-thirties [2], it is more common for patients that are past puberty to require surgical options for ME cases[3], [4], as the MPS must be surgically separated due to high levels of fusing or interdigitization of the bone margins [5, p. 18]. Needless to say, it is advantageous for ME treatment to be treated during adolescence.

Appliance types that can affect ME include designs that generate outward forces from mini-screw-jacks (hyrax), springs, shape memory alloys, or magnets [6]. The most common designs tend to be of the mini screw-jack type. Indeed, the first published description of ME in 1860 utilized a screw-type device activated by a notched coin.[7], [8]

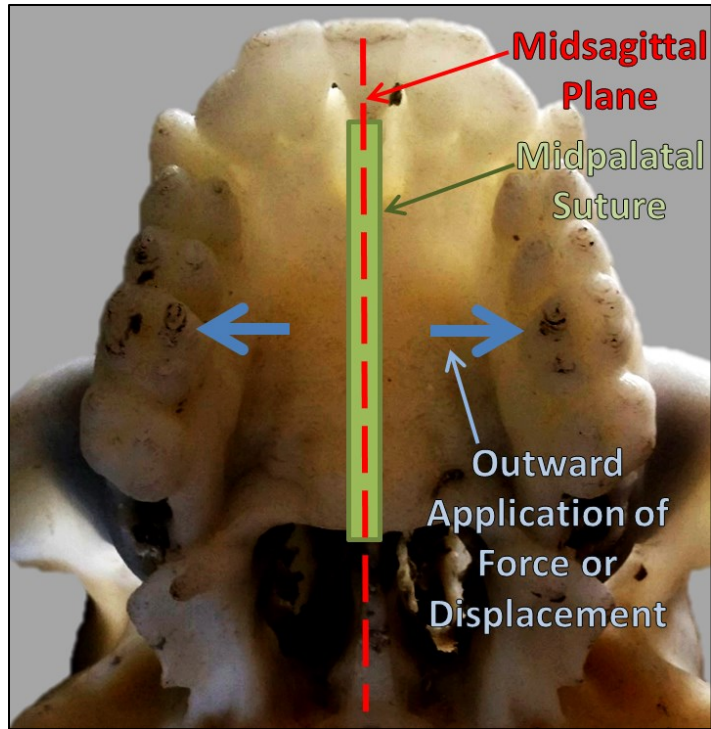


Fig. 1-1: Depiction of Outward Application of Expansion Forces or Displacement on a Picture of a 3-D Printed Cranium (Dentition of 3-D Printed Skull is not anatomically correct as there are an odd number of teeth)



Fig. 1-2: A Bone-Borne Appliance in a Patient's Mouth

## **1.2 Aims and Motivation**

The aim of this study was to take the innovative material models developed for the MPS by Romanyk et al. [9], [10] and incorporate them into 3-D FEA simulations. These models were to employ the non-linear strain creep and stress relaxation material models such that the interaction between the MPS and the maxillary palate would be better understood. Hopefully this research would allow for a greater understanding of the ME procedure, and create a foundation from which more advanced material models could be trained. Full skull FEA models built on this foundation could one day be used as research models or predictive models to test new appliances and expansion procedures. To understand the motivations behind this research, a clearer picture of the current state of FE modelling with regards to the MPS and ME is required.

### **1.2.1 Pre-2013 FEA Research in Modelling the MPS and ME**

In looking at the state of the research field prior to 2013, we look towards a published review paper by a colleague [11]. This paper was a systematic review of the state of FEA modelling of ME in adolescents. Within this review only papers that modelled a significant portion of the skull were included. Key attention was paid to how the MPS was modelled in the simulations. It was found that simulations fell into several main categories consisting of the maxillary suture being neglected [12]–[16], the suture being assigned a small elastic modulus [15], [17], [18], the suture being assigned a “partially ossified” elastic modulus [17], or the suture being assigned the properties of bone [17], [19]–[22]. Additionally, the 2003 Provatidis [18] study used a “pseudo-viscoelastic” model by applying displacement loads incrementally and reducing the residual stresses to zero between load steps.

Studies that neglect the sutures affect their simulation by causing artificial geometric discontinuities if the suture is not modelled or by changing the stress distribution throughout the model by removing the nodal constraints as the reaction forces on free surfaces must be inherently zero. For models that utilized properties of bone for the midpalatal suture, it was argued [11] that due to the low ossification rates (15%) of the MPS in adults in their 20s and 30s [23] bone properties for the MPS are unrealistic in ME simulations for adolescents.

For the studies included in the review that used low linear elastic properties for the MPS, it was reasoned that the homogenous, isotropic, and linear elastic material properties offered ease of model setup and computational speed advantages over using a non-linear viscoelastic model. Depending on study goals, a simpler material model would be adequate and preferable, even though the non-linear model would be more physically representative. A viscoelastic model would allow researchers to investigate a full ME treatment over time, with a focus on stress results in or near the MPS.

This review paper outlined a future where the MPS, with material specific viscoelastic properties, could be modelled in FEA with viscoelastic properties for the bone in the cranial segments of the model as well [24, Ch. 12], [25]. It is argued here that while a fully viscoelastic model (Bone and Sutures) should be an ultimate goal, the first progress step towards this would be to model just the MPS with non-linear properties.

### **1.2.2 Post-2013 FEA Research in Modelling the MPS and ME**

The findings of the review paper by Romanyk et al. were that although much work has previously been done in modelling the ME procedure, there had been no significant attempts at creating a model with tissue specific non-linear viscoelastic properties for the MPS. Since the 2013 publication of the review paper, the understanding of the non-linear properties of the MPS has been advanced. Additionally, several additional FEA studies have been published modelling the process of ME.

Romanyk et al. developed a series of constitutive equations and associated constants to describe the creep behavior of the midsagittal suture of New Zealand White Rabbits in the paper *“Towards a viscoelastic model for the unfused midpalatal suture: Development and validation using the sagittal suture in New Zealand White Rabbits”* [9]. These models were based upon experimental expansion data from a previous study by SS Liu et al. [26]. The models developed include the Quasi-Linear Viscoelastic method, the Modified Superposition Theory (MST) model, the Schapery’s method, and the Burgers model. Based on the fit results and comparisons, the MST model was determined to have the best fit for the experimental data. For the purposes of this study, the MST model was chosen for adaptation for FEA. This is due to

the more accurate fit of the model, as well as the simplistic equation form which would be less complicated to code into the FORTRAN based material subroutines of *ANSYS® Academic Teaching Advanced Mechanical APDL, Release 14.5.7* (ANSYS).

In “*Consideration for determining relaxation constant from creep modeling of nonlinear suture tissue*”, the subsequent paper by Romanyk et al. [10], the author determines relaxation constants for four different relaxation models. The four relaxation models include the two-term inseparable function, the three-term inseparable function, the three-term separable function, and the single term function. Each of these models are mathematically associated with a corresponding creep function. Utilizing the original New Zealand White Rabbit expansion data, creep constants were determined and transformed into relaxation model constants. Of the four models evaluated in this paper, the single term and three-term inseparable models were evaluated to be good approximations of the suture response. As the single term model was based upon the MST creep model that had previously been verified this is the model that was selected for this FEA study for the stress-relaxation adaptation. Although these models were again based upon a single force-expansion data set, they are the best available until subsequent work is done to base them on stress-relaxation data. This study built upon the work presented by Romanyk et al. at the ASME 2013 Summer Bioengineering Conference [27]

The follow-on study, “*Viscoelastic response of the midpalatal suture during maxillary expansion treatment*”, Romanyk et al. [28] tested the four viscoelastic models described in his previous paper using multiple applied displacement loads to investigate the effect of different appliances on suture tissue. Additionally, the single term model based on the MST creep model was tested to evaluate its suitability for use in simulating the suture response to a spring or magnet type device with decaying expansion forces.

In addition to this foundational work to characterize the viscoelastic behavior of the MPS, several other studies have been published by various authors looking at ME in adolescents. Of these, only a handful have been FEA focused. FEA work by Ludwig et al. in 2013 [29] simulated the procedure of ME while utilizing a viscoelastic model for the cranial bone structures. These

properties were not tissue specific and were not detailed in the paper. No craniofacial sutures were specifically incorporated and the MPS was neglected in the model.

Publications by Serpe et al. [30]–[32] focused on characterizing the mechanical environment of the maxillary complex utilizing densely meshed models. The model geometries in the 2014 papers modelled a partial skull geometry comprised of just the maxilla and some surrounding bone, MPS, and upper dentition [30], [31]. These models utilized a variety of boundary conditions to approximate the connection of the maxilla to the rest of the cranium. All material properties of these two models were linear elastic and the MPS and intermaxillary suture were treated as a single volume. In their 2015 paper[32], Serpe modelled a significant portion of the skull, the periodontal ligaments, the upper dentition, and a steel stepwise displacement tooth-borne expansion appliance. This analysis was unique in that in addition to the linear material properties for all other structures, it utilized a bilinear material model for the MPS and intermaxillary suture to simulate a mid-expansion partial suture failure. The bilinear model had an initial Modulus of Elasticity of 1MPa, with a transition stress of 0.1MPa, and a final modulus of 0.01MPa. The bilinear model simulations were consistent with the linear simulations, and it was conjectured by Serpe that a bilinear model would be a good option as it might have a lower computational time than a viscoelastic model.

### **1.2.3 Recent Microstructure Modelling of Sutures**

Although the creep and stress-relaxation models by Romanyk et al. can be considered macroscopic bulk material behavior models where the overall effect and reaction of the suture are presented, they do not consider the interdigitization or complexity of the bone-suture interfaces. Some research has been done in this field by authors such as Jasinowski et al.[33] and Maloul et al.[34] where the interdigitization of the bones has been modelled. This is by no means an in depth review of the subject, as it is only used for discussion and background information on additional directions that FEA modelling of cranial sutures can be taken.

The work of Jasinowski et al. in 2010 investigated a simplified waveform of the suture at multiple levels of interdigitization under both compressive and tensile loads [33]. These models investigated isotropic and orthotropic (matched orientation n-loading) material models. Key

results of this study included the observations that even under global compressive loads, portions of the suture material were still under tension due to shearing effects. As would be expected, the highest stresses were observed at the apexes of the suture waveform. The orthotropic material model simulated the embedded fiber structure of the suture.

Maloul et al. performed a similar FEA study on a coronal suture in 2014 [34]. This study looked at the effects of bone bridging across the suture gap of an idealized, interdigitized waveform suture geometry. This bone bridging was investigated as  $\mu$ CT images of the coronal suture showed morphology with both differing levels of interdigitization and bone bridging of the suture soft tissue. The idealized FEA geometry was also compared to  $\mu$ CT image derived FE models. Maloul et al. concluded that loading direction directly affected the energy absorption within the suture tissues, and that although the degree of interdigitization and bone connectivity impact the mechanical response of the suture, an overall distribution of variations within a given suture may cause an evening out of overall properties. This is used here as justification that depending on the goals of a study, a macroscopic bulk behavior model may be both adequate and advantageous due to the lower computation requirements than a fully meshed micro-scale geometry.

### 1.3 Creep

Creep, in reference to non-linear material models, is the tendency of some materials to continue to deform over time when a constant force is applied. Subjected to constant force, some materials experience creep strain curves, as seen in Fig. 1-3, that can go through three main phases. The primary phase (I) is characterized by a high initial deformation rate that starts to decelerate. The secondary phase (II) is characterized by a more constant deformation rate. In the tertiary phase (III), the deformation rate starts to accelerate towards part failure as the cross section of the material shrinks [35, p. 625]. This shrinkage, sometimes known as 'necking', is due to the partial incompressibility of most materials.

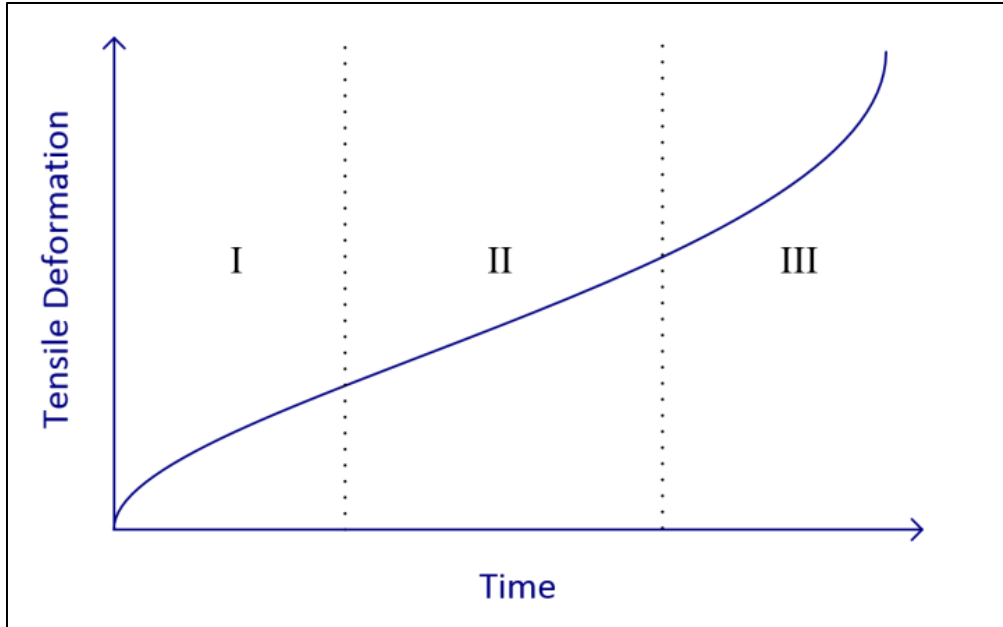


Fig. 1-3: Depiction of the Tensile Deformation of a Material Over Time Highlighting the Three Phases of Creep  
 I – Primary Creep; II – Secondary Creep; III – Tertiary Creep

Creep models describe the strain within a material as a function of the elapsed time and the previous strain within a material. Two of the common creep models are time hardening, eq. (1-1), or strain hardening eq. (1-2) [36]. Creep material models often incorporate a temperature dependency, as metals and plastics tend to soften at higher temperatures. Temperature dependency is not a concern in biological systems as warm blooded creatures maintain a fairly constant temperature, such that  $C_4 = 0$ .

$$\frac{d\varepsilon}{dt} = C_1 \sigma^{C_2} t^{C_3} e^{-\frac{C_4}{T}} \quad (1-1)$$

$$\frac{d\varepsilon}{dt} = C_1 \sigma^{C_2} \varepsilon_{cr}^{C_3} e^{-\frac{C_4}{T}} \quad (1-2)$$

Alternate and more complex creep models exist, however they were not relevant to this study and are not discussed here.

### 1.3.1 Overview of MPS Specific 1-D Creep Model

The 1-D Creep model used in this study was the MST model developed by Romanyk et al. [9]. This 1-D creep model, shown in eq. (1-3), was developed based on experimental measurements taken from a study done by S. Liu that expanded the Mid-Sagittal Suture of New Zealand White Rabbits using assumed constant force springs.

$$\varepsilon(t) = 2.2492\sigma_0^{0.4894}t_{weeks}^{0.4912} \quad (1-3)$$

This 1-D mathematical model is founded upon several base assumptions that are important to note. Without completely re-iterating the Romanyk paper, it is important to understand that this is a model that is very much based on the initial system conditions.

The creep model assumed that the applied tensile force from the expansion springs was constant and that the system maintained a constant cross sectional area as the suture tissue was stretched. These two assumptions thereby created a constant tensile stress within the system for the duration of the expansion. Additionally, this model assumed that the suture region is an isolated system that did not interact with the remainder of the skull system. Based on experimental measurements, this model utilized width measurements taken at the mini-screw implants. These implants transferred forces from the expansion springs to the bone and were implanted about 4 mm from the suture tissue. Utilizing these assumptions, a set of load specific material coefficients were determined. The material constants are discussed in further detail in Chapter 2.

This material specific creep equation model can be classified as a time-hardening model, and is not temperature dependent.

## 1.4 Viscoelastic Relaxation

A viscoelastic relaxation model can be characterized by the non-linear stress response of a material to a given deformation. When a viscoelastic material is subjected to a constant applied tensile strain, the stress within the material will peak. As time passes, the stresses within the material relax. Fig. 1-4 shows a characterization of the stress reaction of a viscoelastic material being subjected to series of stepped tensile displacements.

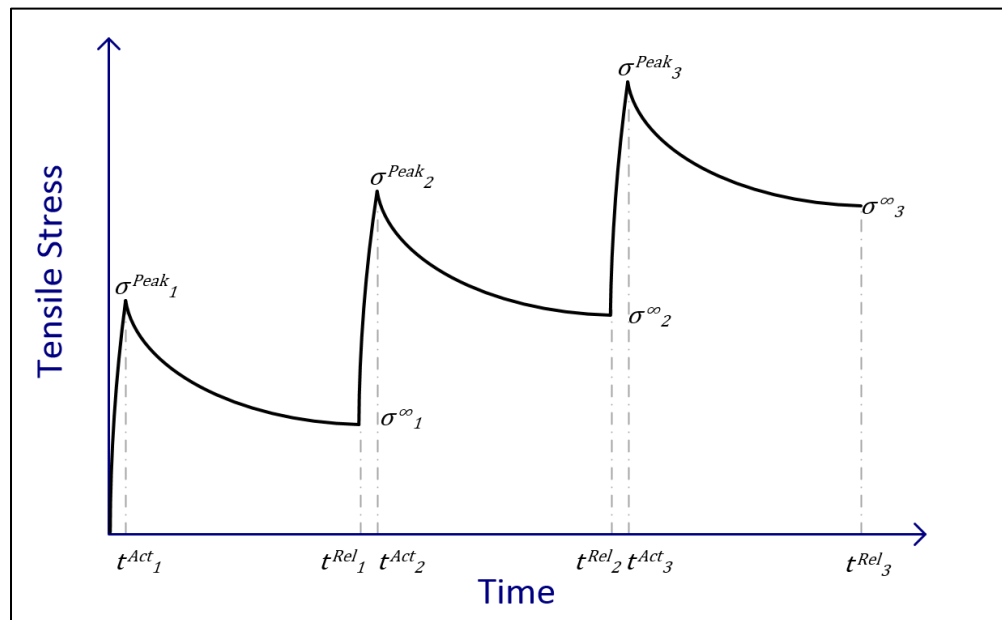
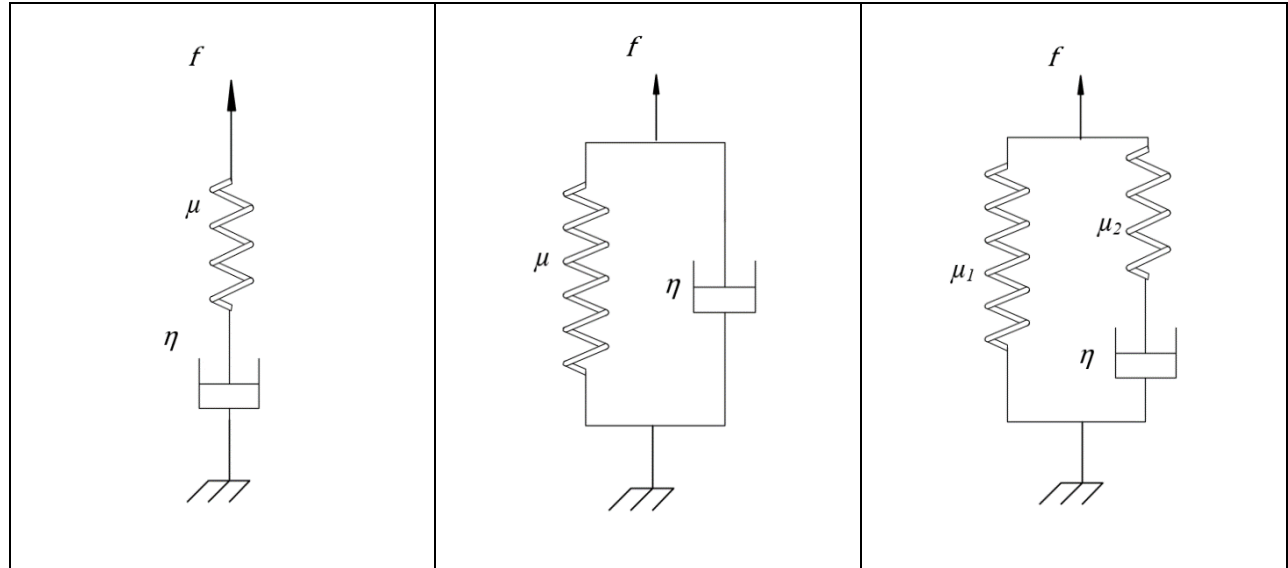


Fig. 1-4: Depiction of the Stress Relaxation of a Viscoelastic Model Subjected to Sequentially Applied Displacements

As can be seen, this material experiences a peak stress,  $\sigma_{peak_n}$ , after the application of each application of displacement. As time passes the stresses relax towards a constant stress,  $\sigma_{\infty_n}$ , which describes the material's relaxed state.

Viscoelastic materials are often mathematically described using a combination of linear elastic springs and viscose dampers, hence the name. Common simplistic viscoelastic models include the Maxwell model [37, p. 17], eq. (1-4), the Kelvin-Voigt model [37, p. 20], eq. (1-5), and the Simplified Linear Solid model [37, p. 32], eq. (1-6). Spring-damper diagrams of these three models are presented in Fig. 1-5.



(A)  
Maxwell Model

(B)  
Kelvin-Voigt

(C)  
Standard Linear Solid

Fig. 1-5: Simple Viscoelastic Models Represented Using Linear Springs and Dampers

$$\sigma(t) = \left( \frac{d\varepsilon}{dt} - \frac{1}{\mu} \frac{d\sigma}{dt} \right) \eta \quad (1-4)$$

$$\sigma(t) = \mu\varepsilon(t) + \eta \frac{d\varepsilon(t)}{dt} \quad (1-5)$$

$$\sigma(t) = \frac{d\varepsilon}{dt} (\mu_1 + \mu_2) \frac{\eta}{\mu_2} + \mu_1\varepsilon(t) - \frac{\eta}{\mu_2} \frac{d\sigma(t)}{dt} \quad (1-6)$$

These equations, derived using lumped capacitance methods, show the 1-D stress responses of the three models over time when subjected to changing stresses and strains. These are by no means the only viscoelastic models, but are included here for background theory. Non-linear viscoelastic models differ from linear viscoelastic models in that the instantaneous relaxation moduli of the materials are also dependent on the magnitude of strain they are subjected to, i.e.  $\mu(\varepsilon)$ .

The Generalized Maxwell model [38], which can be visualized as a Standard Linear Solid model in parallel with an n-count of simple Maxwell models, is a viscoelastic model that can be used to approximate the relaxation behavior of many materials. This model is discussed in greater detail in Chapter 2 as part of the Theory and Methods.

### 1.4.1 Overview of the MPS Specific 1-D Viscoelastic Relaxation Model

The 1-D Relaxation model, see eq. (1-7), adapted for FEA in this study was created by Romanyk et al. [10] as a mathematical development of the previously discussed creep model. The numerical coefficients of this model are based on the averaged load specific coefficients of the creep model.

$$\sigma(t) = 0.4894(0.2880\varepsilon_0 t_{weeks}^{-0.4912})^{\frac{1}{0.4894}} \quad (1-7)$$

This model is utilized to determine the decaying stress within the suture as a function of time and as a function of initially applied stress. As a mathematical adaptation of the creep model, the stress relaxation is not directly based on experimental stress-time data of the suture tissue. Consequently, this model does not incorporate a term to define a relaxed elastic modulus at infinite time. This means that mathematically this stress model tends towards zero stress as time increases.

The assumptions that underpin this model are the same as for the creep model; i.e. – the model is one dimensional, describes a macroscopic bulk material behavior of the suture-bone interface region, does not consider material deformation or reformation, and is based on initial conditions.

### 1.5 Additional Craniofacial Sutures

The main focus of this thesis was the incorporation of the non-linear creep and relaxation models into the ANSYS FEA program and the testing of the relaxation model in a partial skull geometry. During the background research for this study, it was hypothesized that the other craniofacial sutures may play a large part in both the final displacement of the dentition after ME as the sutures may act as hinging points. It was also thought that having the craniofacial sutures deform as the maxilla move would have an effect on the forces required to affect expansion. This line of reasoning was derived from reading “*The Human Facial Sutures: A Morphologic and Histologic Study of Age Changes from 20 to 95 years*” by Miroue et al. [2] which tracked the ossification of the craniofacial sutures and found that CFS are not completely fused before the fifth to eighth decade of life. Additionally, a study by Wang et al. [39] which

simulated a full skull FEA of a macaque skull showed that CFS with soft linear elastic properties provide an impact buffer during chewing mechanics. Provatidis et al (2006) looked at the effect of using un-ossified linear material properties for the maxillary, midsagittal, median palatine sutures in addition to the MPS. [19]

To this end, additional craniofacial sutures were incorporated into this study's partial skull geometry. As literature is lacking in exact material properties or models of these sutures, stiff linear elastic properties were used to assign the same properties as the surrounding bone to these structures or soft linear elastic properties. The results of these two configurations were then compared and discussed.

## **1.6 Outline of Overall Method of Thesis Research**

As made apparent in the preceding sections, ME is an orthodontic procedure that is utilized to widen the upper dental arch to alleviate dental alignment issues and nasal respiratory issues. The biomedical understanding of the procedure has previously studied the overall geometry of the system, without including tissue specific non-linear material properties of the craniofacial sutures involved. A main factor for previous studies forgoing non-linear material models for the MPS is the lack of tissue specific models due to the difficulty in procuring material specific experimental data.

Armed with creep and relaxation models developed specifically for the MPS, this thesis aims to adapt these models for use in FEA. The flowchart in Fig. 1-6 provides an outline of the path taken in undertaking this research project.

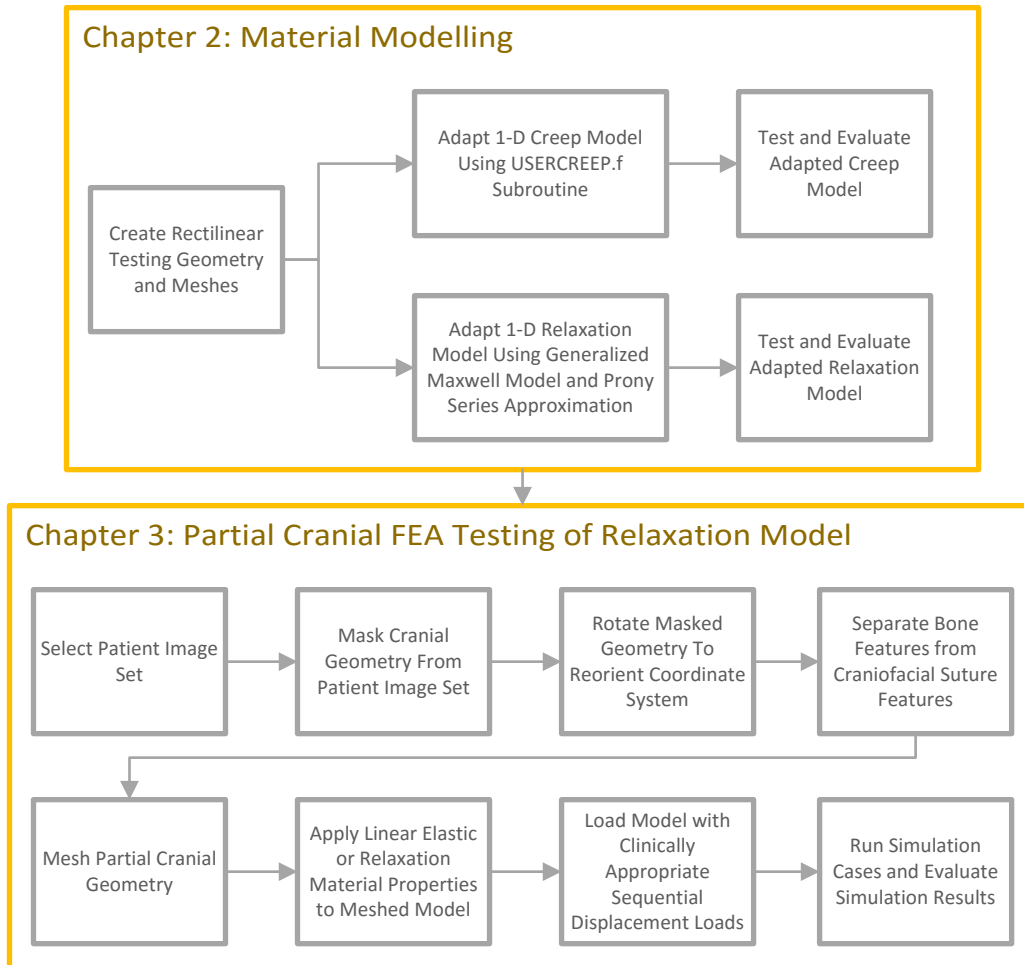


Fig. 1-6: Flowchart Outlining Overall Thesis Structure

The first stage, as detailed in Chapter 2 of this thesis, implemented in ANSYS 14.5 the creep and relaxation material models. The implementation of the 1-D models involved modifying an ANSYS material subroutine for the creep model and utilized an existing viscoelastic curve fitting routine for the relaxation model. In Chapter 2 the FEA implementation of the two models was tested utilizing a rectilinear testing geometry loaded. This verified the behavior of the material models in 3-D space under applied boundary conditions use to mimic the clinical loads used to develop both models. As detailed in Chapter 3 of this thesis, the relaxation material model was then incorporated in a partial skull model. Geometry for this model was based on cone beam CT image data taken of a patient prior to ME treatment. This patient had a bone-borne hyrax-type expander appliance. The testing of this model looks at how the final cumulative deformation of the model was affected by the material models of the midpalatal, intermaxillary,

zygomaticotemporal, zygomaticomaxillary, nasal, and frontozygomatic sutures [5, p. 3]. Of particular note was the difference in final expansion between models that utilized the relaxation model for the MPS in comparison to neglecting the suture or assigning soft linear elastic properties to the suture. Finally, in Chapter 4, the conclusions of this thesis will be discussed, identifying key results and their implications. The limitations of this study will be recognized and recommendations to correct for them will be discussed. Alongside this, a potential roadmap will be built for future research using this study as a springboard.

## 1.7 References

- [1] C. M. Cielo and A. Gungor, "Treatment Options for Pediatric Obstructive Sleep Apnea," *Curr. Probl. Pediatr. Adolesc. Health Care*, vol. 46, no. 1, pp. 27–33, Jan. 2016.
- [2] M. A. Miroue, "The Human Facial Sutures: A Morphologic and Histologic Study of Age Changes from 20 to 95 Years," Master of Science in Dentistry, University of Washington, 1975.
- [3] M. O. Lagravère, P. W. Major, and C. Flores-Mir, "Dental and skeletal changes following surgically assisted rapid maxillary expansion," *Int. J. Oral Maxillofac. Surg.*, vol. 35, no. 6, pp. 481–487, Jun. 2006.
- [4] M. Persson and B. Thilander, "Palatal suture closure in man from 15 to 35 years of age," *Am. J. Orthod.*, vol. 72, no. 1, pp. 42–52, Jul. 1977.
- [5] D. P. Rice, Ed., *Craniofacial sutures: development, disease and treatment*, vol. 12. Basel; New York: Karger, 2008.
- [6] D. L. Romanyk, M. O. Lagravere, R. W. Toogood, P. W. Major, and J. P. Carey, "Review of Maxillary Expansion Appliance Activation Methods: Engineering and Clinical Perspectives," *J. Dent. Biomech.*, vol. 1, no. 1, pp. 496906–496906, Jan. 2010.
- [7] E. Angell, "Treatment of irregularity of the permanent or adult teeth. Part 1.," *Dent. Cosm.*, vol. 1, pp. 540–544, 1860.
- [8] E. Angell, "Treatment of irregularity of the permanent or adult teeth. Part 2.," *Dent. Cosm.*, vol. 1, pp. 540–544, 1860.
- [9] D. L. Romanyk, S. S. Liu, M. G. Lipsett, R. W. Toogood, M. O. Lagravère, P. W. Major, and J. P. Carey, "Towards a viscoelastic model for the unfused midpalatal suture: Development and validation using the midsagittal suture in New Zealand white Rabbits," *J. Biomech.*, vol. 46, no. 10, pp. 1618–1625, Jun. 2013.
- [10] D. L. Romanyk, S. S. Liu, R. Long, and J. P. Carey, "Considerations for determining relaxation constants from creep modeling of nonlinear suture tissue," *Int. J. Mech. Sci.*, vol. 85, pp. 179–186, Aug. 2014.
- [11] D. L. Romanyk, C. R. Collins, M. O. Lagravere, R. W. Toogood, P. W. Major, and J. P. Carey, "Role of the midpalatal suture in FEA simulations of maxillary expansion treatment for adolescents: A review," *Int. Orthod.*, vol. 11, no. 2, pp. 119–138, Jun. 2013.
- [12] A. Jafari, K. S. Shetty, and M. Kumar, "Study of Stress Distribution and Displacement of Various Craniofacial Structures Following Application of Transverse Orthopedic Forces—A Three-dimensional FEM Study," *Angle Orthod.*, vol. 73, no. 1, pp. 12–20, Feb. 2003.

- [13] H. Işeri, A. E. Tekkaya, Ö. Öztan, and S. Bilgiç, "Biomechanical effects of rapid maxillary expansion on the craniofacial skeleton, studied by the finite element method," *Eur. J. Orthod.*, vol. 20, no. 4, pp. 347–356, 1998.
- [14] L. Culea and C. Bratu, "Stress Analysis of the Human Skull due to the Insertion of Rapid Palatal Expander with Finite Element Analysis (FEA)," *Key Eng. Mater.*, vol. 399, pp. 211–218, 2009.
- [15] H. Lee, K. Ting, M. Nelson, N. Sun, and S.-J. Sung, "Maxillary expansion in customized finite element method models," *Am. J. Orthod. Dentofacial Orthop.*, vol. 136, no. 3, pp. 367–374, Sep. 2009.
- [16] P. Gautam, A. Valiathan, and R. Adhikari, "Stress and displacement patterns in the craniofacial skeleton with rapid maxillary expansion: A finite element method study," *Am. J. Orthod. Dentofacial Orthop.*, vol. 132, no. 1, p. 5.e1-5.e11, Jul. 2007.
- [17] C. G. Provatidis, B. Georgiopoulos, A. Kotinas, and J. P. McDonald, "Evaluation of craniofacial effects during rapid maxillary expansion through combined in vivo/in vitro and finite element studies," *Eur. J. Orthod.*, vol. 30, no. 5, pp. 437–448, Oct. 2008.
- [18] C. Provatidis, B. Georgiopoulos, A. Kotinas, and J. P. McDonald, "In-vitro validation of a FEM model for craniofacial effects during rapid maxillary expansion," presented at the Proceedings of the IASTED International Conference on Biomechanics, 2003, pp. 68–73.
- [19] C. Provatidis, B. Georgiopoulos, A. Kotinas, and J. P. MacDonald, "In vitro validated finite element method model for a human skull and related craniofacial effects during rapid maxillary expansion," *Proc. Inst. Mech. Eng. [H]*, vol. 220, no. 8, pp. 897–907, Aug. 2006.
- [20] C. Provatidis, B. Georgiopoulos, A. Kotinas, and J. P. McDonald, "On the FEM modeling of craniofacial changes during rapid maxillary expansion," *Med. Eng. Phys.*, vol. 29, no. 5, pp. 566–579, Jun. 2007.
- [21] C. Holberg, N. Holberg, K. Schwenzer, A. Wichelhaus, and I. Rudzki-Janson, "Biomechanical Analysis of Maxillary Expansion in CLP Patients," *Angle Orthod.*, vol. 77, no. 2, pp. 280–287, Mar. 2007.
- [22] C. Holberg, L. Mahaini, and I. Rudzki, "Analysis of Sutural Strain in Maxillary Protraction Therapy," *Angle Orthod.*, vol. 77, no. 4, pp. 586–594, Jul. 2007.
- [23] B. Knaup, F. Yildizhan, and P. D. D. H. Wehrbein, "Age-Related Changes in the Midpalatal Suture," *J. Orofac. Orthop. Fortschritte Kieferorthopädie*, vol. 65, no. 6, pp. 467–474, Nov. 2004.
- [24] Y. C. Fung, *Biomechanics : mechanical properties of living tissues /*, 2nd ed. New York : Springer-Verlag, 1993.

- [25] T. P. M. Johnson, S. Socrate, and M. C. Boyce, "A viscoelastic, viscoplastic model of cortical bone valid at low and high strain rates," *Acta Biomater.*, vol. 6, no. 10, pp. 4073–4080, Oct. 2010.
- [26] S. S.-Y. Liu, L. A. Opperman, H.-M. Kyung, and P. H. Buschang, "Is there an optimal force level for sutural expansion?," *Am. J. Orthod. Dentofacial Orthop.*, vol. 139, no. 4, pp. 446–455, Apr. 2011.
- [27] D. L. Romanyk, S. S. Liu, M. G. Lipsett, M. O. Lagravere, R. W. Toogood, P. W. Major, and J. P. Carey, "Incorporation of Stress-Dependency in the Modeling of Midpalatal Suture Behavior During Maxillary Expansion Treatment," p. V01BT55A002, Jun. 2013.
- [28] D. L. Romanyk, C. Shim, S. S. Liu, M. O. Lagravere, P. W. Major, and J. P. Carey, "Viscoelastic response of the midpalatal suture during maxillary expansion treatment," *Orthod. Craniofac. Res.*, vol. 19, no. 1, pp. 28–35, Feb. 2016.
- [29] B. Ludwig, S. Baumgaertel, B. Zorkun, L. Bonitz, B. Glasl, B. Wilmes, and J. Lisson, "Application of a new viscoelastic finite element method model and analysis of miniscrew-supported hybrid hyrax treatment," *Am. J. Orthod. Dentofacial Orthop.*, vol. 143, no. 3, pp. 426–435, Mar. 2013.
- [30] L. C. T. Serpe, L. A. González-Torres, R. L. Utsch, A. C. M. Melo, and L. C. De, "Evaluation of the mechanical environment of the median palatine suture during rapid maxillary expansion," presented at the Biodental Engineering II - Proceedings of the 2nd International Conference on Biodental Engineering, BIODENTAL 2012, 2014, pp. 63–68.
- [31] L. C. T. Serpe, L. A. G. Torres, F. P. De, A. C. M. M. Toyofuku, and L. C. De, "Maxillary biomechanical study during rapid expansion treatment with simplified model," *J. Med. Imaging Health Inform.*, vol. 4, no. 1, pp. 137–141, 2014.
- [32] L. C. T. Serpe, L. Casas, E. B. De, A. C. M. M. Toyofuku, L. A. González-Torres, L. C. T. Serpe, L. Casas, E. B. De, A. C. M. M. Toyofuku, and L. A. González-Torres, "A bilinear elastic constitutive model applied for midpalatal suture behavior during rapid maxillary expansion," *Res. Biomed. Eng.*, vol. 31, no. 4, pp. 319–327, Dec. 2015.
- [33] S. C. Jasinowski, B. D. Reddy, K. K. Louw, and A. Chinsamy, "Mechanics of cranial sutures using the finite element method," *J. Biomech.*, vol. 43, no. 16, pp. 3104–3111, Dec. 2010.
- [34] A. Maloul, J. Fialkov, D. Wagner, and C. M. Whyne, "Characterization of craniofacial sutures using the finite element method," *J. Biomech.*, vol. 47, no. 1, pp. 245–252, Jan. 2014.
- [35] A. P. Boresi, *Advanced mechanics of materials*, 6th ed. New York : John Wiley & Sons, c2003.

- [36] “Ch. 3.5.5: Creep,” in *ANSYS® Academic Teaching Advanced, Release 14.5, Help System, Mechanical APDL Material Reference*, .
- [37] R. M. Christensen, *Theory of viscoelasticity an introduction*, 2nd ed. New York : Academic Press, 1982.
- [38] “Ch. 3.7.1: Viscoelastic Formulation,” in *ANSYS® Academic Teaching Advanced, Release 14.5, Help System, Mechanical APDL Material Reference*, ANSYS, Inc.
- [39] Q. Wang, A. L. Smith, D. S. Strait, B. W. Wright, B. G. Richmond, I. R. Grosse, C. D. Byron, and U. Zapata, “The Global Impact of Sutures Assessed in a Finite Element Model of a Macaque Cranium,” *Anat. Rec. Adv. Integr. Anat. Evol. Biol.*, vol. 293, no. 9, pp. 1477–1491, Sep. 2010.

## **2 Adapting a 1-D Constitutive Models for Use in 3-D Finite Element Modeling**

### **2.1 Introduction**

Previous Finite Element Analysis (FEA) modelling studies of the maxillary expansion procedure have neglected the presence of the Midpalatal Suture (MPS), used linear material properties, or utilized unspecified viscoelastic material properties [1]. The structural response of the cranium and MPS to maxillary expansion could be better understood in FEA using tissue specific material models for the MPS. Romanyk et al. [2], [3] developed 1-D creep and relaxation constitutive equations to describe the non-linear material response of the MPS.

In this chapter, the details of the work done to incorporate these creep and relaxation material models in the ANSYS Mechanical APDL (ANSYS® Academic Teaching Advanced, Release 14.5.7) program such that the non-linear material properties of the MPS can be simulated in FEA are presented. Adaptation of the creep and relaxation material models in ANSYS was limited to using the existing user modifiable capabilities of the software. This streamlined the process, avoided the creation of new material subroutines, and allowed easy replication of these methods on other computer systems.

### **2.2 Theory and Methods**

In FEA, three aspects are critical to achieving accurate results: geometry, mesh resolution, and material properties [4]. The following sections detail the adaptation of the 1-dimensional (1-D) material models developed by Romanyk et al. such that the non-linear material responses they describe are properly simulated in FEM. First, the tissue specific creep and relaxation models will be reviewed and the model testing geometry detailed. Secondly, a geometrically driven modification factor will be derived and applied to both models. Next, the method of incorporating the creep model an ANSYS user modified subroutine will be detailed. Following this, the process of approximating the time dependency of the relaxation model using a Maxwell viscoelastic model will be detailed. Finally, the FEA load cases used to test both material models will be discussed.

### 2.2.1 Model Development Evolution

The progression from the original experimental data and the 1-D creep and relaxation models through to the FE material modelling presented in this chapter needs clarification. To begin, the original rabbit experiments performed by Liu [5] applied force using springs with force values of 0.49N, 0.98N. Width measurements were taken 2-weeks apart at the Mini-screw Implants (MSI) over the course of 6-weeks. These expansion measurements were taken such that expansion of the Midsagittal Suture (MSS) may be correlated to the tensile forces applied to suture material.

From this, Romanyk developed 1-D creep and relaxation models. The 1-D creep model was trained and verified using the experimental expansion data, while the 1-D relaxation model was mathematically derived from the finalized 1-D creep model. As such, the relaxation model was not verified against experimental data, since experimental stress versus time data was unavailable.

Finally, the FE material modelling of this study aimed to replicate the behavior of these 1-D material behaviour models in ANSYS. To do this, the 1-D models had to be improved to account for a change in assumed suture region initial dimensions. This material dimension change effected the resultant strain values for the creep model as well as the input strain value for the relaxation model. This will be discussed further in Section 2.2.4. FE simulation results were compared to the theoretical suture responses as calculated by the 1-D models. This was done to have a consistent methodology between the two models. As the FE material models aimed to replicate the 1-D model behavior, they are not directly related to the experimental rabbit data.

### 2.2.2 Creep and Relaxation Models

The Modified Superposition Theory (MST) Creep Model created by Romanyk was based on experimental data collected by S. Liu regarding the MSS expansion of New Zealand White Rabbits [2], [3], [5]. The S. Liu study subjected the rabbits to constant force expansion of the MSS with expansion measurements taken over six weeks. The forms of the two material models were based on the geometry detailed in Fig. 2-1. The strains in the following models are calculated with regard to the original distance between the Mini-Screw Implants (MSI), 9.72 mm, and the stresses are calculated with respect to the cross sectional area of 2.19mm x 24 mm (52.56 mm<sup>2</sup>) [5], [6].

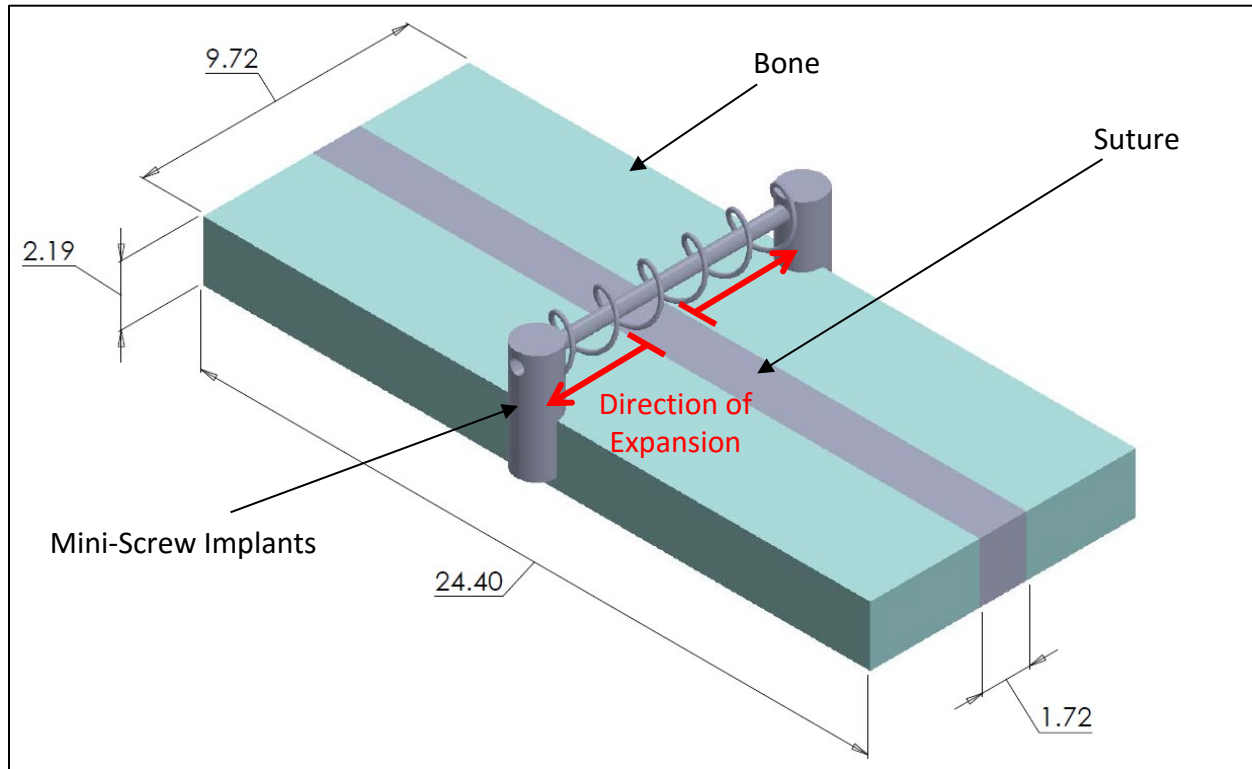


Fig. 1-7: MSS Geometry Approximation Utilized by Romanyk et al.

The MST model eq. (2-1) describes the progression of strain in the MPS as a function of time and constant applied stress; the time variable  $t$  is in units of weeks. Coefficients  $C_1$ ,  $C_2$ , and  $C_3$  were determined for the 3 separate constant force loading cases (0.49N, 0.98N, and 1.96N) applied to the rabbits [2]. The stress,  $\sigma_0$ , was defined by dividing the applied spring force by the cross sectional area of the suture. The load specific coefficients determined by Romanyk, as well as the average coefficients used for general force loading cases are listed in Table 2-1 below.

$$\varepsilon_R(\sigma_0, t_w) = 2 * C_1 t_w^{C_2} \sigma_0^{C_3} \quad (1-8)$$

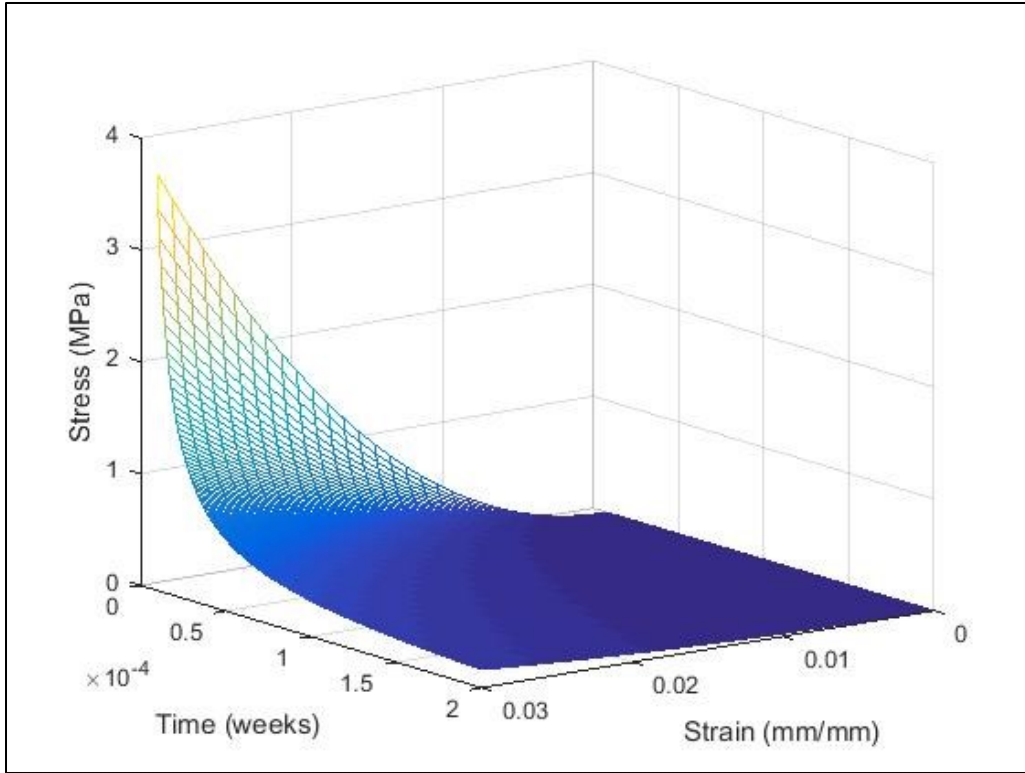
Table 1-1: MST Model Coefficients

Coefficients	Nominal Coefficients			Average Coefficients
	50g (0.49N)	100g (0.98N)	200g (1.96N)	
$C_1$ (1/wk <sup>C2</sup> MPa <sup>C3</sup> )	1.0981	1.1275	1.1481	1.12457
$C_2$	0.5777	0.5077	0.3883	0.4912
$C_3$	0.5211	0.4634	0.4837	0.4894

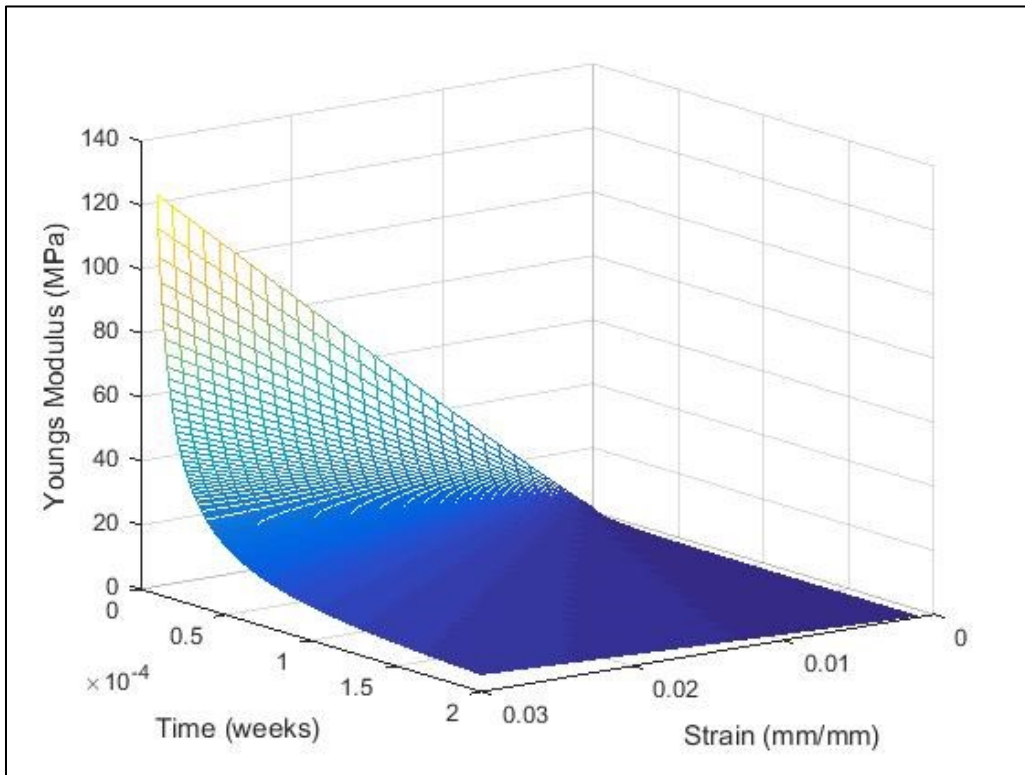
The single-term relaxation model eq. (2-2) [3] is a further development of the MST creep model that was based on the S. Liu constant force expansion data. This model calculates tissue stress as a function of time,  $t_w$ , in weeks, as well as the initial applied strain,  $\varepsilon_0$  in mm/mm.

$$\sigma_R(\varepsilon_{0R}, t_w) = 0.4894(0.2880\varepsilon_{0R} t_w^{-0.4912})^{\frac{1}{0.4894}} \quad (1-9)$$

The numerical coefficients utilized in the published form of the equation were derived from the averaged coefficients from the creep model, detailed in Table 2-1 above. The surface plots in Fig. 2-2 visually demonstrate the stress (A) and elastic modulus (B) response of the relaxation equation as functions of time and applied strain. Fig. 2-2 (A) shows how the stress response has a nearly parabolic relationship to the applied strain component, but that in Fig. 2-2 (B) the Elastic Modulus response to the applied strain becomes a nearly linear relationship.



(A)



(B)

Fig. 1-8: Stress (A) and Elastic Modulus (B) Response of the Relaxation Model Over Time to Variation in Applied Strain.

### 2.2.3 Rectilinear Testing Geometry

The Rectilinear Testing Geometry (RTG) used in the FEA verification of the material model verification analysis was derived from the measurements used by Romanyk in developing both the creep and relaxation mathematical models. As can be seen in Fig. 2-1, the distance between the MSI was approximated as 9.72mm, based on measurement averages in S. Liu's study [5]. The thickness of the bone suture interface was 2.19mm [5]. Additionally, the length of the considered suture was 24mm [6]. The main unknown of this geometry was the actual distance between the center of the MSI and the bone/suture interface, due to measurement limitations and irregularities of biological structures [5]. The creep and relaxation models were based on this approximation of a uniform rectilinear geometry. Romanyk et al. estimated this distance as approximately 4 mm [2]. For this analysis, 4mm was used for the finite element model. Physiologically, there is bone growth during suture expansion and causal relationships have been identified relating bone formation to expansion forces [5]. Since the bone formation rate had not been quantified as a function of applied forces, it was unaccounted for in the creep and relaxation models [2], [3]. As such, bone formation was not modelled in this FEA study. This limited scope and focused the study on the material behavior of the suture tissue.

In creating the RTG for use in ANSYS, it was decided to utilize the sagittal plane as a symmetry boundary condition, thereby requiring only half of the overall geometry to be modelled. This was done to increase computational speed and reduce memory requirements by reducing the number of nodes and elements required. This geometry is shown in Fig. 2-3 with the natural and applied boundary conditions highlighted.

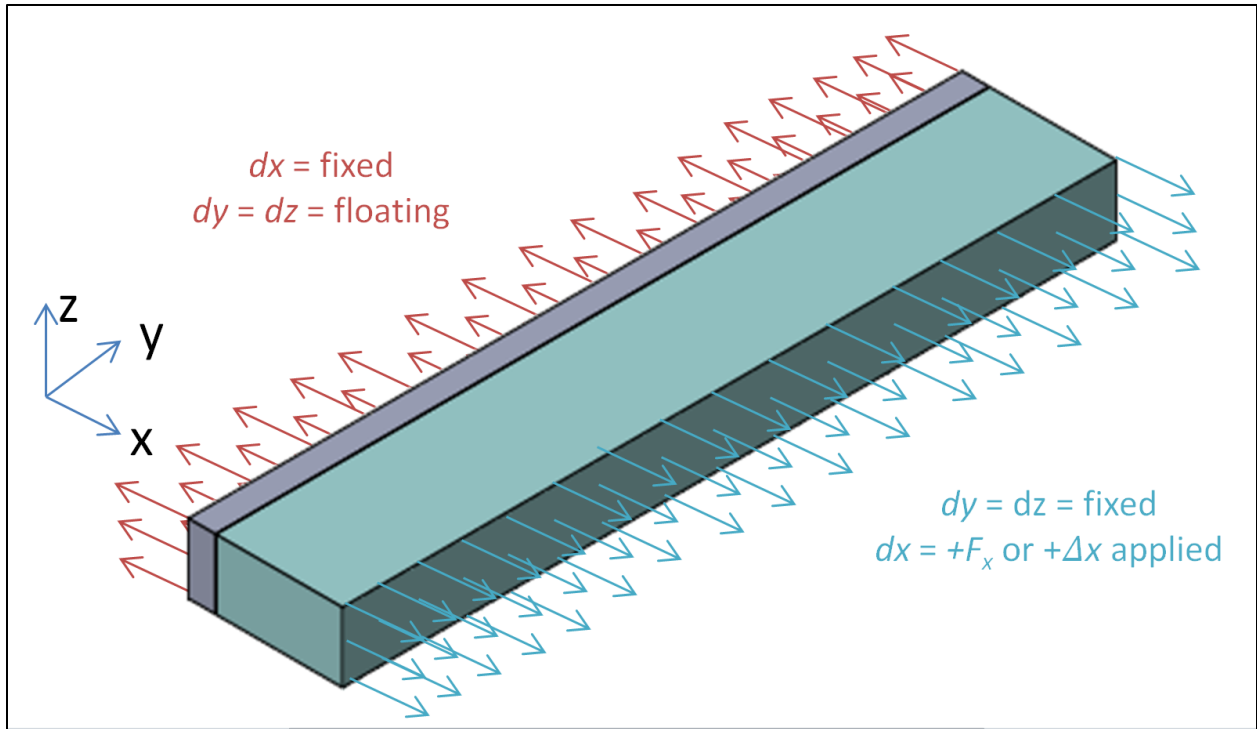


Fig. 1-9: Depiction of RTG with Applied and Natural Boundary Conditions

It should be noted that the applied boundary conditions shown in Fig. 2-3 would be an applied force, an applied pressure, or an applied displacement, depending on the simulation and element configuration. Forces and displacements were uniformly applied to the bone surface opposite the midsagittal plane. This uniform load application was used in FE to replicate the uniform loading assumed by Romanyk et al. in deriving the creep and relaxation constants. This was done even though the Lui et al. rabbit experiments applied expansion loads to the MSIs, which could be better approximated as point application of loads.

The RTG was meshed in multiple configurations for different tests. Table 2-2 details the various model mesh configurations.

Table 1-2: RTG Mesh Configurations

Simulation Sets	Suture Material Element Type	Suture Element Mesh Size	Bone Material Element Type	Bone Element Size	Meshing Method
USERCREEP.f Simulations	2-Node Bar (LINK180)	0.86mm long	8-Node Brick (SOLID185)	0.219 mm x 0.244 mm x 1mm	Manual
		constant cross sectional area			
	2-Node Bar (LINK180)	0.86mm long rigid volume	8-Node Brick (SOLID185)	0.219 mm x 0.244 mm x 1mm	
		16-Node Brick (SOLID186)	0.2 mm x 1mm x 1mm	16-Node Brick (SOLID186)	
0.05 mm x 0.5 mm x 0.5 mm	0.5 mm x 0.5 mm x 0.5 mm				
Relaxation Simulations		0.2 mm x 3 mm x 3 mm		3 mm x 3 mm x 3 mm	Auto-Meshed

The models utilized multiple element types, summarized in Table 2-3, particularly for creep related simulation such that the multiple available element types could be evaluated for their accuracy in replicating the predicted material model responses to loading.

**Table 1-3: Summary Element Types Used in ANSYS FEA Simulations**

Element Name	Element Type	Usable in 3-D Space	Mid-Side Nodes	Material Model Applicability	Model Use
LINK180	2-Node Bar Constant Cross Sectional Area	Yes	N/A	Linear and Non-Linear	RTG
LINK180	2-Node Bar Rigid Element Volume	Yes	N/A	Linear and Non-Linear	RTG
SOLID185	8-Node Brick; 4-Node Tetrahedral	Yes	No	Linear and Non-Linear	RTG; Partial Skull*
SOLID186	20-Node Brick	Yes	Yes	Linear and Non-Linear	RTG

\*Utilized In Partial Skull Models Due to Simpleware Mesher

Of the element types detailed in Table 2-3, all elements, except the 2-node bar elements, require the assumption that the material of the bone-suture region behaves in a homogenous manner regardless of direction of deformation (shear, compression, tension) and are therefore isotropic. The two-node bar elements are almost direct approximations of the Romanyk 1-D models. Even though the bar elements exist and act in 3-D space; they are essentially 1-D elements in their local geometry. For the 2-node bar element, the user can specify either a rigid cross section or an incompressibility condition. The rigid cross section ensures a constant stress for a given applied force, however the elements' volume will change as the length of the bar element changes. The incompressibility condition specifies a constant element volume where the cross sectional area reduces as the element lengthens along its axis. Under the rigid cross section element option, the principal stress remains constant and reflects the original 1-D creep model initial constant stress condition. Conversely, the elements' incompressibility option approximates the cross sectional necking deformation under tensile stain. The entire SOLID18X family of elements are compatible with ANSYS' Creep and Prony models [7]. They are able to calculate large deflection and strain.

## FE Model Meshing for 2-Node Bar Element Suture

The first FE model configuration was manually meshed as it utilized bar elements for the suture region due to the inclusion of both 2-node bar and 8-node brick element types. The code used to mesh the model can be found in Appendix A. The code utilized the dimensions of the RTG model and parametric variables to define a nodal mesh of the model. A set of 2-node bar elements were generated between the sagittal plane and the suture-bone interface plane, and 8-node brick elements were then generated to define the bone region of the RTG. This FEA model is shown in Fig. 2-4.

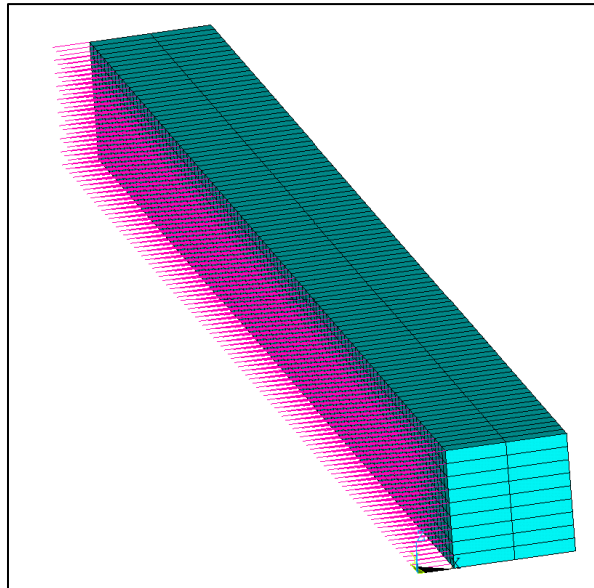


Fig. 1-10: Figure of FEA model with 2-Node Bar and 8-Node Brick Elements

The 2-node bar RTG was not generated using primitive shapes; as such, faces could not be selected. Natural and applied boundary conditions were applied on user-selected node sets instead of user-selected areas. For applied force/pressure boundary conditions, the overall applied pressure,  $P$ , was multiplied by the cross sectional area of the model,  $A$ , and divided by the number of nodes,  $N$ , on the relevant model surface. This resulted in a force per node,  $F_n$ , value that was then applied to each individual node on the relevant model surface, eq. (2-3).

$$F_n = \frac{P}{A * N} \quad (1-10)$$

## FE Model Meshing for 8-Node Brick Element Suture

The second FEA model configuration utilized the 8-node brick elements for both the suture and bone regions of the RTG. Automatic meshing routines in ANSYS were utilized for this model configuration. The bone region was coarsely meshed, with a control size of 1mm, as the deformation anticipated in the region was anticipated to be negligible. A finer mesh control size of 0.2mm was used for the suture region. This process resulted in nearly cubic elements in the bone region. Brick elements in the suture region had a flattened profile, measuring 0.172mm thick by 0.976mm wide and 0.73mm tall. The model is depicted in Fig. 2-5.

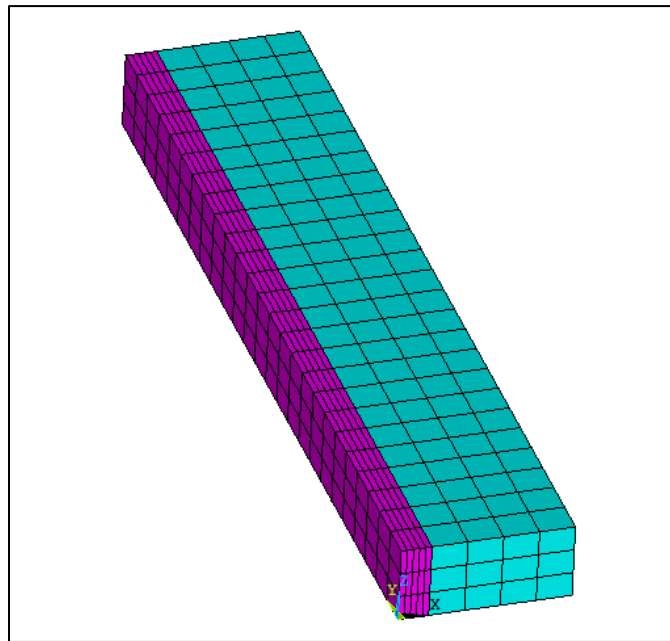


Fig. 1-11: Figure of FEA model with 8-Node Brick Elements

The flattened profile of the elements in the suture region allowed the same element density in the  $x$ - and  $y$ -directions as the bone volume, negating any requirements for a mesh size transition. The higher density across the halved width of the suture region, as can be seen in Fig. 2-4, allows for more detail of the deformed suture geometry.

The flattened initial profile of the suture elements would allow for a better aspect ratio of the deformed shape compared to an initially cubic element. Fig. 2-6 shows the anticipated deformation of two elements of identical volume, one initially cubic and the other initially flattened.

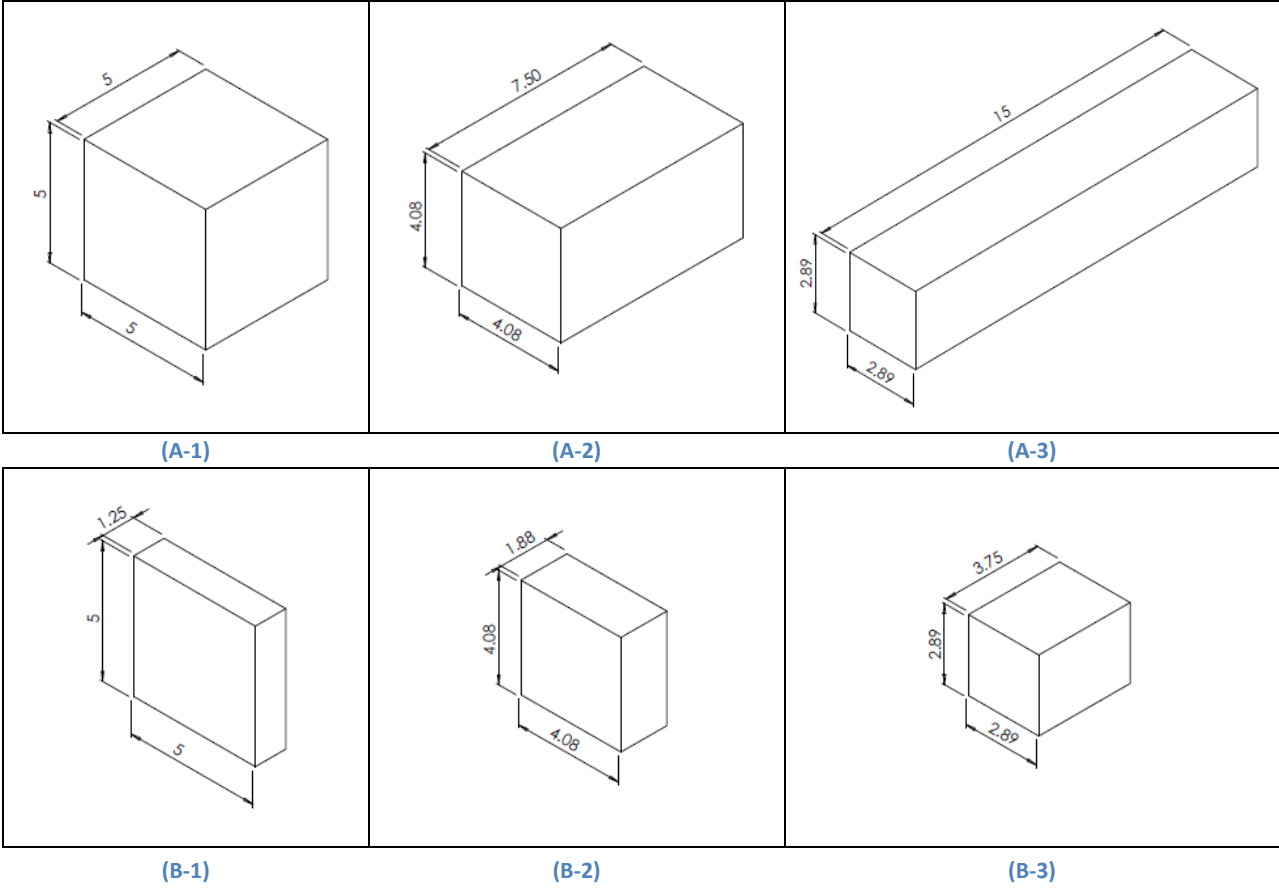


Fig. 1-12: Anticipated Deformation of Initially Cubic (A) and Flattened (B) Elements Under 0%, 50%, and 200% Tensile Strain

#### 2.2.4 Geometrically Derived Gamma Coefficient

The original creep and relaxation models, as derived by Romanyk, were based on the geometry in Fig. 2-3. These models were developed using strain values calculated from radiograph measurements taken from the width between the MSI using the eq. (2-4). The reasoning for this assumption was that using the MSI width measurements made the two material models less sensitive to errors in measurement, and a lack of data of the actual widths of the rabbit's MSS widths throughout the S. Liu experiments. The equations are therefore bulk property models of the behavior of the combined bone-suture materials in a volume region similarly sized to the volume bounded by the MSI of 9.72mm x 2.14mm x 24.4mm.

$$\varepsilon_R = \frac{X_i - X_0}{X_0} \quad (1-11)$$

Where  $X_0$  was the initial measurement of the width between the MSIs in the S. Liu rabbit experiment,  $X_i$  was the MSI width measurement after appliance activation, and  $\varepsilon_R$  is defined as the strain value as calculated by Romanyk from the original measurement set.

Defining  $dx$  as the appliance activation distance, we can define the identity of  $X_i$  in eq. (2-5). Substituting the eq. (2-5) identity of  $X_i$  into eq. (2-4) yields the equation set in eq. (2-6).

$$X_i = X_0 + dx \quad (1-12)$$

$$\varepsilon_R = \frac{(X_0 + dx) - X_0}{X_0} = \frac{dx}{X_0} \quad (1-13)$$

The original system width,  $X_0$ , utilized by Romanyk in calculating strain was 9.72mm. This is based on the average initial widths between the MSIs, which were placed a distance from the rabbit MSS. However, for an FEA simulation it is impractical for a nearly 1cm thick volume of tissue to be sectioned from the geometry of an adolescent skull to be allocated non-linear tissue properties. To do so would be quite geometrically dissimilar to the actual physical system. For the purpose of this FEA analysis, the suture region of the bulk macro material behavior of the Romanyk models was changed to the assumed 1.72mm width of the MSS.

Essentially, the original width of 9.72mm is not representative of the width of the suture region in an adolescent skull, therefore an initial width of 1.72mm was utilized. To produce the same results as the unmodified system, the two 1-D models required a modification factor to account for the change to the initial system dimensions.

To accomplish this, the equations had to be modified to account for the smaller original width from which strain would be calculated. These improvements to the original 1-D models introduced a correction factor,  $\gamma$ , that replaced the original Romanyk strain variable,  $\varepsilon_R$ , with the term  $\gamma\varepsilon_\gamma$  which is defined in the following derivations.

In order to do this, the variable  $x_F$ , which is the original width of the FE model suture region, was defined along with  $x_R$ , which is the original width of the MSS in the simplified Romanyk geometry.  $x_R$ , based on the MSS width, is equal to 1.72mm. Meanwhile,  $x_F$  is variable depending on the geometry of the FE model. In the case of the RTG,  $x_F$  is 1.72mm. Multiplying eq. (2-6) by  $x_R/x_F$ , which is essentially a factor of 1, and rearranging results in eq. (2-7).

$$\varepsilon_R = \frac{dx}{X_0} * \frac{x_R}{x_F} = \frac{dx}{x_F} * \frac{x_R}{X_0} \quad (1-14)$$

From this equation, the adjustment variable  $\gamma$  was defined and calculated in eq. (2-8):

$$\varepsilon_R = \gamma * \frac{dx}{x_F}, \text{ where } \gamma = \frac{x_R}{X_0} = \frac{1.72mm}{9.72mm} = 0.1769547 \dots \quad (1-15)$$

This then allowed the Romanyk case strain values to be related to the effective strain,  $\varepsilon_{eff}$ , within the width of the FE model suture region using the variable  $\gamma$  in eq. (2-9).

$$\varepsilon_R = \gamma * \varepsilon_{eff} \quad (1-16)$$

Term  $\gamma$  was utilized to adjust the creep and relaxation models for strain using smaller suture widths. For the creep model, the change in distance between the MSI posts needed to stay the same. This meant the strain in the smaller suture would be higher. The relaxation model needed to produce a similar peak stress for the same activation distance. The higher input strain needed to be compensated for. Re-writing the original creep equation using the  $\varepsilon_R$  term

in eq. (2-10) and modifying it with the identity in eq. (2-9) resulted in the modified creep equation, eq. (2-11).

$$\varepsilon_R(\sigma_0, t_w) = 2 * C_1 * t_w^{C_2} * \sigma_0^{C_3} \quad (1-17)$$

$$\varepsilon_\gamma(\sigma_0, t_w) = \frac{\varepsilon_R(\sigma_0, t_w)}{\gamma} = \frac{2 * C_1 * t_w^{C_2} * \sigma_0^{C_3}}{\gamma} \quad (1-18)$$

Fig. 2-7 shows the strain and MSI widths of the  $\gamma$  adjusted creep model, eq. (2-11), versus the unadjusted creep model, eq. (2-10). The overall expanded width remained the same, but a higher strain value was present in the adjusted model.

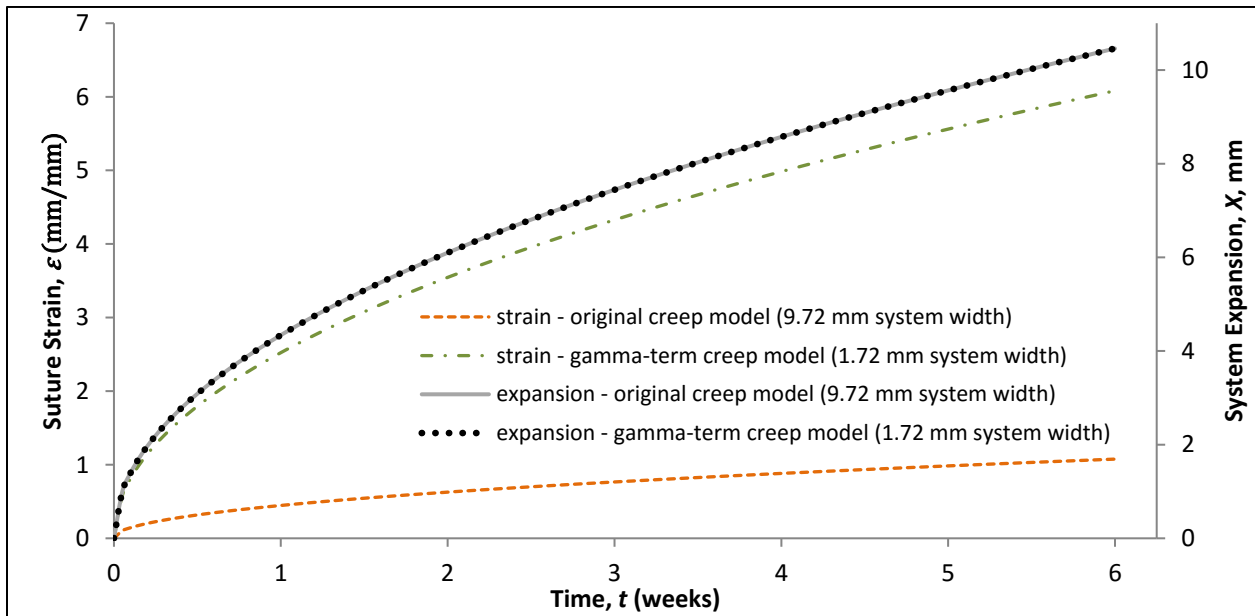


Fig. 1-13: Suture Strain and System Expansion Comparison of 1-D Creep Model Formulations  
1.96N Applied Force, Average Creep Coefficients

Fig. 2-8 shows the resulting strain and stress curves for the adjusted relaxation model eq. (2-12) in comparison to the unadjusted Romanyk relaxation model eq. (2-2). It can be seen in the figure that the adjusted model brought the stress curve in line with the predicted curve of the original relaxation model and 9.72mm width geometry.

$$\sigma_\gamma(\varepsilon_{S_0}, t_w) = 0.4894(0.2880(\gamma\varepsilon_{S_0})t_w^{-0.4912})^{\frac{1}{0.4894}} \quad (1-19)$$

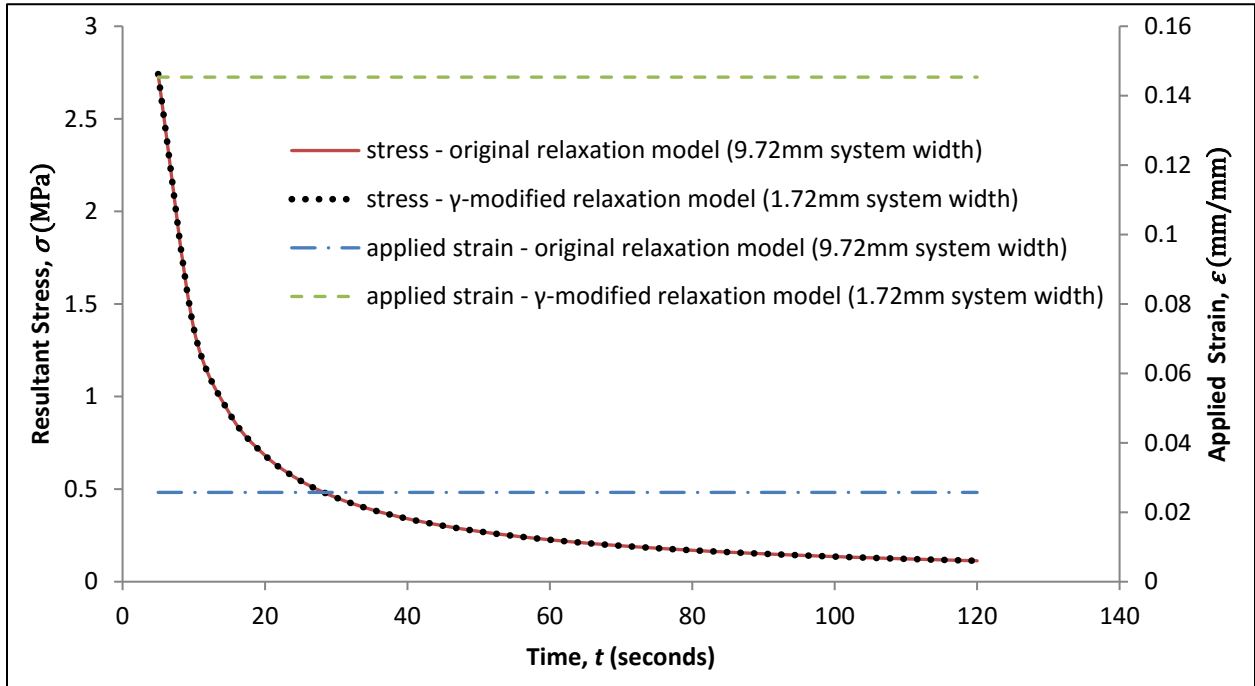


Fig. 1-14: Stress and Strain Comparison of the 1-D Relaxation Model Formulations  
0.25mm Applied Expansion

### Spring Model Justification for Relaxation method using Gamma term

Further justification for using the  $\gamma$  term in both models was done by creating a simplified spring model of the MSS geometry. This was done to verify the assumption that the additional coefficient  $\gamma$  is an appropriate modifier for the constitutive relaxation and creep models. As seen in Fig. 2-9, the MSS system was approximated as two simple springs arranged in a series configuration.

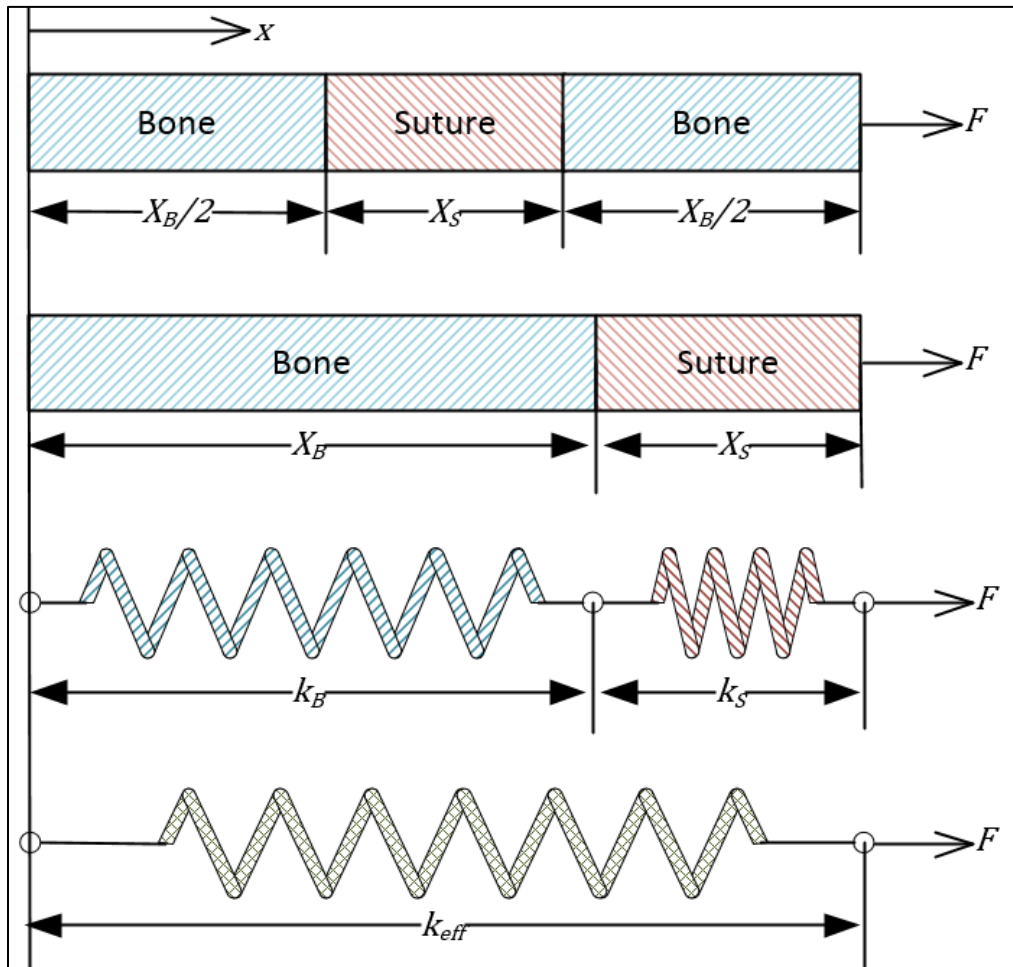


Fig. 1-15: Simplified Spring-Model Approximation of RTG Geometry

The spring model's modulus of elasticity for the suture,  $E_{SS}(t_w, \varepsilon_{eff})$ , was derived for comparison with the modulus of elasticity from the  $\gamma$  modified relaxation model,  $E_{\gamma S}(t_w, \varepsilon_S)$ . This spring system assumes a constant linear elastic modulus for the bone volume,  $E_B$ , while

the original relaxation and creep models were developed assuming negligible strain in the bone [2], [3].

This simplified spring model has force, eq. (2-14), and physical constraints, eq. (2-16), that was used to determine both the stresses and strains in each tissue. The simple spring equation, eq. (2-13), was utilized to begin the analysis.

$$F = kx \quad (1-20)$$

Here,  $F$  is the force applied to a given spring,  $k$  is the spring constant, and  $x$  is the displacement within each the spring. Since the springs were arranged in series, the force balance is defined in eq. (2-14).

$$F_{eff} = F_B = F_S \quad (1-21)$$

The subscript nomenclature for this derivation is  $B$  for bone tissue,  $S$  for suture tissue, and  $eff$  for effective over entire model. Substituting from eq. (2-13) into the force balance in eq. (2-14), we get eq. (2-15):

$$k_{eff}x_{eff} = k_Bx_B = k_Sx_S \quad (1-22)$$

The physical constraint of the system are defined in eq. (2-16)

$$x_{eff} = x_B + x_S \quad (1-23)$$

Utilizing the physical constraints in eq. (2-16), the spring equation in eq. (2-13), and the equality of forces, eq. (2-14), we find:

$$\frac{1}{k_{eff}} = \frac{1}{k_B} + \frac{1}{k_S} \quad (1-24)$$

Knowing that  $F = \sigma * A$ , where  $\sigma$  is the tensile stress and  $A$  is the cross sectional area, eq. (2-14) can be rewritten as eq. (2-18).  $A$  is defined for the spring model using the initial cross sectional area of the RTG.

$$\begin{aligned}\sigma_{eff} * A &= \sigma_B * A = \sigma_S * A \\ \therefore \sigma_{eff} &= \sigma_B = \sigma_S\end{aligned}\tag{1-25}$$

Stress is defined using instantaneous elastic moduli,  $E$ , and the strain,  $\varepsilon$ , in eq. (2-19).

Substituting this relationship into eq. (2-18) produces the relationship in eq. (2-20).

$$\sigma = E * \varepsilon\tag{1-26}$$

$$E_{eff} * \varepsilon_{eff} = E_B * \varepsilon_B = E_S * \varepsilon_S\tag{1-27}$$

Substituting in the deformation,  $x$ , and the original widths,  $X$ , for the strain results in eq. (2-21).

$$E_{eff} * \frac{x_{eff}}{X_{eff}} = E_B * \frac{x_B}{X_B} = E_S * \frac{x_S}{X_S}\tag{1-28}$$

Rearranging to give a more familiar form eq. (2-22) allows the three spring constants to be defined by the elastic moduli and the original widths in eq. (2-23).

$$\frac{E_{eff}}{X_{eff}} * x_{eff} = \frac{E_B}{X_B} * x_B = \frac{E_S}{X_S} * x_S\tag{1-29}$$

$$k_{eff} = \frac{E_{eff}}{X_{eff}}; k_B = \frac{E_B}{X_B}; k_S = \frac{E_S}{X_S}\tag{1-30}$$

Recalling equation eq. (2-17) and utilizing the relationships in eq. (2-23) gives the relationships in eq. (2-24) and eq. (2-25). Rearranged, eq. (2-26) defines the  $E_S$  as a function of the moduli of elasticity of both effective system moduli and bone moduli, as well as the original lengths.

$$\frac{X_{eff}}{E_{eff}} = \frac{X_B}{E_B} + \frac{X_S}{E_S}\tag{1-31}$$

$$\frac{X_S}{E_S} = \frac{X_{eff}}{E_{eff}} - \frac{X_B}{E_B}\tag{1-32}$$

$$E_S = \left( \frac{\frac{X_{eff}}{E_{eff}} - \frac{X_B}{E_B}}{X_S} \right)^{-1} \quad (1-33)$$

Eq. (2-27) utilizes several identities to relate the total system length and moduli to the appliance activation distance,  $x_{act}$ , and the effective system stress. Substituting this identity into eq. (2-26) produces a new definition of the time dependent moduli of the suture in eq. (2-28).

$$\frac{X_{eff}}{E_{eff}} = \frac{\varepsilon_{eff}}{\sigma_{eff}} X_{eff} = \frac{1}{\sigma_{eff}} * \frac{x_{act}}{X_{eff}} * X_{eff} = \frac{x_{act}}{\sigma_{eff}} \quad (1-34)$$

$$E_S(t_w) = \left( \frac{\frac{x_{act}}{\sigma_{eff}(t_w)} - \frac{X_B}{E_B}}{X_S} \right)^{-1} \quad (1-35)$$

Substituting into eq. (2-28) the original relaxation formulation, eq. (2-2), resulted in eq. (2-29). This new equation defined the elastic modulus of the suture at any time as a function of the original widths, and the appliance activation distance.

$$E_S(t_w) = \left( \frac{\frac{x_{act}}{0.4894(0.2880\varepsilon_{eff}t_w^{-0.4912})^{\frac{1}{0.4894}}} - \frac{X_B}{E_B}}{X_S} \right)^{-1} \quad (1-36)$$

The formulation of  $E_S$  used in eq. (2-29) undergoes a minor change in nomenclature and is now referred to as  $E_{SS}$ , as seen in eq. (2-30). This was to differentiate it from  $E_{\gamma S}$ , eq. (2-31), which was the gamma modified relaxation model utilizing the strain within the suture volume.

$$E_{SS}(t_w) = \left( \frac{\frac{x_{act}}{0.4894(0.2880\varepsilon_{eff}t_w^{-0.4912})^{(1/0.4894)}} - \frac{X_B}{E_B}}{X_S} \right)^{-1} \quad (1-37)$$

$$E_{\gamma S}(t_w) = \frac{0.4894(0.2880(\gamma\varepsilon_S)t_w^{-0.4912})^{1/0.4894}}{\varepsilon_S} \quad (1-38)$$

In comparing  $E_{\gamma S}$  and  $E_{SS}$  it was necessary to evaluate for both the same time values and appliance activation distance. Comparisons were done with an appliance activation distance of 0.25mm over a time range from 5 seconds to 12 hours. Values for  $X_S$  and  $X_B$  were 1.72mm and 8mm, respectively. Results for this comparison are detailed in Section 2.3.1.

### Sensitivity Analysis of Suture Width Assumption

A sensitivity analysis of the bone segment width assumption was needed, as it directly affected the derivation both of the  $\gamma$ -term, eq. (2-8), and simplified spring model. The assumption of 4mm width of bone on either side of the sutures [2] was used. This analysis focussed on a range of bone widths,  $X_B$ , in the total system width,  $X_{eff}$ , of 9.72mm. The range of the bone widths investigated was 4mm  $\pm$  0.5mm on each side of the suture. The resultant original suture width range was from 0.72-2.72mm. The stress vs. strain and Young's moduli v. strain for the  $\gamma$  modified relaxation model were calculated for a time range from 5 seconds to 12 hours. The results are also discussed in Section 2.3.1.

### 2.2.5 Adapting the Creep Equation to the ANSYS USERCREEP.f Subroutine (Implicit method subroutine)

The creep equation, in both its unmodified and Gamma-modified forms, was adapted for use in ANSYS by utilizing the USERCREEP.f user programmable sub-routine. This subroutine was chosen since it had an implicit calculation method, was simple to code and compile, and was compatible with current technology elements. Coding included the conversion of time from units of seconds to units of weeks. This user subroutine was configured to use either

hard-coded default material coefficients or user supplied material coefficients at run-time. The modified subroutine could not be appended as it contains code that is under ANSYS' copyright.

The ANSYS 'custom' and 'customize' directories were copied into the ANSYS program directory. The USERCREEP.f subroutine was edited in Microsoft Visual Studios 2008, utilizing the FORTRAN 77 coding language and format. Subroutine compiling used the Intel 11.1 FORTRAN compiler as specified by the ANSYS documentation [8]. Compilation was performed using the supplied ANSUSERSHARED.bat file<sup>1</sup>, and ANSYS had to be configured to link with the compiled files<sup>2</sup>.

In editing the USERCREEP.f function, it was necessary for equations (2-10) and (2-11) to be differentiated with respect to time, and further differentiated with respect to both stress and strain. Eq. (2-32) and eq. (2-33) are the time differentiation of original and gamma-edited creep models, respectively.

$$\frac{\delta \varepsilon_r(\sigma, t_w)}{\delta t_w} = 2 * C_1 * C_2 * t_w^{C_2-1} * \sigma^{C_3} \quad (1-39)$$

$$\frac{\delta \varepsilon_\gamma(\sigma, t_w)}{\delta t_w} = \frac{2 * C_1 * C_2 * t_w^{C_2-1} * \sigma^{C_3}}{\gamma} \quad (1-40)$$

Eq. (2-34) and eq. (2-35) are the stress differentiation of the time differentiation of the creep models (eq. (2-32) and eq. (2-33)).

$$\frac{\delta^2 \varepsilon_r(\sigma, t_w)}{\delta t_w \delta \sigma} = 2 * C_1 * C_2 * C_3 * t_w^{C_2-1} * \sigma^{C_3-1} \quad (1-41)$$

$$\frac{\delta^2 \varepsilon_\gamma(\sigma, t_w)}{\delta t_w \delta \sigma} = \frac{2 * C_1 * C_2 * C_3 * t_w^{C_2-1} * \sigma^{C_3-1}}{\gamma} \quad (1-42)$$

Eq. (2-36) and eq. (2-37) show that the strain differentiations of the time differentiations are equal to zero.

---

<sup>1</sup> The ANSUSERSHARED.bat file was copied from ANSYS 12.0 installation media, and the .bat file was edited so that the revision numbers in the .bat file reflected the highest installed ANSYS version.

<sup>2</sup> To connect ANSYS to the correct compiled subroutine, which for convenience was typically stored in the anticipated working directory of the FEA run case, the Windows User Environment Variable ANS\_USER\_PATH was changed to the correct directory name.

$$\frac{\delta^2 \varepsilon_r(\sigma, t_w)}{\delta t_w \delta \varepsilon_r} = 0 \quad (1-43)$$

$$\frac{\delta^2 \varepsilon_\gamma(\sigma, t_w)}{\delta t_w \delta \varepsilon_\gamma} = 0 \quad (1-44)$$

The subroutine was coded for one single continuous spring-type appliance activation. The flowchart shown in Fig. 2-10 illustrates the subroutine path and the creep model coefficients utilized for testing are detailed in Table 2-1.

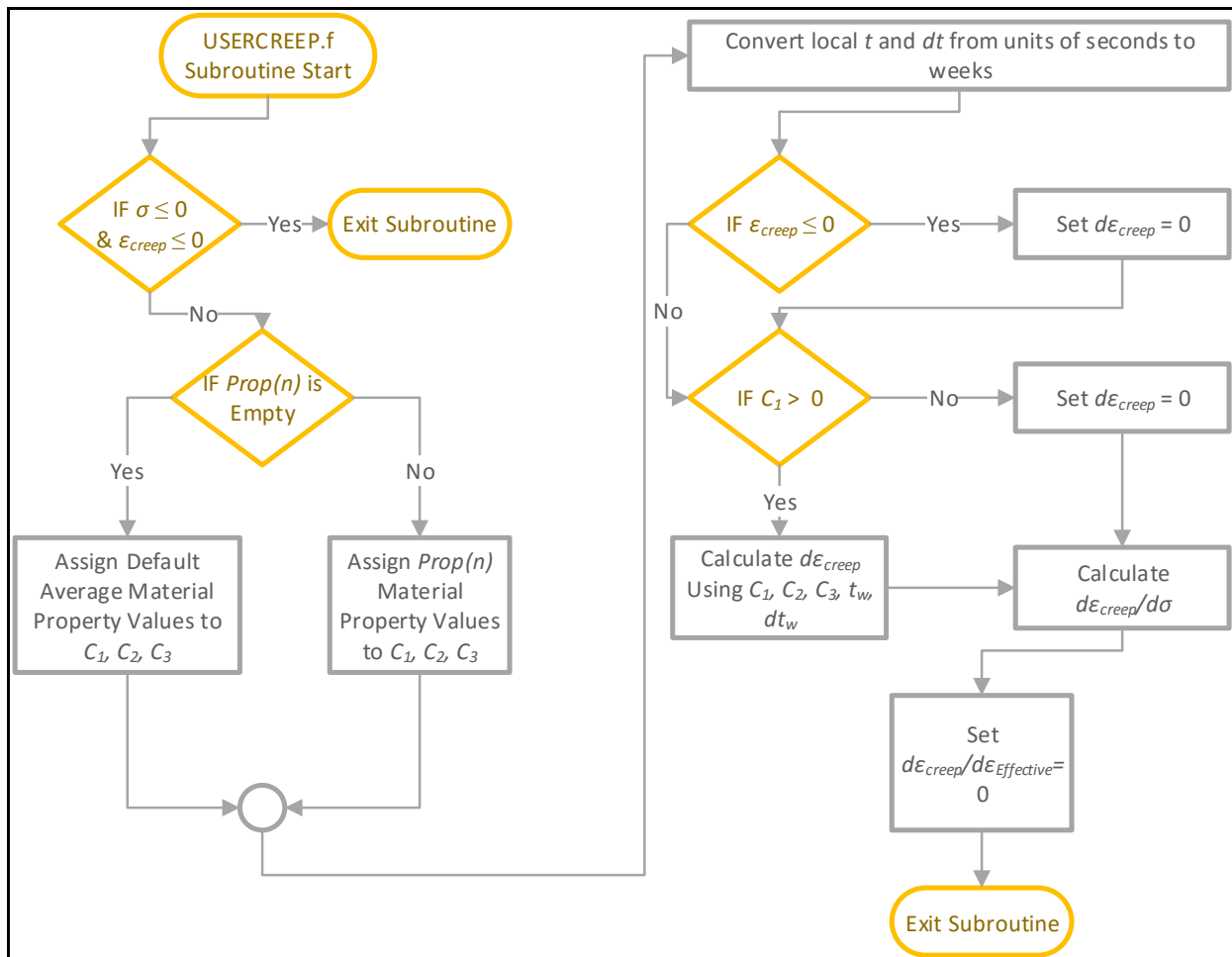


Fig. 1-16: USERCREEP.f Subroutine Flowchart

### 2.2.6 Adapting the Relaxation Equation for Use in ANSYS

Unlike the method used for adapting the creep constitutive equation for ANSYS, the  $\gamma$  modified relaxation model in eq. (2-12) could not be adapted using a user programmable subroutine. This was due to a lack of built-in functionality in ANSYS to compile and link a customized viscoelastic material subroutine. The built-in generalized Maxwell material model [9] approximated the relaxation model for use in ANSYS. The Maxwell model was able to approximate the time-dependant non-linearity of the relaxation model, but not the strain-dependent non-linearity. An unsuccessful attempt to incorporate the strain-dependent non-linearity is detailed Appendix B. The following section details how the relaxation model was approximated using a Prony series curve fitting routine such that the Maxwell model could be implemented in FEA.

The generalized Maxwell viscoelastic model, eq. (2-38), [9] can be visualized as a generalized spring-damper model, as seen in Fig. 2-11.

$$\sigma_c = \int_0^t 2G(t - \tau) \frac{de}{d\tau} d\tau + I \int_0^t 2K(t - \tau) \frac{d\Delta}{d\tau} d\tau \quad (1-45)$$

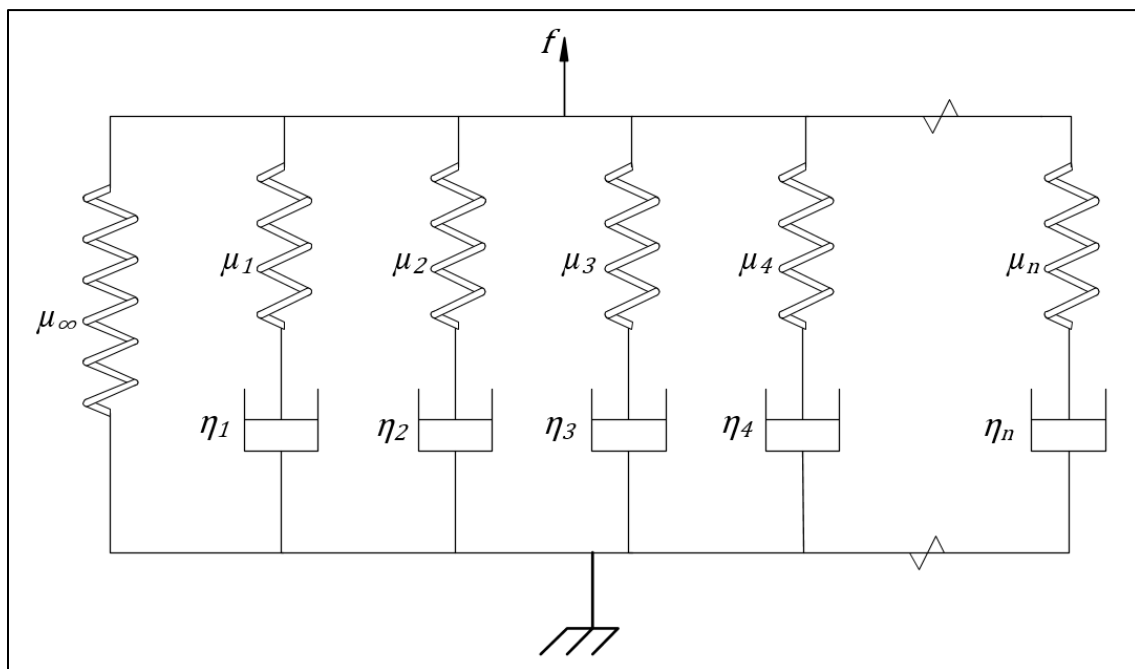


Fig. 1-17: Generalized Maxwell Spring-Damper Model Diagram

The variable  $\tau$  in eq. (2-38) is defined as the time at the end of the previous load sub-step, and  $t$  is the simulation time in seconds.  $I$  is the identity tensor.  $\sigma_c$  is the Cauchy stress.  $G(t)$  and  $K(t)$  are the shear and bulk moduli, respectively. Variables  $e$  and  $\Delta$  signify the deviatoric and volumetric strains, respectively.

The time dependent shear and bulk moduli were defined non-linearly using Prony Series approximations, in eq. (2-39) and eq. (2-40) [9]. The term  $(t_{seconds} - T)$  from the Maxwell model was passed to the Prony Series approximations as the input variable  $t_p$ . This ensured that the non-linear time decay function begins anew at the beginning of each load step.

$$G(t_p) = G_0 \left[ \alpha_\infty^G + \sum_{i=1}^{n_G} \alpha_i^G \exp\left(-\frac{t_p}{\tau_i^G}\right) \right] \quad (1-46)$$

$$K(t_p) = K_0 \left[ \alpha_\infty^K + \sum_{i=1}^{n_K} \alpha_i^K \exp\left(-\frac{t_p}{\tau_i^K}\right) \right] \quad (1-47)$$

The coefficients of the Prony series,  $\alpha$  and  $\tau$ , were determined in ANSYS 14.5 using the built in curve fitting functionality. The variables  $G_0$  and  $K_0$  are the relaxation moduli at  $t_0$ . The  $\alpha$  terms,  $\alpha_i^G$  and  $\alpha_i^K$ , are the relative moduli. The  $\tau$  terms,  $\tau_i^G$  and  $\tau_i^K$ , are the relaxation time constants.

The  $n$  variables,  $n_G$  and  $n_K$ , signify the order of the Prony approximation.

The ANSYS curve fitting routine for determining the Viscoelastic coefficients[10],  $\alpha_i$  and  $\tau_i$ , requires datasets of bulk and shear moduli with respect to time in seconds. This data was generated from the stress values calculated from the gamma modified relaxation model, eq. (2-12), using MATLAB® (MathWorks®, Natick, Massachusetts, USA). The  $G(t)$  and  $K(t)$  datasets were calculated using eq. (2-41) and eq. (2-42).

$$G(t) = \frac{E(t)}{2(1+\nu)} = \frac{1}{2(1+\nu)} * \frac{\sigma_\gamma(\varepsilon_{S_0}, t)}{\varepsilon_{S_0}} \quad (1-48)$$

$$K(t) = \frac{E(t)}{3(1-2\nu)} = \frac{1}{3(1-2\nu)} * \frac{\sigma_\gamma(\varepsilon_{S_0}, t)}{\varepsilon_{S_0}} \quad (1-49)$$

The starting conditions variables for generating the moduli data are the initial time,  $t_0$ , initial applied strain,  $\varepsilon_0$ , and assumed Poisson's ratio,  $\nu$ . The number of data points written to the input file was  $n=200$  for a time range of 5 seconds to 10000 seconds. This was done for computational efficiency as additional points were observed to have a negligible effect on the curve fitting accuracy.

The relaxation model cannot actually be defined at  $t_0$  as it asymptotes towards infinite strain at zero time, eq. (2-43). Therefore, a dataset could not be generated for a time value of zero.

$$\lim_{t \rightarrow 0} \left( 0.4894(0.2880(\gamma \varepsilon_{S_0}) t_w^{-0.4912})^{\frac{1}{0.4894}} \right) = \lim_{t \rightarrow 0} \left( \frac{0.03846 * \gamma \varepsilon_{S_0}^{2.0433}}{t_w^{1.0037}} \right) \rightarrow \infty \quad (1-50)$$

Additionally, it was estimated by Romanyk et al. that the appliance activation period takes approximately 5 seconds. Therefore, bulk and shear datasets were generated for three variations of  $t_0$ . The variations of initial time variables that used for curve fitting are detailed in Table 2-4.

**Table 1-4: Time Variations of Relaxation Data for Prony Series Curve Fitting**

Supplied Data Sets	Data Set Calculation Time, $t_c$	Time Shift to Dataset Time Signature	Data Set Time Signature, $t_d$ , defined using Data Set Calculation Time, $t_c$
Shear and Bulk Moduli Adapted From Relaxation Model Stress Results	5s <= $t_c$ < 6hrs	No	$t_d = t_c$
	0.1s <= $t_c$ < 6hrs	No	$t_d = t_c$
	5s <= $t_c$ < 6hrs	Yes	$t_d = t_c - 4.99 \text{ seconds}$

The resultant  $\alpha_i$  and  $\tau_i$  values for each initial time variation were tested in ANSYS using the RTG and multiple appliance activations. The results of this set of simulations are discussed in Section 2.3.3.

As with any approximation, the Prony series does not perfectly mimic the supplied dataset. The order of the Prony fit,  $n$ , contributes to and determines the accuracy of the approximation. In a situation where the calculation speed is not a factor, it would be advantageous to maximize the

order of the Prony series. However, the material model was being developed for FEA models that were to be used to simulate periods of potentially weeks. It was advantageous to strike a balance between model accuracy and model speed of calculation. To this end, Prony fits of order 3-, 5-, 7-, and 9-terms were generated. To assess the fit accuracy, a least squares regression was done using the ANSYS curve fitting protocols. A maximum deviation error was calculated between the input data versus the curve fit results in MATLAB. Multiple appliance activation tests were subsequently run on the RTG using the different curve fits, and the simulation run times were recorded.

To implement the Maxwell model in ANSYS material variables were required. These include the  $\alpha_i^G$ ,  $\alpha_i^K$  and  $\tau_i^G$ ,  $\tau_i^K$  sets of the Prony coefficients, a Poisson's Ratio ( $\nu$ ), and quite importantly, an initial Young's Modulus,  $E_0$ . The supplied  $E_0$  and  $\nu$  terms allow for ANSYS to calculate values for  $G_0$  and  $K_0$ . As the relaxation model cannot be defined at a  $t_0$  of zero, eq. (2-43), an additional modifier term,  $\beta$ , was derived such that an  $E_0$  specific to the Prony fit could be calculated.

To begin the derivation, it was required that the  $t_p$  value for when the Prony Fit was exactly equal to the supplied dataset be known. To do this, the resultant  $A_i$  values for both shear and bulk moduli datasets was recorded for each curve fit.  $A_i^G$  and  $A_i^K$ , defined in eq. (2-44) and eq. (2-45).

$$\alpha_i^G = \frac{A_i^G * A_i^G}{G_0} \rightarrow A_i^G = \sqrt{G_0 * \alpha_i^G} \quad (1-51)$$

$$\alpha_i^K = \frac{A_i^K * A_i^K}{K_0} \rightarrow A_i^K = \sqrt{K_0 * \alpha_i^K} \quad (1-52)$$

A vector,  $D$ , was defined in eq. (2-46) utilizing the  $A_i$  and  $\tau$  pairs, as well as the originally supplied moduli databases. The intercept; time,  $t_{int}$ , was determined using a MATLAB code to search for the first  $t$  value for which  $D(t) = 0$ .

$$D(t) = \left( \frac{1}{2(1 + \nu)} * \frac{\sigma_\gamma(\varepsilon_{s_0}, t)}{\varepsilon_{s_0}} - A_\infty^G + \sum_{i=1}^{n_G} A_i^G \exp\left(-\frac{t_p}{\tau_i^G}\right) \right) \quad (1-53)$$

Once  $t_{int}$  was known, it was possible to derive and define the modifier term  $\beta$  in eq. (2-47)

$$G(t = 0) = \beta * G(t_{int}) \rightarrow \beta = \frac{G(t = 0)}{G(t_{int})} \quad (1-54)$$

By substituting in eq. (2-39), eq. (2-47) was re-written as eq. (2-48)

$$\beta = \frac{G_0 \left[ \alpha_{\infty}^G + \sum_{i=1}^{n_G} \alpha_i^G \exp\left(-\frac{0}{\tau_i^G}\right) \right]}{G_0 \left[ \alpha_{\infty}^G + \sum_{i=1}^{n_G} \alpha_i^G \exp\left(-\frac{t_{int}}{\tau_i^G}\right) \right]} \quad (1-55)$$

Simplifying results in eq. (2-49)

$$\beta = \frac{[\alpha_{\infty}^G + \sum_{i=1}^{n_G} \alpha_i^G]}{\left[ \alpha_{\infty}^G + \sum_{i=1}^{n_G} \alpha_i^G \exp\left(-\frac{t_{int}}{\tau_i^G}\right) \right]} \quad (1-56)$$

Referring back to eq. (2-39) and eq. (2-40), and knowing that at  $t_p = 0$  the time dependent moduli is equivalent to the initial moduli, eq. (2-50). This confirmed that the sum of  $\alpha_i$  terms is equivalent to 1 (eq. (2-51)).

$$G(t_p = 0) = G_0 \left[ \alpha_{\infty}^G + \sum_{i=1}^{n_G} \alpha_i^G \exp\left(-\frac{0}{\tau_i^G}\right) \right] = G_0 \left[ \alpha_{\infty}^G + \sum_{i=1}^{n_G} \alpha_i^G \right] \quad (1-57)$$

$$\left[ \alpha_{\infty}^G + \sum_{i=1}^{n_G} \alpha_i^G \right] \equiv 1 \quad (1-58)$$

Knowing that the numerator of eq. (2-49) is always equal to 1, it allowed  $\beta$  to be defined in eq. (2-52) as:

$$\beta^G(t_{int},) = \frac{1}{\alpha_{\infty}^G + \sum_{i=1}^{n_G} \left( \alpha_i^G + e^{-\frac{t_{int}}{\tau_i^G}} \right)} \quad (1-59)$$

With the  $\beta$  term now defined, it was possible to define eq. (2-53) to calculate the initial Young's modulus,  $E_0$ , for input in ANSYS for any given Prony fit and peak initial activation strain,  $\varepsilon_0$ .

$$E_0(\varepsilon_0, t_{int}) = \frac{\beta(t_{int}) * 0.4894(0.2880 * \gamma * \varepsilon_0 * t_{int}^{-0.4912})^{\frac{1}{0.4894}}}{\varepsilon_0} \quad (1-60)$$

Curve fitting a Prony expansion to the relaxation model allowed for the time dependent non-linearity of the relaxation model to be replicated for FEA in ANSYS. The strain term,  $\varepsilon_0$ , in eq. (2-53) was defined as the peak strain in the suture from a single appliance activation in a preliminary FEA simulation. This preliminary simulation used linear elastic material properties for the suture. Section 2.3.3 discussed the results of the FEA simulation cases for the completed Prony model.

### 2.2.7 Testing of Creep FEA Model

Testing of the creep material model using the RTG was completed in ANSYS 13.0 and 14.5. Models were tested for a simulated period of 6-weeks. Initial tests were performed using the load specific coefficients (Table 2-1) and the dynamic solving engine. Additional tests were completed with the static solving engine. Creep simulation configurations detailed in Table 2-5.

Table 1-5: Creep Model FEA Case Configuration Summary

Suture Element Type	Loads	Coefficients	Solution Engine	$\gamma$ -term Modified Subroutine	
2-Node Bar w/Constant Cross Section	0.49N, 0.98N, 1.98N	Nominal/Load Specific	Transient	No	
		Average			
Nominal/Load Specific		Static	Yes		
Average					
2-Node Bar w/Rigid Volume		0.49N, 0.98N, 1.98N	Nominal/Load Specific	Transient	No
			Average		
Nominal/Load Specific					
Average					
8-Node Brick	0.49N, 0.98N, 1.98N		Nominal/Load Specific	Static	Yes
			Average		

The ANSYS dynamic solution method accounts for inertia of the moving masses and was chosen for initial testing due to the use of a non-linear material properties. Additional testing was done using the static solution method. The static solution method neglects the effect of the inertia of moving bodies. As the simulations are pseudo-static (i.e. they do not involve fast moving masses that change direction quickly) and do not undergo near-instantaneous large changes in load magnitude (e.g. impacts) this simulation method was considered applicable. Comparisons of the results and computation duration of the two methods were done to determine which solver was optimal.

The default full-tangent Newton-Rapson solution method was utilized in ANSYS using the sparse-direct solver[11]. For convergence, the default simulation criteria of force and displacement L2 norm residuals were utilized in both cases [12]. The parameters used for the FEA experiments for the automatic time stepping were a minimum allowable time step of 1e-08 seconds, a maximum allowable time step of 12 hrs, and an arbitrary initial time step of 1e-08 seconds.

All creep FEA simulations used two separate solution steps. The first step solved to a time of 1e-8 seconds, with non-linear material models turned off. This created the initial conditions for the creep loading. The second solution step activated the non-linear material model. This step simulated a time of six weeks. This separation of solution steps was done as per the ANSYS material reference materials.

To investigate the relative accuracy of the time stepping inherent to the USERCREEP.f subroutine, the in-subroutine time stepping method was modified to have a Runge-Kutta 4<sup>th</sup> (RK4) order time stepping. This was done to determine if there was undue truncation error from the time stepping method used in the USERCREEP.f subroutine from the progression of the simulation time. The original time stepping method locally used in the subroutine was the explicit first order forward Euler method, with a global error  $O(1)$ [13, p. 63]. The adjusted in-subroutine method was a forward 4 term Runge-Kutta method with a global error order of  $O(4)$  [5, p. 64]. The default Euler method was evaluated to be sufficient, as the RK4 did not have

a noticeable effect on the solution, nor were the multiplied number of function evaluations worth the negligible change in accuracy of the solution.

### 2.2.8 Testing of Relaxation FEA Model

To test the Prony series approximation of the relaxation model, the RTG was utilized to allow for comparison to the original Relaxation model. Testing for this material model was performed only utilizing the 8-node brick elements SOLID185, which are compatible with both the non-linear material Prony material model, as well as the non-linear geometry options available in ANSYS [7].<sup>3</sup>

Both the static and dynamic solution engines were tested to evaluate the numerical stability, accuracy of result, and compare calculation durations. Additionally, the difference in numerical results was evaluated between the linear and non-linear geometry simulation options. The solver configurations that were tested are outlined in Table 2-6.

Table 1-6: FEA Cases for Relaxation Model Tests

Order of Prony Fit	Prony Data Set Time Signatures	Number of Activations	Solution Engine	Non-Linear Geometry Control
5	td = tc; 5s <= tc < 6hrs	6	Transient	Non-Linear
7	td = tc; 5s <= tc < 6hrs	6	Transient	Non-Linear
9	td = tc; 5s <= tc < 6hrs	6	Transient	Non-Linear
7	td = tc - 4.99s; 5s <= tc < 6hrs	6	Transient	Linear
7	td = tc - 4.99s; 5s <= tc < 6hrs	6	Transient	Non-Linear
7	td = tc - 4.99s; 5s <= tc < 6hrs	6	Static	Linear
7	td = tc - 4.99s; 5s <= tc < 6hrs	6	Static	Non-Linear
7	td = tc - 4.99s; 5s <= tc < 6hrs	29	Static	Non-Linear

<sup>3</sup> Limiting RTG testing to this element family was done because the SimpleWare 6.0 +FE meshing algorithms that were later used for meshing the 3-D skull geometry was limited to the SOLID18X class of elements in ANSYS, with focus on the SOLID187 element.

To allow for adaptable time steps and to focus data points at time points with anticipated high levels of change, parameterized solution processor APDL code was written for use in ANSYS (Appendix A). The flow chart in Fig. 2-12 visually represents the code structure of the solution method.

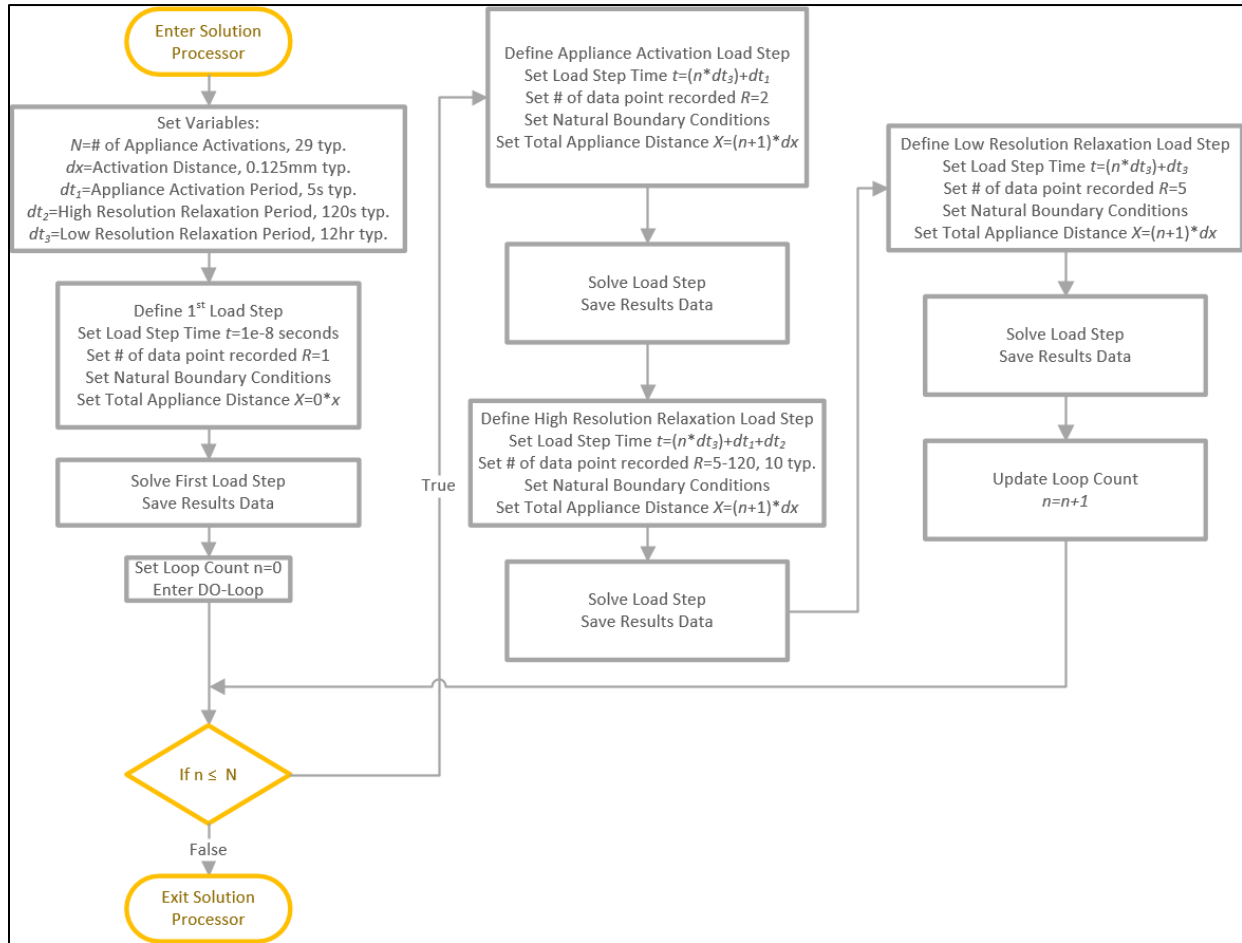


Fig. 1-18: Flowchart Detailing Solution Sub-Step DO-loop Code for Relaxation Simulations

As seen in Fig. 2-3, the natural boundary conditions are once again applied at the sagittal symmetry plane as a symmetry condition. Displacements were applied in the outward direction perpendicular to the face opposite the sagittal symmetry plane.

## 2.3 Results and Discussion

Previous studies of maxillary expansion have thus far neglected the time dependent response of the MPS. To simulate the non-linear tissue properties of this suture in FEA, the creep and relaxation models were adapted for implementation in ANSYS. Presented here are the results of adapting the two constitutive response models for use in ANSYS. These include the verification of  $\gamma$ , the results of the FEA simulations of the creep model, and the results of simulating the approximated relaxation model in ANSYS.

### 2.3.1 $\gamma$ -term and Simplified Spring Model Comparison and Sensitivity Analysis

The  $\gamma$ -term was derived to modify the creep and relaxation models. This converted the models from describing a bone/suture region of 9.72mm width to that of a suture with a 1.72mm width. The  $\gamma$ -term was necessary because the change in width affected the resultant strain magnitude for a given distance of expansion. To verify that this term is an appropriate approximation, it was compared to a lump-sum approximation of the bone-suture system (Section 2.2.3).

The two methods of calculating the relaxing elastic modulus, using  $E_{SS}$  in eq. (2-30) and  $E_{\gamma S}$  in eq. (2-31) were compared for a time range of 5 seconds to 12 hours. The applied expansion was 0.25mm in both cases with a suture width of 1.72mm. The results of this comparison at several time points are detailed in Table 2-7. The maximum variation between the two methods was found to be 0.008279 MPa at 5 seconds, with a minimum variation of 1.04e-10 MPa at the conclusion of the 12-hour period.

Table 1-7: Comparison of Spring Model and  $\gamma$ -modified Elastic Moduli Over Time for an Assumed Bone Width of 4mm

Time	Peak Elastic Moduli from Simplified Spring Model	Peak Elastic Moduli from Gamma Derived Model	Relative Difference in Peak Elastic Moduli
$t$	$E_S$ (MPa)	$E_\gamma$ (MPa)	
5 seconds	18.87246	18.86418	0.043870%
10 seconds	9.41013	9.40807	0.021879%
30 seconds	3.12361	3.12338	0.007264%
1 minute	1.55777	1.55771	0.003623%
4 minutes	0.38745	0.38745	0.000901%
30 minutes	0.05128	0.05128	0.000119%
1 hour	0.02557	0.02557	0.000059%

The sensitivity of the  $\gamma$  term and the spring approximation model to changes in the assumed width of the bone segments (3.5mm-4.5mm per side) of the model is presented in Fig. 2-13 and Table 2-8. The peak elastic moduli vary between 7.897 MPa and 29.832 MPa for the relaxation model with the  $\gamma$ -term, and 7.901 MPa and 29.843 MPa for the spring suture model.

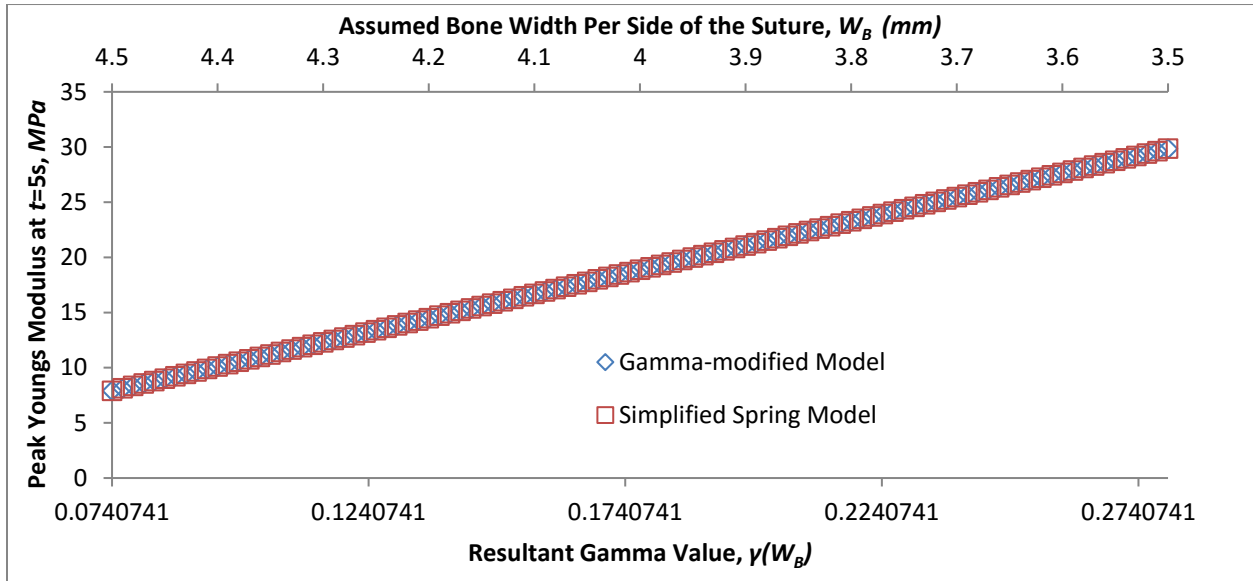


Fig. 1-19: Peak Elastic Modulus for Relaxation Models at t=5s for Varied Bone Widths; 0.25mm System Expansion

Table 1-8: Sensitivity of  $\gamma$ -modified and Simplified Spring Models to Changes in Assumed Bone Width

Amount of Bone Assumed Per Side	Resultant Suture Width	Resultant Gamma	Resultant Suture Strain	Peak Elastic Moduli from Simplified Spring Model	Peak Elastic Moduli from Gamma Derived Model	Relative Difference in Peak Elastic Moduli	Peak Tensile Stress from Simplified Spring Model	Peak Tensile Stress from Gamma Derived Model	Relative Difference in Peak Tensile Stress
$W_B$	$W_S$	$\gamma$	$\epsilon_s$	$E_S$	$E_\gamma$		$\sigma_s$	$\sigma_\gamma$	
mm	mm		mm/mm	MPa	MPa		MPa	MPa	
3	3.72	0.383	0.0672	40.813	40.799	3.29E-04	2.743	2.742	3.29E-04
3.25	3.22	0.331	0.0776	35.328	35.315	3.56E-04	2.743	2.742	3.56E-04
3.5	2.72	0.280	0.0919	29.843	29.832	3.84E-04	2.743	2.742	3.84E-04
3.75	2.22	0.228	0.1126	24.358	24.348	4.11E-04	2.743	2.742	4.11E-04
4	1.72	0.177	0.1453	18.872	18.864	4.39E-04	2.743	2.742	4.39E-04
4.25	1.22	0.126	0.2049	13.387	13.380	4.66E-04	2.743	2.742	4.66E-04
4.5	0.72	0.074	0.3472	7.901	7.897	4.94E-04	2.743	2.742	4.94E-04
4.75	0.22	0.023	1.1364	2.414	2.413	5.21E-04	2.743	2.742	5.21E-04

The  $\gamma$ -model is in accordance with the spring-suture approximation model, with low relative error (0.0329-0.0521%) for peak stress and peak elastic moduli. It is evident that both the  $\gamma$ -model and the spring-approximation model are sensitive to variations in bone width. This highlights the degree to which the peak elastic modulus is dependent on the bone segment width and confirms that the peak stress remain constant as RTG geometry changes with the  $\gamma$ -term. The nominal bone width of 4mm per side was used for all subsequent RTG testing. The resultant value for  $\gamma$  of 0.17695 was utilized for further implementation of the FEA material models.

### 2.3.2 Creep Model Results

The USERCREEP.f implementation of the creep model was tested in ANSYS using the RTG. The simulations were grouped in three categories. First, the unmodified creep equation was simulated using the dynamic solution engine. Secondly, the unmodified creep equation was tested using the static solution engine. Finally, the  $\gamma$ -modified creep equation was run using the static solution engine. The three sets of tests allowed for the comparison of the dynamic and static solution engines, as well as a comparison of the results of the original and  $\gamma$ -modified creep equations as run on the RTG. Additionally, these tests generated a sample from which the most effective element type could be determined for simulating the creep in the suture.

#### Evaluation of Element Types for Creep Simulations

Initial tests utilizing the dynamic solution engine focused on determining the optimum element type to simulate the suture tissue response. The creep response of the MPS was simulated using several different element types, load specific creep coefficients, and the unmodified creep model subroutine. The elements tested included 8-node brick elements of the SOLID18X family, 2-node bar elements (LINK180) with a fixed cross sectional area condition, and the 2-node bar elements with a constant volume condition. Fig. 2-14 shows the strain results plot for the 0.98N load simulations in comparison to the strain results of the 1-D constitutive equation. Additionally, Fig. 2-15 shows the absolute relative error of the different element types with respect to the 1-D strain results. The data points in both these figures have been linked using continuous lines for improved visual comprehension.

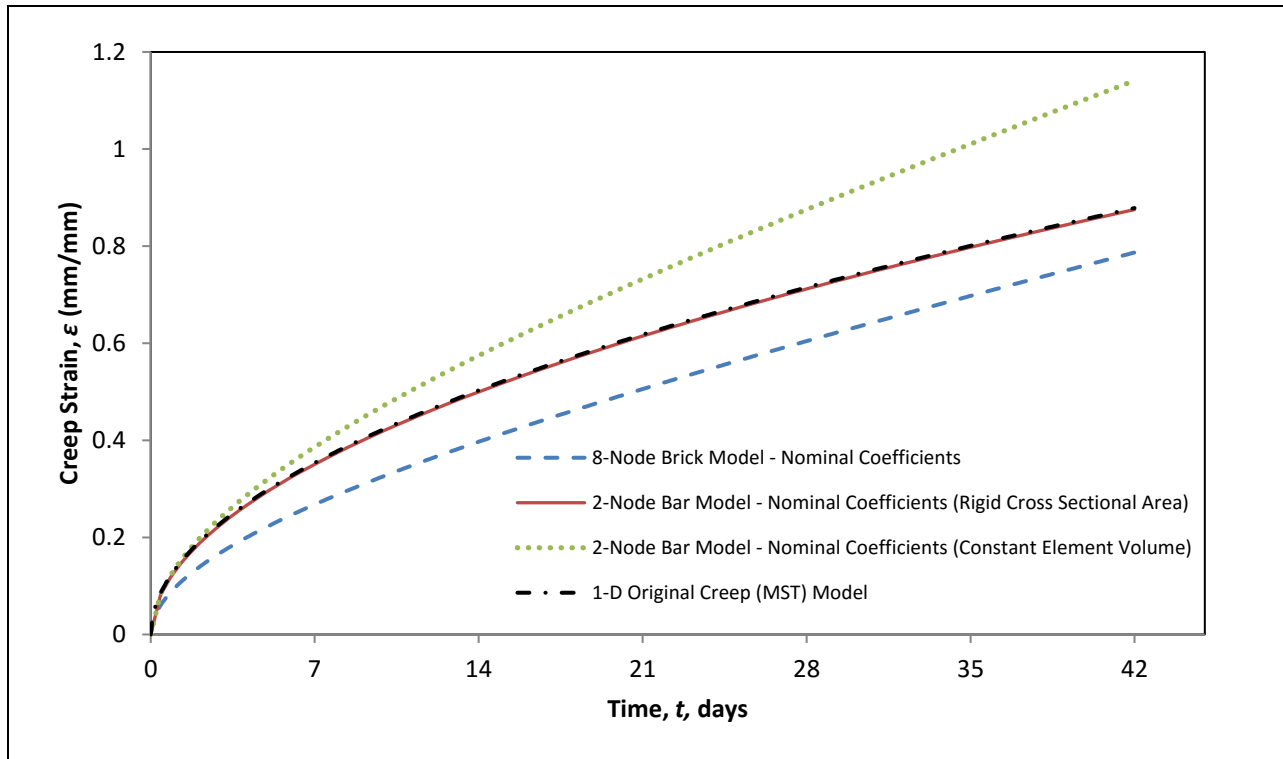


Fig. 1-20: 100g (0.98N) Unmodified Creep Model Strain ( $\epsilon$ ) Results

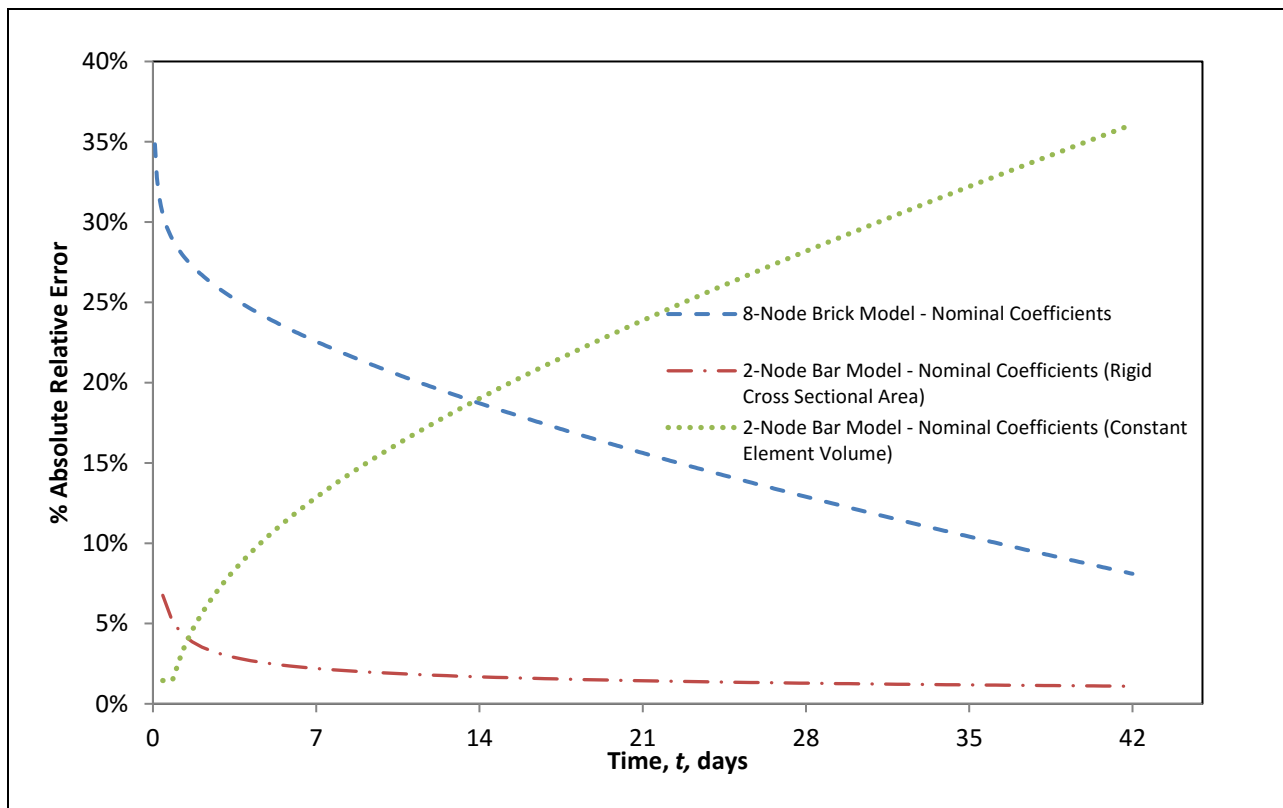


Fig. 1-21: 200g (1.96N) Unmodified Creep Model Strain ( $\epsilon$ ) Abs. Relative Error

As can be seen in Fig. 2-15, the relative error of the 2-node suture element best conforms to the cumulative strain of the theoretical model. The relative errors for the simulation results of the full set of load cases are summarized in Table 2-9.

**Table 1-9: Peak Relative Error of Creep Model Simulations for 0.49N, 0.98N, and 1.96N Cases**

Mesh Method	Load	Maximum and Minimum Relative Error	Time of Peak Error (Seconds)
2-Node Bar w/ Constant Cross Section	50g (0.49N)	2.81%	3.63E+04
		0.20%	3.63E+06
	100g (0.98N)	3.59%	3.63E+04
		0.35%	3.63E+06
	200g (1.96N)	6.76%	3.63E+04
		1.10%	3.63E+06
2-Node Bar w/ Rigid Volume	50g (0.49N)	17.75%	3.63E+06
		0.03%	3.63E+04
	100g (0.98N)	29.89%	3.63E+06
		1.02%	3.63E+04
	200g (1.96N)	36.08%	3.63E+06
		1.49%	3.63E+04
8-Node Brick	50g (0.49N)	32.17%	7.26E+03
		20.92%	3.63E+06
	100g (0.98N)	31.81%	7.26E+03
		10.42%	3.63E+06
	200g (1.96N)	34.85%	7.26E+03
		8.10%	3.63E+06

Of the three element types, the suture model that best represents a 3-D extrapolation of the 1-D model was the brick element. The brick element simulates material necking under tension. This reduction in cross section causes an increase in stress for a given application of force, leading the material to undergo an accelerating strain rate in the tertiary creep phase. The 2-D models do not consider necking nor do they consider the effect of the Poisson’s ratio. Instead, they are direct implementations of a 1-D model in 3-D space. They either have a constant cross section with an increasing volume, or a constant volume with a uniform inverse change of cross section as a function of length. This is a severe limitation of the 2-node bar element model, even though the 2-node bar element suture with constant cross sectional area best emulated the original 1-D creep model. The 3-D elements produced simulation results for strain and stress with components in all three dimensions while the 2-node bar elements only produced strain results along the axis of the element and stress elements perpendicular to the element axis.

Using the dynamic solution engine, the 2-node bar element models solved the 6-weeks of simulated time in ~5 days, while the 20-node brick element models solved the 6-weeks of simulated time in ~13.5 days. However, using the static solution engine, the difference in solution time between the models was negligible; both models solved in a matter of minutes. The anticipated reduction in calculation time by meshing the suture out of 2-node bar elements in the eventual skull model was estimated to be negligible; the rest of the skull model will be comprised of 3-D elements.

Weighing the advantages of low relative error, increased level of detail, and a more realistic 3-D implementation of the creep equations against a marginal increase in calculation speed, the 20-node brick element of the SOLID18X family of elements was chosen as the optimal element type to model the suture tissue in ANSYS.

### **Comparison of Dynamic and Static Solution Engines**

The solution speed and relative accuracy of both the dynamic and static solving engines was investigated in anticipation of running simulations with a much higher element count. The aim was to evaluate any differences in the strain results between the two solution engines for identical loads and material properties over the course of the six simulated weeks of time. The measurement of solution times for the two solvers were measured with an accuracy of  $\pm 0.25$  days in the case of the dynamic solvers and an accuracy of  $\pm 5$  minutes in the case of the static solvers.

The differences in suture expansion and maximum 1<sup>st</sup> principal strain in the suture were compared between the two solvers. The meshes, creep coefficients, and applied forces were identical across the compared simulations. Figure Fig. 2-16 shows the comparison of the strain values for the 200g load simulations with the averaged coefficient set, and Figure Fig. 2-17 shows the comparison of the suture expansion for the same set of simulations. Continuous lines were utilized in these figures for visual purposes.

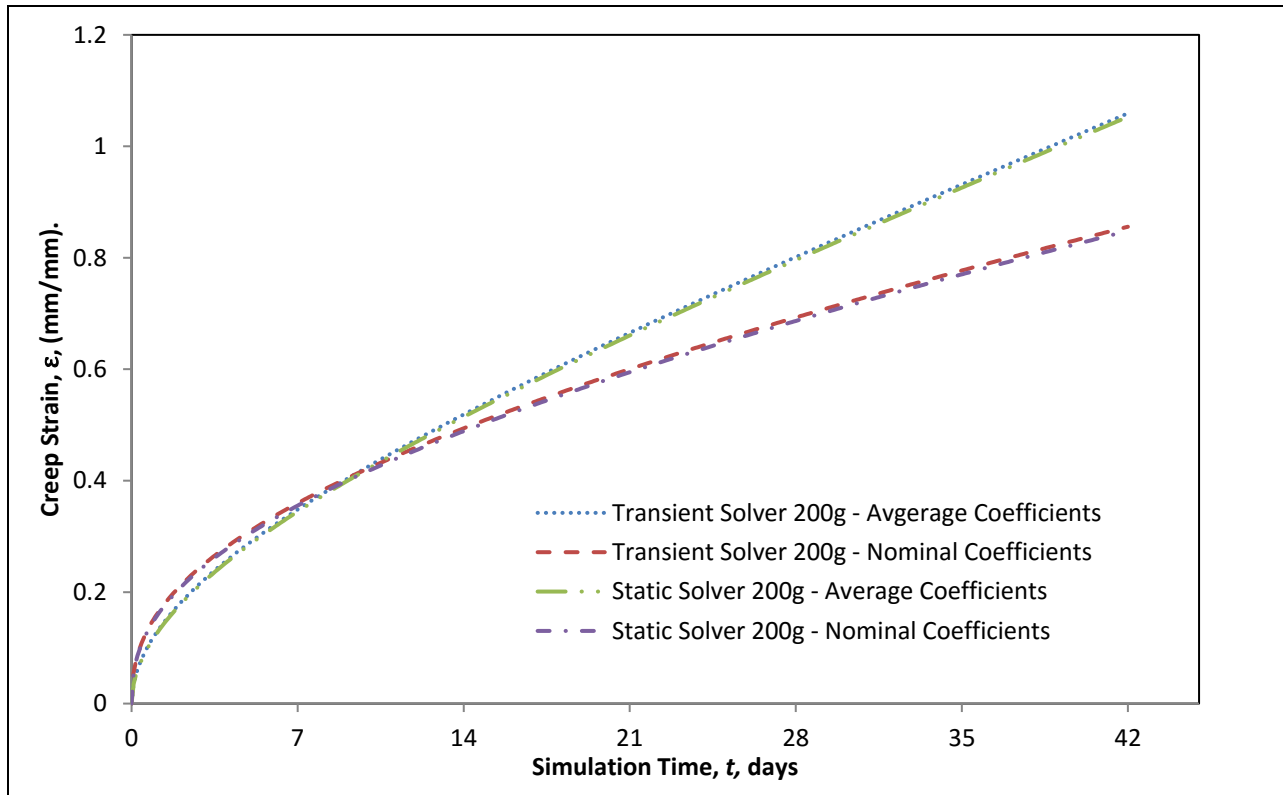


Fig. 1-22: Comparison of Strain ( $\epsilon$ ) Results for 200g (1.96N) Static and Dynamic Simulations

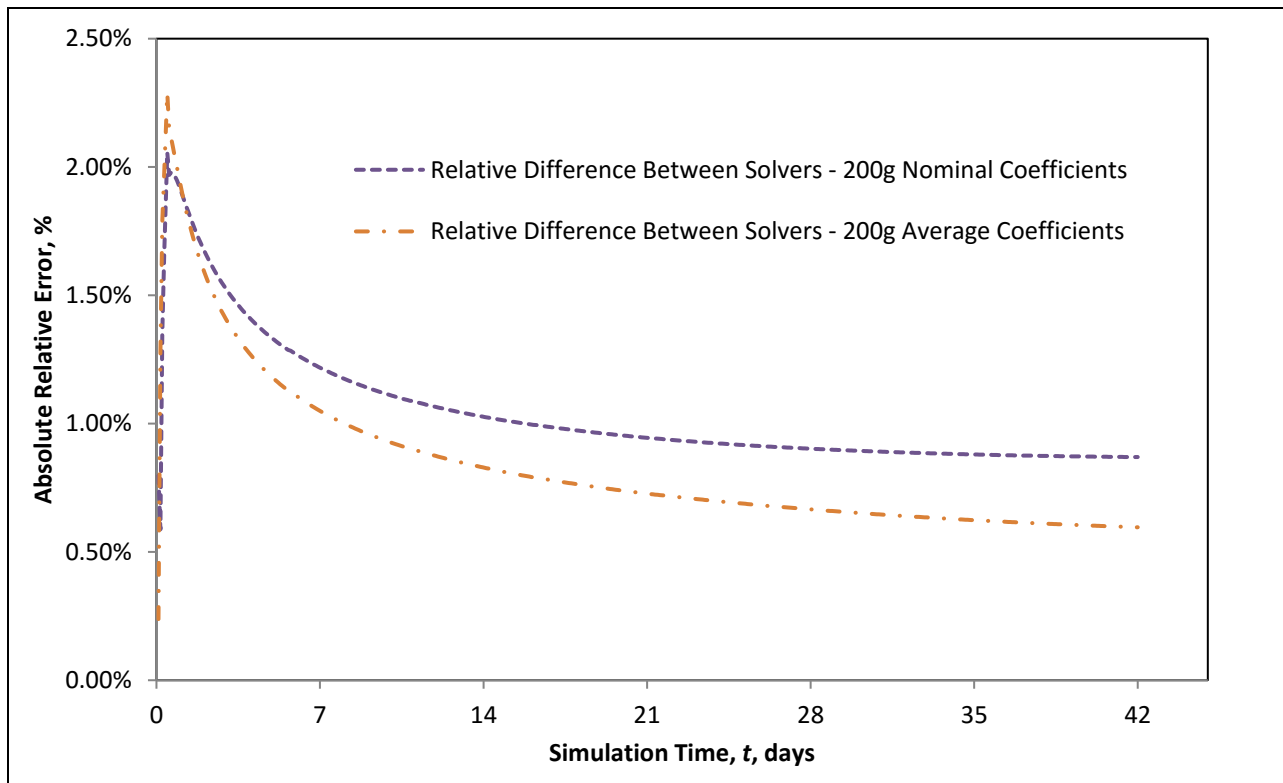


Fig. 1-23: Comparison of Abs. Relative Error for 200g (1.96N) Static and Dynamic Simulations

These figures show that the creep strain curves are both smooth and similar in magnitude of relative error when compared with the 1-D creep model. The solve time of the dynamic simulation was ~1.6 weeks, while the same simulation solved with the static engine solved in ~15 minutes. As both simulations produced similar results, the determining factor between the two solution methods was the massive reduction in calculation time. Therefore, the static solution engine was preferable for simulations of the creep material model over the dynamic solution method.

### **Effect of the $\gamma$ -modification on Strain and Expansion Results**

The  $\gamma$ -modified creep subroutine was simulated using the RTG to determine how the geometry would react to the increased rate of creep strain of the modified 1-D creep equation and to see if it would effectively emulate the suture width expansion of the original 1-D creep model. The 1-D strain equation (equation number), coupled with the original MSI width, was used to calculate the reference expansion. This  $\gamma$ -modification was necessary as a suture volume in a partial skull model with the MSI width would be geometrically unrealistic. This comparison looked at the SOLID185 8-node brick element suture and investigated both the load specific material coefficients and the averaged coefficients [2], [3], [14]. Additional tests with the constant cross section LINK180 2-node bar elements were also performed.

Figs. 2-18 to 2-20 show the width expansion over time for the 50g, 100g, and 200g tests in comparison to the 1-D anticipated expansion. As these figures show, the creep strain within the Link180 elements for the  $\gamma$ -modified creep models closely match the theoretical creep strain of the 1-D original model. However, the cumulative expansion of the RTG model utilizing the suture LINK180 elements, shown in Figs. 2-21 to 2-23, do not match the expected expansion curves. Further review of the available result outputs in ANSYS show the expected levels of elastic and creep strain in the LINK180 elements. This suggests a level of tertiary strain is in effect.

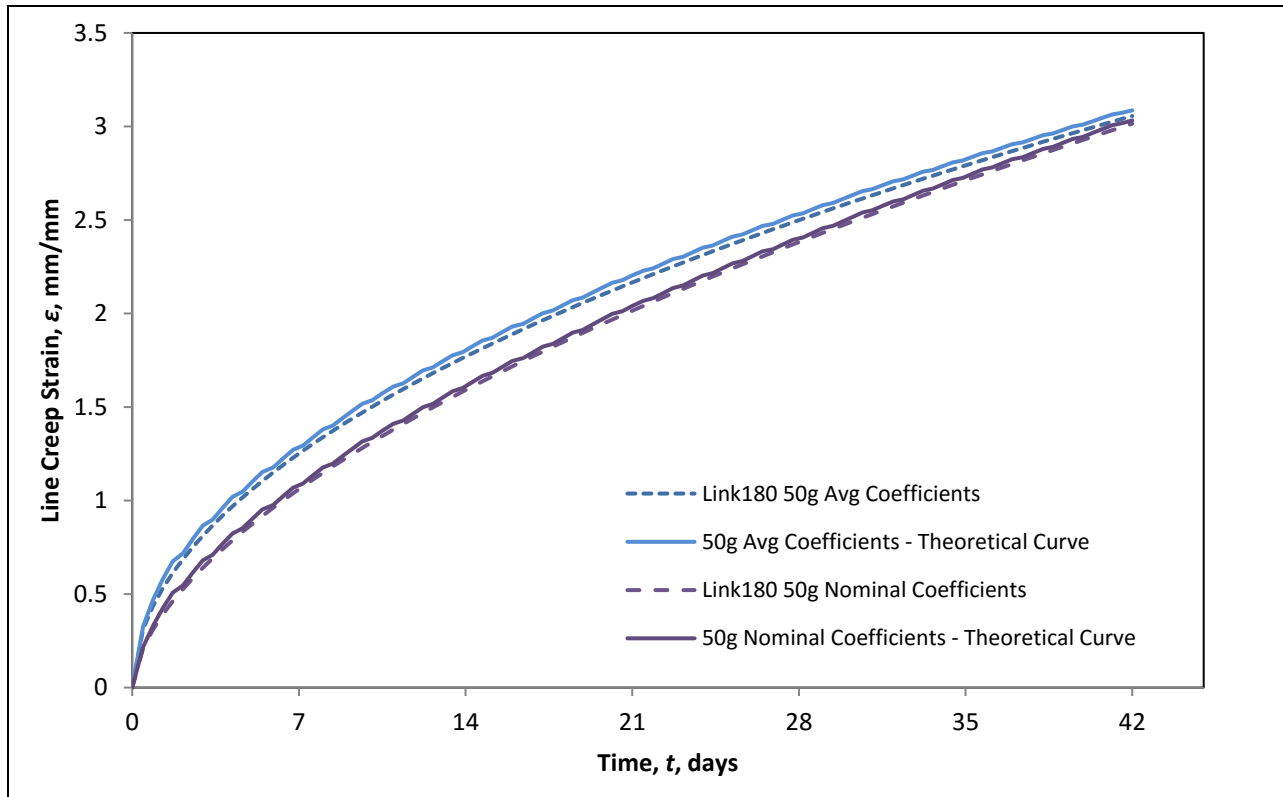


Fig. 1-24: 0.49N (50g) Load –  $\gamma$ -modified Model Strain

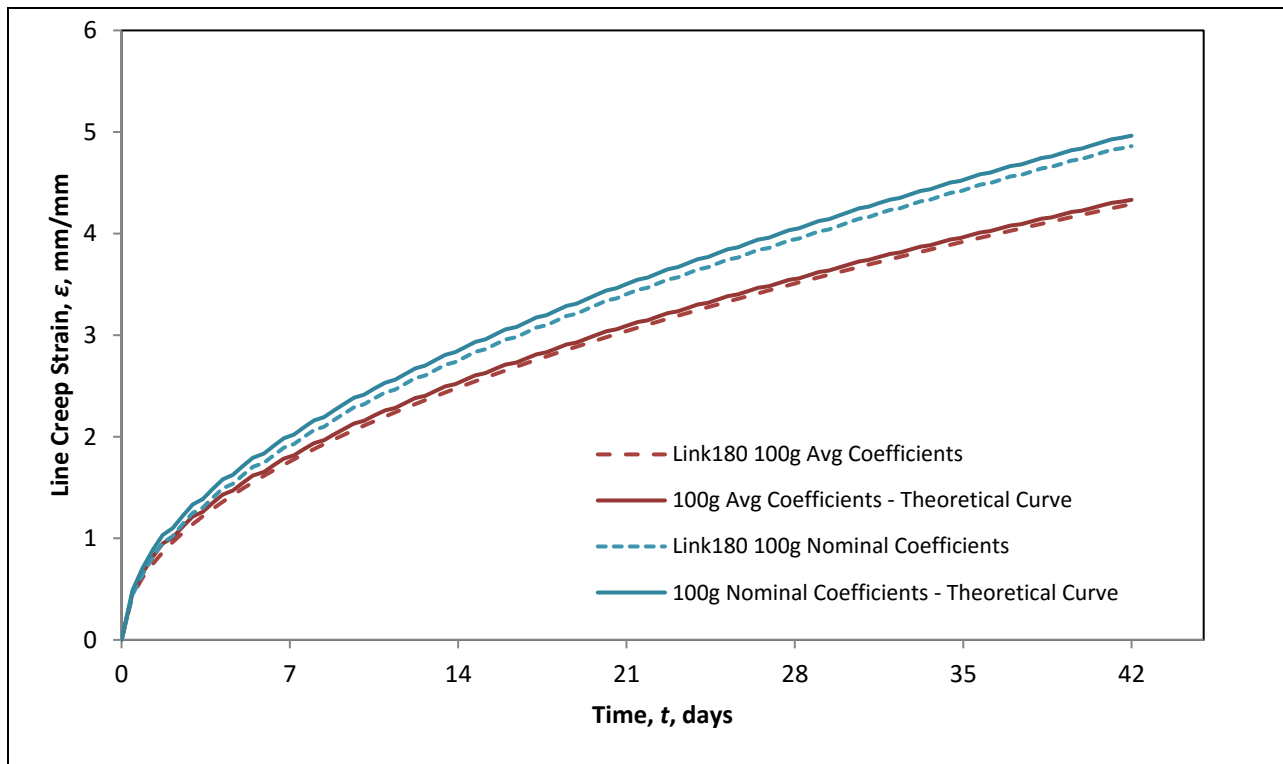


Fig. 1-25: 0.98N (100g) Load –  $\gamma$ -modified Model Strain

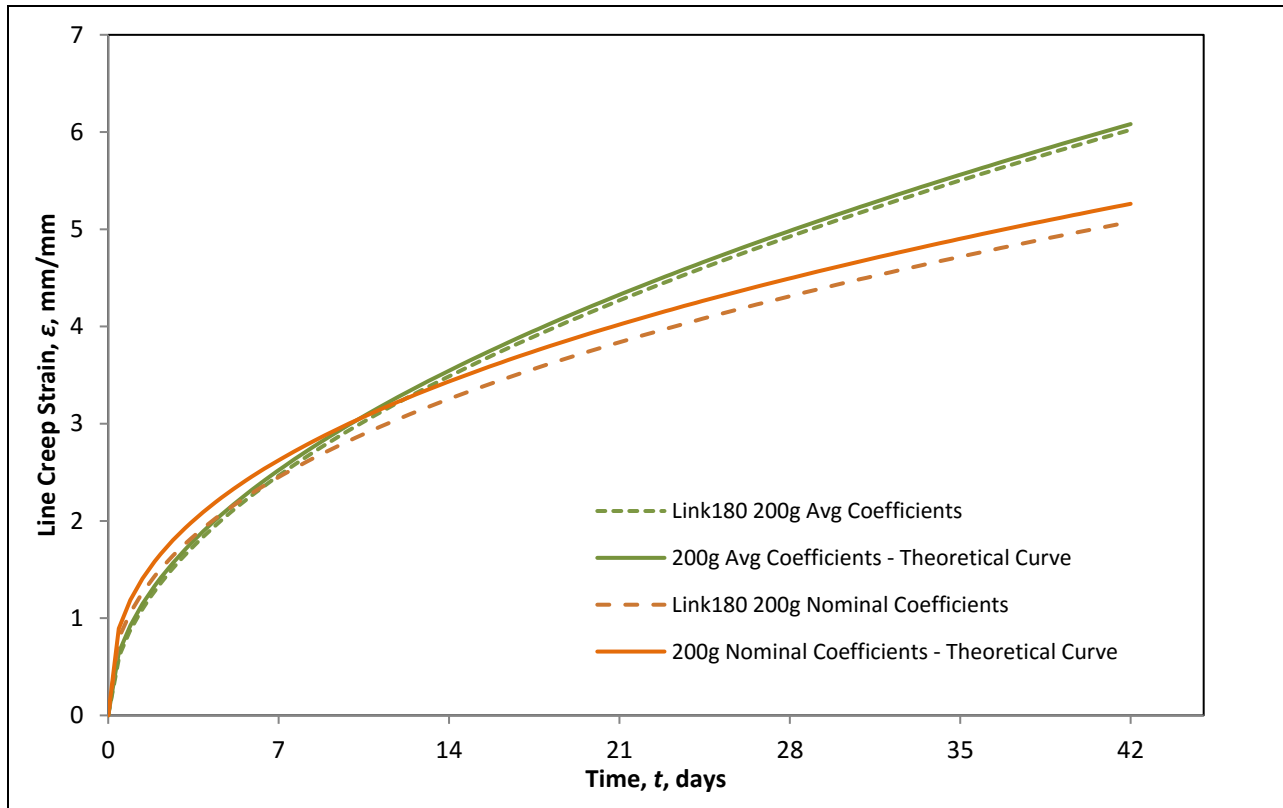


Fig. 1-26: 1.96N (200g) Load –  $\gamma$ -modified Model Strain

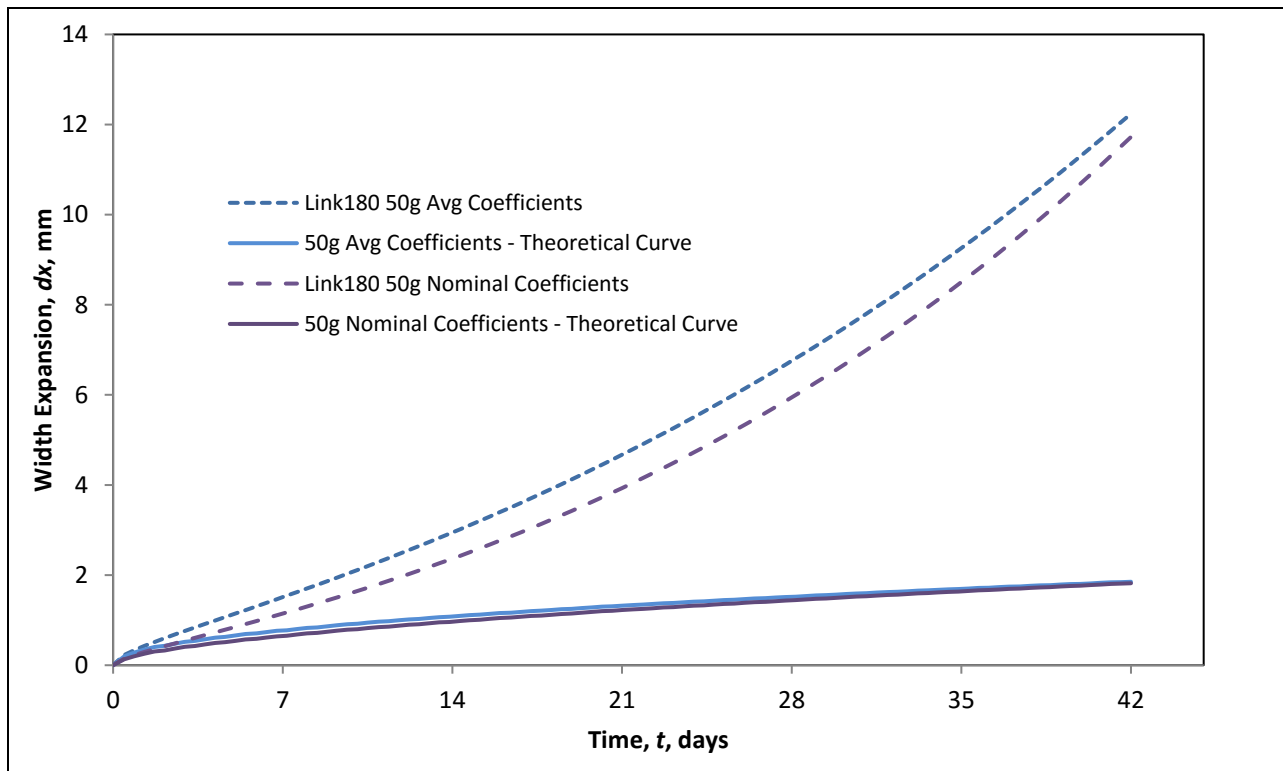


Fig. 1-27: 0.49N (50g) Load Test Strain –  $\gamma$ -modified Expansion

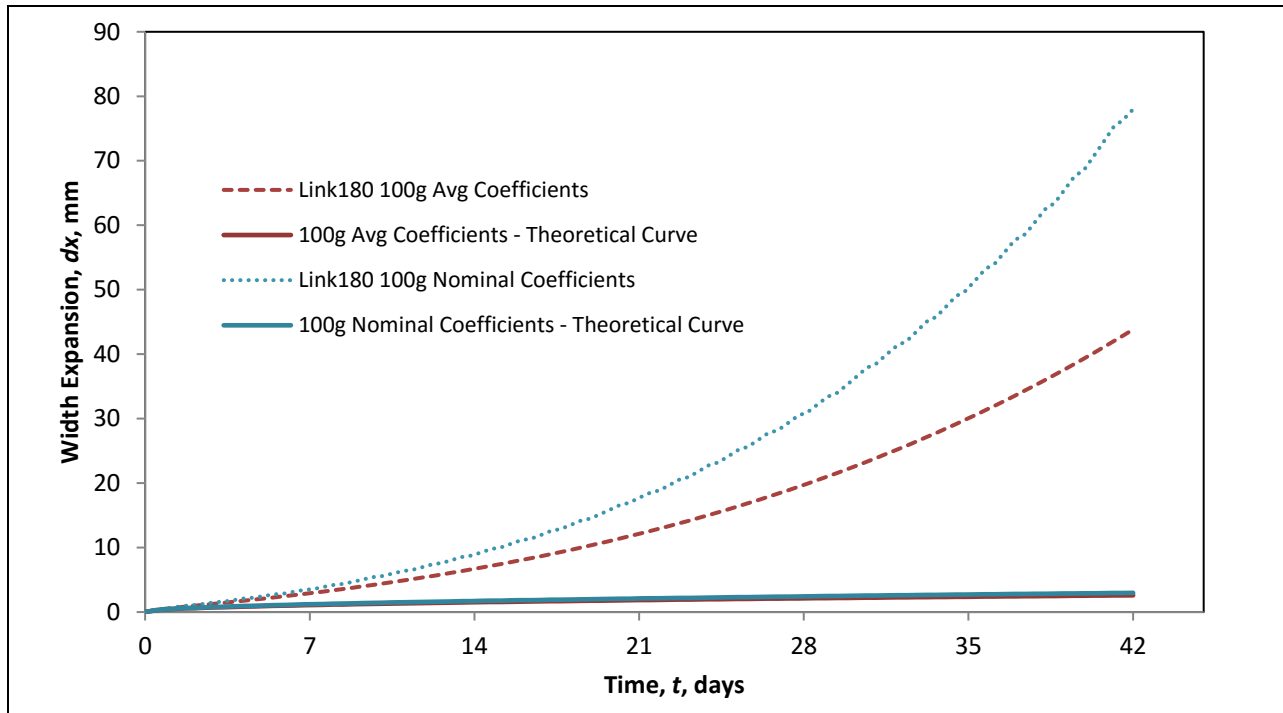


Fig. 1-28: 0.98N (100g) Load –  $\gamma$ -modified Expansion

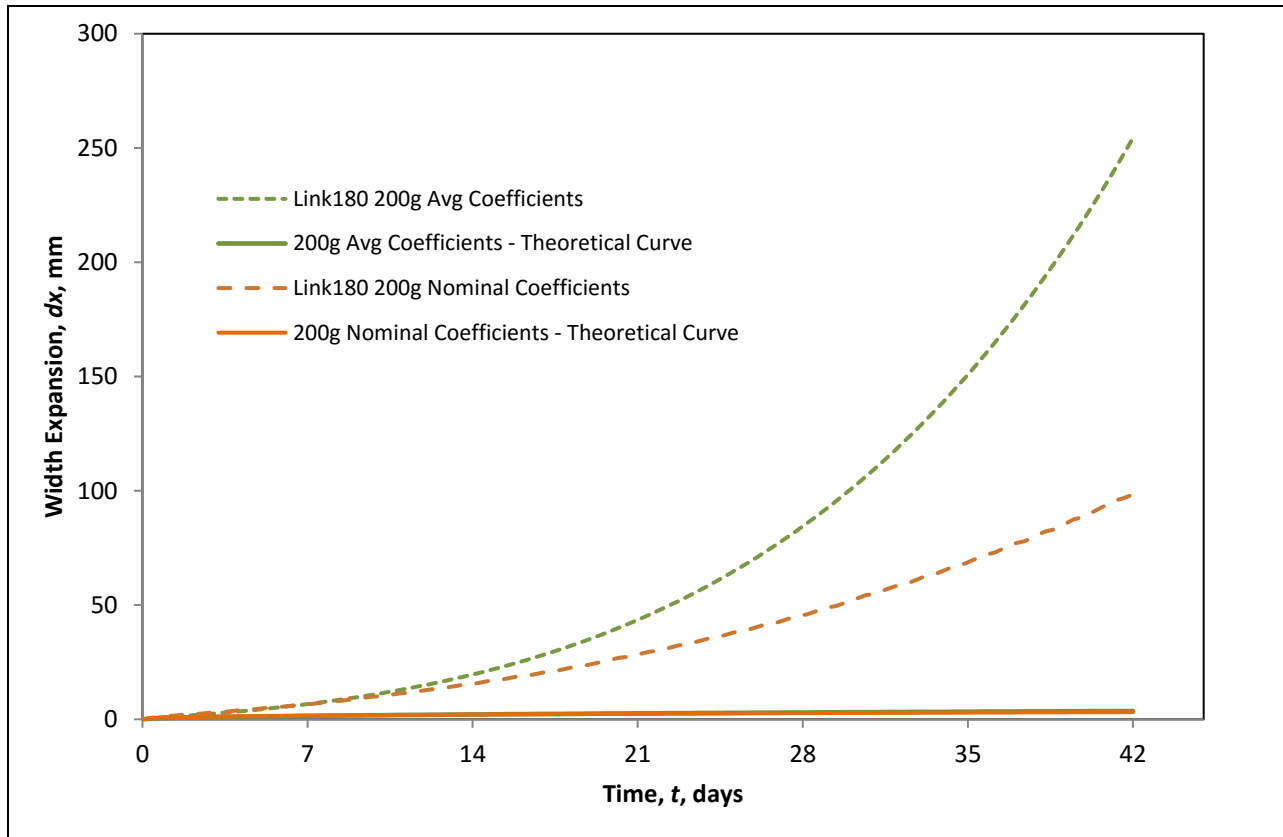


Fig. 1-29: 1.96N (200g) Load –  $\gamma$ -modified Expansion

The SOLID185 brick element simulations were unable to run to completion. This was due high geometric distortions caused by the early onset of tertiary-stage creep strain. This highly deformed geometry, shown in Fig. 2-24, was caused by the dramatically increased x-component strain and reduced the suture cross section. The reduced cross sectional area created highly increased stresses. Fig. 2-25 highlights the strain and stress curves at the sagittal plane over the simulated time, showing the effect of tertiary-stage creep.

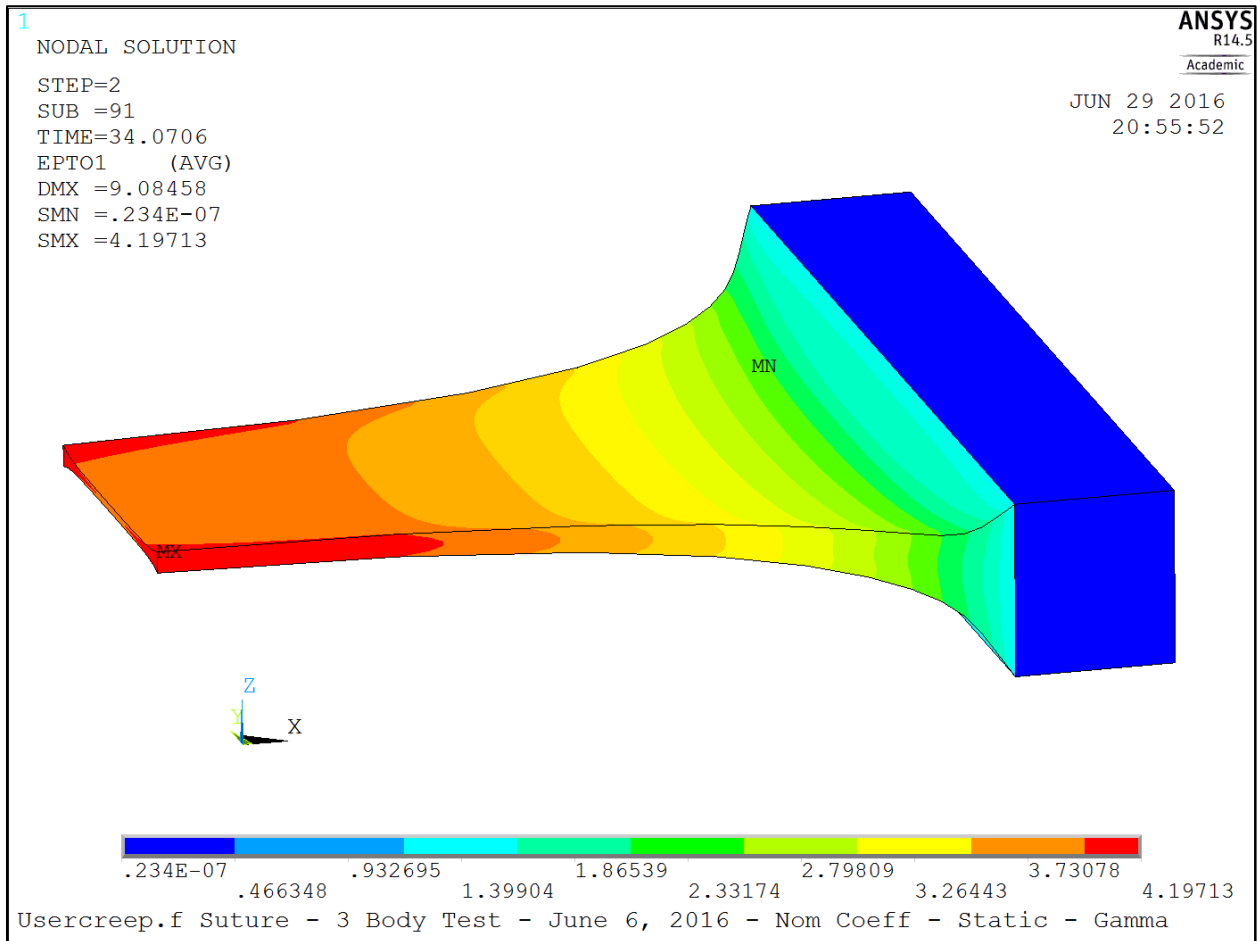


Fig. 1-30: Deformed Geometry of SOLID185  $\gamma$ -term Creep Simulation – 1<sup>st</sup> Principal Strain for Last Resolved Time Step  
 Legend presents of strain,  $\epsilon$  in mm/mm

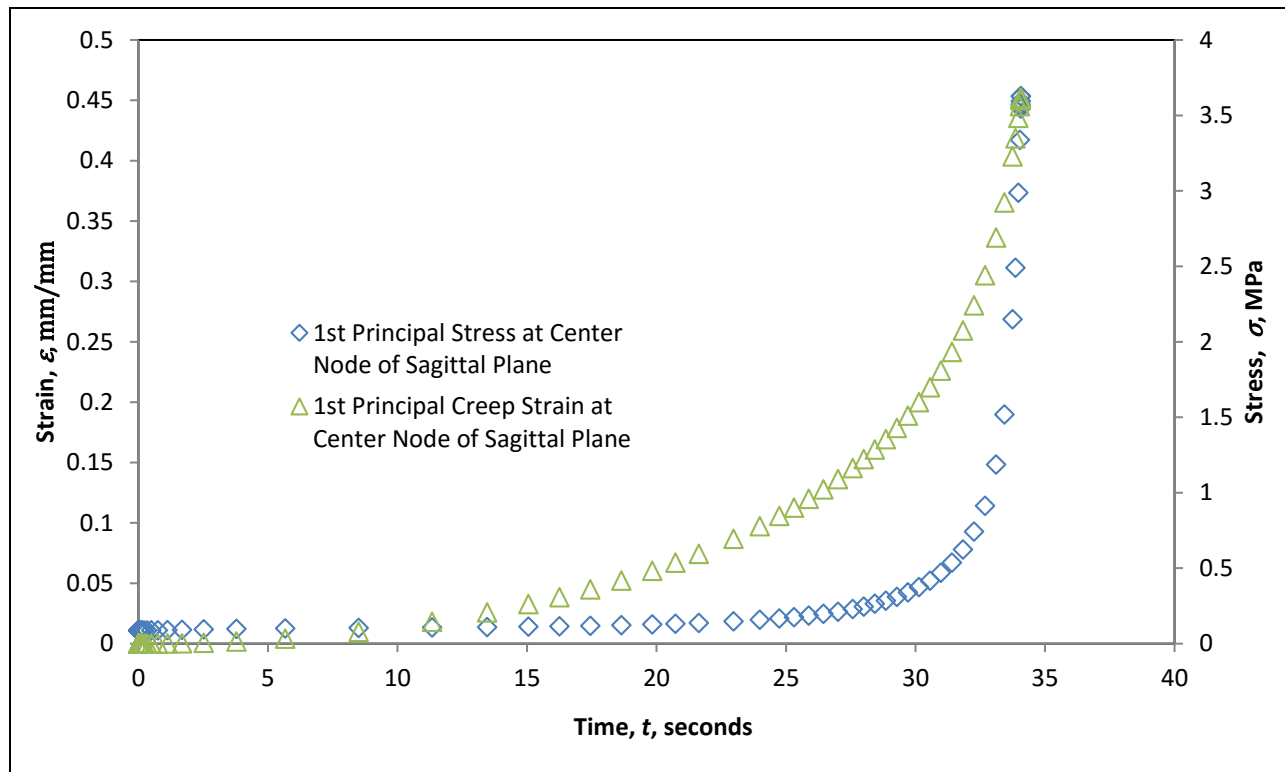


Fig. 1-31: Stress and Strain vs. Time for SOLID185  $\gamma$ -term Creep Simulation, 50g Simulation

From these results, it can be seen that the  $\gamma$ -modified creep model subroutine effectively replicates the non-linear material creep strain curve of the MPS under a constant tensile force using the LINK180 elements. This shows the promise of using the  $\gamma$ -modified creep subroutine in applications that look to determine the effect of the suture's expansion rate on the cranial structure, however the divergence between the expected system expansion and the ANSYS model suture expansion is of concern. The LINK180 elements utilized a constant cross sectional area condition and therefore do not consider material necking under tensile forces.

The reason for the divergence from the anticipated suture expansion has very much to do with the assumptions within the original creep model as seen in eq. (2-1). The assumptions that underpin the original model, as stated in Section 1.3.1, are that the 1-D creep equation is fundamentally based on the initial conditions of the system. This pertains to the original suture width, a constant cross sectional area, the applied force, and the time from initialization of loading. Additionally, it does not consider how the rest of the skull system affects mechanics of the suture expansion, nor does it consider the biomechanical changes to the suture. As it

pertains to adaptation to FEA, the mathematics of the original equation fails. Numerically solving the FEA model and the creep subroutine calculates the creep expansion,  $dX_n$ , for each new time interval based on the suture dimension,  $X_{n-1}$ , at the end of the preceding time step as per eq. (2-54), and not the initial suture width that the original equation uses as per eq. (2-4).

$$dX_n = (d\varepsilon_n * dt_n) * X_{n-1} \quad (1-61)$$

So although the LINK180 element model replicates the creep strain curve of the 1-D creep model on which it is based, it does not accurately replicate the expected suture expansion.

The  $\gamma$ -modified creep model failed to converge when simulated using the 8-node brick elements. This simulation failure invites discussion of numerical results of adapting the creep model. It incorporates the expected material necking that should occur for three dimensional materials. Unlike the 1-D equation on which it is based, the numerical FEA model can fail due to high levels of geometry distortion and it is subject to the actual geometry deformations that materials endure under load. The model as it currently exists cannot converge under such extreme deformation, and therefore should not as the suture may have failed before it reaches the high levels of strain in Fig. 2-25. However, it could be used to predict suture failure at high strain levels in a skull model. Additionally, the creep model could be retrained using the RTG iteratively in FEA to better simulate the suture expansion used by Romanyk et al. [2], [5] to train the original model. The advantages of using a 3-D numerical solver to train the material model include incorporation of geometry deformations under load, utilization of a 3-D system versus a 1-D approximation, and employment of the same numerical stepping method as the eventual FEA implementation of the model. It may be necessary to look into implement some form of strain hardening to prevent the system from expanding out of control.

Possible future paths of research may also look to find ways to simulate bone growth during expansion or fluid in-rush as the soft tissues expand. Both these avenues may reduce the material necking experienced by the solid suture volume utilized here, as both bone growth during expansion and the semi-fluidic construction of biological tissues are not included in this model.

### 2.3.3 Relaxation Model Results

As quite a few maxillary expansion procedures use hyrax-type expanders, developing a FEA non-linear relaxation material model for the MPS was paramount. This required determining an adequate curve fit for the Maxwell model Prony approximation and determining the initial conditions based on model activation strain. Additionally, non-linear geometry conditions were verified, and the static and dynamic solution engines were re-evaluated. Finally, multiple device activations were tested with a selection of different activation distances.

#### Determining the Optimum Order of Prony Fit

Curve fitting of the Prony approximation was completed using MATLAB® to generate time versus bulk and shear stress datasets and ANSYS to generate the Prony coefficients. The data sets were generated using the  $\gamma$ -modified creep equation and a Poisson's ratio ( $\nu$ ) of 0.3. Orders of fit ( $n$ ) of 3, 5, 7, and 9 were used. Following the decision to utilize a 7-term fit, multiple dataset time signatures were evaluated for ability to emulate the expected stress decay in ANSYS<sup>4</sup>. Although necking of the suture was not observed experimentally in the rabbit MSS expansion experiments, it cannot be definitively stated that Poisson's ratios of 0 (compressible) or 0.5 (incompressible) are applicable. As such, a midrange Poisson's ratio of 0.3 was conservatively assumed for this FE study.

These initial curve fit tests utilized a data set of  $n=200$  data points for a time range of 5 seconds to 10000 seconds. The fitting procedure [10] was iterated twice for each fit order. Resultant shear,  $G$ , coefficient sets are reported in Table 2-10 along with the regression error results.<sup>5</sup>

---

<sup>4</sup> Dataset time signatures outlined in Table 2-4

<sup>5</sup> Bulk,  $K$ , coefficients are not reported as the material was assumed isotropic and the resultant curve fit coefficients were found to be identical for both moduli.

Table 1-10: Summary of Shear Modulus Prony Curve Fit Regression Errors for Different Fit Orders

<b>3rd Order Prony Fit</b>								
$\alpha_1$	$\alpha_2$	$\alpha_3$	$\alpha_4$	$\alpha_5$	$\alpha_6$	$\alpha_7$	$\alpha_8$	$\alpha_9$
0.98479	0.01363	0.00144	N/A	N/A	N/A	N/A	N/A	N/A
$\tau_1$	$\tau_2$	$\tau_3$	$\tau_4$	$\tau_5$	$\tau_6$	$\tau_7$	$\tau_8$	$\tau_9$
5.00	242.98	2141.60	N/A	N/A	N/A	N/A	N/A	N/A
<i>Regression Residual: 83.02666</i>								
<b>5th Order Prony Fit</b>								
$\alpha_1$	$\alpha_2$	$\alpha_3$	$\alpha_4$	$\alpha_5$	$\alpha_6$	$\alpha_7$	$\alpha_8$	$\alpha_9$
0.85531	0.02209	0.11549	0.00534	0.00157	N/A	N/A	N/A	N/A
$\tau_1$	$\tau_2$	$\tau_3$	$\tau_4$	$\tau_5$	$\tau_6$	$\tau_7$	$\tau_8$	$\tau_9$
6.99	190.46	41.90	754.8848	3485.782	N/A	N/A	N/A	N/A
<i>Regression Residual: 0.139192</i>								
<b>7th Order Prony Fit</b>								
$\alpha_1$	$\alpha_2$	$\alpha_3$	$\alpha_4$	$\alpha_5$	$\alpha_6$	$\alpha_7$	$\alpha_8$	$\alpha_9$
0.79591	0.14287	0.01340	0.03979	0.00500	0.00205	0.00084	N/A	N/A
$\tau_1$	$\tau_2$	$\tau_3$	$\tau_4$	$\tau_5$	$\tau_6$	$\tau_7$	$\tau_8$	$\tau_9$
5.00	20.38	173.23	62.85909	457.1911	1265.574	4897.945	N/A	N/A
<i>Regression Residual: 0.0089837</i>								
<b>9th Order Prony Fit</b>								
$\alpha_1$	$\alpha_2$	$\alpha_3$	$\alpha_4$	$\alpha_5$	$\alpha_6$	$\alpha_7$	$\alpha_8$	$\alpha_9$
0.73158	0.11943	0.10994	0.00296	0.02599	0.00133	0.00597	0.00111	0.00150
$\tau_1$	$\tau_2$	$\tau_3$	$\tau_4$	$\tau_5$	$\tau_6$	$\tau_7$	$\tau_8$	$\tau_9$
2.95	9.70	28.94	83.90255	194.9495	247.6402	701.2233	841.7454	3500.94
<i>Regression Residual: 0.026628</i>								

As is clear from the results in Table 2-10, the high order fits resulted in lower regression error in comparison to the supplied dataset. In this regard, the 7-term Prony fit is the most accurate with a regression error of 0.00898, with the 9-term a close second with 0.026628. However, as calculation speed is a factor in FEA, the models were tested in ANSYS for overall speed of calculation in the dynamic solution engine. These initial tests utilized an activation distance of 0.125 mm ramped over five seconds. Six activation-relaxation load steps followed, with a total simulated time of one hour. From these dynamic simulations, it was found that the 5-term model took an hour to calculate, the 7-term took an hour and five minutes, and the 9-term model took an hour and forty minutes. The 3-term model was not tested due to the poor fit and high regression residual. The 5- and 7-term fits had the edge in solution speed while the

9-term model took 34% longer to solve than the 7-term model. Based on the balance of a significantly lower solution time than the 9-term fit and a better regression residual, the 7-term Prony fit was the optimal approximation and was used for all subsequent testing.

### Time Adjustment of Relaxation Data Sets for Prony Curve Fitting

Accurate simulation of the time dependent stress relaxation of the MPS in FEA required the evaluation of how the time in the dataset affected the FEA stress peak results. 7-term Prony curve fits were generated for the time configurations of time listed in Table 2-4. For simulation in ANSYS these models utilized the  $\beta$ -term definitions for the initial Young's modulus for an activation strain of 0.14535mm/mm.<sup>6</sup> The resultant Prony coefficients for the three time cases, and the associated  $t_{int}$ ,  $\beta$ , and  $E_0$  values, are listed in Table 2-11.

Table 1-11: Prony Coefficients for Shear Moduli (G) for 3 Time Fit Cases

$t_d = t_c$				$t_d = t_c$				$t_d = t_c - 4.99s$			
5s <= $t_c$ < 10000s				0.01s <= $t_c$ < 10000s				5s <= $t_c$ < 10000s			
$\alpha_1$	0.79591	$\tau_1$	5.000	$\alpha_1$	0.99835	$\tau_1$	0.010	$\alpha_1$	0.3927	$\tau_1$	2.8
$\alpha_2$	0.14287	$\tau_2$	20.379	$\alpha_2$	0.0013327	$\tau_2$	4.497	$\alpha_2$	0.40143	$\tau_2$	10.376
$\alpha_3$	0.039795	$\tau_3$	62.859	$\alpha_3$	0.0002386	$\tau_3$	21.532	$\alpha_3$	0.14725	$\tau_3$	39.696
$\alpha_4$	0.013401	$\tau_4$	173.230	$\alpha_4$	0.000055137	$\tau_4$	83.330	$\alpha_4$	0.042999	$\tau_4$	149.81
$\alpha_5$	0.0050017	$\tau_5$	457.191	$\alpha_5$	0.000014857	$\tau_5$	286.359	$\alpha_5$	0.011634	$\tau_5$	575.46
$\alpha_6$	0.0020479	$\tau_6$	1265.574	$\alpha_6$	4.6233E-06	$\tau_6$	947.112	$\alpha_6$	0.0030511	$\tau_6$	2310.1
$\alpha_7$	0.00084392	$\tau_7$	4897.945	$\alpha_7$	1.6057E-06	$\tau_7$	4000.739	$\alpha_7$	0.0008232	$\tau_7$	114455
$\beta$	2.364188177			$\beta$	1469.772066			$\beta$	1.127029		
$t_{int}$	5.6448 seconds			$t_{int}$	5.2986			$t_{int}$	5.6691 seconds		
$E_0$	39.4864 MPa			$E_0$	26167 MPa			$E_0$	18.7425 MPa		

These simulations utilized the same FEA load step procedure as used for evaluating the order of Prony fit. 1<sup>st</sup> principal stress results are shown in Fig. 2-26 as a function of time for Cases 'A' and 'C'. The stress results of the two simulations are compared with the predicted stress from the 1-D  $\gamma$ -modified relaxation equation. Case 'B' was not simulated due to a poorer regression fit and  $E_0$  two orders of magnitude higher than the other two cases.

<sup>6</sup>  $\epsilon_0 = 0.25mm/1.72mm = 0.145mm/mm$

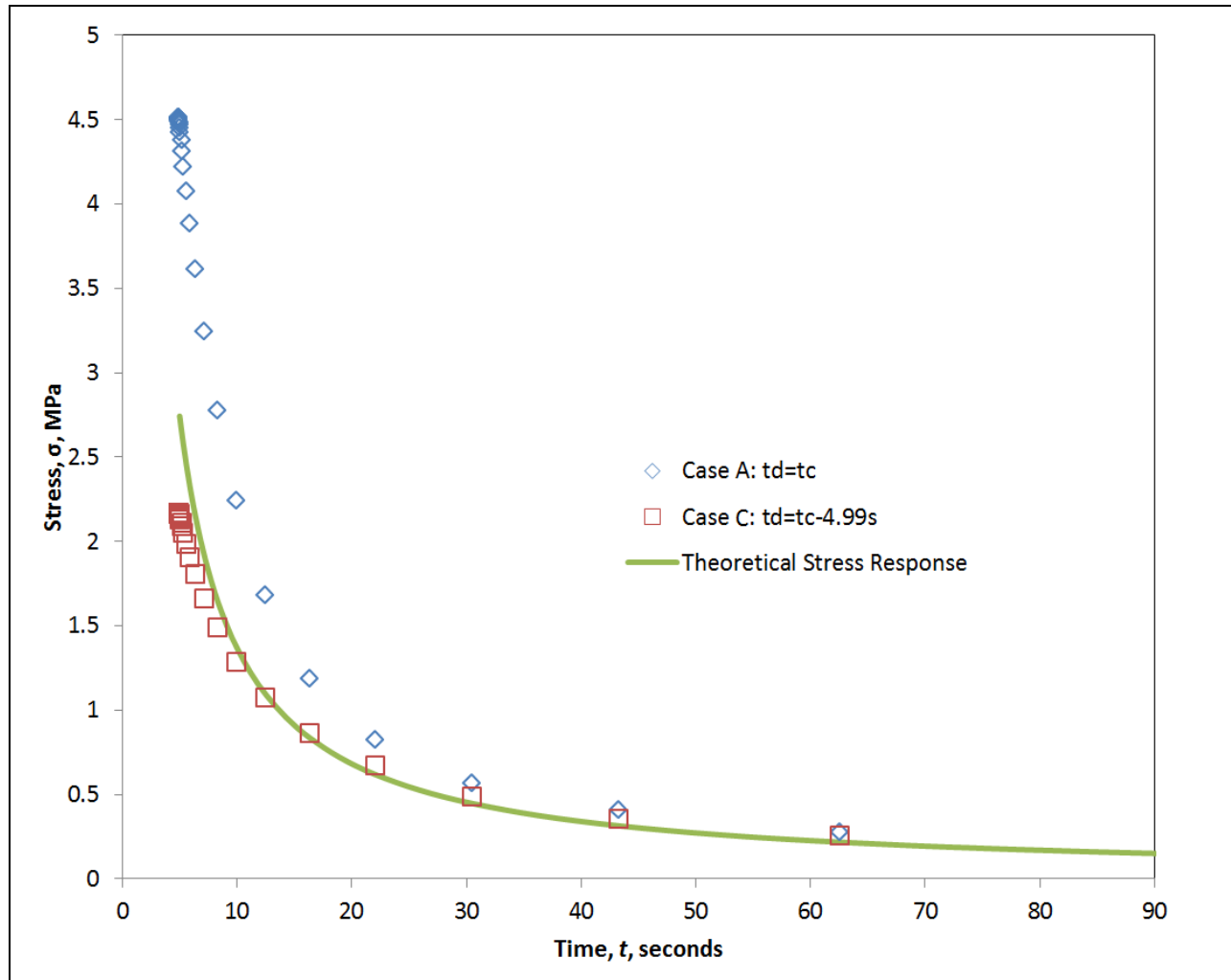


Fig. 1-32: 1<sup>st</sup> Principal Stress in Center of Sagittal Plane of RTG for Prony Fit Time Variations

These results show that the time shifted model ( $t_d = t_c - 4.99$ ) most closely matches the theoretical suture stress. The peak stress in the time shifted model was 2.16MPa, which is a difference of 21.09% in comparison to the 1-D anticipated result of 2.74MPa. This is much better than the peak stress of the non-time shifted model of 4.51MPa, which differed from the anticipated value by a massive 64.34%. Therefore, the best emulation of the stress relaxation response was found to be the time-shifted curve fit. The peak stress difference found between the Case 'C' time shifted model and the anticipated result is likely resulting from mild tissue relaxation in the suture during the 5 second appliance activation period, which the relaxation model does not account for.

## Linear versus Non-Linear Geometry Options

To verify the assumption that the non-linear geometry calculations in ANSYS are required for the relaxation model, the Prony model was run with and without the non-linear calculations enabled. If the linear geometry option were sufficient, it would mean a decrease in overall simulation time. It would be judged as adequate if the strain and stress results were identical between the two methods. Figs. 2-27 and 2-28 shows the results of the 1<sup>st</sup> principal strain and the stress, highlighting the differences between the two geometry calculation options.

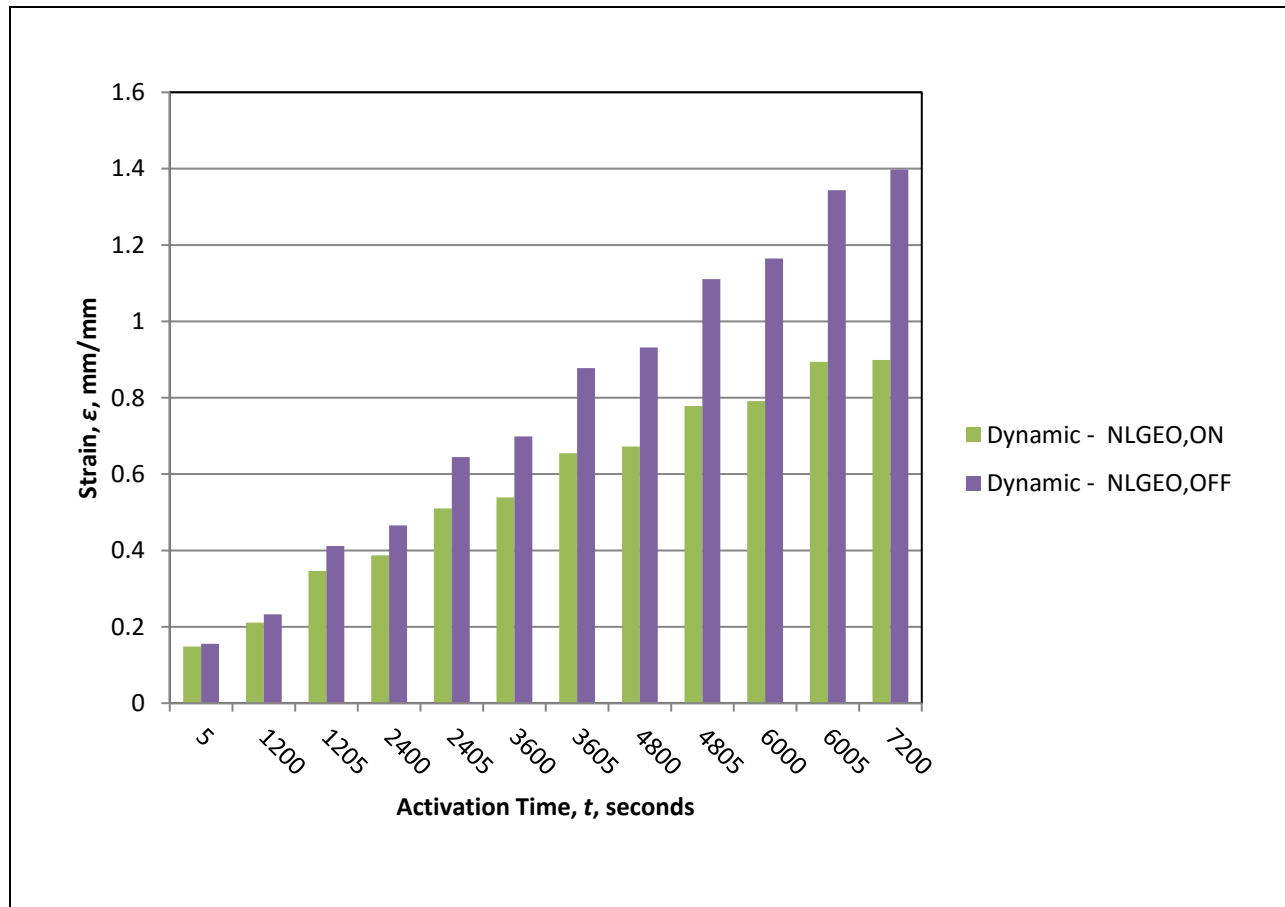


Fig. 1-33: 1<sup>st</sup> Principal Strain Results at Appliance Activation Using Linear and Non-Linear Geometry Options

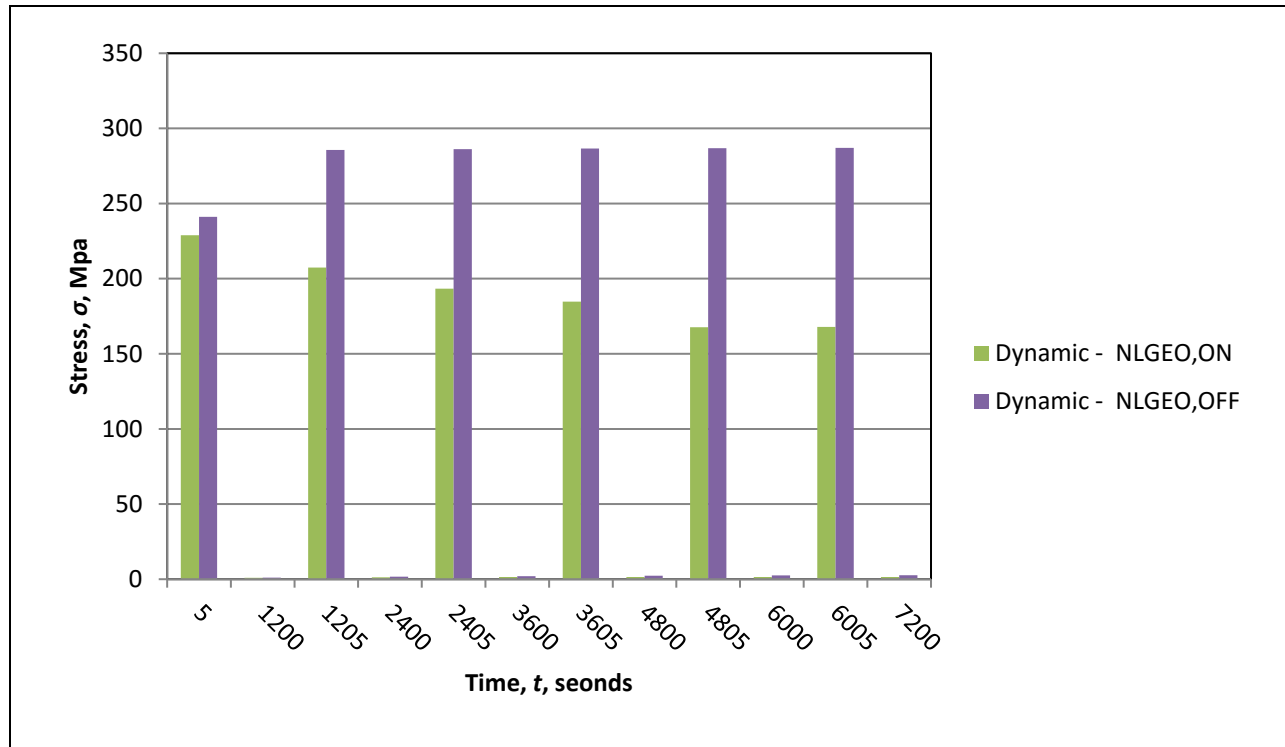


Fig. 1-34: 1<sup>st</sup> Principal Stress Results at Appliance Activation Using Linear and Non-Linear Geometry Options

Evident in Figs. 2-27 and 2-28, the strain and stress results are dissimilar between the linear and non-linear geometry options. This indicates that the linear geometry option is insufficient for simulating the stress relaxation of the MPS; if it were, the results between linear and non-linear geometry options would be virtually identical. As such, the non-linear geometry option is determined to be required for further simulations, despite the additional calculation operations required.

### Static versus Dynamic Solvers Results

As with the creep model, it was necessary to evaluate the relaxation model using both the static and dynamic solution engines. The aim of this portion of the analysis was to determine if the static solution engine produced adequate results while reducing the overall solution time. The static solver disregards the impulse and inertia effects resulting in fewer calculations. The sheer number of calculations was also reduced by having a simpler set of convergence checks [12], [15], [16]. Fig. 2-29 compares 1<sup>st</sup> principal stress of the static and dynamic relaxation simulations.

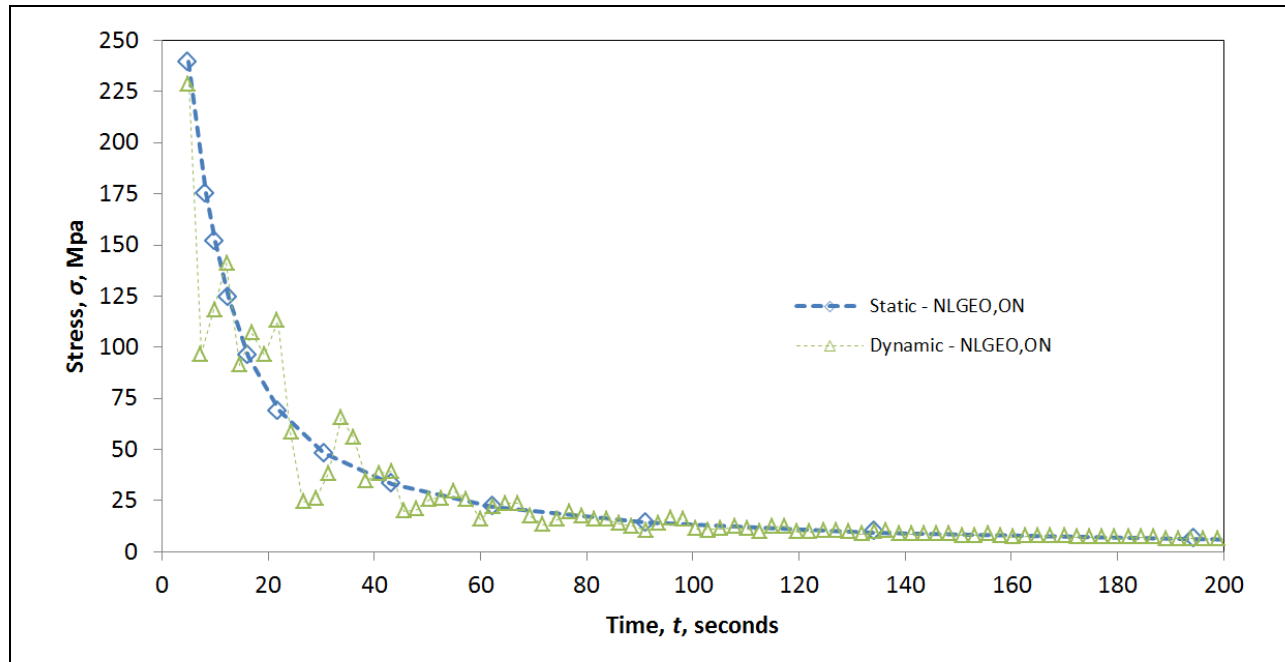


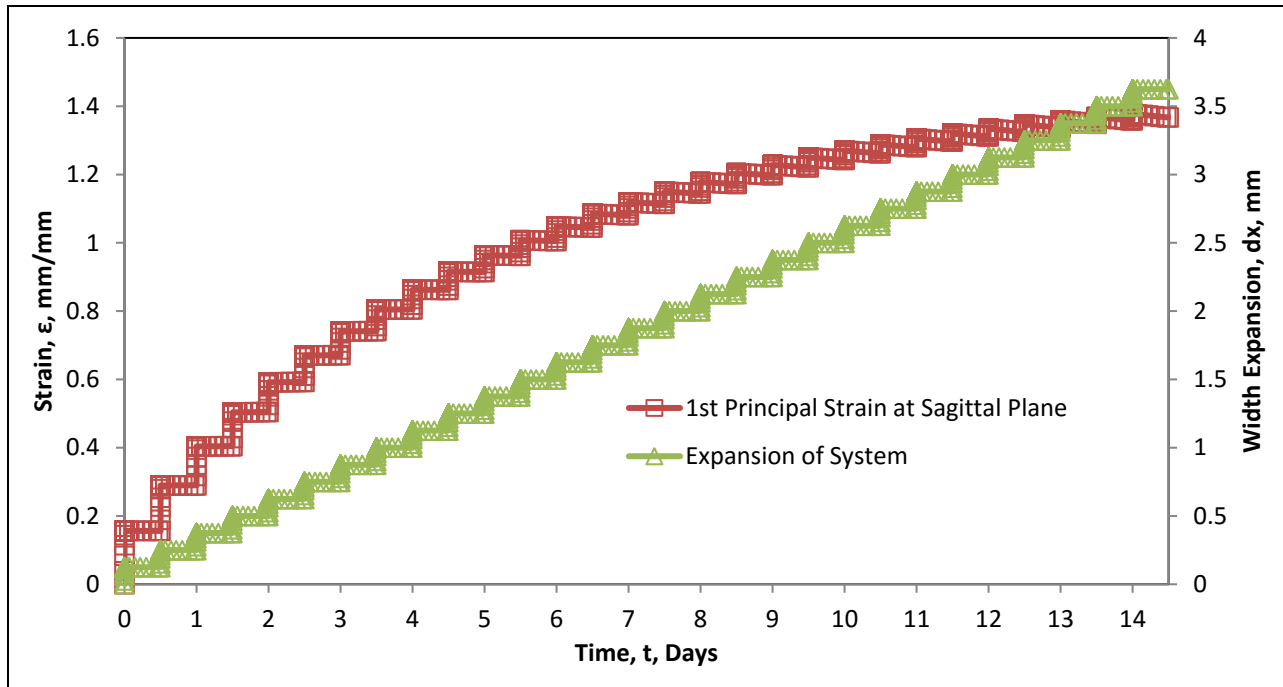
Fig. 1-35: Comparing the Maximum Stress of Relaxation Simulations Using Static and Dynamic Solvers

The dynamic simulation resulted in an unsmooth stress relaxation curve that bounces across the stress curve of the static simulation. The solution stage of the simulation utilized six activations over an hour of simulated time. The relaxation period was set for 10 minutes in these simulations. The solve time for these simulations were approximately an hour for the dynamic simulation and a fraction of that time at about 10 minutes for the static simulation. Overall, the static simulation method displayed adequate convergence and was significantly faster than the dynamic solution. The maximum stress decayed to 7.97% of the calculated peak stress after 91.29 seconds in the time-shifted model, effectively emulating the theoretical stress decay curve.

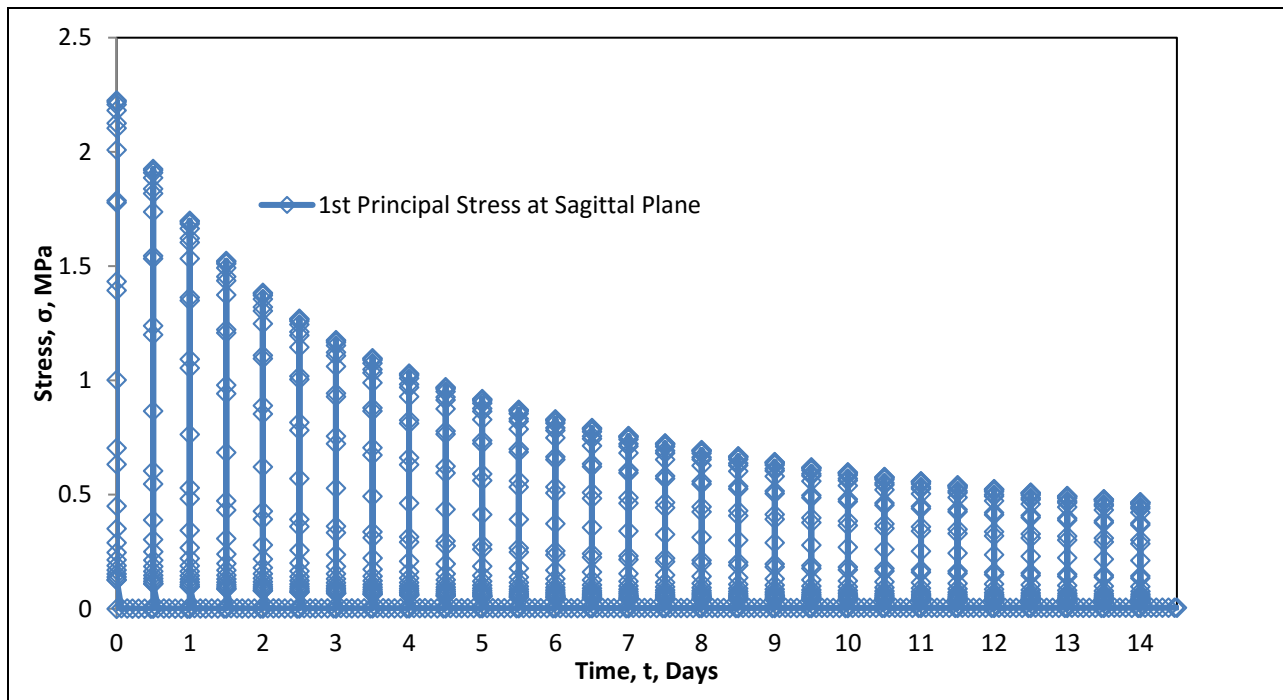
### Full Expansion Treatment Simulation

In advance of incorporating the relaxation model into a partial skull model for simulating an entire ME procedure, it was prudent to simulate a full expansion treatment on the RTG to ensure that the FE method developed was able to withstand the 422% change in width of the suture volume for a full set of appliance activations.

Twenty-nine 0.125mm displacements were sequentially loaded on the RTG, each spaced 6-hours apart. Fig. 2-30 shows the expansion, strain, and stress results of this simulation.



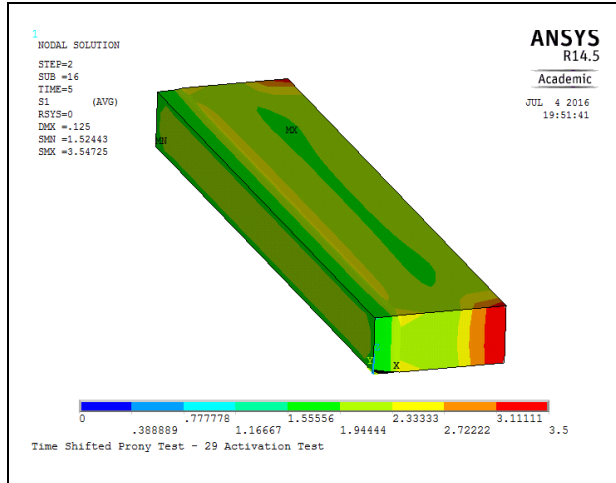
(A): 1<sup>st</sup> Principal Strain At the Sagittal Plane of the Suture and the System Expansion



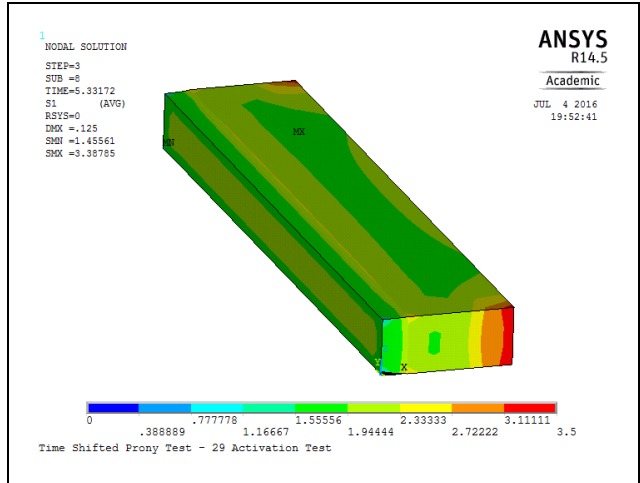
(B): 1<sup>st</sup> Principal Stress at the Sagittal Plane of the Suture

Fig. 1-36: Maximum Displacement, Strain, and Stress Results of 29 Activation Relaxation Simulation

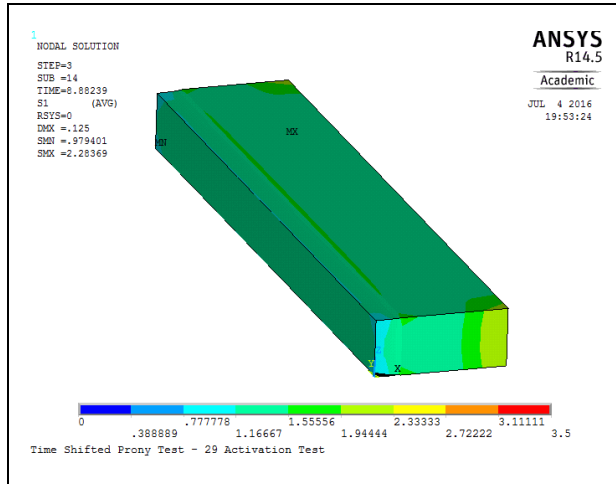
Fig. 2-31 shows the 1<sup>st</sup> principal stress of the deformed FEA model at 6 key frames within the initial relaxation period of the FEA model after the first appliance activation. Fig. 2-32 shows the same for the final appliance activation.



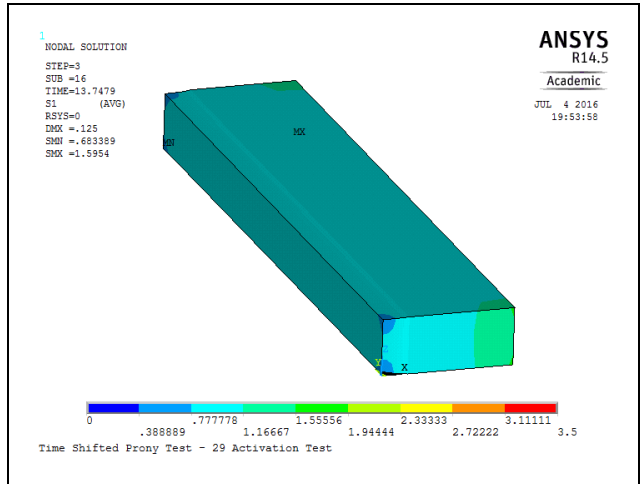
(A)  $t_{act} + 0$  seconds



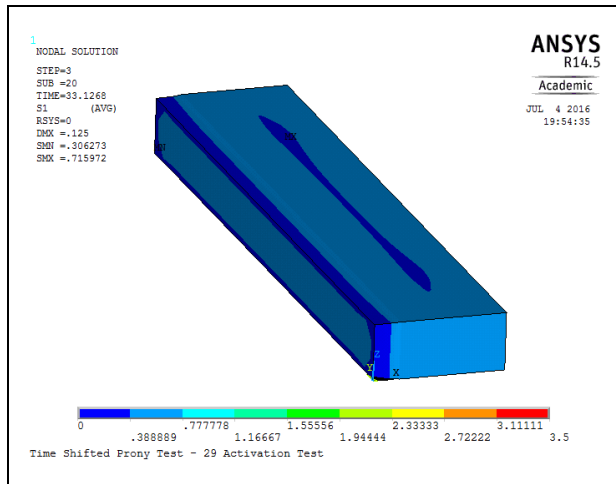
(B)  $t_{act} + 0.332$  seconds



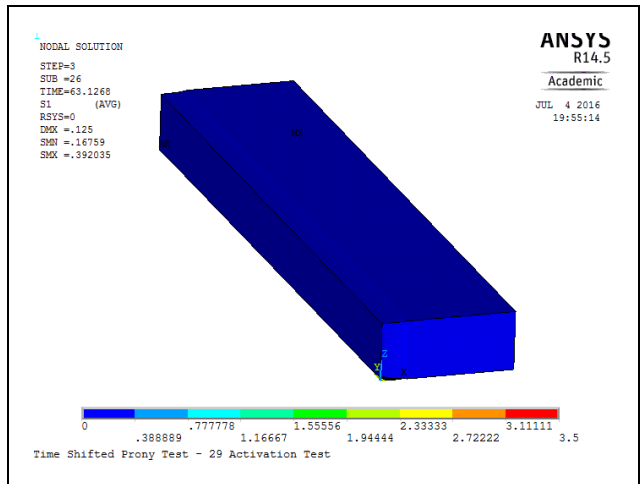
(C)  $t_{act} + 3.882$  seconds



(D)  $t_{act} + 8.748$  seconds

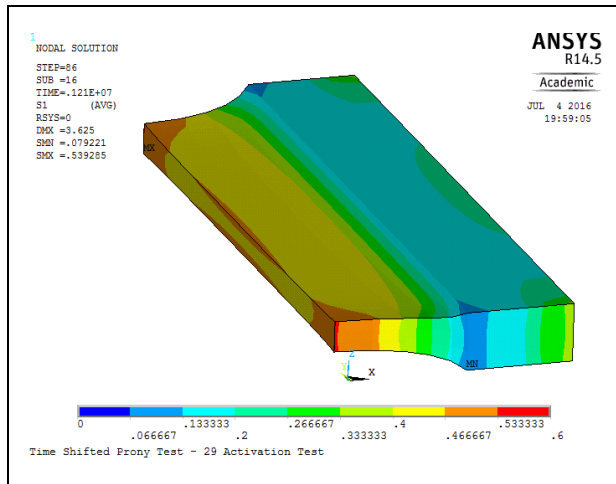


(E)  $t_{act} + 28.127$  seconds

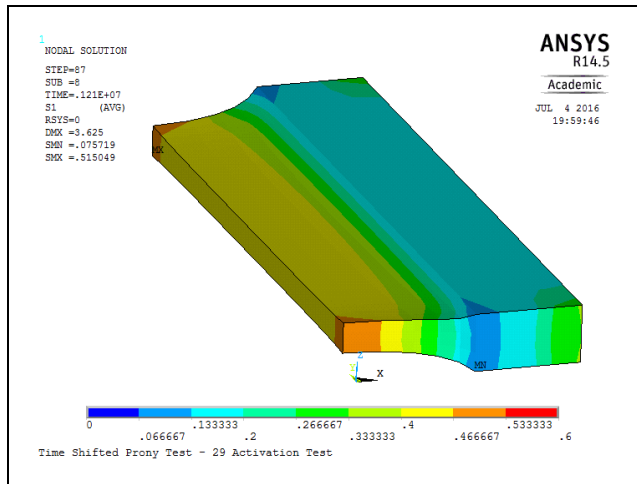


(E)  $t_{act} + 58.127$  seconds

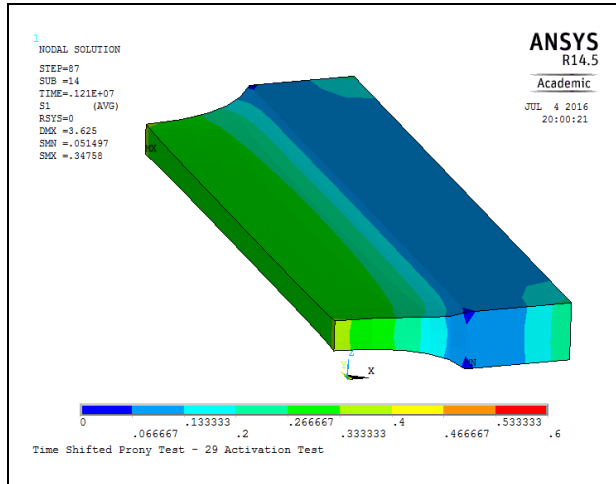
Fig. 1-37: 1<sup>st</sup> Principal Stress Plots of RTG Following 1<sup>st</sup> Appliance Activation  
 Legend shows stress,  $\sigma$ , in units of MPa



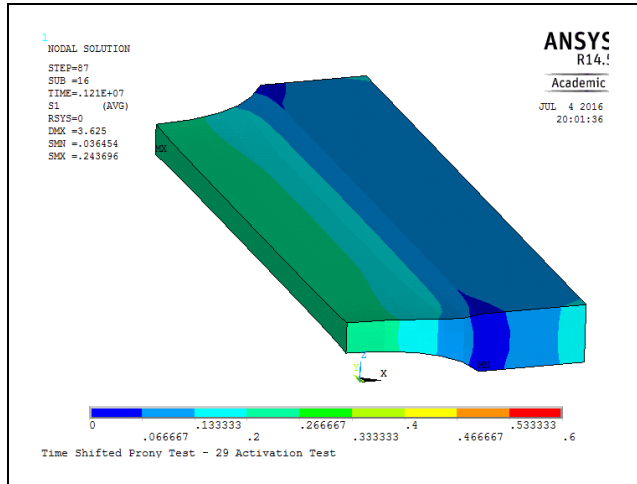
(A)  $t_{act} + 0$  seconds



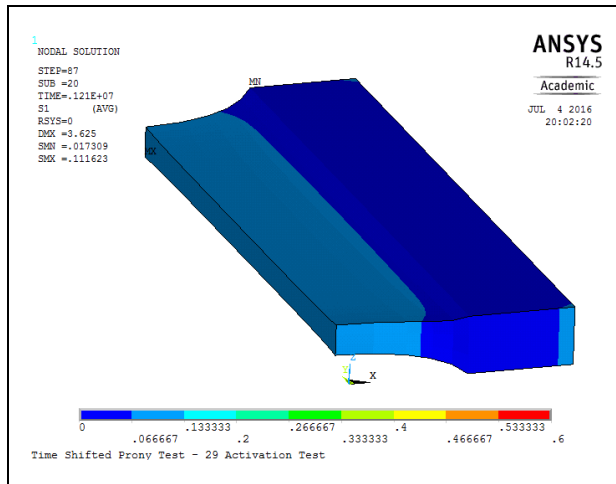
(B)  $t_{act} + 0.332$  seconds



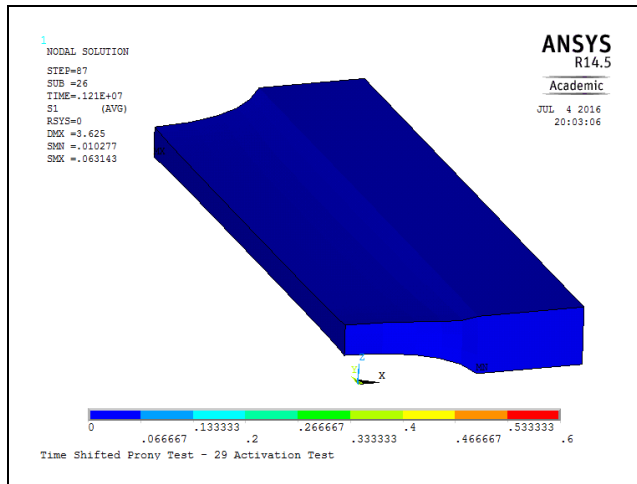
(C)  $t_{act} + 3.882$  seconds



(D)  $t_{act} + 8.748$  seconds



(E)  $t_{act} + 28.127$  seconds



(F)  $t_{act} + 58.127$  seconds

Fig. 1-38: 1<sup>st</sup> Principal Stress Plots of RTG Following 29<sup>th</sup> Appliance Activation  
Legend shows stress,  $\sigma$ , in units of MPa

As can be seen in these images, significant necking occurs by stretching the suture, particularly by the 29<sup>th</sup> appliance activation, Fig. 2-32. Stresses visibly reduce over time, with the stresses within the model decreasing at the sagittal plane last. Stresses concentrate at the edges of the loading face of the model, as clearly seen in Fig. 2-31 (A) at the edges of the bone volume. This simulation confirmed that the Prony approximation of the relaxation material model is able to simulate a full set of appliance activations without geometry failures of the stretched suture elements.

Of particular note in Fig. 2-30 (A) is that for each 0.125mm appliance activation, the step increase in the strain reduces in magnitude for each activation. This verifies that the strain in FEA is calculated based on the suture width at the end of the previous time and load steps, not the original width of the suture. Additionally, the magnitude of the peak stress within the suture reduces for each activation step, Fig. 2-30 (B).

## 2.4 Conclusions and Future Work

To grasp the significance of the FEA material modelling presented in this chapter, it is paramount that the pre-existing state of the field be understood. Prior to the outset of this project, the incorporation of the MPS in FEA studies of the procedure of maxillary expansion in adolescents was in a poor state. Prior full skull modelling either neglected the presence of the suture, assumed it was fully ossified, or assigned linear elastic material properties several orders of magnitude lower than that of bone. “Pseudoviscoelastic” modelling of the suture artificially reduced all stress within the suture to zero between appliance activations. The work of Romanyk et al. to develop MPS specific 1-D creep and stress relaxation mathematical models was pioneering in the field.

Using the creep and relaxation models as a jumping off point, the preceding work endeavoured to adapt the 1-D material models for the ANSYS FEA simulation software. These models were tested using the RTG, based on the same system dimensions used to originally derive the model coefficients by Romanyk et al.

### 2.4.1 $\gamma$ -Modification Term: Sensitivity Analysis Conclusions

One modification that was necessary for modifying both models into forms that could be implemented in FEA geometry was the addition of a geometry correction factor,  $\gamma$ . This change allowed the two models be adapted for a suture width of 1.72 mm from the original 9.72mm volume width used to derive the mathematical models. This was done with the anticipation of incorporating the models into a skull geometry, where it would have been unfeasible for a nearly 10mm volume to be cut out of the model.

The results of comparing the  $\gamma$ -term modified model to that of simple series spring model showed that the assumption that bone is rigid in the development of the 1-D models was valid as the elastic modulus of bone is 3 orders of magnitude higher than that of the elastic modulus typically attributed to non-ossified sutures. This resulted in differences in peak moduli at a time of 5 seconds of only 4.39e-2 %, and a negligible difference at 1 hour of only 5.9e-5 %.

A key observation of the sensitivity analysis showed that the width of bone assumed in the 9.72mm geometry width caused a significant change of the peak elastic modulus as calculated

by the  $\gamma$ -modified model. The assumed width of bone alters the value of  $\gamma$ , which in turn causes the stress and modulus calculated from the  $\gamma$ -modified relaxation model to change. An assumed bone width of 3.9 mm per side of the suture resulted in a peak elastic modulus of 21.1MPa and a  $\gamma$ -value equal 0.1975. Alternately, an assumed bone width of 4.1 mm per side of the suture resulted in a peak elastic modulus of 16.7MPa and a  $\gamma$ -value equal 0.156379. This shows a high sensitivity of the  $\gamma$ -term relaxation model to changes in the amount of bone assumed in the 9.72mm system width, a sensitivity of 11.5% difference for every 0.1mm of bone assumed per side of the suture.

Although this is a significant change, the actual width of bone in the system geometry utilized by Romanyk et al. is unknown. As such, the 4mm assumed width of bone per side was determined to be reasonable, resulting in a  $\gamma$ -value of 0.17696 utilized for both the creep and relaxation models going forward.

#### **2.4.2 Creep Model Conclusions**

Adapting the 1-D creep model required the assumption that the bulk material behaviors of the suture volume behave isotopically and homogeneously. The time and stress differentials of the creep model were encoded into the ANSYS USERCREEP.f subroutine and implemented in the FEA software. This portion of the study focused both on the performance of the adapted model as well as the model setup and solution method within ANSYS as pertaining to the application of the non-linear material model.

It was found that the solution method that would work the best for models utilizing non-linear materials was the static solution engine over dynamic engine. Although the material model is non-linear with respect to time, the actual model is not undergoing significant amounts of acceleration or inertia, nor is it subject to impact loading. Additionally, it was found through comparison of simulation results that the difference between the creep strain results between the two methods was negligible. A maximum relative difference of 2.29% between the two solution engines was found. This decreased to 0.87% relative difference at the end of the 6 weeks of simulated time. A key factor in this decision is the change in computational time required to solve these simplistic models under each solution engine.

In terms of model setup, the creep strain profile of the 1-D model was most closely replicated by the 2-node bar elements with a fixed cross sectional area. If the effect of the suture on the surrounding system is of highest interest to the researcher, this is the optimal element type for modelling the suture. If the incorporation of 3-D deformation within the suture is of highest interest, the brick elements are more desirable as they simulate 3-D tissue deformation and necking under tensile strain. However, this violates the constant stress assumption utilized by Romanyk when developing the creep model. Consequently, using the brick elements for simulating creep would require a re-training of the constitutive creep equation using the RTG in ANSYS.

In implementing the  $\gamma$ -modified creep model in ANSYS, two key results should be highlighted. First, in the 2-node bar element simulations the creep strain profile closely matches the anticipated profile from the 1-D model. However, importantly the width expansion of the model accelerates through time. Resulting in a relative difference between FEA system expansion and expected system expansion of 8063% in the 1.96N simulation set using averaged model coefficients. This is due to the calculation of expansion based on the system width from the previous solution step, not the original width. This key difference in calculating width creates the wrinkle of needing to modify the creep model to compensate for this. Secondly, simulating the  $\gamma$ -modified creep model using brick elements shows the unfortunate effect of multiplying this acceleration of system expansion even further. An argument for the validity of this simulation over the mathematical model is that under high levels of strain, the suture may fail. Nonetheless, this extreme failure of the suture elements within 40 seconds of simulated time indicates that further training of the constitutive model coefficients would be required to adapt the material model for accurate representation of the suture expansion behavior in 2-D FEA.

The result of this analysis shows that additional training of the creep model is required prior to further implementation of the adapted non-linear creep model in FEA studies. It is not recommended for implementation in a partial skull model at this point.

### 2.4.3 Relaxation Model Conclusions

As a high portion of maxillary expansion treatments utilize hyrax-type screw jack appliances, the implementation of the non-linear stress relaxation model in FEA is of great importance in furthering the understanding of the suture-bone interaction during the expansion process. In adapting the relaxation model, it was decided to approximate the time dependency of the stress relaxation using a generalized Maxwell model and a Prony series approximation. The non-linear initial strain dependency was not accounted for dynamically in FEA.

As the Prony series approximation is not a direct encoding of the 1-D relaxation model, the first task was to determine the degree of the Prony fit that was appropriate. The key factors were solution speed and closeness of fit. Of the 3-, 5-, 7-, and 9-term fits attempted the fit with the lowest regression residual was the 7-term fit with a value of 0.0089837, versus the next lowest of 0.026628 for the 9-term fit. Additionally, in the favour of the 7-term fit was the lower solution time than that of the 9-term model. Using the dynamic solution engine to give a more accurate comparison between solve times, the 7-term fit model was 34% faster than the 9-term fit. Although for the RTG the difference in solve time using the static solution engine would be inconsequential, this is a major factor when scaling up the degrees of freedom of the model and increasing the length of the simulation for a partial skull model.

Following this, it was necessary to create a 7-term Prony fit to accommodate that the 1-D relaxation model is not valid in the time interval between 0 and 5 seconds. This was incorporated in the original equation as an appliance activation period of 5 seconds was reasonable and because the equation asymptotes towards infinite stress at time approaching zero. To this end, FEA results were compared for Prony fits of the original stress-time dataset generated from the 1-D relaxation model, and a time-shifted dataset generated from the relaxation model. The FEA trial of the time shifted fit resulted in a peak stress (2.16 MPa) much closer to the anticipated peak stress of the 1-D model (2.74 MPa) versus the original fit (4.51 MPa). The time shifted model more accurately represented the peak stress and the stress relaxation profile of the 1-D model. The lower peak stress is attributable to the relaxation of the

tissue during appliance activation, which the 1-D model does not account for. It is recommended that the time shifted Prony fit be used for future FE modelling.

Using the static solution engine for numerical stability and the non-linear geometry options to account for high deformation magnitudes, a full expansion (29-activations) set was attempted using the 7-term time shifted Prony fit. The results of this showed decreasing stress peaks throughout the simulation. Additionally, it can be seen that different points in the suture geometry experienced different magnitudes of stress. This was caused by the geometry deformation and material necking in the simulation and was expected.

It is concluded that time dependency of the material stresses of the relaxation model has been implemented adequately in ANSYS. Further research may look to improve upon this by finding a way to incorporate the strain dependency of the original model. It should be noted that the model calculated peak stresses based on the net change in system strain between activations, not the absolute mechanical strain values.

## 2.5 References

- [1] D. L. Romanyk, C. R. Collins, M. O. Lagravere, R. W. Toogood, P. W. Major, and J. P. Carey, "Role of the midpalatal suture in FEA simulations of maxillary expansion treatment for adolescents: A review," *Int. Orthod.*, vol. 11, no. 2, pp. 119–138, Jun. 2013.
- [2] D. L. Romanyk, S. S. Liu, M. G. Lipsett, R. W. Toogood, M. O. Lagravère, P. W. Major, and J. P. Carey, "Towards a viscoelastic model for the unfused midpalatal suture: Development and validation using the midsagittal suture in New Zealand white Rabbits," *J. Biomech.*, vol. 46, no. 10, pp. 1618–1625, Jun. 2013.
- [3] D. L. Romanyk, S. S. Liu, R. Long, and J. P. Carey, "Considerations for determining relaxation constants from creep modeling of nonlinear suture tissue," *Int. J. Mech. Sci.*, vol. 85, pp. 179–186, Aug. 2014.
- [4] K.-J. Bathe, *Finite element procedures*. Upper Saddle River, N.J. : Prentice Hall, c1996.
- [5] S. S.-Y. Liu, L. A. Opperman, H.-M. Kyung, and P. H. Buschang, "Is there an optimal force level for sutural expansion?," *Am. J. Orthod. Dentofacial Orthop.*, vol. 139, no. 4, pp. 446–455, Apr. 2011.
- [6] A. M. Burrows, J. T. Richtsmeier, M. P. Mooney, T. D. Smith, H. W. Losken, and M. I. Siegel, "Three-Dimensional Analysis of Craniofacial Form in a Familial Rabbit Model of Nonsyndromic Coronal Suture Synostosis Using Euclidean Distance Matrix Analysis," *Cleft Palate. Craniofac. J.*, vol. 36, no. 3, pp. 196–206, May 1999.
- [7] "Ch. 2: Material Model Element Support," in *ANSYS® Academic Teaching Advanced, Release 14.5, Help System, Mechanical APDL Material Reference*, .
- [8] "Ch. 1.10: Compiling and Linking UPFs on Windows Systems," in *ANSYS® Academic Teaching Advanced, Release 14.5, Help System, Mechanical APDL Programmer's Reference II: Guide to User-Programmable Features*, .
- [9] "Ch. 3.7.1: Viscoelastic Formulation," in *ANSYS® Academic Teaching Advanced, Release 14.5, Help System, Mechanical APDL Material Reference*, ANSYS, Inc.
- [10] "Ch. 5.2: Viscoelastic Material Curve Fitting," in *ANSYS® Academic Teaching Advanced, Release 14.5, Help System, Mechanical APDL Material Reference*, ANSYS, Inc.
- [11] "XV: N Commands - NSEL," in *ANSYS® Academic Teaching Advanced, Release 14.5, Help System, Mechanical APDL Command Reference*, .
- [12] "Ch. 15.12.2: Convergence," in *ANSYS® Academic Teaching Advanced, Release 14.5, Help System, Mechanical APDL Theory Reference*, .

- [13] P. Moin, *Fundamentals of engineering numerical analysis*, 2nd ed. New York : Cambridge University Press, 2010., 2010.
- [14] D. L. Romanyk, C. Shim, S. S. Liu, M. O. Lagravere, P. W. Major, and J. P. Carey, "Viscoelastic response of the midpalatal suture during maxillary expansion treatment," *Orthod. Craniofac. Res.*, vol. 19, no. 1, pp. 28–35, Feb. 2016.
- [15] "Ch. 17.2: Transient Analysis," in *ANSYS® Academic Teaching Advanced, Release 14.5, Help System, Mechanical APDL Theory Reference*, .
- [16] "Ch. 17.1: Static Analysis," in *ANSYS® Academic Teaching Advanced, Release 14.5, Help System, Mechanical APDL Theory Reference*, .

## 3 Implementation and Evaluation of the Relaxation Model Using a 3-D Partial Skull Geometry

### 3.1 Introduction

Orthodontic treatments often cause pain and discomfort, have a long duration of treatment, and are effected by obtrusive corrective appliances. Through computer simulations, gaining a greater understanding of how soft tissues react to orthodontic forces may help in increasing patients' quality of life during treatment. Lessons learned in simulating a full Maxillary Expansion (ME) procedure using tissue specific material models may aid in future design of expansion appliances and development of more efficient treatment protocols. This research study focused on simulating ME with the non-linear viscoelastic properties of the Midpalatal Suture (MPS). FEA models require both representative material models and geometries to be effective. Previous FEA simulations of the ME procedure in literature neglected the MPS, treated it as linearly elastic, or utilized pseudo-viscoelastic modeling [1]. The time dependent non-linear material response<sup>7</sup> of the MPS was previously adapted for use in FEA. This relaxation model was a 7-term Prony series approximation of the time-domain response of the original constitutive equation as an isotropic generalized Maxwell model (see Chapter 2). The relaxation model was tested and verified in FEA using a simplified geometry. With the working non-linear relaxation model, the focus was now to simulate the expansion procedure on representative 3-D skull geometry.

Since it is believed that MPS plays an important role in the end results of the ME process, the objectives of the work in this chapter are to create a 3D skull geometry undergoing ME and to investigate the effect of the MPS having non-linear properties. This involved developing a 3-D partial skull geometry from CT image sets taken of an ME patient. Part of the hypothesis of this

---

<sup>7</sup> Modified from the 1-D constitutive stress relaxation equations of Romanyk et al. [2]

investigation is whether several of the craniofacial sutures, in addition to the MPS, have a significant effect in the final displacement results of a simulated ME treatment. This is of interest as previous histological studies have found that these sutures do not fully ossify until later in adult life [3]. Thus, incorporating craniofacial sutures to the model geometry, in addition to the MPS, was also considered. The model geometry was meshed for FEA.

Expansion forces are commonly generated by Hyrax-type expansion appliances. To create the loading from a Hyrax-type appliance in FEA, a clinical appliance loading protocol [4] was parameterized as a stepped displacement profile. A variety of tissue properties for the suture were then simulated in FEA using the full loading profile. This was done for comparison of model results to determine the effect of the non-linear relaxation model. Using a 3-D skull geometry and an MPS-specific non-linear model will help advance the understanding of how non-linear tissue properties affect the ME process.

### **3.2 Materials and Methods**

To further test the relaxation model, it was necessary to create the partial cranium testing geometry from patient DICOM images. Simpleware's ScanIP v6.0 software (Simpleware Ltd. Exeter, UK) was used to mask up the cranial geometry. The +FE module for ScanIP was used to mesh the masked geometry and export for FEA. The ANSYS® Academic Teaching Advanced Mechanical APDL, Release 14.5.7 (ANSYS) was used for FEA simulations. The following sections will discuss the development of the geometry and setup of the FEA model. The selection of patient DICOM images will be detailed. The techniques and tools used in ScanIP to isolate the partial cranium geometry will be covered, as will the steps taken to prepare it for meshing. The meshed model was then loaded into ANSYS. Simulations of the ME procedure were setup with varying tissue properties and loading conditions were run.

### 3.2.1 Geometry Creation Considerations

In setting out to create the partial skull FEA geometry, it was important to consider several factors. These included accurate replication of the maxilla palate, inclusion of the dental arch for measurement purposes, bi-lateral symmetry, removal of unnecessary geometry, and incorporation of craniofacial sutures.

An accurate representation of the maxillary palate was critical as the MPS was of primary interest. The maxillary palate needed to be fully discernable in the CT scan data such that the final geometry would accurately transmit structural forces into the MPS. Additionally, as a slice of the geometry would be defined as the MPS, the geometry of the MPS was directly dependent on that of the palate. The representation of the dental arch was not necessary in FEA for simulating the effect of the relaxation model in the MPS; however, it was included for post-processing comparisons to clinical data. Thus two requirements were identified for consideration during selection of patient CT data: an easily discernable maxillary palate, and a well-defined dental arch.

Bilateral symmetry of the geometry had two main purposes. First, this reduced the volume requiring meshing in half. This reduced the total amount of elements the model required. Secondly, a higher resolution of features resulted from modelling only half the skull. This was due to a limited number of elements being available for use as a condition of the ANSYS software license.<sup>8</sup> A secondary item during model geometry creation was the elimination of unnecessary features. This included portions of the cranium and small features with complex geometries that were expected to experience negligible strain. By eliminating unnecessary features the available elements could be better purposed for representing critical geometry.

---

<sup>8</sup> ANSYS Academic Teaching Advanced license allowed a maximum of 250,000 elements

## Craniofacial Sutures

Previous histological studies found that craniofacial sutures do not fully ossify until later in adult life. The bone knitting and ossification process occurs at different rates for the various sutures of interest. The ages of closure for the craniofacial sutures of interest are detailed in Table 3-1.

Table 3-1: Ages of Craniofacial Suture Fusion

Suture	Typical Age Range of Full Synostosis
Nasomaxillary	Seventh Decade
Frontonasal and Frontomaxillary	Seventh Decade
Zygomaticotemporal	Eighth Decade
Midpalatal	Third and Fourth Decades
Zygomaticomaxillary	Eighth Decade

[3]

Creation of the cranial model geometry considered the incorporation of these sutures, including how they would be located in the model and how to segment them from the bone portions of the model. Although the synostosis ages for the sutures have been found to be in mid- to late-decades of life, the histological nature of the Miroué study noted that increasing levels of suture interdigitization happen throughout life, generally starting to increase in degree beginning in the mid-twenties. [3]

These sutures would likely be under a state of compression and physiologically there may be minimal strain in these sections as the actual bone/suture/bone interface of softer tissue is quite very thin. In tension the soft tissue of the sutures would potentially stretch to a high degree, however under compression the sutures may behave rather stiffly with the bone segments nearly in contact. The testing of the FEA model investigated the effect of utilizing different material models for the sutures.

### 3.2.2 Selection of Patient DICOM Images

The CT DICOM image stacks utilized for this FEA study were provided by Dr. Manuel Lagravere.<sup>9</sup> Images were from a previous clinical study comparing the skeletal expansion between typical screw-jack tooth-borne appliances, and screw-jack bone-borne appliances. The provided image stacks included at least one scan taken prior to the start of expansion, and one scan of the same patient following the completion of the expansion treatment for each patient. Of the two data sets provided, one was randomly selected from each of the two appliance types. Table 3-2 details the image sets provided, and the voxel resolution of the stacks. It should be noted that all DICOM stacks were examined using ScanIP v.6.0. This software can evaluate 8-bit DICOM stacks natively but down samples 16-bit DICOM stacks<sup>10</sup>.

Table 3-2: Patient DICOM Image Set Summary

	Patient A		Patient B		
Appliance Type	Tooth-Borne Hyrax Style		Bone-Borne Hyrax Style		
Image Set	T1	T2	T1	T2	T3
Time Of Image	Appliance Installed Pre-Expansion	Appliance Installed Post-Expansion	Pre-Appliance Pre-Expansion	Appliance Installed Pre-Expansion	Appliance Installed Post-Expansion
x-direction voxel dimension	0.3mm	0.3mm	0.5mm	0.3mm	0.5mm
y-direction voxel dimension	0.3mm	0.3mm	0.5mm	0.3mm	0.5mm
z-direction voxel/layer dimension	0.3mm	0.3mm	0.5mm	0.3mm	0.5mm

<sup>9</sup> The ethics approval number for this use of these images is PRO-00013376.

<sup>10</sup> ScanIP v.7.0 added the 16-bit (signed and un-signed) functionality, but was not available for this study.

All image sets, save one, were taken with the expansion appliance already affixed to the patient. This is important to note as metal appliances cause excessive streaking artifacts in X-ray based images, with streaks radiating from the metal in the image, as noted by Barrett and Keat [5]. The image noise from the metal artifacts caused great difficulty when masking DICOM stacks to create the skull geometry volume. To this end it was decided to utilize the T1 image set from the patient that had the bone-borne appliance. Despite the lower voxel resolution in this image set, it was possible to determine the boundaries of the teeth in the upper dental arch and separate the cranium from the mandible.

### 3.2.3 Masking Techniques Utilized in Simpleware

Creating a usable geometry from CT images is largely a trial and error process. As such this section will detail the final method utilized to create the model masks in a step-wise manner, providing a comprehensive roadmap. Fig. 3-1 shows a flowchart of the process utilized for masking the model geometry. Key steps in the process are detailed in the following paragraphs.

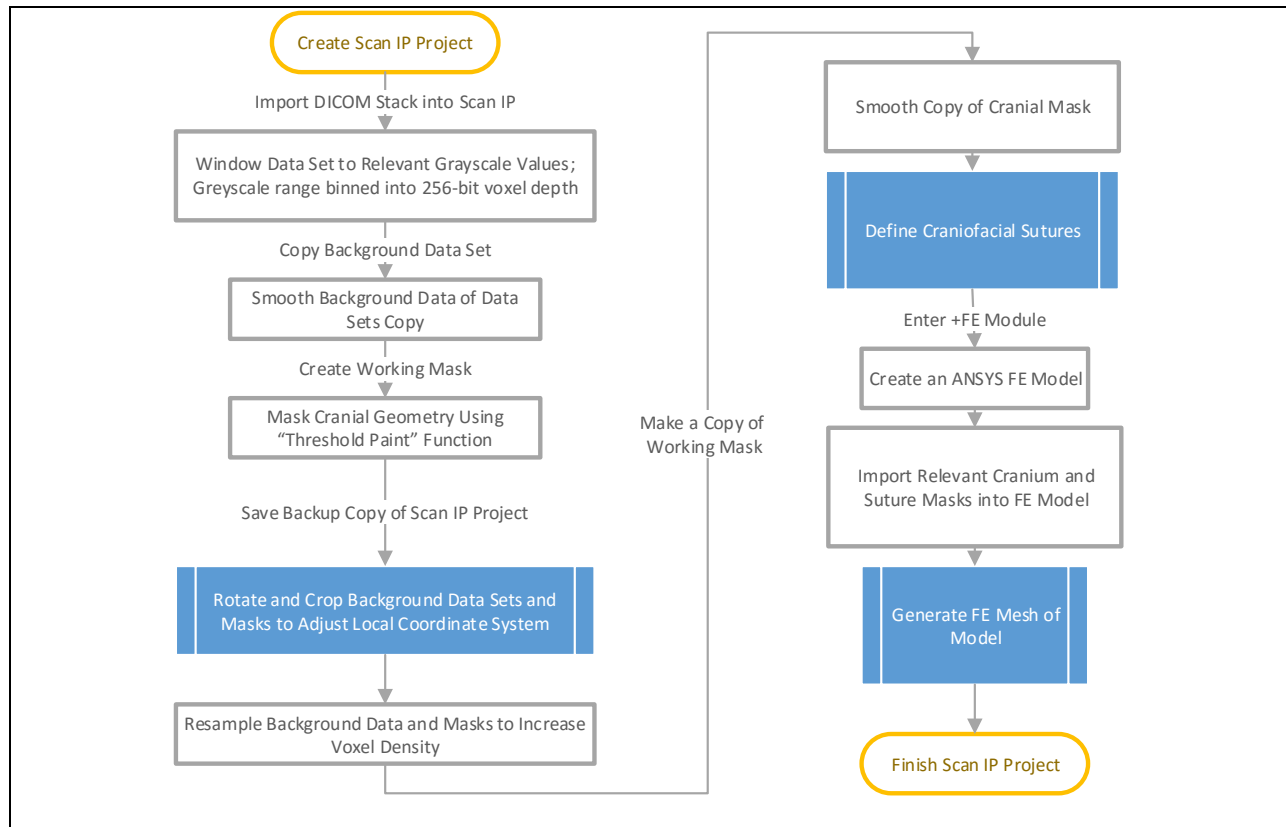


Fig. 3-1: ScanIP Workflow

**Data windowing** was performed on the DICOM image stacks when they were imported. The default Bone-CT setting was utilized. Both the full background data set and the windowed data set were brought into the ScanIP project file. ScanIP bins imported and windowed greyscale CT data such that it is displayed and processed in 8-bit greyscale. Due to this binning of the dataset, the windowing procedure aids in distinguishing cranial geometry from soft tissue and air. Fig. 3-2 shows the same DICOM slice in the (A) un-windowed state and the (B) windowed state.

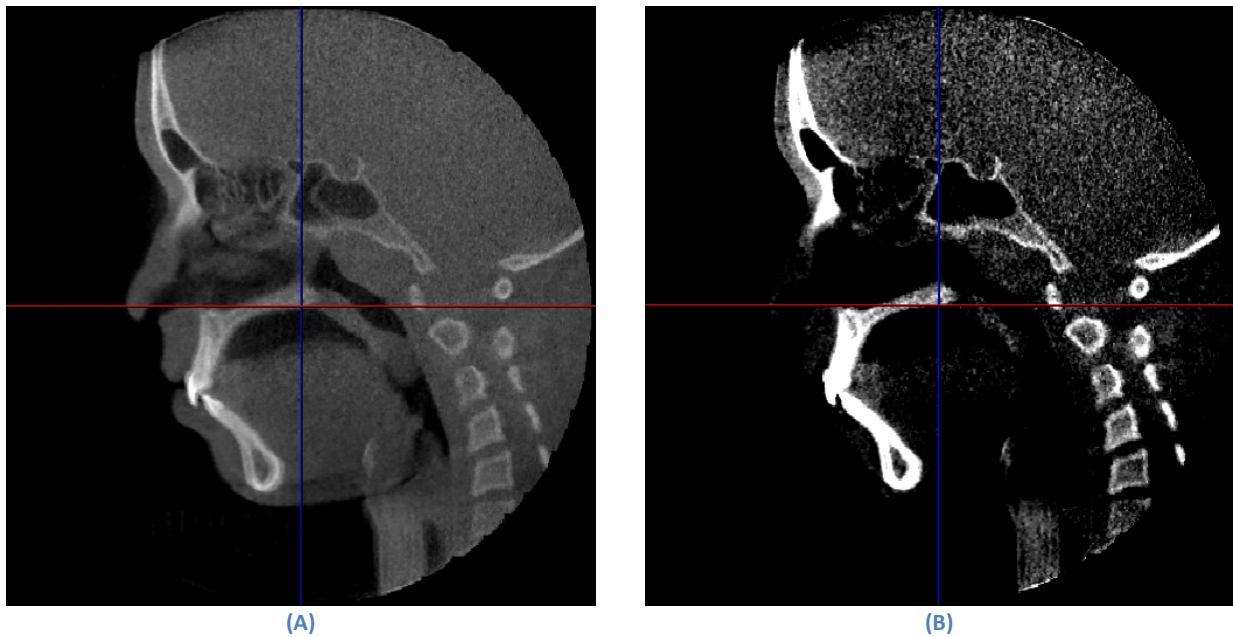
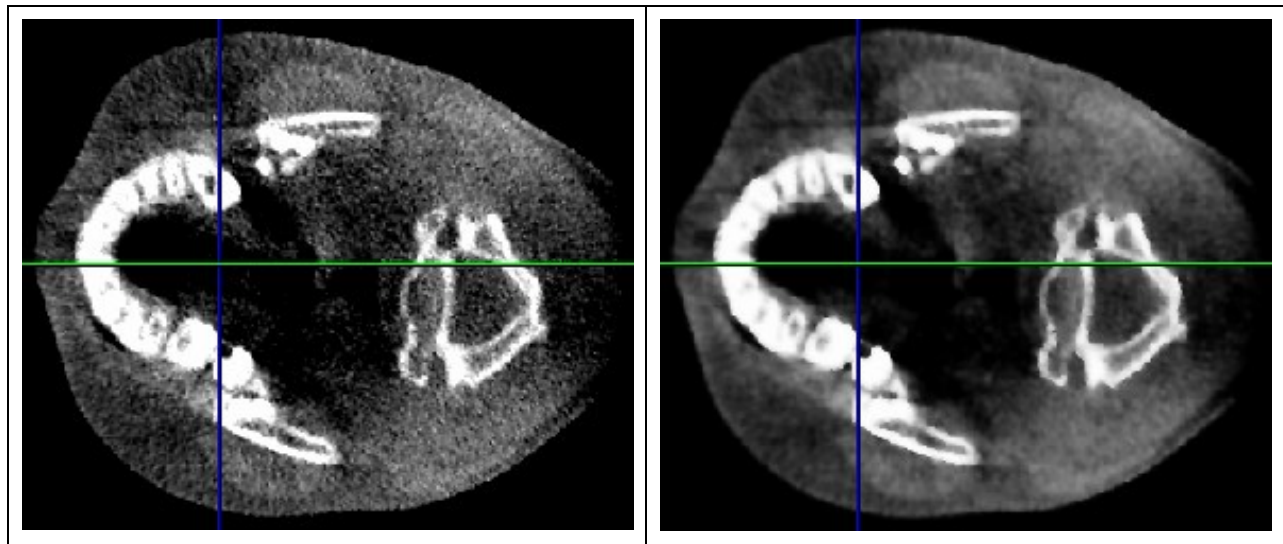


Fig. 3-2: Comparison of Full (A) and Windowed (B) Binned Background Data

**Smoothing of background data** was completed prior to geometry masking. This reduces difficulties in distinguishing image noise from cranial features. The smoothing filter that was used was “Gradient Anisotropic Diffusion” filter using a conductance of 3.5. The smoothing operations were performed on copies of the background data (full and windowed), such that the un-smoothed copies are still available for reference. A side by side comparison of a cross section of the raw and smoothed windowed data is shown in Fig. 3-3.



(A) (B)  
Fig. 3-3: Comparison of Raw (A) and Smoothed (B) Background Data

**Masking** of the cranial geometry was done using the “threshold paint” function. This tool required a lot of manual adjustment due to the large variability in greyscale values representing the bone tissue. Extra care was taken in sections of the geometry where the cranium was in close proximity to other skeletal bodies such as:

- Cranial base and C1 vertebrae
- Mandible and temporal bone
- Mandible and sphenoid bone
- Mandible and maxilla bone
- Mandible and zygomatic bone
- Upper dental arch and lower dental arch

The attention required in masking these areas was necessary as the voxel resolution (0.5mmx0.5mmx0.5mm) is low enough that the proximity of these structures can make them difficult to distinguish when using threshold fill/paint tools because either the distance between the features is <1.0mm caused them to occupy the same voxel space, or the proximity of the features caused the edge bleed of the features to superimpose such that the value of the voxel was within the threshold range for selection.

Taking this into account while manually painting each and every layer of the DICOM stack, some features could not be separated perfectly. In areas that would not experience high load or strain, effort was taken to have representative geometry. Extra effort was taken to have recognizable teeth in the dental arch such that expansion measurements could be taken from the tooth geometry. The teeth are not separate bodies from the maxilla in this model and have the same material properties of maxilla.

A **mask smoothing** operation was performed on the cranial mask to smooth out the transitions between different CT slices. The smoothing tool utilized was the Mean filter with a 2-cubic pixel smoothing on the active mask of the full cranium. A comparison of smoothed and un-smoothed cranial masks is show in Fig. 3-4.

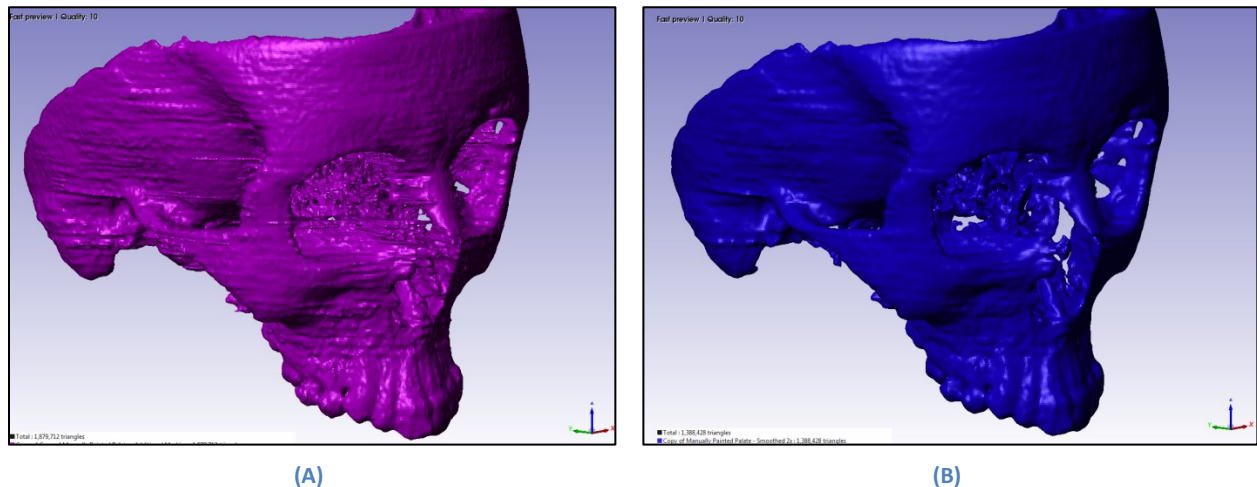


Fig. 3-4: Comparison of Pre-Smoothed (A) and Post-Smoothed (B) Cranial Mask

The ScanIP project was then **rotated and cropped** in preparation for eventual loading of the model in FEA. This must be done as the planes of the global coordinate system of the CT data are not aligned with the anatomical planes of the scanned patient. Misalignment of the planes, in particular the sagittal plane, presented an increase in difficulty in the application of loads required for expansion in the FEA simulations. Rotation of the local coordinate system allows the applied displacement to be along the local x-direction of the FEA model, instead of a vector with multiple direction components. A vectored displacement load could have introduced additional sources of calculation error. Additionally, rotation of the model will produce a flat

sagittal plane boundary, instead of the jagged boundary that would occur without rotation due to voxel stepping. The workflow of the rotation and crop method is presented in Fig. 3-5.

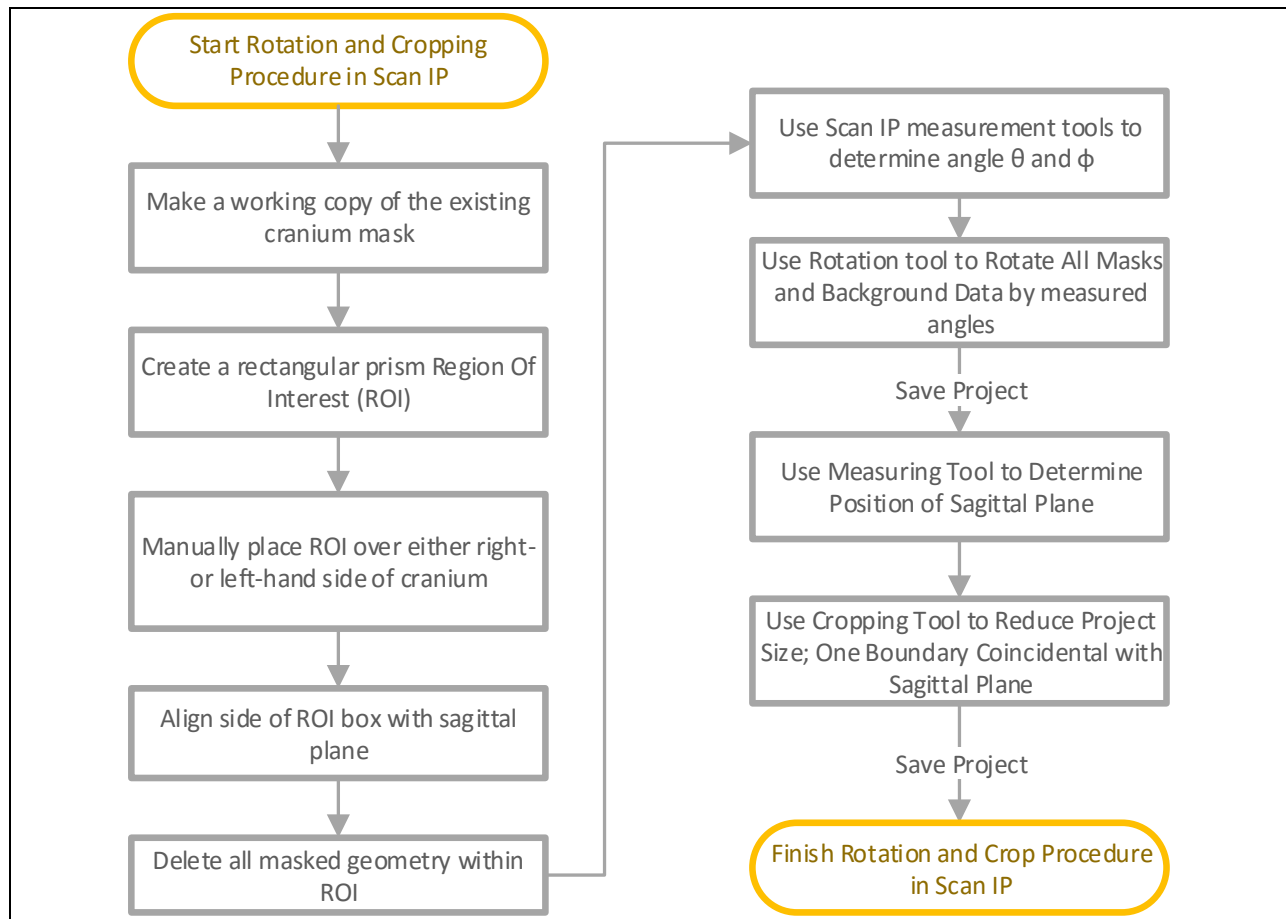


Fig. 3-5: Workflow of the Rotation and Crop Procedure

To rotationally transform the completed cranial mask, first a copy of the cranial mask was created as a working copy. In the copy, a Region of Interest (ROI) was manually positioned to remove the half of the cranium that was not to be meshed. The ROI was aligned with the following visual landmarks on the mask (Fig. 3-6):

- The center of the spinal cord channel, the foramen magnum, in the cranial base
- The gap between the central incisors, which was well aligned with the intermaxillary suture
- The center of the top of the nasal cavity in the face at the internasal suture

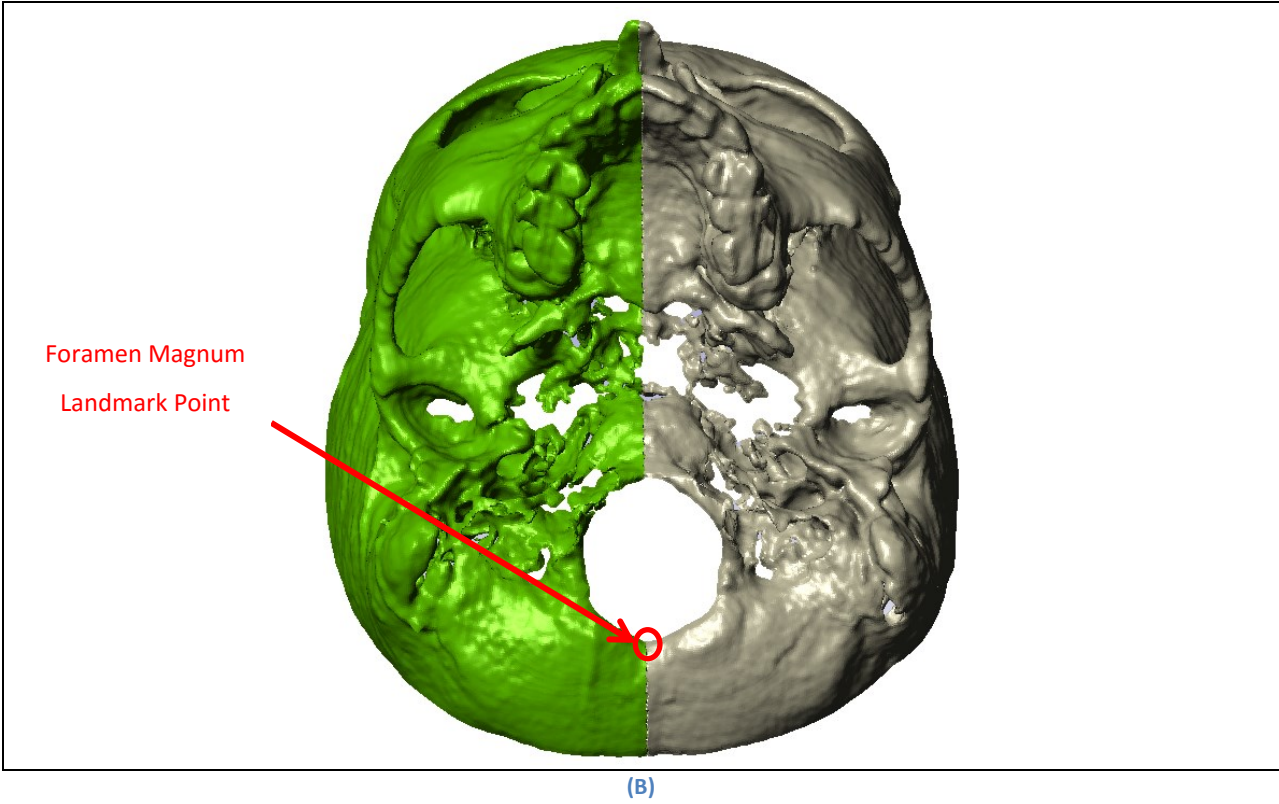
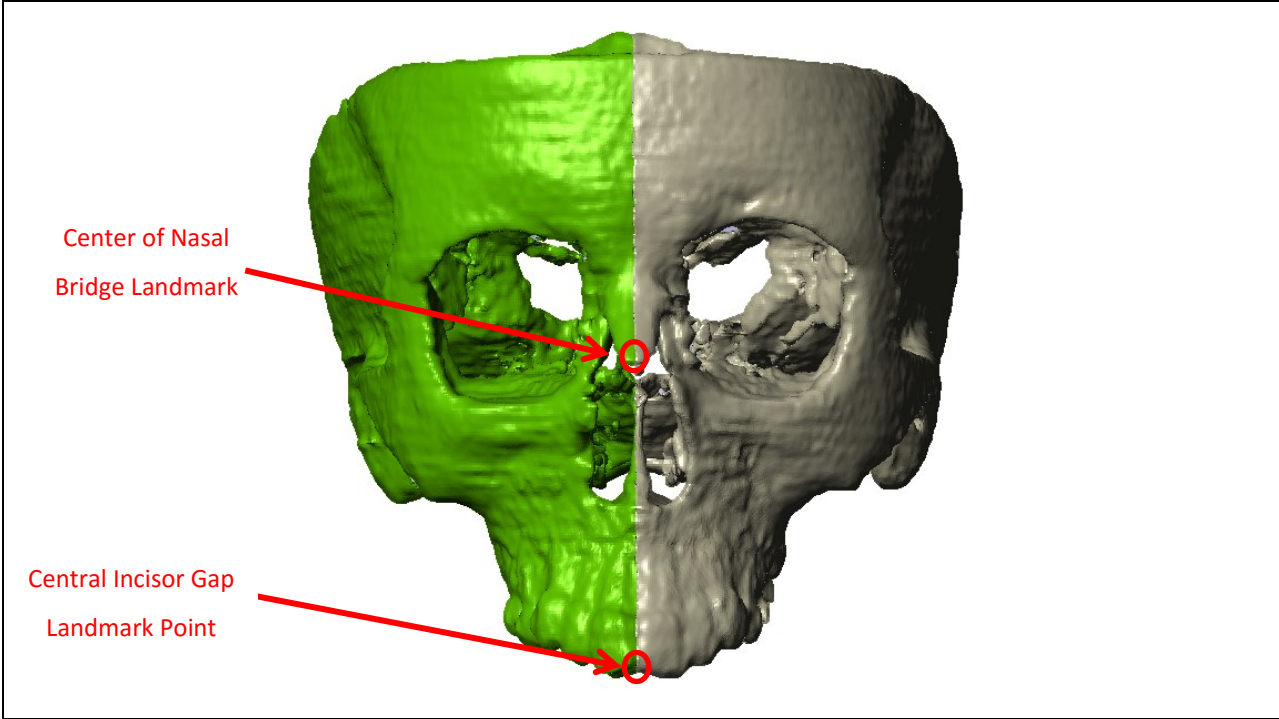
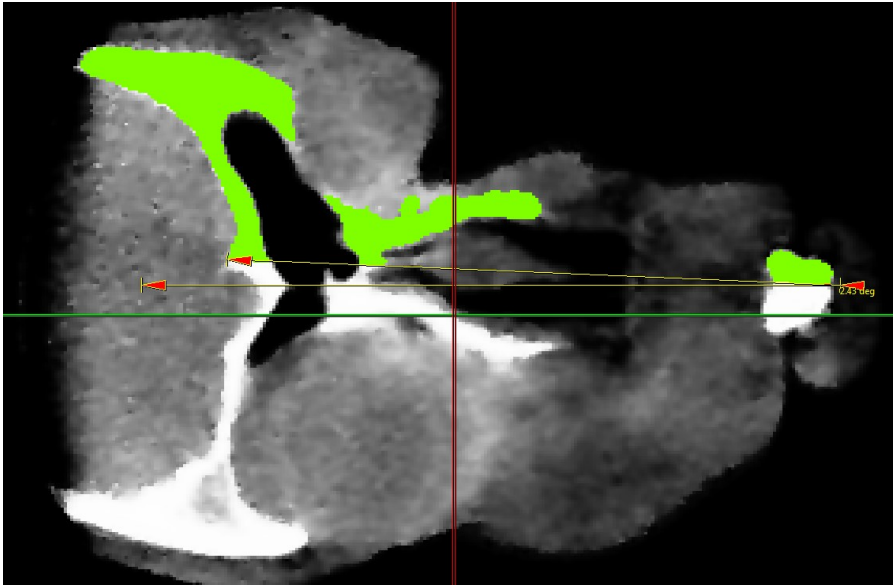
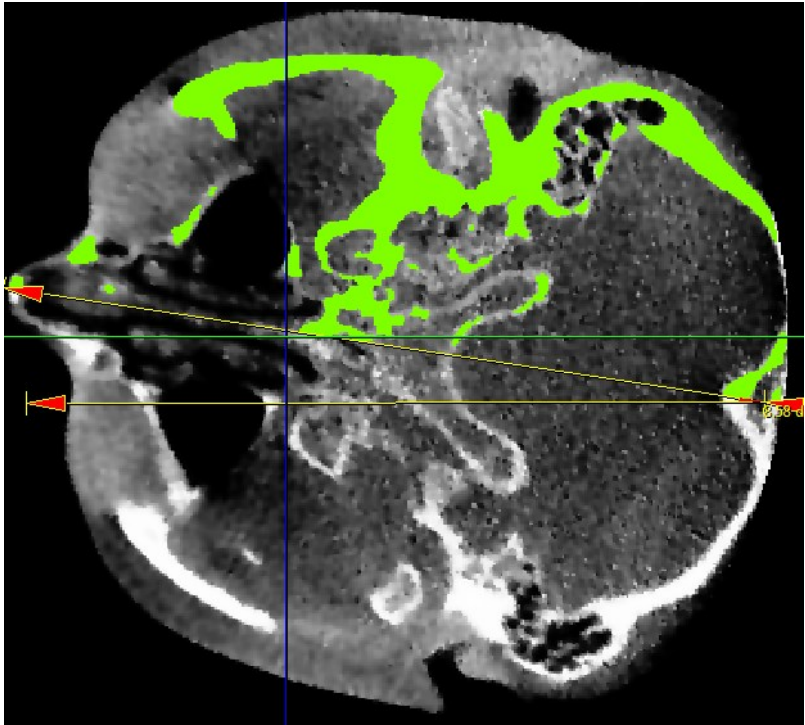


Fig. 3-6: ROI Positioning Landmarks On a Partial Mask (Deleted Right Hand Half of Mask Shown Greyed Out)  
(A) Anterior (Frontal) Aspect (B) Inferior Aspect

Using these three points of alignment the model's sagittal plane was defined by the ROI. Half of the cranium mask was unmasked by the ROI. The Angle Measurement tool was used to determine the two angles of rotation. Fig. 3-7 shows an example of the measurements of the two angles in slices looking at the frontal and inferior aspects of the CT images.



(A)



(B)

Fig. 3-7: Angle Measurements (A) XY-Plane View (B) XZ-View

Using the rotation tool, it is possible to then take the measured angles and rotate the project. Although the angle measurement tool is accurate to two decimal points, the project rotation tool is only accurate to the nearest degree. The rotation action causes a spherical rotation transformation of the entire project, including all masks and background data sets. For information on how the greyscale values of the transformed voxels are calculated in ScanIP, refer to the Simpleware Help Documentation [6, Sec. 7.1.7, 7.1.8].

After the entire project was rotationally transformed and saved, both the full cranium mask and the accompanying background data was cropped. This operation was performed on a new copy of the Simpleware project for backup purposes. Cropping of the project was done to reduce the project memory requirements and to remove all cranial structures on the left-hand side of the sagittal plane. The position of the sagittal plane was determined, and the project volume was cropped up to the sagittal plane on the x- boundary. The remaining five boundaries (x+, y+, y-, z+, and z-) were cropped to within 15 voxels of the edges of the cranial mask.

The project was **resampled** following the rotation and cropping operations. This operation decreased the voxel size from  $0.5\text{mm}^3$  to  $0.25\text{mm}^3$ . A higher voxel density resulted, however it dramatically increased the memory requirements of the project. The higher voxel density allowed for better definition of thin suture features. The resampling filter was applied to all background data set and masks. Subsequently, the cranial mask was **smoothed** with a 2 pixel Recursive Gaussian filter.

To **incorporate the craniofacial sutures** in the mask, the main geometry considerations were how to locate the sutures in the model and how to segment them from the rest of the model.

With the lower resolution of the original CT-DICOM stacks ( $0.5 \times 0.5 \times 0.5$  mm), it was not possible to identify and mask the sutures in the patient images. Suture locations in the model were based on cranial anatomy images from "*Clinically Oriented Anatomy*" by K.L. Moore et al. [7, pp. 889–890]

The overall method for incorporation of the sutures into the craniofacial geometry is outlined in Fig. 3-8. Rectangular prism ROIs were utilized to select the portions of the skull geometry where the suture elements were to be eventually located. The ROI volumes were 1mm thick [8], which was similar in thickness to the 1.72mm suture width used by Romanyk et al [9].

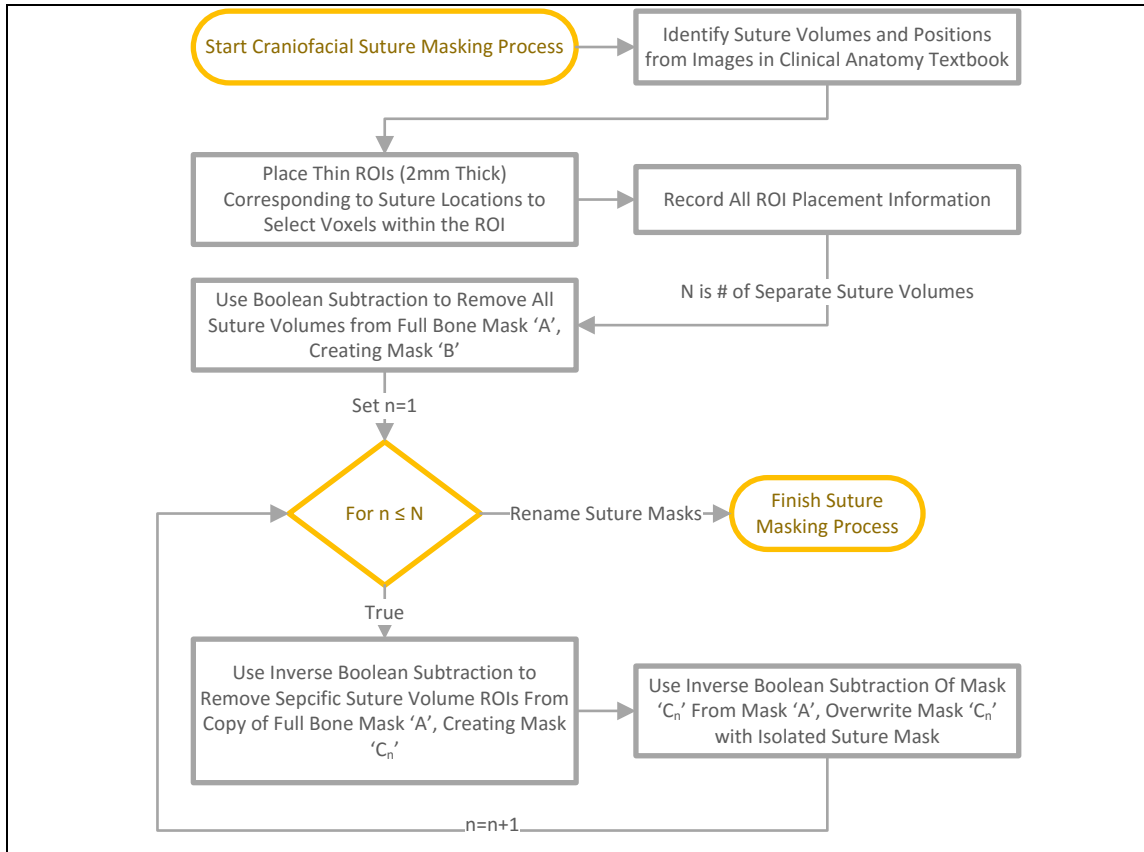
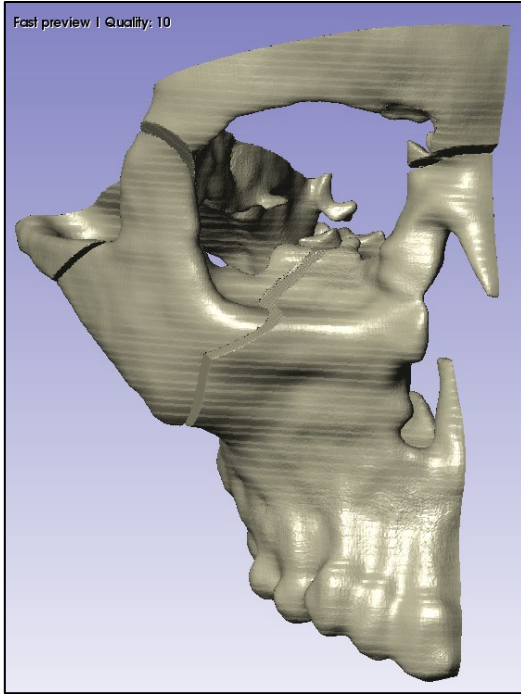
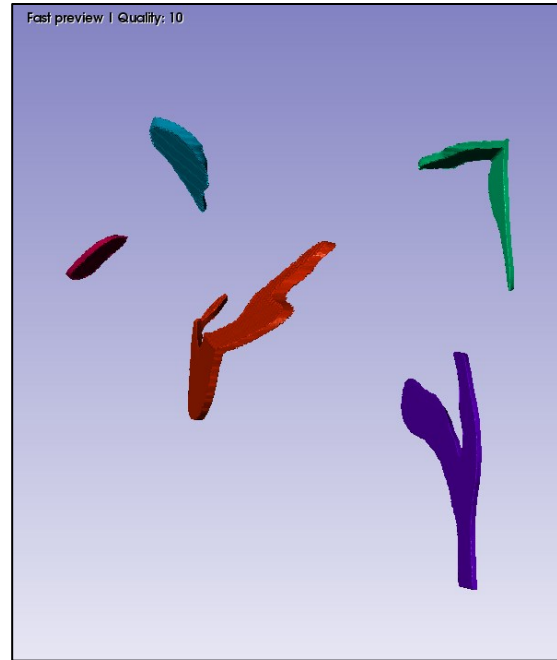


Fig. 3-8: Workflow of the Suture Masking Procedure

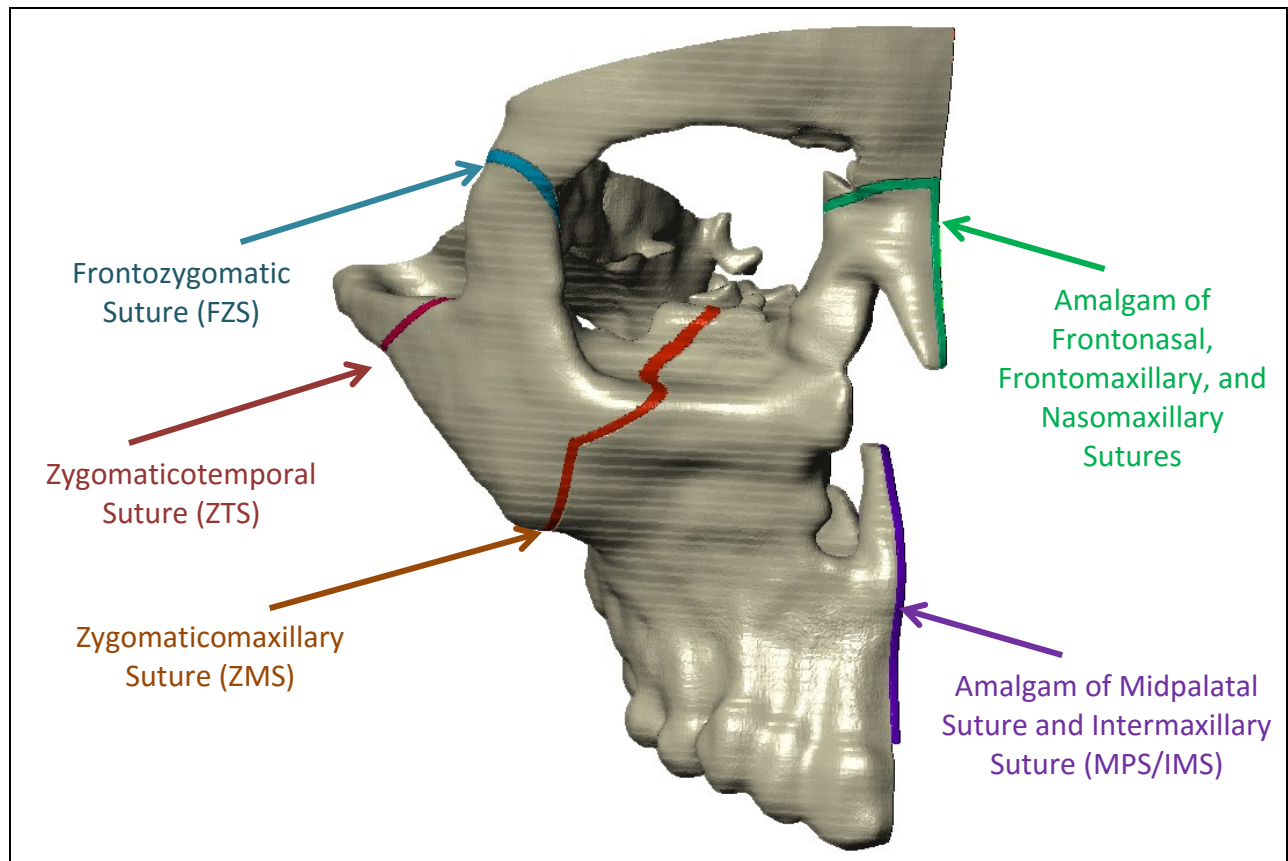
As can be seen in Fig. 3-8, this method resulted in multiple masks in the project file. To simplify the geometry for FEA, some craniofacial sutures were combined into single suture volumes as they were in close proximity. The maximum element count constraints (max 250,000 elements) would have made using multiple small suture volumes in close proximity prohibitive. Reducing the quantity of suture volumes allowed meshing of the FEA model to be within the license limit of elements and nodes. It also avoided a further reducing of mesh quality at high gradient mesh density transitions, which would have reduced the reliability of the model and the trustworthiness of the results. Fig. 3-9 shows the completed and annotated masks.



(A)



(B)



(C)

Fig. 3-9: Model Masks; (A) Bone Masks, (B) Isolated Suture Masks, (C) Assembled Masks

### 3.2.4 Preparing the Partial Cranium FEA Model

This section will first discuss the procedure that was used to mesh, constrain, and load the partial cranium FEA models. It discusses the various models that were generated and comparisons between the models. It will also discuss methods used for constraining and loading the models. The summary of the workflow for preparing the FEA model is presented in Fig. 3-10. The APDL code utilized to prepare the final meshes in ANSYS is presented in Appendix C.

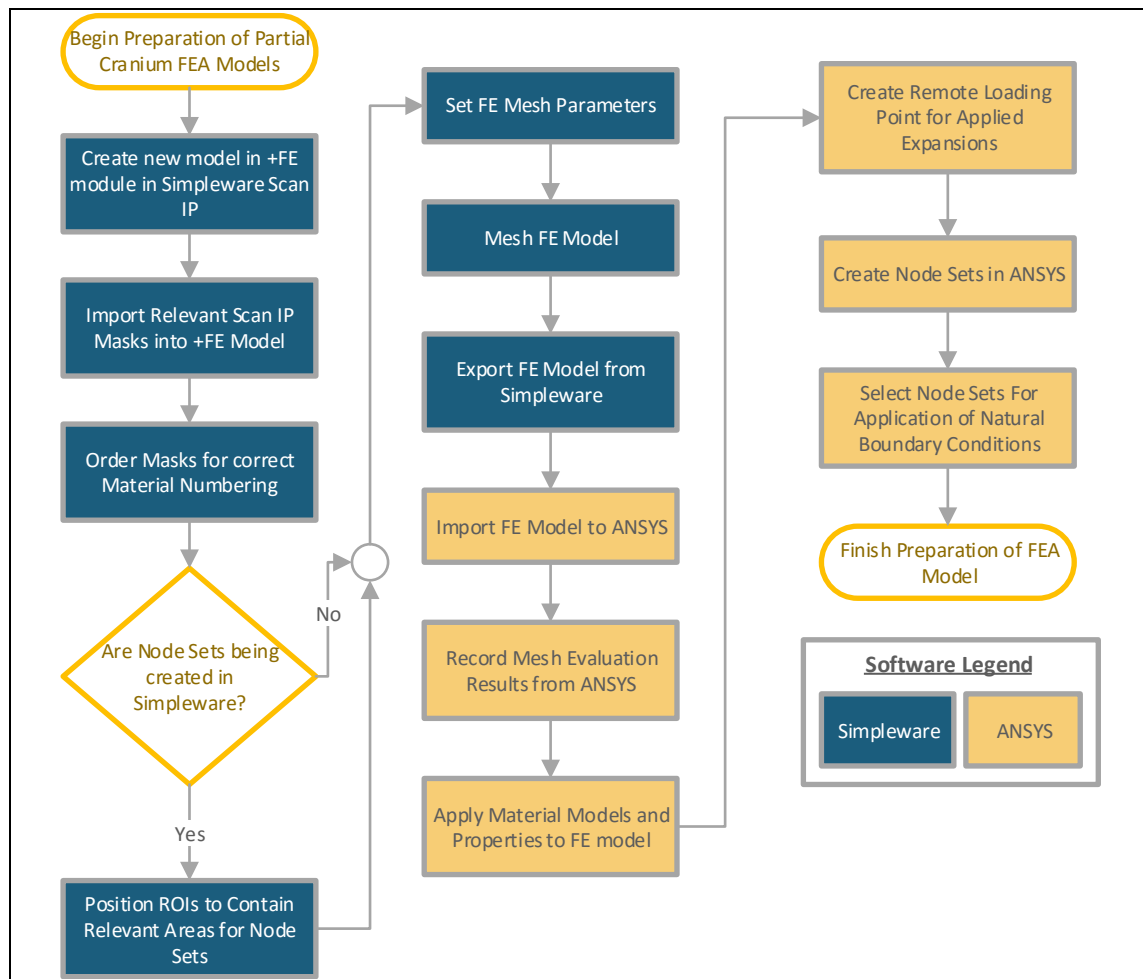


Fig. 3-10: FEA Model Preparation Workflow

To mesh the model, a new +FE model was created in Simpleware. As the meshed model was for use in ANSYS, it was a requisite that the model export setting was set to “ANSYS FEA”. For each FE model that was created, the relevant masks were imported into the model. Table 3-3 details the various models that were meshed in each model.

Table 3-3: FE model Masks

Masks	FE Model		
	Half Skull	Trimmed Half Skull	Trimmed Model with Sutures
<i>Full Bone Mask without MPS/IMS Suture</i>	Yes	No	No
<i>Bone Mask with Back Removed without MPS/IMS Suture</i>	No	Yes	No
<i>Fully Trimmed Bone Mask with All Sutures Removed</i>	No	No	Yes
<i>Amalgam of Midpalatal and Intermaxillary Suture</i>	Yes	Yes	Yes
<i>Frontozygomatic Suture</i>	No	No	Yes
<i>Zygomaticotemporal Suture</i>	No	No	Yes
<i>Zygomaticomaxillary Suture</i>	No	No	Yes
<i>Amalgamated Nasal Sutures</i>	No	No	Yes

Once the model in the +FE module was associated with the correct masks, the **meshing parameters** were applied. Meshing was performed in the +FE module with the aim of good element quality for a high percentage of the mesh and a total element count of less than 250,000 elements. In this study the element count was restricted by the available ANSYS license.<sup>11</sup>

To allow Simpleware to generate meshes that fit within the budget of 250,000 elements, the +FE Free meshing algorithm was employed using the most coarse mesh settings. Tetrahedral elements, without mid-side nodes, were utilized<sup>12</sup>. This element type was used as Simpleware first generates a tetrahedral mesh. A hexahedral mesh could not be specified as the meshing algorithm splits each tetrahedral element into five hexahedral elements [6, p. 197]. This would

<sup>11</sup> Project utilized the ANSYS Academic Teaching Advanced license

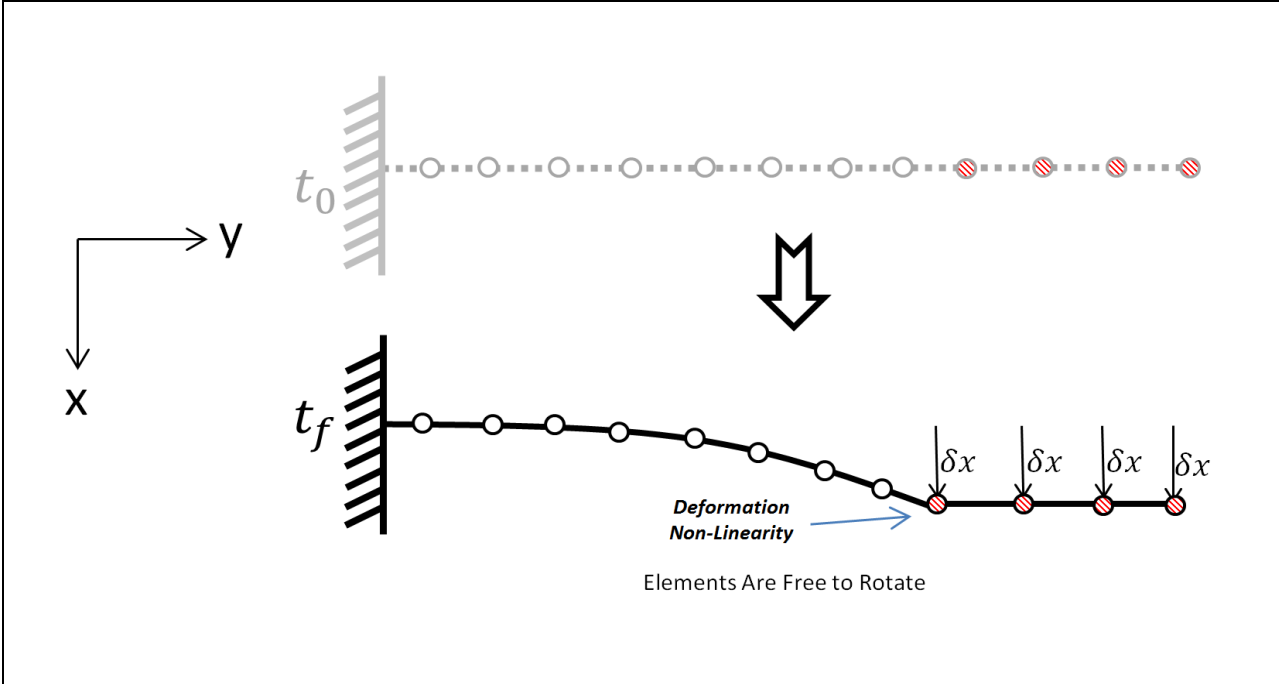
<sup>12</sup> Current technology 4-node tetrahedral elements in ANSYS are known as SOLID187

have dramatically increased the element count and would have exceeded the budget of available elements. The +FE Free algorithm does not generate mixed tetra/hexahedral meshes. An element quality Jacobian goal of 0.9 was specified to increase mesh quality, however this goal was not met for all generated elements. Multiple meshes were generated of each model by varying the surface and volume element size change rates.

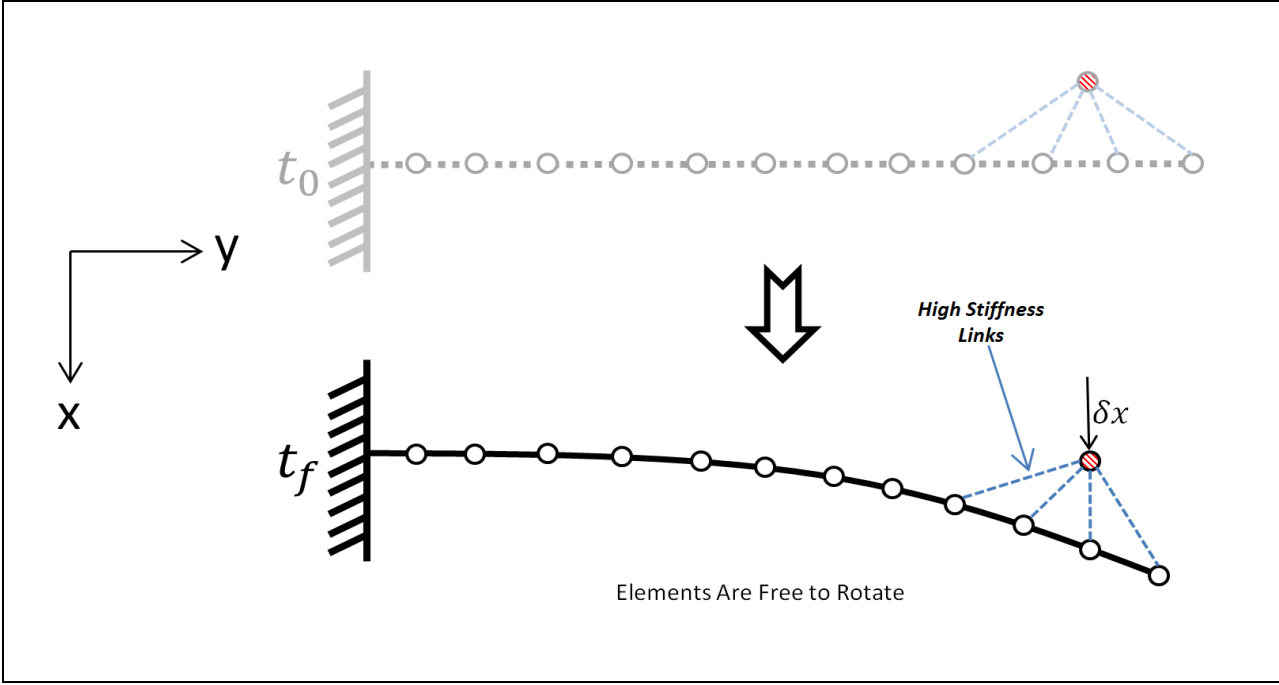
**Evaluation of mesh quality** was determined after the mesh file was loaded into ANSYS. The evaluation was based on the default ANSYS element shape checking criteria [10]. The meshes with the fewest warnings per total element count were utilized for each model. Element errors were not tolerated. Of the meshes generated, the mesh with the fewest warnings and the lowest shape warnings per total element count had 210880 elements and only 246 warnings. Shape warnings were detected in only 0.1167 % of the total number of elements.

**Application of material models and properties** was completed using parameterized APDL code in ANSYS. After manually determining which material number corresponded to each craniofacial feature for a given mesh, the correlation was recorded and utilized in the APDL code. Specific details on material models and material properties used are discussed in Section 3.2.5.

A **remote loading point** was created to apply the displacement caused by the expansion implant. In this case study, the implant was a Hyrax type bone-borne expander. The loading location was visually identified in the both the T2 and T3 CT-images to be between the 2<sup>nd</sup> premolar and the 1<sup>st</sup> molar, at mid-root. A remote loading point was preferable to directly loading the nodes on the cranial model as it reduced local non-linearity in mesh deformation. The non-linear mesh deformations from direct loading were caused by restrictions on element rotation. This can be visualized using a simplified cantilever beam example. Fig. 3-11 (A) shows the cantilever beam with a directly applied displacement at mid-span, while Fig. 3-11 (B) shows the same system with a remotely applied displacement.



(A)



(B)

Fig. 3-11: Fixed Cantilever Beam Under (A) Directly Applied Displacement (B) Remotely Applied Displacement

In Fig. 3-11 (A) the displacement,  $\delta x$ , is directly applied to the 4-nodes at the end of the beam. This causes a deformation non-linearity adjacent to the loading area. Fig. 3-11 (B) shows a system with a remote loading point which is connected to the beam with high stiffness link elements. The links are of a stiffness of orders of magnitude higher than the cantilever beam. This is done such that a negligible amount of deformation occurs in the links. Fig. 3-11 (B) shows that the stiff deformation non-linearity is eliminated. The resultant high local strains and stresses caused by the non-linearity are also eliminated. Therefore a remote loading method was utilized to apply the displacement loads caused by a Hyrax-type expansion appliance.<sup>13</sup>

To create a remote loading point in ANSYS, 34 nodes were manually selected at the location at which the expansion appliance was clinically attached to the maxilla. The coordinates of these nodes were recorded and averaged. Eq. (3-1) shows the formula used to define the nodal position of the remote loading location.

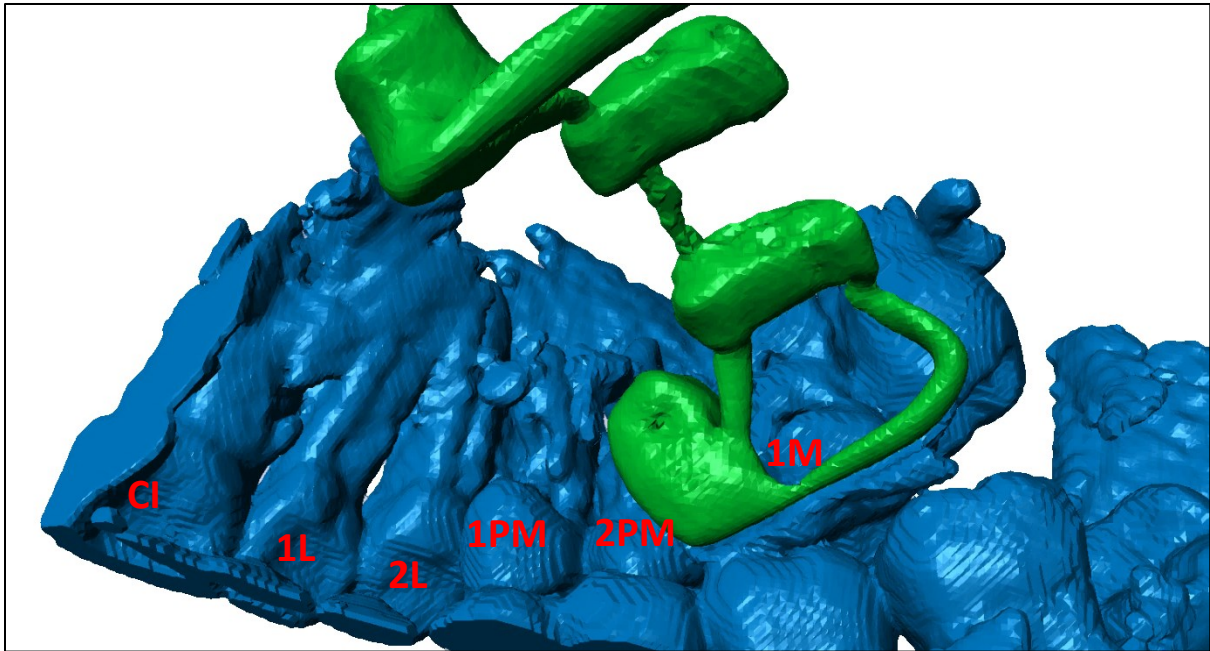
$$\begin{bmatrix} x \\ y \\ z \end{bmatrix}_{n_{100,000}} = \begin{bmatrix} x_{avg} + 2mm \\ y_{avg} \\ z_{avg} \end{bmatrix}_{n_{100,000}} \quad (3-1)$$

2-node bar elements<sup>14</sup> of stiffness 2.0E7 MPa were created between the selected nodes and the remote loading location at node 100,000. The virtual cross sectional area for these bar elements was 100mm<sup>2</sup>. Loading profiles for this applied boundary condition are discussed in section 3.2.5. Fig. 3-12 compares the load location of the expander in the CT images to the loading location selected in ANSYS.

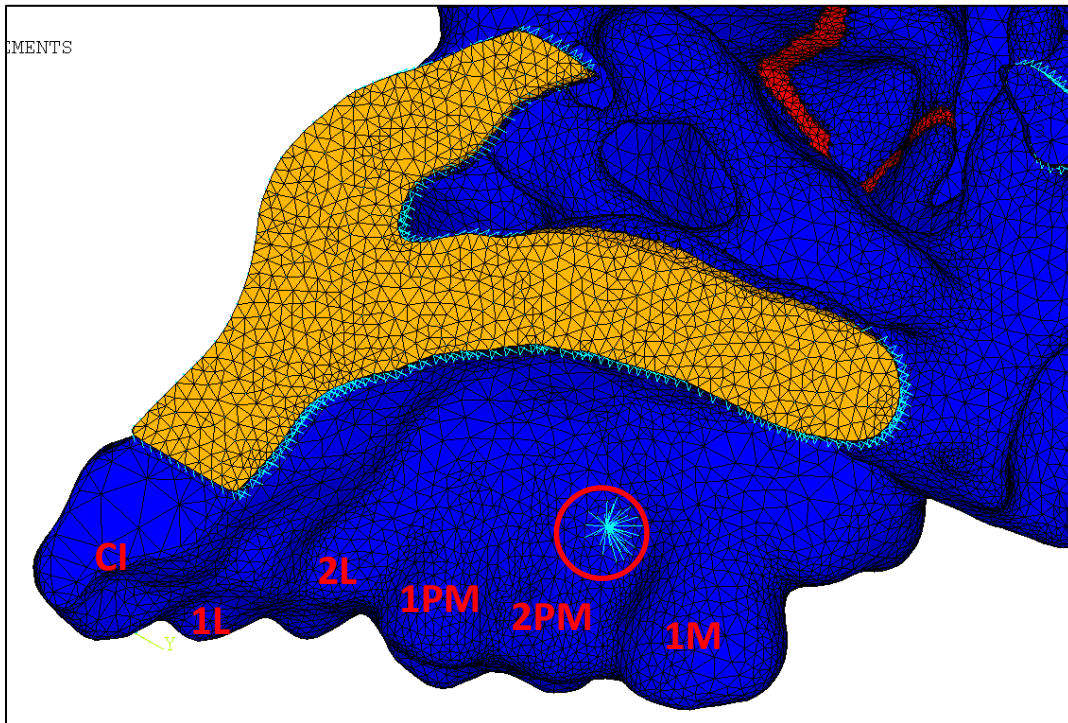
---

<sup>13</sup> Remote loading is unnecessary for ME cases that have appliances that are better simulated as an applied force load. Deformation non-linearity does not occur for directly applied forces. A remote load point could also introduce a non-clinical and unwanted applied moment.

<sup>14</sup> LINK180 3-D bar elements in ANSYS



(A) - Expansion Appliance In-Situ in Masked CT Dataset



(B) - Loading Location in Partial Skull FE Model in ANSYS (Circled in Red)

Fig. 3-12: Comparison of CT and FE Appliance Loading Point  
 CI - Central Incisor, 1L - 1<sup>st</sup> Lateral Incisor, 2L - 2<sup>nd</sup> Lateral Incisor, 1PM - 1<sup>st</sup> Premolar, 2PM - 2<sup>nd</sup> Premolar, 1M - 1<sup>st</sup> Molar

To **apply natural boundary conditions** to the FEA model, node sets must be selected and created. Natural boundary conditions are used to fix the FEA model in space, to provide a virtual connection to the rest of the skull, and to apply any symmetry conditions that are required. The node sets can either be selected in the +FE module of Simpleware or in the preprocessor of ANSYS. Both methods were used in this study and will be discussed.

The selection of node sets in Simpleware was done in the +FE module prior to meshing the geometry. ROIs were manually placed intersecting the top and rear of the cranium to define portions of the geometry that will encompass new node sets. Additionally, points where the geometry masks intersected with the bounds of the project volume could also be specified as node sets. This method was utilized for FEA cranium models 1 and 2 (see Table 3-3).

Simpleware node component selection was not used further as the meshing algorithms reduced the mesh quality by forcing nodes to lie on the boundary of the ROIs. This distorted the initial element shapes, and caused an unnecessary increase in element count for the model in non-critical areas.

Node selection within ANSYS was performed in the preprocessor. This method required considerable manual input by the user initially; however it was highly repeatable after being coded in APDL. For each cut plane on the top and rear of the cranium, a new local coordinate system was created. This was done by selecting three nodes on the model boundary plane to define a coordinate plane and selecting a normal for the z-axis. Nodes that were located within  $\pm 1.5mm$  of the locally defined  $xy$ -plane were selected<sup>15</sup>. The selected nodes were assigned to a new node group for later application of boundary conditions. For the sagittal plane, only nodes that were exactly coincidental with the plane at  $x = 67.125mm$  were selected.

---

<sup>15</sup> NSEL command was utilized in ANSYS for the purpose of selecting nodes; Error in distance from selection plane can be determined in ANSYS Help Utility [11]

Natural boundary conditions for the FEA model were comprised of fixing the position of the selected nodes in the  $x$ -,  $y$ -, and  $z$ -directions for all cranium trimming planes, excluding the sagittal plane. Nodes coincidental with the sagittal plane were fixed only in the  $x$ -direction thereby creating the symmetry condition. Fig. 3-13 shows the natural boundary conditions applied to the partial skull model highlighted in light blue. Fig. 3-13 also depicts the coordinate system used in the FEA simulations and results.

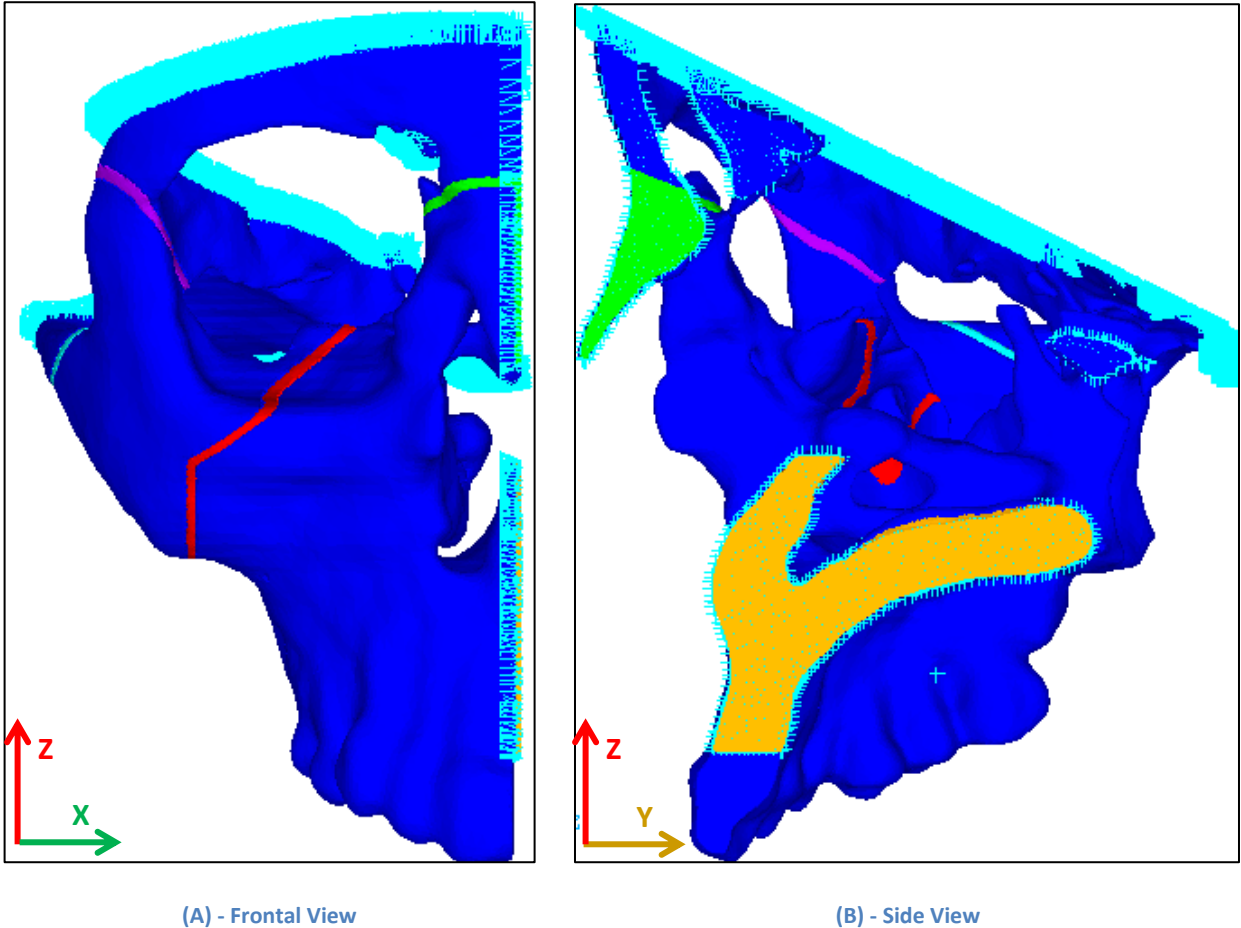


Fig. 3-13: Natural Boundary Conditions for Partial Skull Model

### 3.2.5 FEA Trials and Loading Conditions

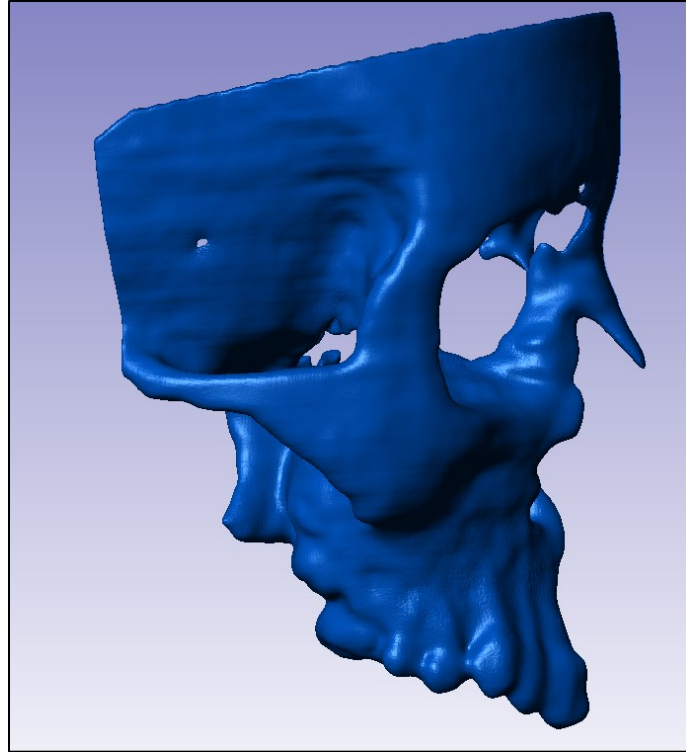
The FEA models were tested in two main phases. First, a comparison between the un-trimmed and trimmed cranial models was needed to verify that the trimmed geometry resulted in similar stress and strain results as the untrimmed model. Secondly, the trimmed model was tested using multiple material models over the course of an expansion procedure.

All cranium simulations utilized the default full-tangent Newton-Raphson solution method using the sparse-direct solver. For convergence, the default simulation criteria of force and displacement L2 norm residuals were utilized. Time stepping was handled utilizing the automatic time stepping methods in ANSYS.

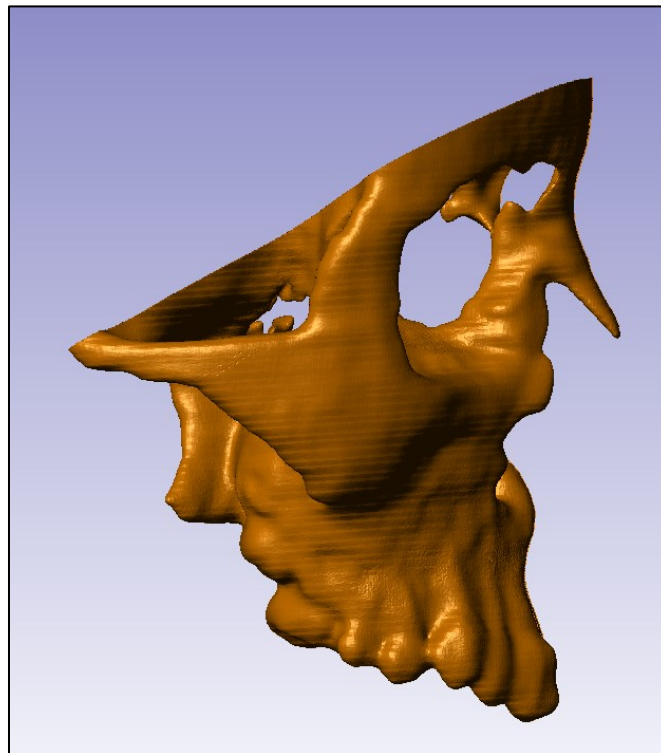
#### **Geometry Trimming and Natural Boundary Conditions Verifications**

In an effort to reduce geometry complexity and increase the fidelity of the mesh resolution of the remaining features, the cranium model was trimmed down from its initial masking volume. To verify that this was an appropriate decision, it was necessary to perform simulations of meshes of both the models utilizing only linear elastic bone characteristics. The two models utilized in this analysis did not contain separate suture volumes, thereby neglecting the sutures. Both meshes were subject to the same application of force and displacement.

Meshes for both models were generated utilizing ROIs to select the node groups for natural boundary conditions. These preliminary models were utilized for evaluating geometry deletion, and only one mesh was generated for each model. Mesh quality was not evaluated. Fig. 3-14 (A) and (B) highlight the differences in the skull geometry between the fully masked and partial half-craniums. These tests did not apply a symmetry boundary condition to the MPS/IMS, as the sutures were neglected for these tests.



(A)



(B)

**Fig. 3-14: Partial Cranium Models (A) Untrimmed Geometry (B) Trimmed Geometry**

For this initial set of tests, force was directly applied to a node set selected by a cylindrical ROI in Simpleware. The ROI was located approximately at the root end of the 1<sup>st</sup> molar and between

the 1<sup>st</sup> molar and the 2<sup>nd</sup> molar. This is load location did not match the location of the bone-borne appliance the patient received. This non-clinical load placement was used for these initial tests as it was further away from anticipated regions of high strain than the clinical appliance location. It would also induce larger moments at the ocular and nasal cavities. A higher cumulative displacement of the 1<sup>st</sup> molar was also anticipated. This would provide a better opportunity to compare displacements at the central incisor and the 1<sup>st</sup> molar.

Both models used the same properties material properties for this set of simulations. Linear elastic properties were used, with a Young's modulus ( $E$ ) of 20 GPa and a Poisson's ratio ( $\nu$ ) of 0.46 applied to all elements [12, Ch. 12].

A 500N load was ramped over 60 seconds. The load directed outward from the sagittal plane and was split among the selected nodes according to the formula presented in Eq. (3-2).

$$F_n = \frac{F_{Tot}}{N} \quad (3-2)$$

Where  $N$  is the number of selected nodes,  $F_{Tot}$  is the full 500N load, and  $F_n$  is the load on each node. The applied force was directly applied to the cranial geometry.

The 500N load was chosen as it was high enough to deform the model and was half the expansion force value used by Ludwig et al. in their viscoelastic cranium simulation [13]. Although this force is higher than necessary to be clinically relevant, it was chosen to test the model capabilities. This ensured that clinically relevant forces would not exceed the capabilities of the model.

## Partial Cranium Testing Procedure

The Partial Cranium testing procedure focused on the evaluation of the single term stress relaxation model [2] as applied to the MPS over the course of a full clinical expansion procedure. The effect of applying non-bone material properties to additional craniofacial sutures was also simulated. The setup of the FEA model required applying natural boundary conditions, applying the material models of interest, and creating a remote loading point.

Natural boundary conditions were applied to nodes that signified connection to the removed portions of the skull. These nodes were coincidental with the trimming planes used in the Simpleware +FE module and were selected using the plane selection method in ANSYS. The position of these nodes was fixed. A plane symmetry boundary condition was applied to nodes that were positioned on the sagittal symmetry plane. The sagittal symmetry condition was always applicable to bone structures, and was selectively applied to the MPS based on the test being run.

A remote load point was utilized for the application of sequential displacement loads. The 2-node bar elements between the cranial geometry and the remote loading node were of a stiffness of  $2.0E7$  MPa and a virtual cross section of  $100 \text{ mm}^2$ . This combination of material strength and size were used to limit the compressive deformation of the bar elements.

Displacements were applied to the remote loading point sequentially in steps of  $0.125\text{mm}^{16}$ . For computational expediency the simulations utilized 4 activations a day for a total of twenty-nine activations. This activation frequency was more frequent than a clinical activation [4] schedule. The load stepping sequence is detailed in Figure 2-12.

---

<sup>16</sup> This distance is  $\frac{1}{2}$  of the  $0.25\text{mm}$  of expansion generated per turn of the appliance screw. Due to the symmetry condition, only half the expansion is applied to this model.

The linear elastic properties used for bone in these simulations were a Young's modulus ( $E$ ) of 20 GPa and a Poisson's ratio ( $\nu$ ) of 0.46 [12, Ch. 12]. The value of 20GPa is higher than typically used for cranial bone. The modulus of tooth enamel was chosen as an approximation of the higher strain rate elastic response of bone to sudden applied loads. This allowed for a rudimentary approximation of the peak strength caused by a viscoelastic response to loads, even though a relaxation behavior model was unavailable. The Young's modulus ( $E$ ) for bone was assumed to be uniform throughout the model. This simplification was justified as the models were subjected to applied displacements and were being compared against one another. The low stiffness linear elastic properties used for sutures were a Young's modulus ( $E$ ) of 1.27 MPa and a Poisson's ratio ( $\nu$ ) of 0.3 [9], [14]. For sutures simulated as non-linear tissues, a stress relaxation model was employed.

The relaxation model used in ANSYS was a Prony series approximation (Eq. (3-3) and (3-4)) of the  $\gamma$  modified Romanyk et al. single term stress relaxation equation [12, Ch. 12]. In the Prony approximation the shear,  $G$ , and bulk,  $K$ , moduli are functions of time from activation,  $t_p$ . Relative moduli,  $\alpha_i^G$  and  $\alpha_i^K$ , and relaxation time constants,  $\tau_i^G$  and  $\tau_i^K$ , are determined by curve fitting. [15], [16]

$$G(t_p) = G_0 \left[ \alpha_\infty^G + \sum_{i=1}^{n_G} \alpha_i^G \exp\left(-\frac{t_p}{\tau_i^G}\right) \right] \quad (3-3)$$

$$K(t_p) = K_0 \left[ \alpha_\infty^K + \sum_{i=1}^{n_K} \alpha_i^K \exp\left(-\frac{t_p}{\tau_i^K}\right) \right] \quad (3-4)$$

As seen in Eq. (3-5), this relaxation model utilized experimentally derived coefficients to determine the material stiffness as a function of applied strain,  $\varepsilon_s$ , and time since application,  $t_w$  in weeks.

$$E(\varepsilon_s, t_w) = \frac{0.4894(0.2880(\gamma\varepsilon_s)t_w^{-0.4912})^{\frac{1}{0.4894}}}{\varepsilon_s} \quad (3-5)$$

As discussed in Section 2.3.1, the coefficient  $\gamma$  is a value derived from the geometry of the Rectilinear Testing Geometry and has a unit-less value of 0.17696. Also, the Prony model was curve fit in ANSYS as a 7-term approximation. The data used for curve fitting was time-shifted by -5 seconds to account for the appliance activation time. The resultant coefficients are presented in Table 3-4.

Table 3-4: Prony 7-term Approximation Coefficients

$t_d = t_c - 4.99s$			
$5s \leq t_c < 10000s$			
$\alpha_1$	0.3927	$\tau_1$	2.8
$\alpha_2$	0.40143	$\tau_2$	10.376
$\alpha_3$	0.14725	$\tau_3$	39.696
$\alpha_4$	0.042999	$\tau_4$	149.81
$\alpha_5$	0.011634	$\tau_5$	575.46
$\alpha_6$	0.0030511	$\tau_6$	2310.1
$\alpha_7$	0.00082323	$\tau_7$	114455
$\beta$	1.127029		
$t_{int}$	5.6691 seconds		
$E_0$	16.0136 MPa		

This approximation replicates the time dependency of the relaxation model in Eq. (3-5), but not the strain dependency. To approximate the initial strain dependency, the Prony series was supplied with an initial elastic modulus value. Calculated using Eq. (3-6), the initial elastic modulus was determined by the Prony coefficients and the resultant maximum strain,  $\epsilon_0$ , in the MPS from a single activation simulation. The single activation simulation utilized low stiffness linear elastic properties for the MPS.

$$E_0(\epsilon_0, t_{int}) = \frac{\beta(t_{int}) * 0.4894(0.2880 * \gamma * \epsilon_0 * t_{int}^{-0.4912})^{\frac{1}{0.4894}}}{\epsilon_0} \quad (3-6)$$

As derived in Chapter 2, the value for the intercept time,  $t_{int}$ , was 5.6691 seconds (9.37E-6 weeks). The variable  $\beta(t_{int})$  was determined using Eq. (3-7) and the Prony constants in Table 3-4.

$$\beta^G(t_{int,}) = \frac{1}{\alpha_{\infty}^G + \sum_{i=1}^n \left( \alpha_i^G + e^{-\frac{t_{int}}{\tau_i^G}} \right)} \quad (3-7)$$

The simulations that were run and the material models used for each structure are summarized in Table 3-5.

**Table 3-5: Summary of Partial Skull Simulation Cases**

Simulation Case	FE Model	Applied Boundary Condition	Bone Material Properties	MPS/IMS Material Properties	Other CFS Material Properties
1	Untrimmed Skull	100N	Linear Elastic; E=20 GPa v=0.46	Neglected	N/A
2	Back Removed Skull	100N			Linear Elastic; E=20 GPa v=0.46
3	Trimmed Model with CFS Volumes	4 Act. of 0.125mm; 29 Act. of 0.125mm			Linear Elastic; E=1.27 MPa v=0.3
4				Linear Elastic; E=20 GPa v=0.46	
5				Prony Series Viscoelastic	
6				Linear Elastic; E=20 GPa v=0.46	
7				Linear Elastic; E=1.27 MPa v=0.3	
8	MPS as Prony Series Viscoelastic; IMS Using Stiff Lin. Elastic Properties	Linear Elastic; E=20 GPa v=0.46			

The meshed model did not separate cortical and cancellous bone and only one Young's Modulus value was utilized for bone. Although the 20 GPa value is higher than the 13.7 GPa normally attributed to cortical bone [13], the stepwise applied displacement boundary conditions mean the dental expansion should be unaffected. Reaction forces at the load location will be higher than expected, but the overall force trends should be unaffected.

Simulations used the static solution engine as it had much faster model convergence than the dynamic solution engine. As the model was not undergoing impact loading or high amounts of acceleration, the dynamic solution engine was not required. The full-tangent Newton-Raphson solution method was used. Automatic time stepping was used to control solution advancement. The code used to setup and apply load to the partial cranium FEA model is presented in Appendix C.

### 3.3 Results and Discussion

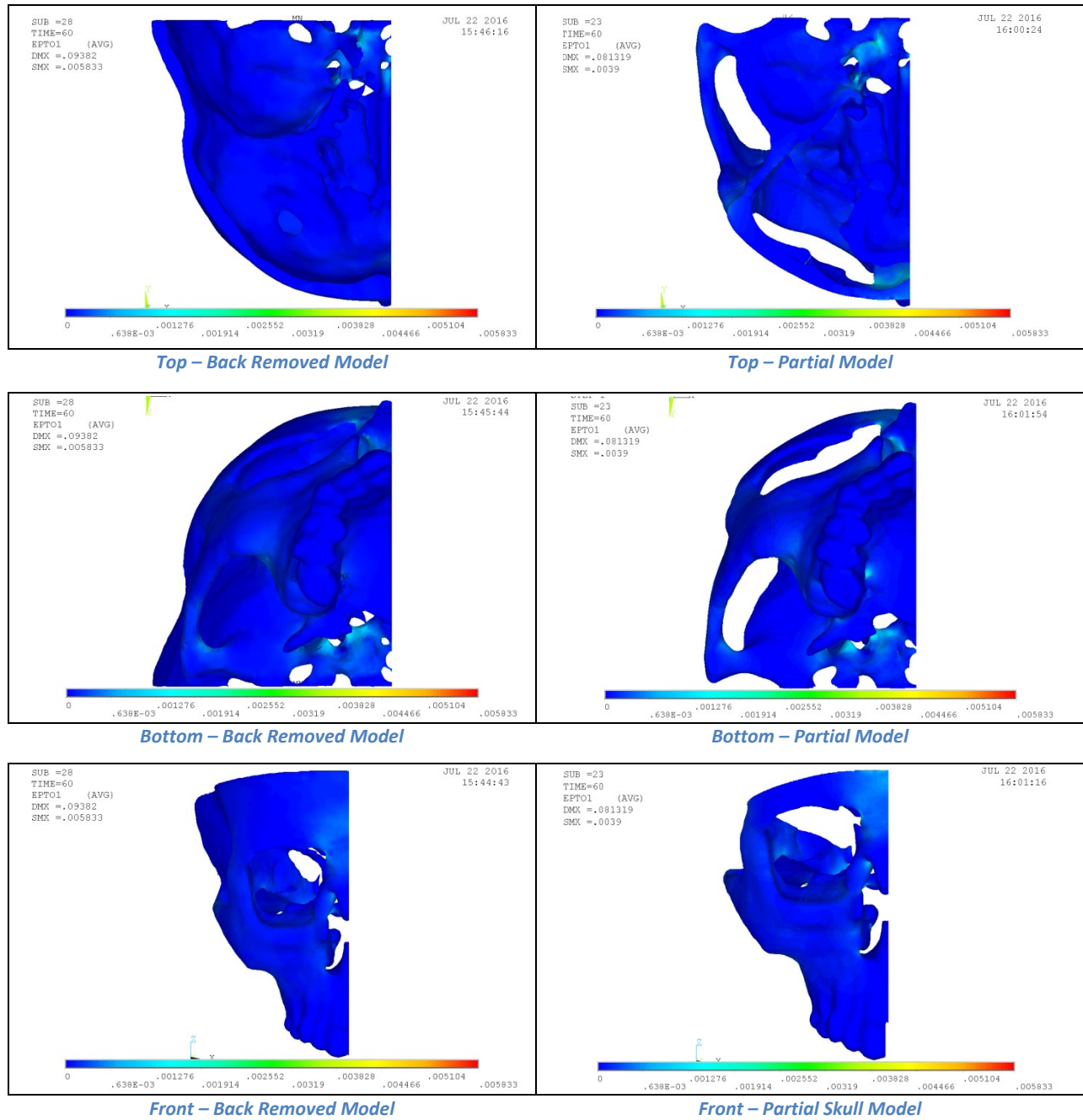
How do the non-linear tissue properties of the MPS affect the ME procedure? Using FE analysis, this study attempted to understand this interaction by simulating a ME protocol that utilized a bone-borne hyrax-type expander. An increased understanding of the effect of the stress relaxation of the MPS may aid future design of new expansion appliances and improved protocols.

Initial static simulations were run to verify the reduction of the model's geometric complexity using an applied force. Following this verification, the patient-derived cranial geometry was simulated multiple times using different material models for the sutures and different boundary conditions for the MPS. The material model and boundary conditions were outlined in Table 3-5.

#### 3.3.1 Geometry Trimming and Natural Boundary Conditions Verification

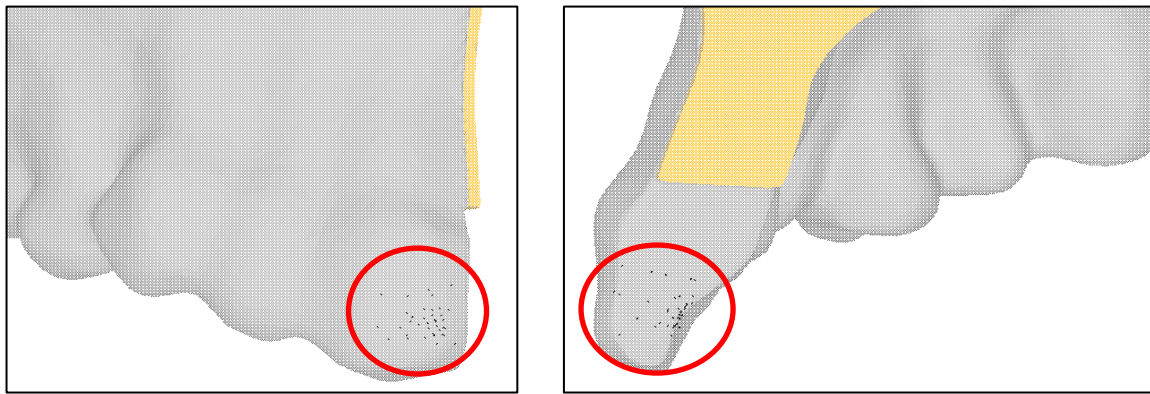
Verification of the trimmed geometry was done by directly loading the model with a 100N force and comparing it to a similarly loaded untrimmed geometry. This static simulation set served to confirm that the models were both experiencing similar strain patterns and ultimate displacements resultant from the static load.

Fig. 3-15 shows a side by side comparison of the strain plots of the two models. As can be seen in these models, the 1<sup>st</sup> principal strains are localized in the same locations of the models. Fig. 3-15 utilizes the same range on the color contour legend, which shows the magnitude of strain in those locations is nearly identical. The maximum strain magnitudes are quite similar, with maximum values of 5.833  $\mu\epsilon$  for the back removed model at the loading location and 3.9  $\mu\epsilon$  for the trimmed model nearer to the skull base. The strain images shown in, show the strain is localized in the posterior nasal spine, foramen lacerum, and nasion areas of the skull.



**Fig. 3-15: Strain Contour Plot Comparison of Back Removed and Partial Skull Models**  
 Legend shows strain,  $\epsilon$ , in mm/mm; Contour Scale from 0mm/mm (Blue) to 0.005833mm (Red)

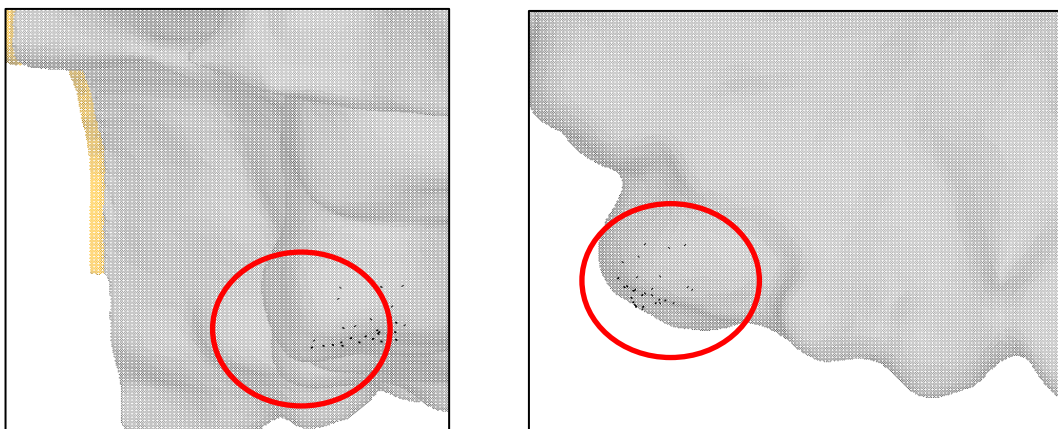
Both models show nearly identical final displacements, which are particularly noticeable when comparing the final displacement of the 1<sup>st</sup> molar, and the central incisor. As the models have dissimilar meshes, a direct comparison of the final nodal position was not possible. Instead, nodes within a 5mm cubic space in the two teeth were selected using a coded function for repeatability between both meshes. This made it possible to select several nodes to describe the initial and final position of cubic volumes of the two models. For the central incisor, nodes on the inner tip of the tooth (see Fig. 3-16) were compared. Similarly, nodes on the outer-rear point of the 1<sup>st</sup> molar were compared (see Fig. 3-17). The average initial and final positions and the overall displacements of the two volumes are compared in Table 3-6.



(A)

(B)

**Fig. 3-16: Nodal Selection on Central Incisor  
(Nodes Shown as Black Points; Highlighted by Red Circle)**



(A)

(B)

**Fig. 3-17: Nodal Selection on 1st Molar  
(Nodes Shown as Black Points)**

Table 3-6: Comparison of Averaged Displacements of Selected Node Sets Representing Pulp Chambers

Displacement Component	1st Molar			Central Incisor		
	Back Removed Model (mm)	Partial Skull Model (mm)	Percent Difference	Back Removed Model (mm)	Partial Skull Model (mm)	Percent Difference
UX	-8.17E-02	-7.49E-02	8%	-8.10E-02	-7.14E-02	12%
UY	5.90E-03	5.76E-03	2%	1.15E-02	1.25E-02	8%
UZ	-1.10E-02	-7.98E-03	27%	-3.05E-02	-2.67E-02	13%

These initial sets of comparison tests verify that the two geometries produced similar displacements for a constant directly applied force. The models, having uniform and isotropic material properties to act as control variables, had negligible differences in final deformation at the two measurement points. The measurement points, placed at the two points of maximum deformation, approximate the pulp chamber measurement points used in clinical studies by Lagravere et al. [17]. The partial cranial geometry was therefore used for further FEA simulations testing the non-linear relaxation material response.

### 3.3.2 Maxillary Expansion Simulations with Various Material Models and Sutures

The partial cranium model was simulated in FEA to evaluate how the non-linear tissue response of the MPS reacts to the forces of a stepped displacement ME procedure. Each simulation utilized the same stepped displacement profile as outlined in Section 3.2.5, and varied the material properties and boundary conditions as summarized in Table 3-5. This comparative analysis aimed to highlight any differences in final deformation results or the resultant strains and stresses.

Table 3-7 summarizes the simulation convergence and completion points. Several simulations failed to converge to the end of the 29 activation expansion protocol. The results for simulations that did not complete the expansion protocol will be discussed. However, their results in sub-steps that are close to the point of divergence cannot be considered accurate or reliable. These simulations failed due to extreme element distortions that could not be overcome, and the location of the element failure is also detailed in Table 3-7.

**Table 3-7: Completion Summary of Simulations**

<b>Simulation Case</b>	<b>Model</b>	<b>Simulation Description</b>	<b>Completion Status</b>	<b>Failure Reason (If Applicable)</b>
1	Untrimmed Skull	MPS: Neglected Applied Force	Complete	N/A
2	Trimmed Skull	MPS: Neglected Applied Force	Complete	N/A
3	Partial Skull	MPS: Neglected CFS: Stiff Lin. Elastic Applied Displacement	Complete	N/A
4	Partial Skull	MPS: Neglected CFS: Soft Lin. Elastic Applied Displacement	Incomplete	Element 105535 in Cranial Bone; Failed at 108005.16 seconds (After 6th Activation)
5	Partial Skull	MPS: Soft Lin. Elastic CFS: Stiff Lin. Elastic Applied Displacement	Incomplete	Element 208790 in MPS/IMS; Failed at 43203.49 seconds (During 3rd Activation)
6	Partial Skull	MPS: Prony Model CFS: Stiff Lin. Elastic Applied Displacement	Complete	N/A
7	Partial Skull	MPS: Prony Model CFS: Soft Lin. Elastic Applied Displacement	Incomplete	Element 174831 in ZTS; Failed at 108225.78 seconds (After 6th Activation)
8	Partial Skull	MPS: Prony Model CFS and IMS: Stiff Lin. Elastic Applied Displacement	Complete	N/A

To visually understand the cumulative deformation of the partial cranium model over the course of the 29 activation protocol, Fig. 3-18 shows the Case 6 model at different stages of appliance activation in the simulation.

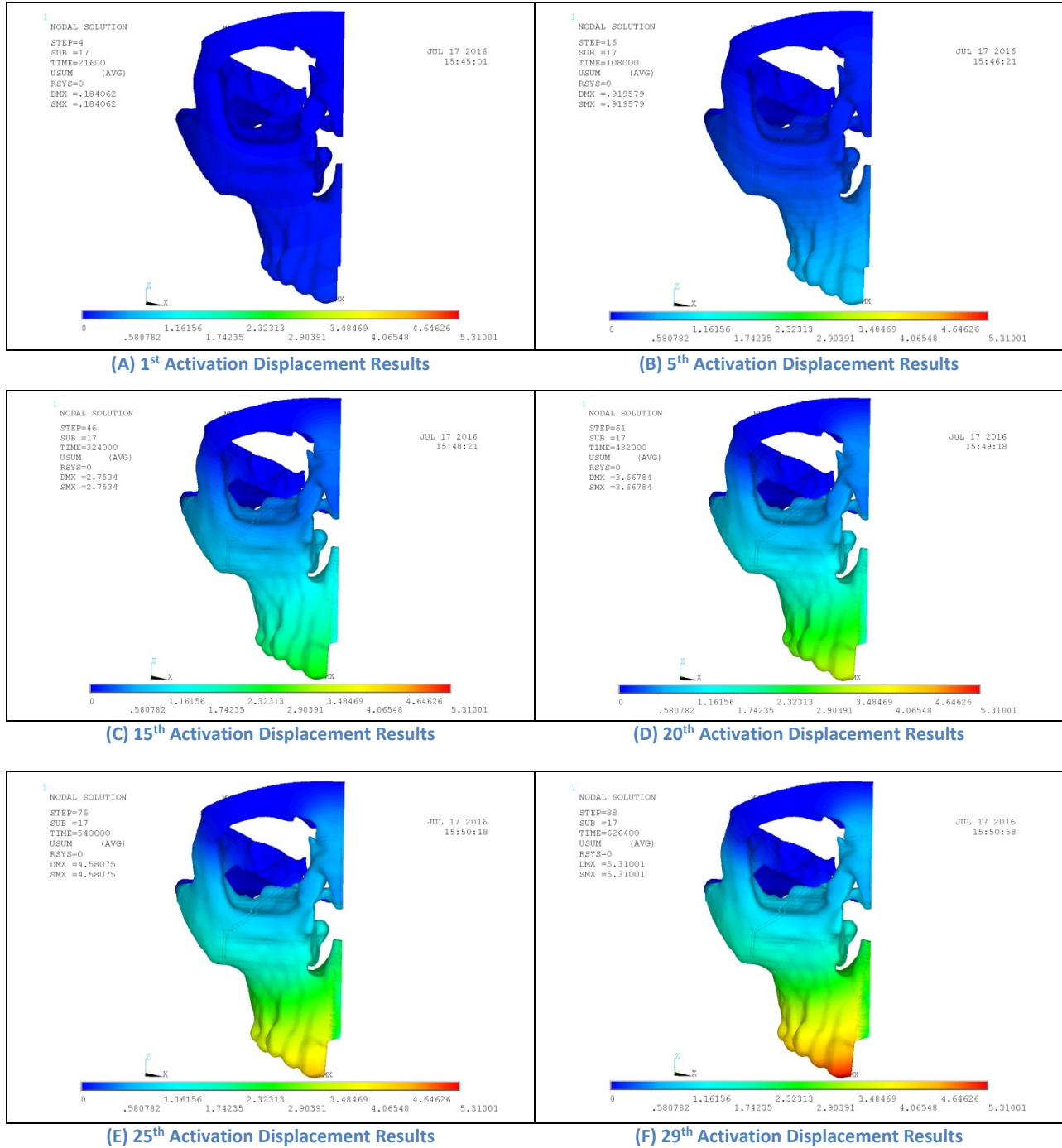


Fig. 3-18: Cumulative Displacement of the Case 6 model  
Color Contour Scale from 0mm (Blue) to 5.31mm (Red)

Average nodal displacement results of the models were taken from nodal points within the same cubic volume within the 1<sup>st</sup> molar and central incisor as used in Section 3.3.1. These expansion results detail the change in  $x$ -position of the two teeth over the course of the simulations. Fig. 3-19 shows the expansion results of the central incisor and Fig. 3-20 shows the expansion results of the 1<sup>st</sup> molar. The figures utilize lines instead of data point symbols for ease of understanding

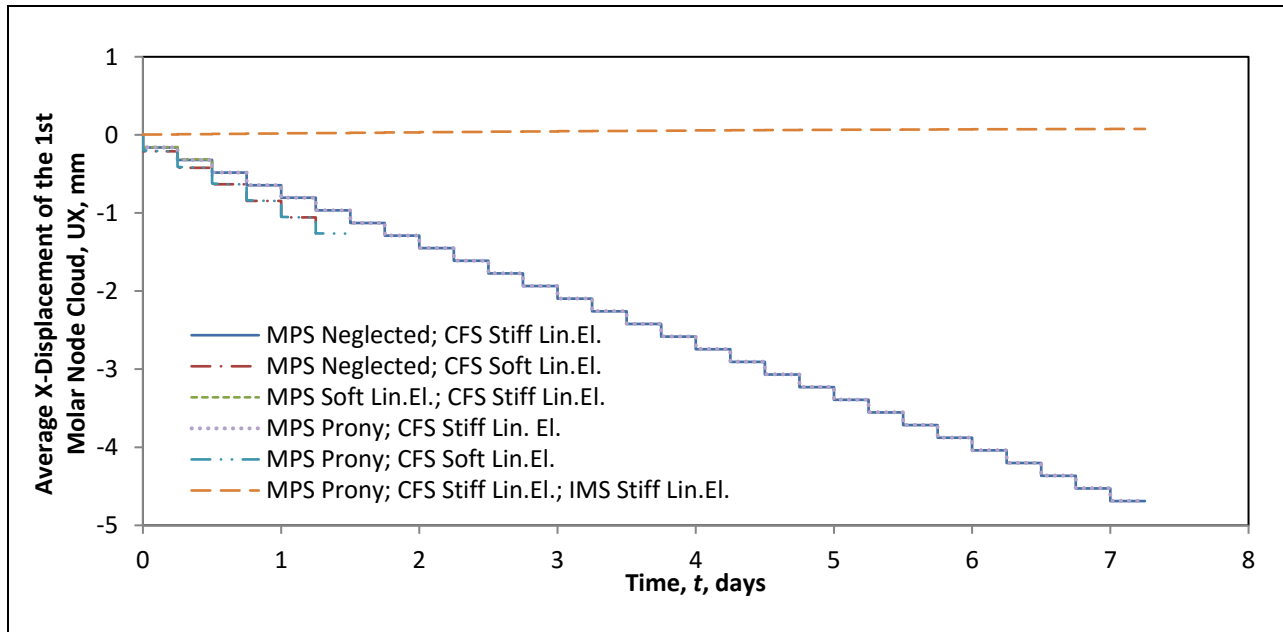


Fig. 3-19: Average X- Component Displacement of Central Incisor Nodes over the Course of the Simulation

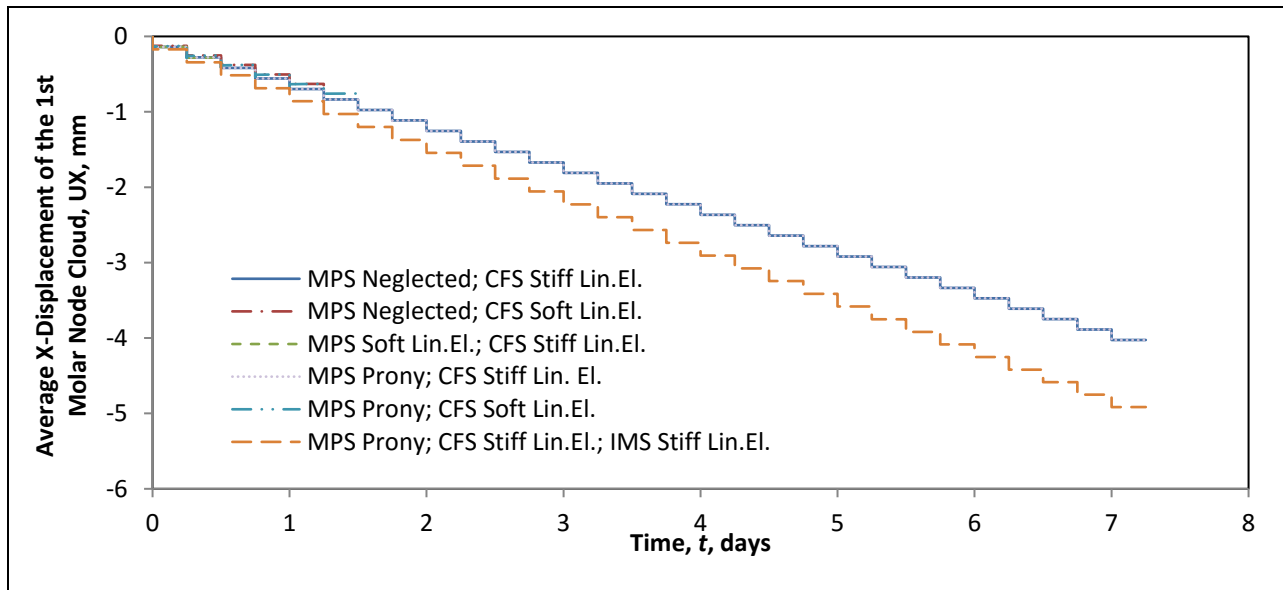
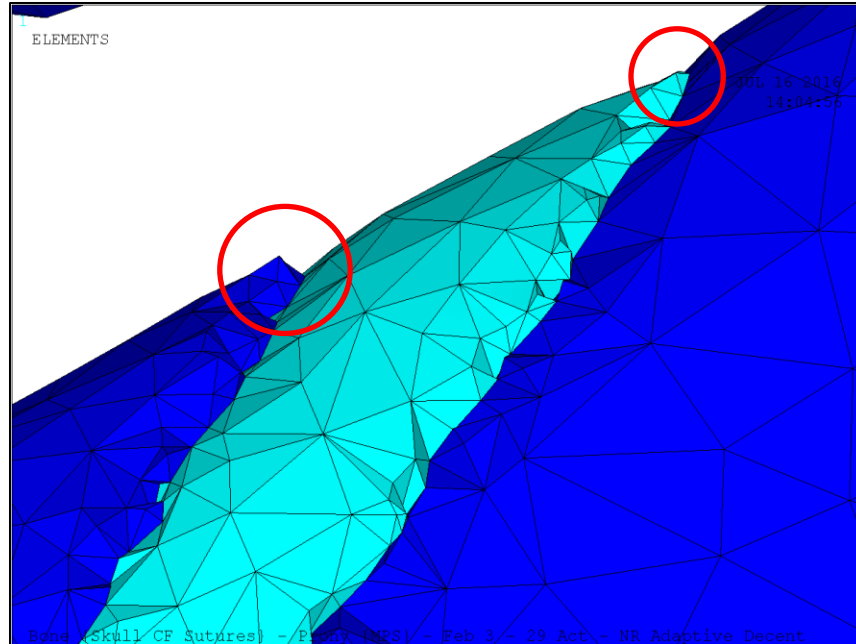


Fig. 3-20: Average X- Component Displacement of 1<sup>st</sup> Molar Nodes over the Course of the Simulation

Simulation cases that ran to completion each have 291 data points over the duration of the simulation. These models required 87+GB of hard disk space to store the results. The models that converged show similar expansion results at the two measurement points. For the models where the non-MPS sutures were given the linear elastic properties of bone, there was negligible differences in expansion between the model where the MPS was simulated using the relaxation model (Case 5) and where it was neglected by removing the symmetry boundary condition on the suture (Case 3). This result was expected as the relaxation model mathematically asymptotes towards a null stiffness, which effectively gave the suture a negligible infinite stiffness as the initial loading stress relaxed, transferring all residual load to the bone of the cranium. Although the simulation that utilized bone properties for non-MPS sutures and a soft linear elastic MPS did not complete all 29-activations, the initial results show minor differences in expansion at the two measurement landmarks. This trend is expected to continue as the low elastic modulus of the CFS would continue to be loaded with expansion forces. The material would linearly continue to yield to the compressive forces, leading to an outward rotation of the maxilla. This would increase 1<sup>st</sup> molar expansion and reduce the central incisor expansion in comparison with the bone-material CFS volume models.

Models that utilized low linear elastic properties for the additional craniofacial sutures were unable to solve to completion. As detailed in Table 3-5, the common cause of failure was elements shape failures under high compressive and shear loads. This lends credence to the hypothesis that the sutures may not react well under compressive loading as there may be bone-bone contact situations; however, it may be a function of the FEA mesh not being smooth across the bone-suture-bone interface. This lack of surface continuity, highlighted in Fig. 3-21, is caused by the Simpleware surface geometry interpretation when meshing. A possible solution to increasing the mesh quality in these regions, detailed in Appendix D, was considered; however, due to time constraints could not be properly implemented.



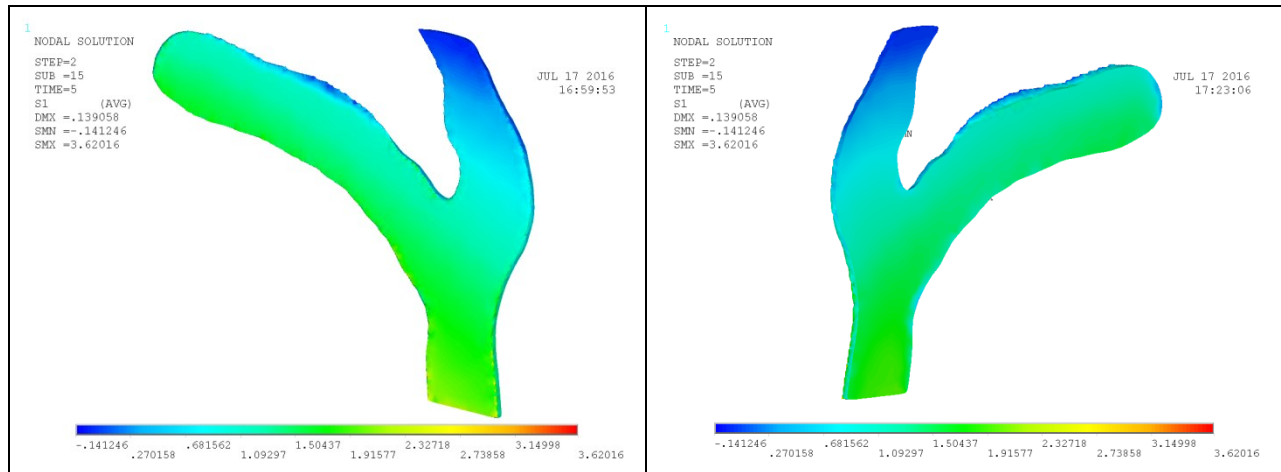
**Fig. 3-21: Bone-Suture Volume Interface; Close-up of the Zygomaticotemporal Suture in the Trimmed Model  
Red Circle Highlights the Un-smooth Suture-Bone Interface**

Additionally, it might be considered in the future to apply non-linear material properties to these suture structures. These hypothetical material models might have strain dependent properties that would increase the material stiffness to that of bone as it deforms under compressive loads, but under tension behave similarly to the strain and time dependent relaxation model described in eq. (2-31). As this proposed material model was outside the scope of this project, it was not pursued any further. What can be learned from the first few appliance activations of these models is that it resulted in a degree of outward tipping of the molars of the dental arch. Comparing the average displacement of the 1<sup>st</sup> molar in Table 3-8, the motion of the 1<sup>st</sup> molar in the y-, and z-directions is in the opposite direction in the CFS Soft Linear Elastic cases versus the Stiff Linear Elastic cases. This indicates an upward (Z+) and rearward (Y-) motion of the maxilla. This shows that studying the effect of different the material properties of the (non-MPS) craniofacial sutures has merit in the overall understanding of ME procedures. The findings of Wang et al., showing the effect of the non-MPS craniofacial sutures serve as cushion points under repetitive cranial loading, also indicate that these sutures are worthy of future study as to their effect on ME.[8]

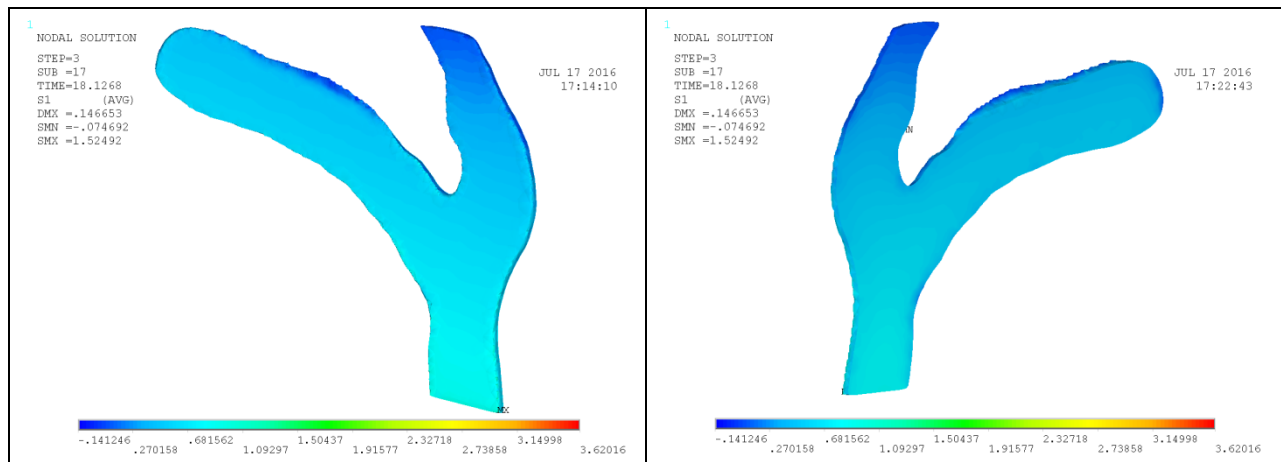
**Table 3-8: Comparison of X-Component of Displacement of the 1<sup>st</sup> Molar in Cranial Simulations; Simulations with Soft Linear Elastic Properties for the CFS are highlighted in green**

Simulation Case	Material Models	Average Displacement	Activation Number				
			1	3	6	29	
3	MPS Neglected; CFS Stiff Lin. El.	X-Component (mm)	-0.139	-0.418	-0.836	-4.026	
4	MPS Neglected; CFS Soft Lin. El.		-0.126	-0.378	-0.756	N/A	
5	MPS Soft Lin. El.; CFS Stiff Lin. El.		-0.141	-0.380	N/A	N/A	
6	MPS Prony; CFS Stiff Lin. El.		-0.148	-0.426	-0.842	-4.028	
7	MPS Prony; CFS Soft Lin. El.		-0.163	-0.411	-0.783	N/A	
8	MPS Prony; CFS Stiff Lin. El.; IMS Stiff Lin. El.		-0.171	-0.514	-1.029	-4.916	
3	MPS Neglected; CFS Stiff Lin. El.		Y-Component (mm)	0.011	0.032	0.066	0.357
4	MPS Neglected; CFS Soft Lin. El.			-0.033	-0.097	-0.194	N/A
5	MPS Soft Lin. El.; CFS Stiff Lin. El.	0.011		0.031	N/A	N/A	
6	MPS Prony; CFS Stiff Lin. El.	0.016		0.037	0.069	0.358	
7	MPS Prony; CFS Soft Lin. El.	-0.010		-0.078	-0.178	N/A	
8	MPS Prony; CFS Stiff Lin. El.; IMS Stiff Lin. El.	0.027		0.080	0.157	0.644	
3	MPS Neglected; CFS Stiff Lin. El.	Z-Component (mm)	-0.015	-0.044	-0.084	-0.287	
4	MPS Neglected; CFS Soft Lin. El.		0.009	0.029	0.062	N/A	
5	MPS Soft Lin. El.; CFS Stiff Lin. El.		-0.015	-0.041	N/A	N/A	
6	MPS Prony; CFS Stiff Lin. El.		-0.018	-0.046	-0.086	-0.288	
7	MPS Prony; CFS Soft Lin. El.		0.003	0.024	0.058	N/A	
8	MPS Prony; CFS Stiff Lin. El.; IMS Stiff Lin. El.		-0.022	-0.066	-0.127	-0.424	

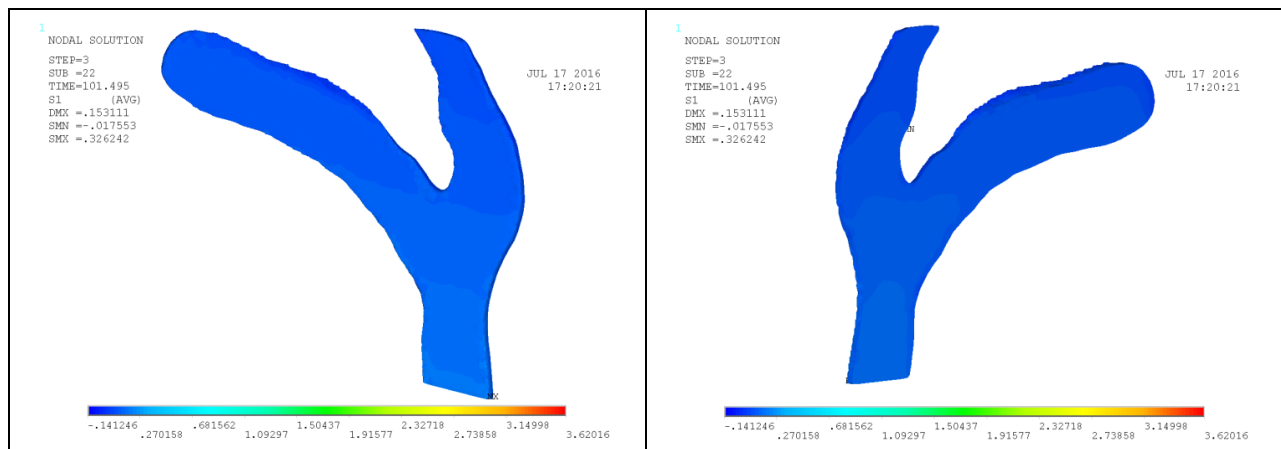
The post activation stresses of the MPS/IMS structure in Simulation Case 6, shown in Fig. 3-22 and Fig. 3-23, show the decreasing stress distribution within the MPS/IMS volume following the 1<sup>st</sup> and 29<sup>th</sup> appliance activations. These plots show that the stresses are not uniform throughout the suture as different portions of the structure experience differing levels of strain.



(a)  $t = 1^{\text{st}}$  Activation + 0 seconds

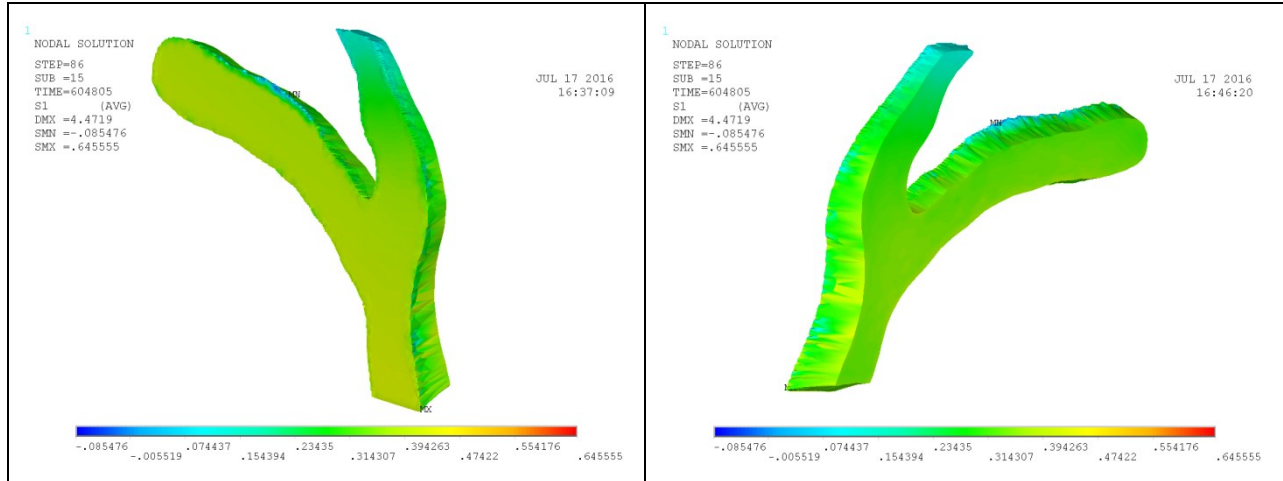


(b)  $t = 1^{\text{st}}$  Activation + 13.1 seconds

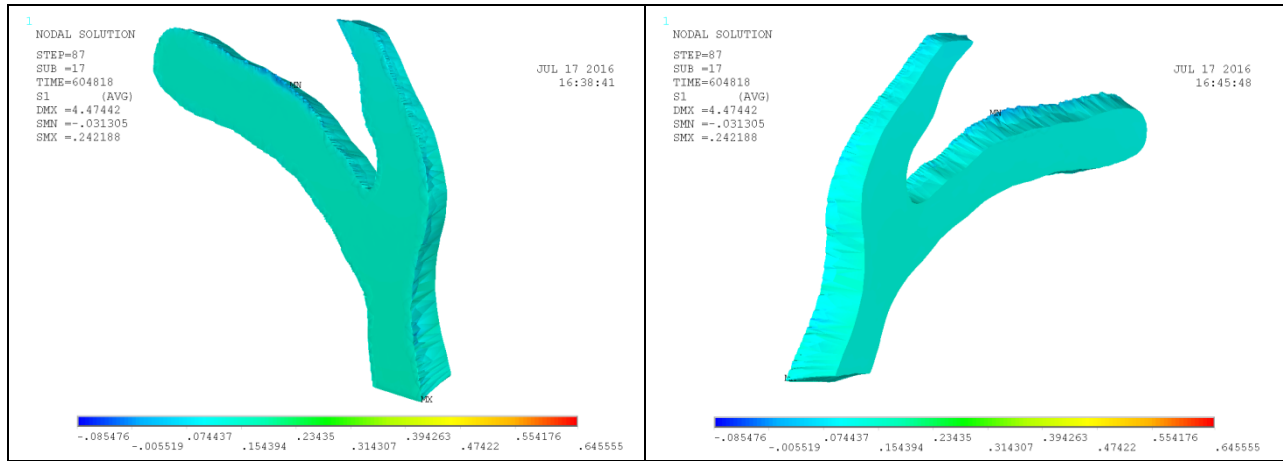


(c)  $t = 1^{\text{st}}$  Activation + 66.5 seconds

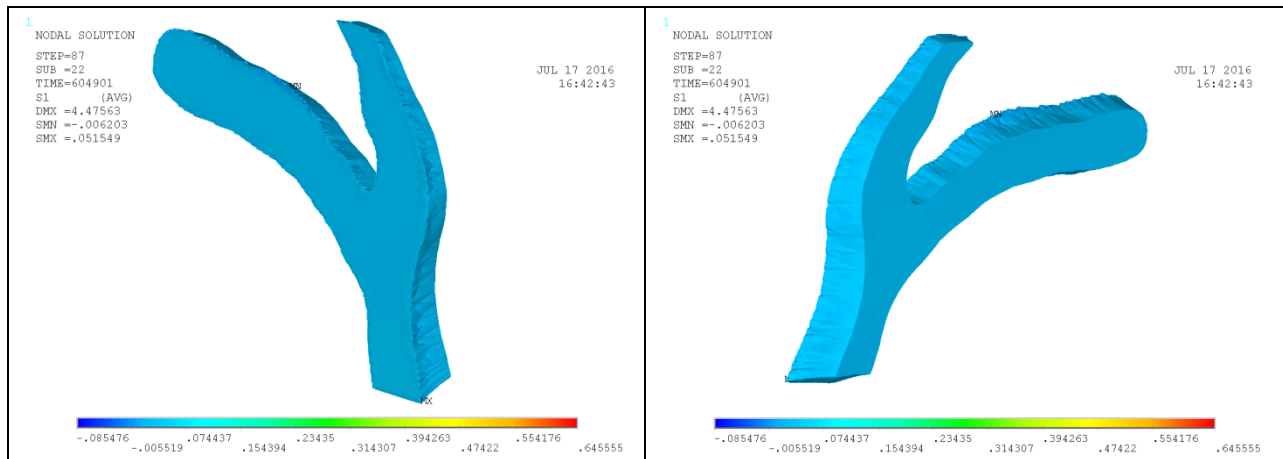
Fig. 3-22: Post Activation 1<sup>st</sup> Principal Stress Contour Plots Following 1<sup>st</sup> Appliance Activation Both Sides of Suture Volume Shown; Bone Adjacent on Left, Sagittal Plane on Right Contour Scale from (Blue) -0.14126 MPa to 3.62016 MPa (Red)



(a)  $t = 1^{\text{st}}$  Activation + 0 seconds



(b)  $t = 1^{\text{st}}$  Activation + 13.1 seconds



(c)  $t = 1^{\text{st}}$  Activation + 66.5 seconds

**Fig. 3-23: Post Activation 1<sup>st</sup> Principal Stress Contour Plots Following 29<sup>th</sup> Appliance Activation Both Sides of Suture Volume Shown; Bone Adjacent on Left, Sagittal Plane on Right Contour Scale from (Blue) -0.085176 MPa to 0.64555 MPa (Red)**

To better understand the rates of relaxation in the MPS/IMS structure 27 nodes were selected within the suture. The locations of these elements are highlighted in Fig. 3-24. The averaged nodal sum 1<sup>st</sup> principal stress results from the nodes shown in Fig. 3-24 were plotted versus time in Fig. 3-25. These results show the reduction of the peak stresses of the MPS/IMS volume as it goes through subsequent activations, mirroring the results seen in Chapter 2. As can be seen clearly in Fig. 3-26, the stresses within the MPS/IMS volumes using the Prony relaxation model do relax within the first two minutes following the 1<sup>st</sup> appliance activation. The peak stresses for the selected nodes for Case 6 are shown in Fig. 3-27, demonstrating the variability of the stresses across the geometry.

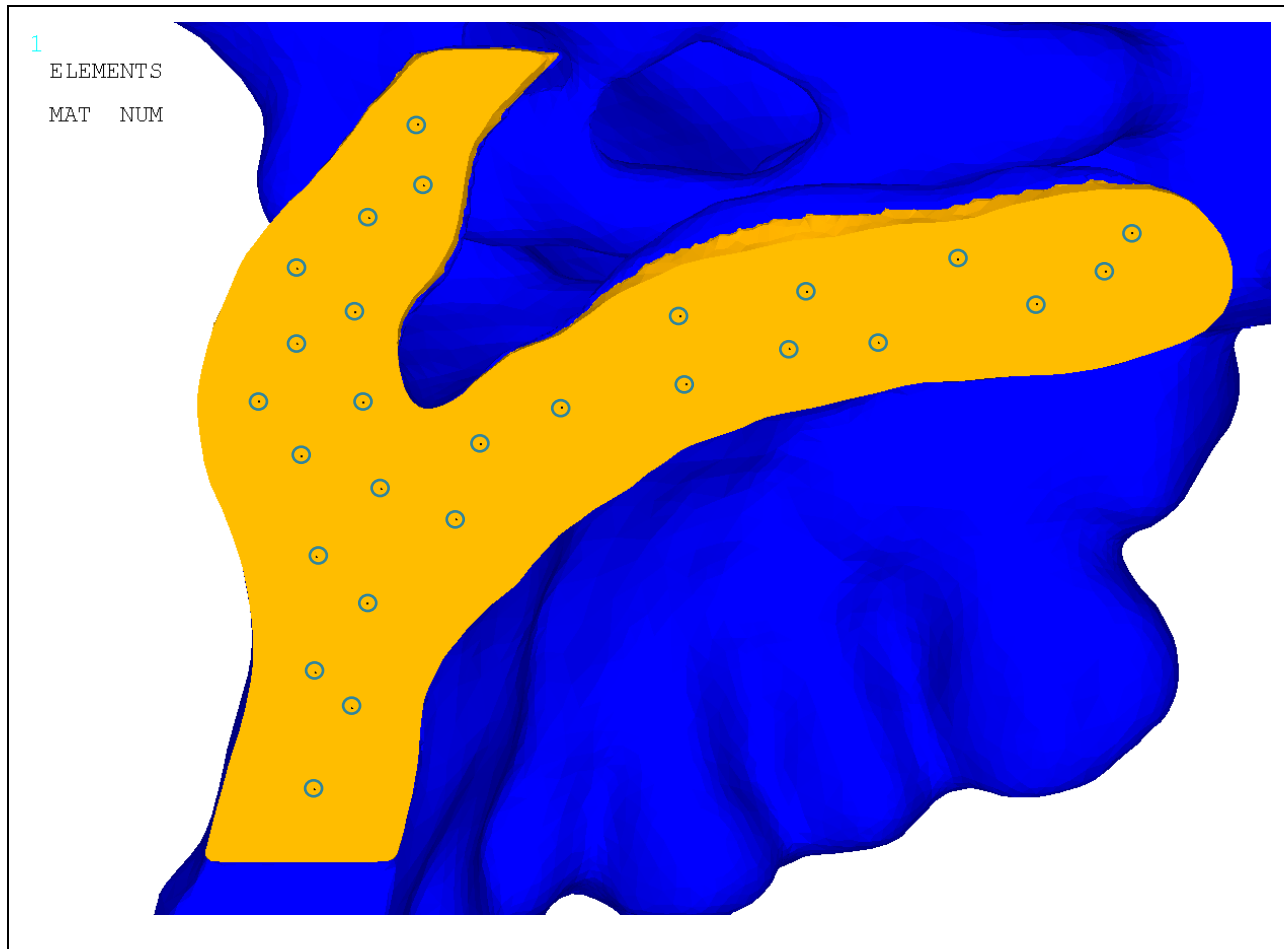


Fig. 3-24: Selected Nodes with the MPS/IMS Structure; Selected Nodes Circled for Ease of Identification

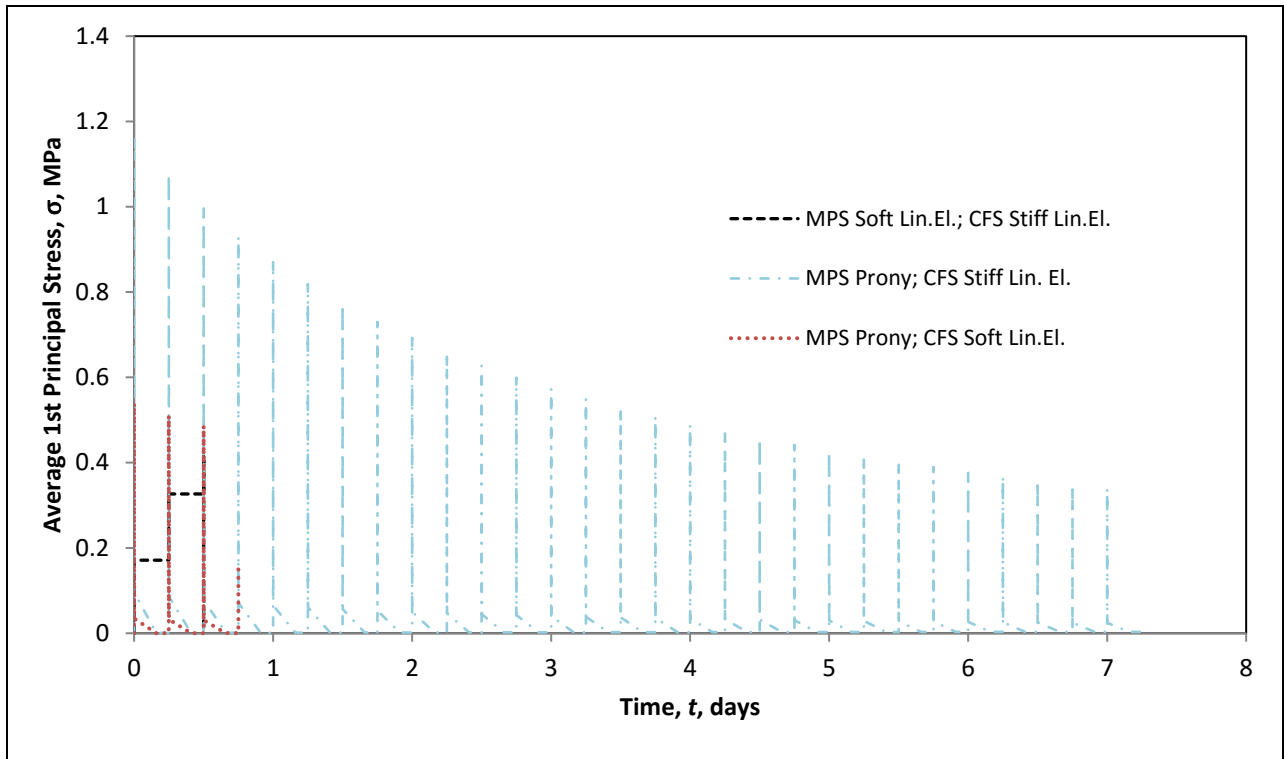


Fig. 3-25: Averaged 1<sup>st</sup> Principal Stress of the Selected MPS/IMS Nodes for Partial Skull Simulation Cases 5, 6, and 7

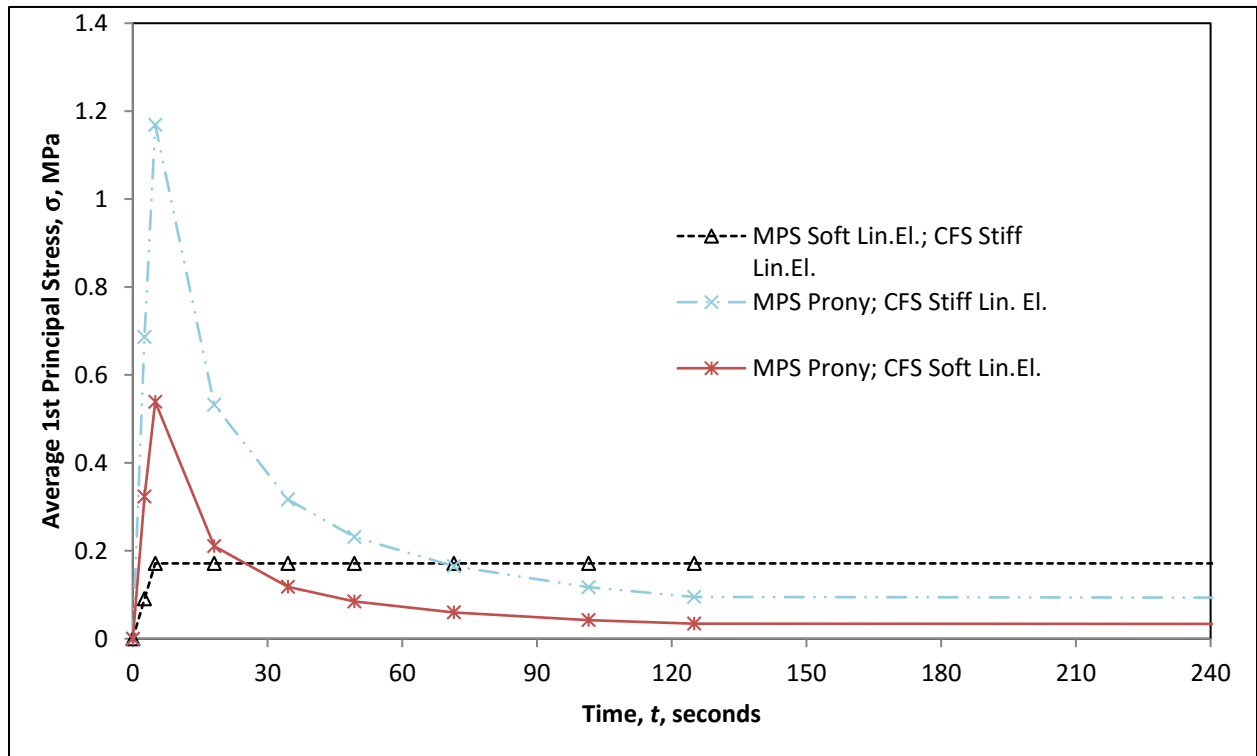


Fig. 3-26: Averaged 1<sup>st</sup> Principal Stress of the Selected MPS/IMS Nodes for Partial Skull Simulation Cases 5, 6, and 7; Only Looking at the 4-minutes following the 1<sup>st</sup> Activation

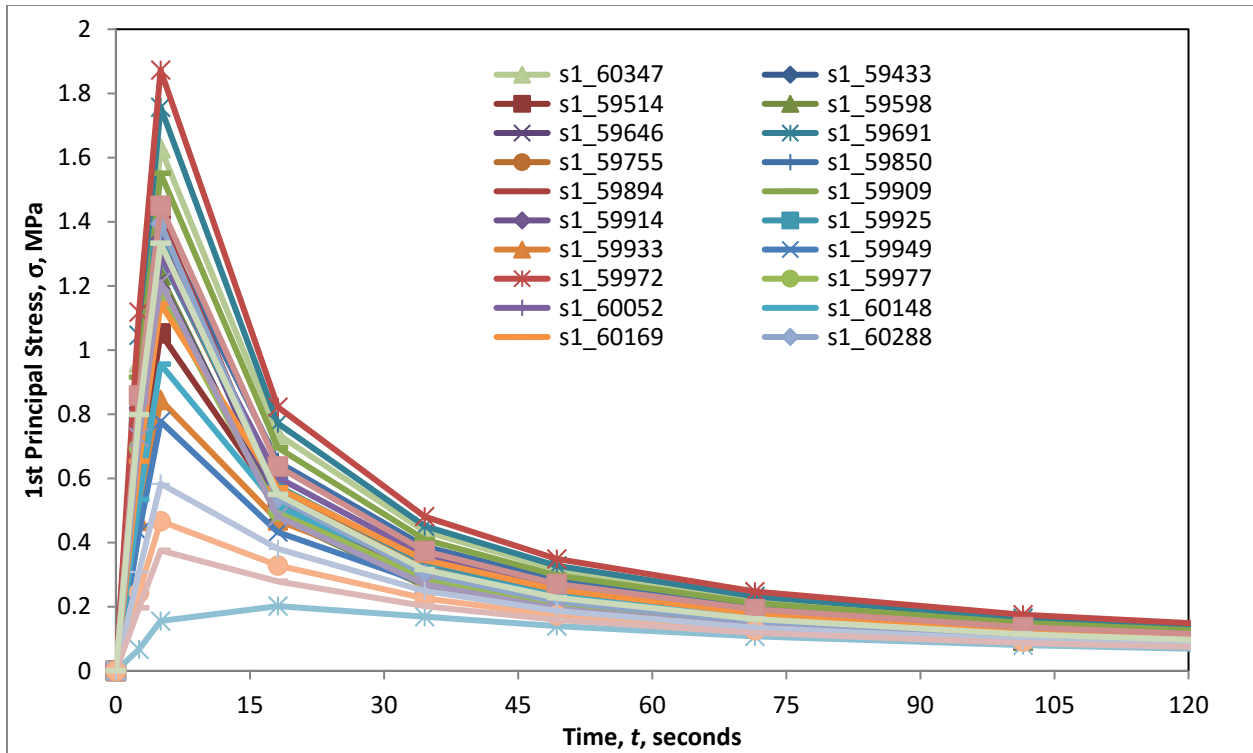


Fig. 3-27: 1<sup>st</sup> Principal Stress of the 18 MPS/IMS Nodes (See Fig. 3-24) for Partial Skull Simulation Case 6; Only Showing First Activation

The results shown in Fig. 3-26 and Fig. 3-27 demonstrate that the stresses within the suture decreased to negligible levels within 2 minutes, as expected. However, as shown in Fig. 3-28, the peak stresses in the MPS/IMS nodes for Case 6 was higher than predicted by the 1-D relaxation equation for most, but not all, of the nodes. The cause of this discrepancy may be due to the three-dimensional implementation of the Prony approximated relaxation curve, or more likely it is caused by the nodal result averaging done by ANSYS prior to exportation of the data. As the peak FEA stress results are quite similar to the 1-D predictions, the relaxation model in cranium simulations is judged to be working as expected.

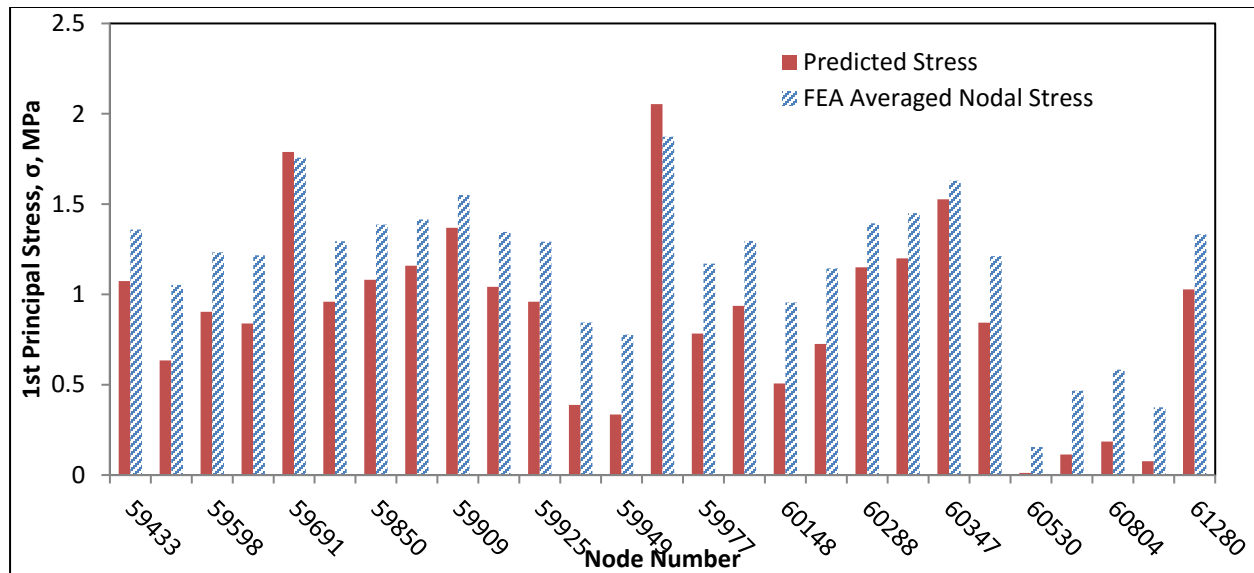


Fig. 3-28: 1<sup>st</sup> Principal Stress of the 18 MPS/IMS Nodes for Partial Skull Simulation Case 6 Compared to The Predicted Stress Based on the 1-D Relaxation Model and the reported 1<sup>st</sup> Principal Strain for the Nodes at 5 seconds

The appliance remote loading point (node 100000) experienced reaction force loads during the application of displacements. The reaction forces of Simulation Cases 3 through 8 (see Table 3-5) are shown in Fig. 3-29 as a function of time. Fig. 3-30 shows the reaction force for the first few appliance activations.

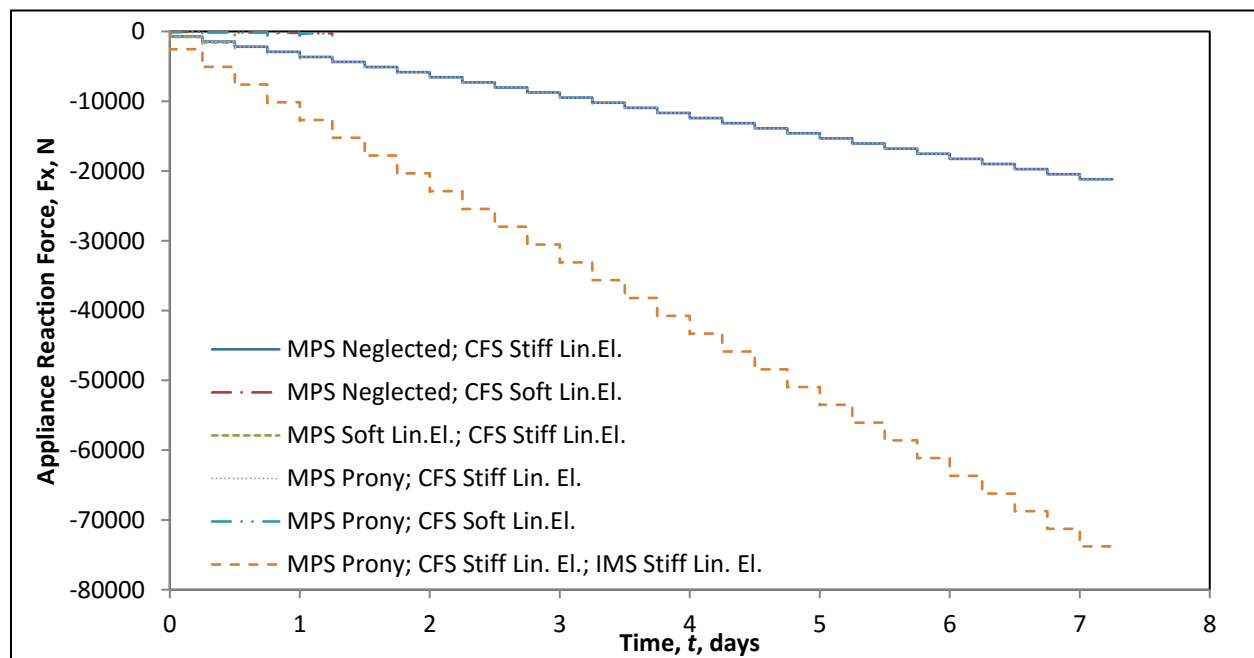


Fig. 3-29: Simulation Load Point Reaction Forces versus Time

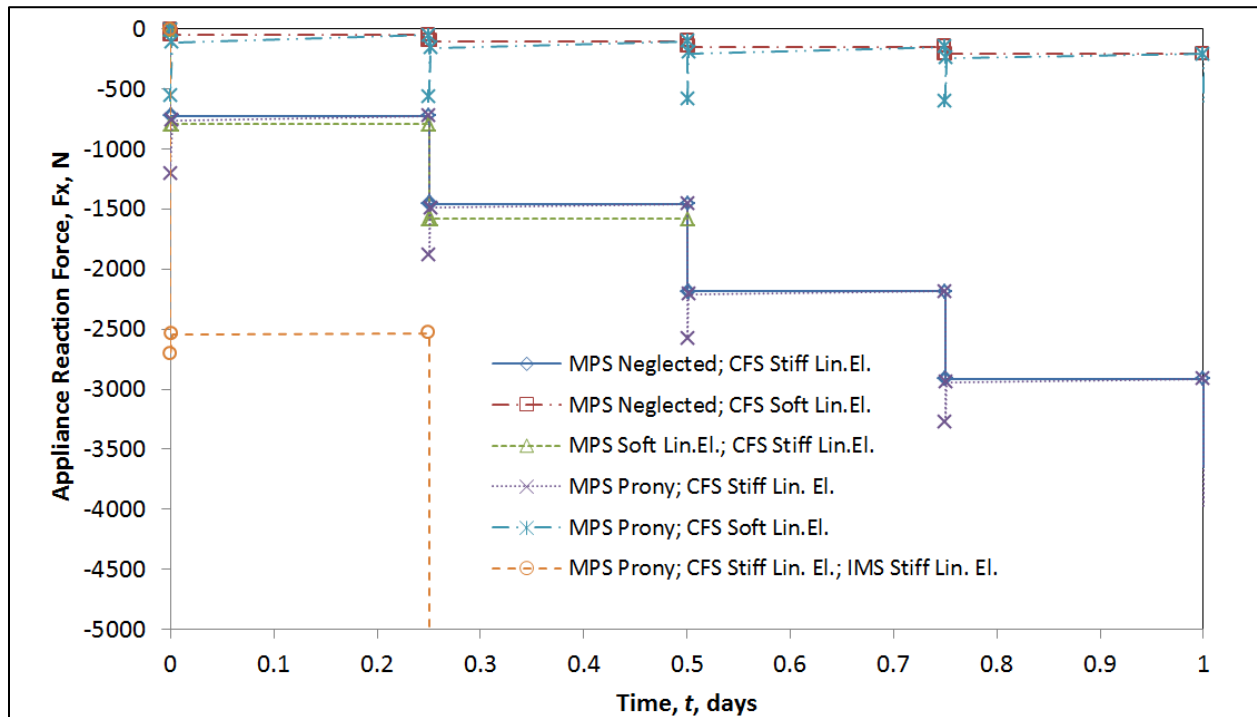


Fig. 3-30: Simulation Load Point Reaction Forces versus Time; First Four Appliance Activations

As can be seen clearly in Fig. 3-29, the magnitude of the  $x$ -component of the reaction force is increasing during the entirety of the simulation. In Fig. 3-30 there is a slight but notable decrease in reaction within the 2-minutes following the appliance activations for simulation cases that incorporated the Prony model for the MPS. This decrease in compressive force acting of the appliance is attributable to the reduction in the stress in the suture. The overall increase of force throughout the simulated treatment is indicative of increasing resistance to expansion caused by deformation of the cranium and its linear material properties. As shown in prior studies, in particular by S. Liu [18], the bone tissue adjacent to the suture undergoes reformation and growth during expansion. As with common orthodontic treatments requiring braces, bone has been shown to reform under load [19]. The effect of material properties on the appliance reaction forces are highlighted in the uncompleted simulations. As can be seen, the material properties of the MPS, IMS, and additional craniofacial sutures had a great effect on the reaction forces imparted by the appliance. The models that utilized soft linear elastic material properties for the craniofacial sutures had significantly lower reaction forces as the strain within the CFS allowed for greater overall model deformation per unit of applied force.

It is recognized that the simulations that utilized stiff linear elastic properties for the additional CFS show abnormally high reaction forces in the kN range, beyond the values that would be experienced by an expansion appliance. This is due to the higher Young’s Modulus used for the properties of bone as discussed in Section 3.2.5, the lack of viscoelastic or soft linear elastic compliance in the additional CFS, and the model not utilizing viscoelastic material properties for bone. These reaction forces are not meant to report the actual reaction forces experienced by the appliance but are included to illustrate the importance of including both the compliance of the CFS and the non-linear properties to approximate the stress relaxation of reforming bone in future predictive models.

Finally, the FE model expansion results were compared to clinical expansion measurements for the patient on which the geometry was based. Clinical expansion values were calculated from the difference between the distances measured between the pulp chambers of the 1<sup>st</sup> molars and the central incisors in the CT image sets taken at T2 (pre-expansion) and T3 (post expansion). Clinical measurements found an overall 1<sup>st</sup> molar expansion of 5.34mm, and an expansion between the central incisors of 1.37mm. These values were then halved for comparison to the FEA model results due to the symmetry condition used in the model. Table 3-9 compares the expansion measurement results of 1<sup>st</sup> molar and central incisor of the FE simulations with the patient expansion results. Values in red font have an expansion distance lower than the clinical results and those highlighted in green are greater.

**Table 3-9: Comparison of Completed Simulation Expansion x-Component to Clinical T2-T3 Measurements for Patient**

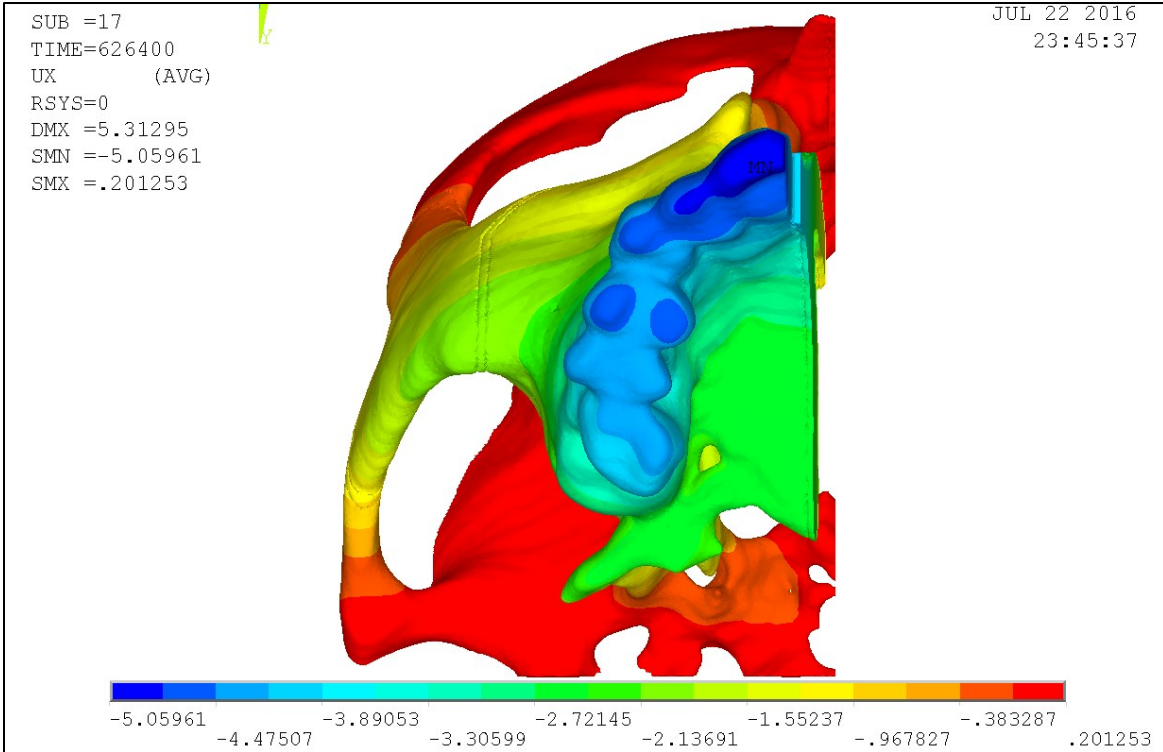
	1st Molar		Central Incisor	
	Activation Number	Expansion (mm)	Activation Number	Expansion (mm)
Case 3	19	2.6428	4	0.6443
	20	2.7815	5	0.8056
	29	4.0263	29	4.6893
Case 6	19	2.6458	4	0.6207
	20	2.7843	5	0.7838
	29	4.0284	29	4.6799
Case 9	15	2.5669	29	-0.0757
	16	2.7368		
	29	4.9156		

It can be seen that none of the simulations correctly emulate the clinically measured expansion. For cases 3 and 6 this is quantifiable with increased 1<sup>st</sup> molar expansion and greatly increased

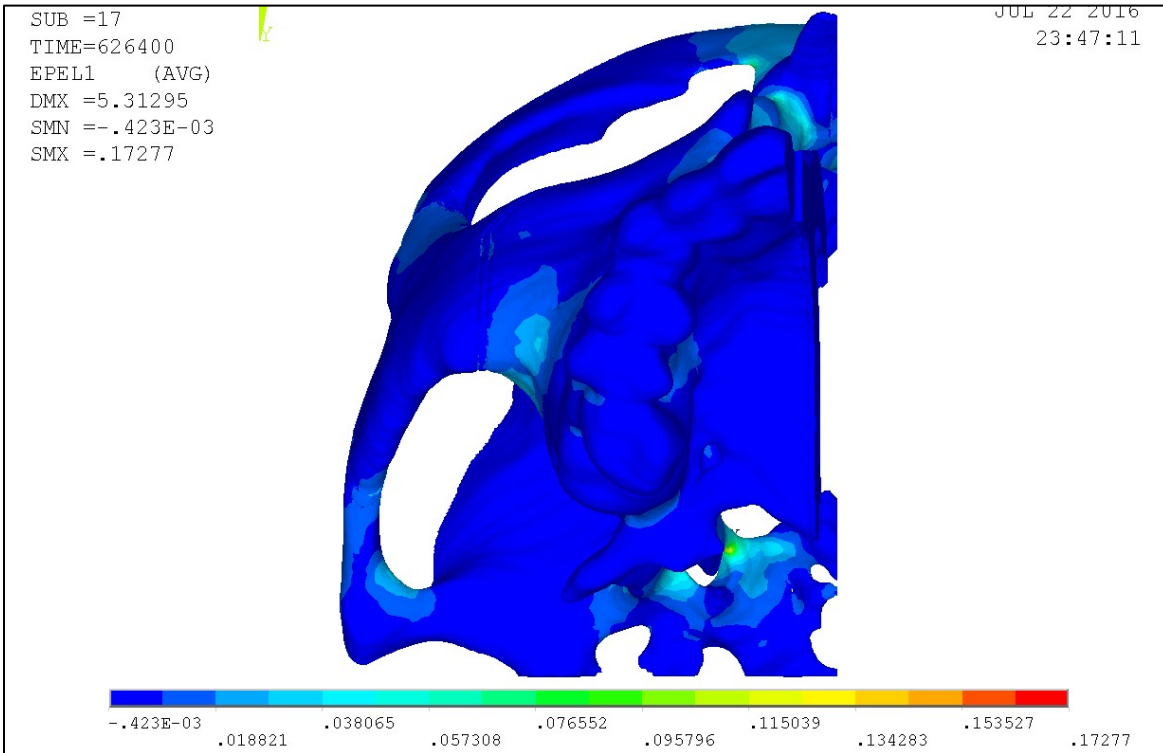
central incisor expansion. This is indicative of reduced outward rotation of the maxilla, most likely due to the amalgamation of the MPS and IMS sutures into a single material volume. Simulation case 9 separated the IMS and MPS, with the IMS having the properties of bone. This material model was manually applied to the IMS region of the MPS/IMS volume (i.e. - the geometry was not re-meshed). The Prony model was used for the remainder of that volume for the MPS. Case 8 is unique in that the average nodal results show that the central incisors moved closer together.

The expansion appliance was present in the patient's mouth in both the T2 and T3 image sets, indicating that there was not a reduction in expansion as the appliance was still in place. However, as the displacement was applied at the location the appliance was in contact with the patient, the simulations neglect any deformation in the armature of the appliance itself. Deformation of the appliance armature would potentially absorb the displacements from the first few appliance activations. Although the displacement results are not directly comparable between the simulations and the clinical results, it can be seen that the both expansion trends reflect the actual clinical trends, especially in simulation case 9. This supports that the simulation results, although not a direct representation of clinical patient results, could be used to help clinicians better understand the impact material properties have on expansion results.

Figs. 3-31 through 3-33 show the inferior view of the models showing the x-component of displacement at the end of the 29<sup>th</sup> activation, as well as the 1<sup>st</sup> principal strain plot of the model cases. As is clear in these images, the Case 8 model has more posterior expansion of the dental arch and the MPS, while the other two models have a higher anterior expansion of the dental arch and MPS. Differences between FEA and clinical expansion results show that the difference in material properties between the IMS and MPS are important to consider. To utilize an FEA model as a predictive tool for simulating new appliances and procedures the material properties of each suture should be better understood.

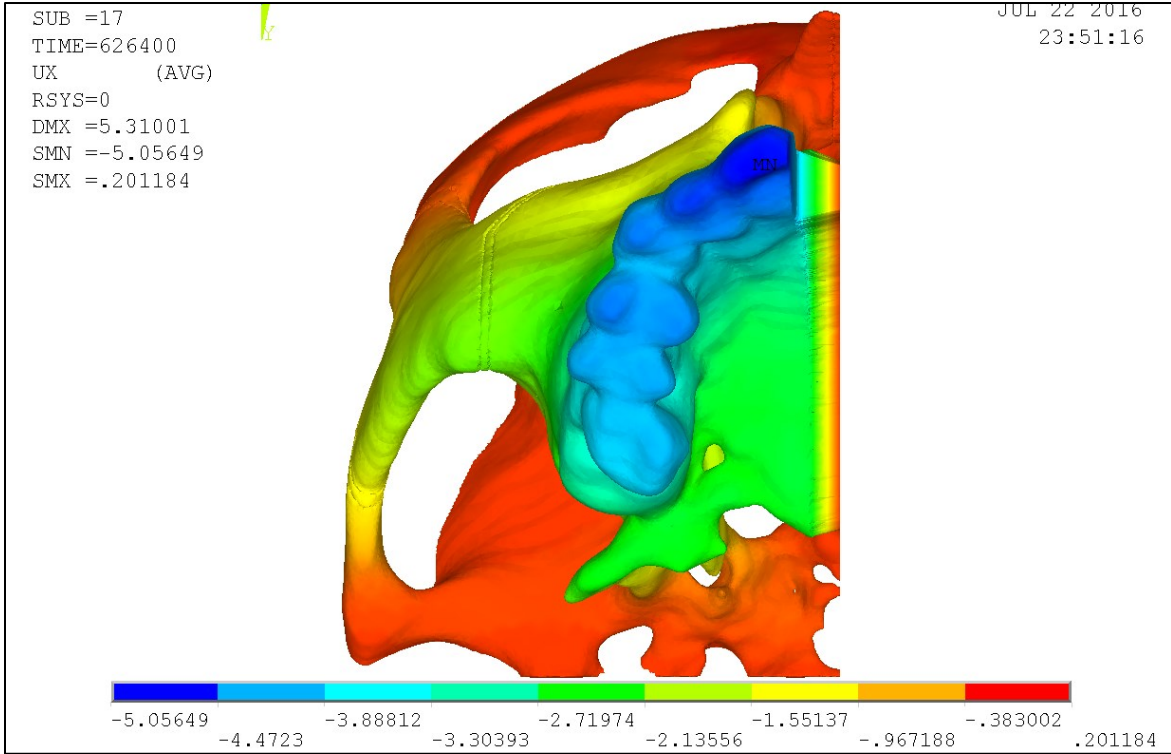


(A) – X-Component of Structural Displacements in mm

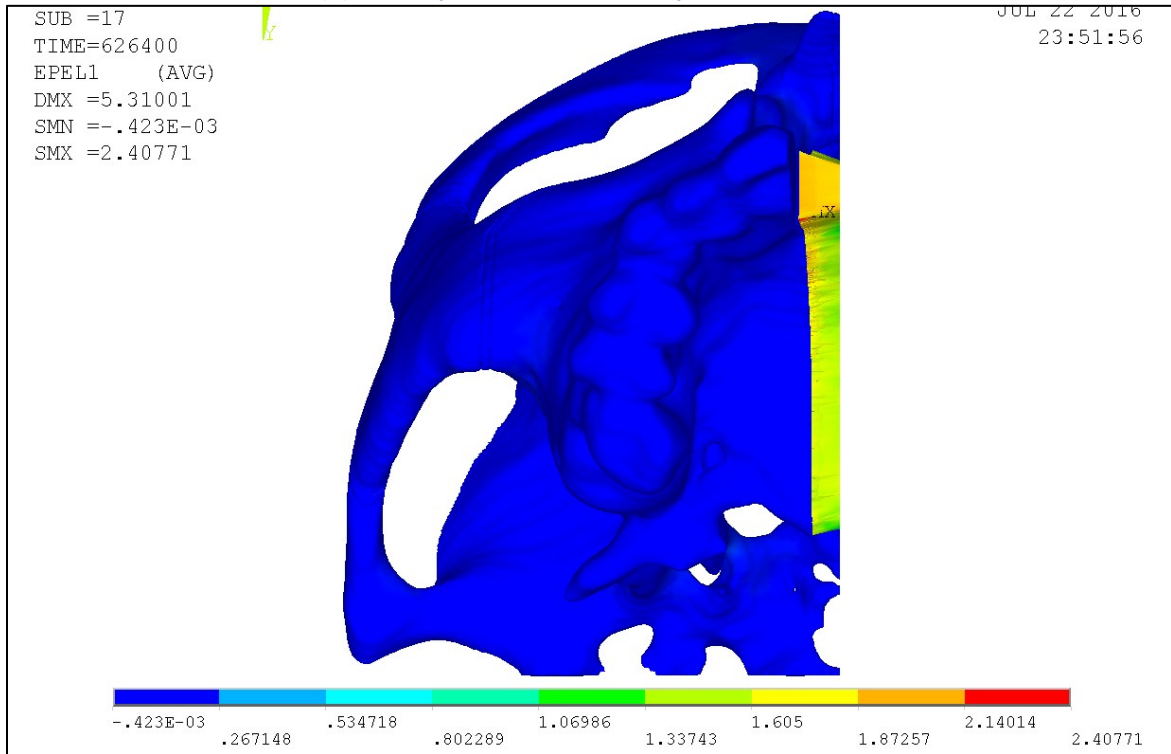


(B) – Strain Contour Plot in mm/mm

Fig. 3-31: Case 3 Partial Skull Model - MPS Neglected; 29<sup>th</sup> Activation

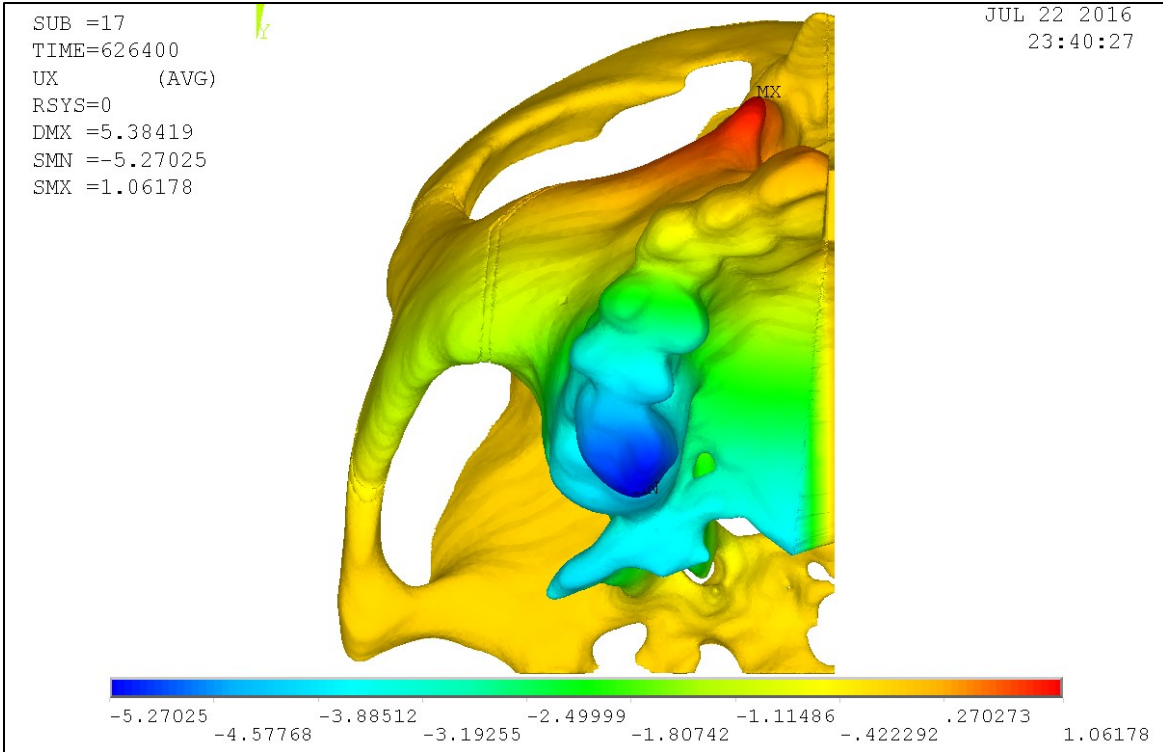


(A) – X-Component of Structural Displacements in mm

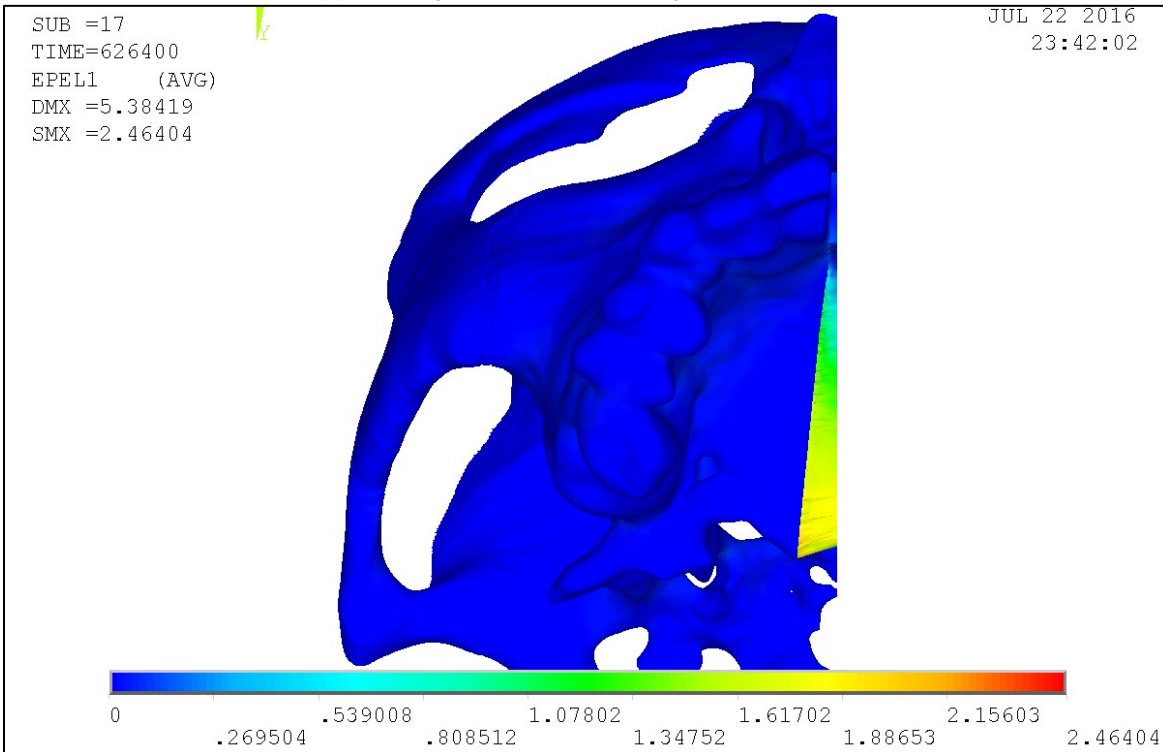


(B) – Strain Contour Plot in mm/mm

Fig. 3-32: Case 6 Partial Skull Model – MPS/IMS Relaxation Model; 29<sup>th</sup> Activation



(A) – X-Component of Structural Displacements in mm



(B) – Strain Contour Plot in mm/mm

Fig. 3-33: Case 8 Partial Skull Model - MPS Relaxation Model, IMS Stiff Linear Elastic Model; 29<sup>th</sup> Activation

### 3.4 Conclusions and Future Work

Predictive computer simulations could one day increase the quality of life of adolescent patients undergoing the orthodontic ME treatment. Simulating the non-linear stress relaxation material properties within the MPS is a step in the long road leading to this future of virtual testing of new treatment protocols on the silicon chips of computers instead of on children. This study looked to incorporate the 1-D stress relaxation model that had been adapted for FEA into partial skull simulations of the ME procedure. This involved generating a model geometry from the pre-procedure CT scans of an adolescent patient, meshing the model for FEA, assigning material models and properties to the different structures within the model, and loading them in a clinically relevant fashion.

Model geometry, developed using Simpleware ScanIP and +FE modules, was created based on semi-automatic masking techniques. The masking process would not be exactly repeatable due to the individual judgment of the user and the gradient of greyscale at the edge of any body. The way to test this would be to have a large group of users mask up several identical CT data sets and do a volumetric comparison analysis of the final masks. As validating the Simpleware method was not within the scope of the study to evaluate the efficacy and effect of the FE relaxation model on ME treatment, this was not considered. Due to differences in the two different model geometries<sup>17</sup> that were tested in Section 3.3.1, the FEA results had small differences in the final stress values, as was expected. This was caused by an additional smoothing operation of the partial skull model that resulted in slight differences in individual structure dimensions, such as bone wall thickness. As the models were under applied displacement loads, the final deformations between the two models were nearly identical, with relative differences in the x-component of displacement of 8% for the 1<sup>st</sup> Molar and 12% for the Central Incisor. It was judged that this small difference justifies the use of the reduced model geometry for simulating the non-linear material properties of the MPS. Additionally, both

---

<sup>17</sup> Half Skull with Back Removed and Partial Half Skulls; Results Discussed in Section 3.3.1

simulations had similar strain values in identical high strain locations, with the variations likely caused by differences individual structure dimensions.

To evaluate the effect of the non-linear stress relaxation model on the ME procedure, multiple material model combinations were simulated for the various suture structures. The 1<sup>st</sup> molar and Central Incisor expansion results show that there is a negligible difference between two of the simulations that were run to completion. The difference between these two simulations are that in the first the MPS/IMS volume was neglected and in the second the MPS/IMS volume had been assigned the Prony series adaptation of the stress relaxation model. The nearly identical final displacement of the two measurement points is as expected due to the fact the Prony model modulus trends towards zero as time increases, mimicking the model with the neglected suture. However, a key difference between the models is caused by the relaxing stress distribution within the suture volume in the 2-minutes following an appliance activation. This stress peak causes a noticeable momentary peak in the reaction force in at the appliance loading node, were as the model with the neglected suture does not have this peak. It is suggested by these results that expansion appliance design in the future could utilize FEA simulations incorporating the viscoelastic stress relaxation model to optimize the energy storage of the appliance armature to promote bone growth at the suture-bone interface. The stress relaxation profiles within the MPS volume behaved as expected following the 5-second ramped applied displacements from the appliance activations.

In simulations that varied the material properties of the non-MPS/IMS craniofacial sutures included in the model, the results are intriguing despite the simulations not running to completion for the full 29-activations. These simulations show that a reduction in the elastic modulus of the CFS can both affect the final displacement of the dental arch, but can greatly affect the reaction forces experienced at the loading location. Although these simulations utilized a linear elastic material model approximating un-ossified suture tissue, this was arbitrary as exact material properties were unavailable. It is theorized here that the material properties of these sutures may also be non-linear in time and may behave differently in compression than in tension. This is hypothesized as there is a reduced compliance in

compression due to the proximity of adjoining bone structures when compared to the range of tensile deformation that could occur before tissue failure. This is suggested as a future avenue of potential investigation to further model development towards a complete predictive model for ME procedures. The relaxation behavior of the MPS/IMS volume behaved as anticipated from the material adaptation development work seen in Chapter 2, with stress peaks appropriate to the applied strains significant relaxation within 2-minutes, and a trend towards a negligible modulus of elasticity as time progressed.

One of the limiting factors in this study was an inability to determine the placement of sutures or the degree of ossification in the sutures from the CT images due to their cubic 0.5mm voxel dimension. With regards to the MPS/IMS suture volume, this inhibited identifying the individual structures and assigning appropriate material properties. To remedy this, the MPS/IMS volume was manually given different material properties with the MPS being assigned the Prony model and the IMS being given the same properties as the surrounding bone. Despite the material discontinuity, the results showed an increased posterior expansion than the simulations with a singular material model for the MPS and IMS volume. Although expected, this highlights the need to understand the material properties of the non-MPS craniofacial sutures. When comparing the displacement results of the simulations that ran to completion to experimental data from the patient the geometry was based on, it is clear that the material properties of the IMS are critical to the future goal of a predictive computer model. This is due to where the simulations show the greatest expansion. The continuous MPS/IMS simulations show that there is more anterior motion (i.e. – the distance between the central incisors widens more than the distance between the 1<sup>st</sup> molars) while the discontinuous MPS/IMS simulation shows that there is more posterior motion. As noted by Wertz in 1970 [20], the posterior maxilla widens more than the anterior aspect. This has been reiterated in literature by Wertz et al. in 1977 [21] and Liu [18] in 2013.

The development of a partial skull model that incorporates an experimentally derived and tissue specific non-linear stress relaxation material model for the MPS is a considerable step forward in FEA studies of the ME procedure. Although the results of this are promising, this

study highlights new avenues of potential research in the developing material models for the other craniofacial sutures and determining the level of suture closure in CT images of patients. Current computational limitations such as processor speed, software licensing, and results data storage limit how many simulations are able to be solved. The 291 data points stored for these partial skull simulations over the simulated time span require just under 100GB of storage per case. Utilizing 2 cores of an i7 CPU running at 3.40 GHz took these models 2 days to solve, while a single test employing 10 cores of an Intel Xeon CPU running at 2.65GHz each still took 8 hours to solve.

Future work may be done to quantify and mathematically model how living cranial bones react to applied forces, and how the stresses within bone decrease over time as it reforms. This could be of high interest as simulated reaction forces could be used design criteria for developing new expanders and incorporating bone stress relaxation behavior could help improve treatment protocols in a predictive model. Additional future directions of study may look to understand how the degree of suture fusing affects expansion. As suture fusion would affect the material properties of any structure, a multi-variable set of simulations could help researchers, and eventually clinicians, understand how a patient will respond to an expansion protocol.

### **3.4.1 Simplifications and Assumptions Identified in this Study**

To simplify the design and preparation of this FEA study, the following assumptions and simplifications were made. First, the properties assigned to the cranial bone structures were assumed to be isotropic, linear, and homogenous. This was done as the particular bone properties would have been difficult to determine from the CT scans, as well as reducing the likelihood of numerical anomalies corrupting the deformation results of the simulation. Secondly, bone growth and reabsorption are not considered in these simulations[18], [19], [22], [23]. This was judged out of scope as this process would be extremely difficult to model accurately and as it was not the focus of this modelling study. Also, the applied displacements were directly applied to the loading location of the model, using the pitch of the screw jack of the hyrax-appliance. This neglects any deformation that may occur in the armature of a ME appliance. As reaction forces increase, these arms may absorb some of the expansion forces generated at the screw and deform acting as springs. As evaluation or generation of appliance design was not a direct focus of this study, this simplification was felt to be justifiable.

### 3.5 References

- [1] D. L. Romanyk, C. R. Collins, M. O. Lagravere, R. W. Toogood, P. W. Major, and J. P. Carey, "Role of the midpalatal suture in FEA simulations of maxillary expansion treatment for adolescents: A review," *Int. Orthod.*, vol. 11, no. 2, pp. 119–138, Jun. 2013.
- [2] D. L. Romanyk, S. S. Liu, R. Long, and J. P. Carey, "Considerations for determining relaxation constants from creep modeling of nonlinear suture tissue," *Int. J. Mech. Sci.*, vol. 85, pp. 179–186, Aug. 2014.
- [3] M. A. Miroue, "The Human Facial Sutures: A Morphologic and Histologic Study of Age Changes from 20 to 95 Years," Master of Science in Dentistry, University of Washington, 1975.
- [4] M. O. Lagravère, J. P. Carey, G. Heo, R. W. Toogood, and P. W. Major, "Transverse, vertical, and anteroposterior changes from bone-anchored maxillary expansion vs traditional rapid maxillary expansion: A randomized clinical trial," *Am. J. Orthod. Dentofacial Orthop.*, vol. 137, no. 3, pp. 304–305, Mar. 2010.
- [5] J. F. Barrett and N. Keat, "Artifacts in CT: Recognition and Avoidance," *RadioGraphics*, vol. 24, no. 6, pp. 1679–1691, Nov. 2004.
- [6] "ScanIP, +FE, +NURBS and +CAD Reference Guide." Simpleware Ltd., 2013.
- [7] K. L. Moore, *Clinically oriented anatomy*, 5th ed. Philadelphia : Lippincott Williams & Wilkins, c2006.
- [8] Q. Wang, A. L. Smith, D. S. Strait, B. W. Wright, B. G. Richmond, I. R. Grosse, C. D. Byron, and U. Zapata, "The Global Impact of Sutures Assessed in a Finite Element Model of a Macaque Cranium," *Anat. Rec. Adv. Integr. Anat. Evol. Biol.*, vol. 293, no. 9, pp. 1477–1491, Sep. 2010.
- [9] D. L. Romanyk, S. S. Liu, M. G. Lipsett, R. W. Toogood, M. O. Lagravère, P. W. Major, and J. P. Carey, "Towards a viscoelastic model for the unfused midpalatal suture: Development and validation using the midsagittal suture in New Zealand white Rabbits," *J. Biomech.*, vol. 46, no. 10, pp. 1618–1625, Jun. 2013.
- [10] "Ch. 13.1: Element Shape Testing," in *ANSYS® Academic Teaching Advanced, Release 14.5, Help System, Mechanical APDL Theory Reference*, .
- [11] "XV: N Commands - NSEL," in *ANSYS® Academic Teaching Advanced, Release 14.5, Help System, Mechanical APDL Command Reference*, .
- [12] Y. C. Fung, *Biomechanics : mechanical properties of living tissues /*, 2nd ed. New York : Springer-Verlag, 1993.

- [13] B. Ludwig, S. Baumgaertel, B. Zorkun, L. Bonitz, B. Glasl, B. Wilmes, and J. Lisson, "Application of a new viscoelastic finite element method model and analysis of miniscrew-supported hybrid hyrax treatment," *Am. J. Orthod. Dentofacial Orthop.*, vol. 143, no. 3, pp. 426–435, Mar. 2013.
- [14] P. Radhakrishnan and J. J. Mao, "Nanomechanical Properties of Facial Sutures and Sutural Mineralization Front," *J. Dent. Res.*, vol. 83, no. 6, pp. 470–475, Jun. 2004.
- [15] "Ch. 3.7.1: Viscoelastic Formulation," in *ANSYS® Academic Teaching Advanced, Release 14.5, Help System, Mechanical APDL Material Reference*, ANSYS, Inc.
- [16] "Ch. 5.2: Viscoelastic Material Curve Fitting," in *ANSYS® Academic Teaching Advanced, Release 14.5, Help System, Mechanical APDL Material Reference*, ANSYS, Inc.
- [17] J. Gamble, M. O. Lagravère, P. W. Major, and G. Heo, "New Statistical Method to Analyze Three-Dimensional Landmark Configurations Obtained with Cone-Beam CT: Basic Features and Clinical Application for Rapid Maxillary Expansion," *Korean J. Radiol.*, vol. 13, no. 2, pp. 126–135, 2012.
- [18] S. S.-Y. Liu, L. A. Opperman, H.-M. Kyung, and P. H. Buschang, "Is there an optimal force level for sutural expansion?," *Am. J. Orthod. Dentofacial Orthop.*, vol. 139, no. 4, pp. 446–455, Apr. 2011.
- [19] S. S.-Y. Liu, H. Xu, J. Sun, E. Kontogiorgos, P. R. Whittington, K. G. Misner, H.-M. Kyung, P. H. Buschang, and L. A. Opperman, "Recombinant human bone morphogenetic protein-2 stimulates bone formation during interfrontal suture expansion in rabbits," *Am. J. Orthod. Dentofacial Orthop.*, vol. 144, no. 2, pp. 210–217, Aug. 2013.
- [20] R. A. Wertz, "Skeletal and dental changes accompanying rapid midpalatal suture opening," *Am. J. Orthod.*, vol. 58, no. 1, pp. 41–66, Jul. 1970.
- [21] R. Wertz and M. Dreskin, "Midpalatal suture opening: A normative study," *Am. J. Orthod.*, vol. 71, no. 4, pp. 367–381, Apr. 1977.
- [22] B. Thilander, S. Nyman, T. Karring, and I. Magnusson, "Bone regeneration in alveolar bone dehiscences related to orthodontic tooth movements," *Eur. J. Orthod.*, vol. 5, no. 2, pp. 105–114, May 1983.
- [23] J. C. Danz, B. M. Bibby, C. Katsaros, and A. Stavropoulos, "Effects of facial tooth movement on the periodontium in rats: a comparison between conventional and low force," *J. Clin. Periodontol.*, vol. 43, no. 3, pp. 229–237, Mar. 2016.

## 4 Summary, Conclusions, Recommendations

By mechanically widening the upper jaw, orthodontists use maxillary expansion to alleviate dental malocclusions and alleviate nasal respiratory issues that can contribute to sleep apnea. This expansion is affected through the use of compressed springs, magnetic repulsion, shape memory alloy, or screw-jack appliances. In adolescents the midpalatal suture is still unfused enough that expansion can be done without additional surgical assistance. The suture is a soft tissue that has been found to behave viscoelastically under external forces.

The preceding chapters detailed work towards improving the quality of life of adolescents undergoing the orthodontic procedure of maxillary expansion through the application of engineering principles and finite element analysis. This was accomplished by adapting, for finite element analysis, two mathematical models that describe the non-linear creep and stress relaxation behavior of the midpalatal suture. The goals of this study were to adapt the two constitutive equations developed by Romanyk et al. [1], [2] for use in “ANSYS® Academic Teaching Advanced Mechanical APDL, Release 14.5.7” (ANSYS);, test and hopefully validate their behavior; and, incorporate the validated material model into a partial skull model and simulate a full expansion procedure. Also investigated were the effects of including additional craniofacial sutures in the partial skull geometry.

The non-linear creep [1] and stress relaxation [2] responses of this suture have previously been characterized as 1-D models based on initial conditions. Romanyk et al. validated the creep model against experimental force-expansion data while his relaxation model was mathematically derived from the creep model, as no stress-time data was available. The original creep model was detailed in eq. (1-3), while the original relaxation model was detailed in eq. (1-7).

#### 4.1 Modification of the 1-D Constitutive Equations

The original 1-D constitutive models do not characterize the collagen fiber-based soft tissue holding the sutures together, but rather they describe the behavior of a macroscopic bulk material behavior of a suture region that is comprised of bone and suture. The variable  $\gamma$  was derived to adjust the region's original width from 9.72mm to 1.72mm such that the midpalatal suture could be modelled in a partial skull with a reasonable initial width. An analogous spring-system comparison model was used to justify the assumption that the bone is significantly stiff to be ignored in the derivation of the  $\gamma$ -term, with a maximum difference between the  $\gamma$ -adjusted relaxation model and the spring model of 0.0439%. Of key concern was the assumed proportion of the 9.72mm width that could be said to be bone. A sensitivity analysis was performed, finding a change of 5.75% per 0.1mm of assumed bone width total (11.5% per 0.1 mm assumed of bone on each side of the suture). As actual width information was not available in the original Romanyk et al. paper [1] and that of Liu et al.[3], 4mm of bone per side was judged to be a reasonable assumption. This resulted in a  $\gamma$ -value of 0.17696 being used for all subsequent analysis.

#### 4.2 Adaptation of 1-D Creep Model for Finite Element Analysis

The 1-D creep model was encoded into the USERCREEP.f material subroutine for use with ANSYS 14.5. This material model was simulated using 3-D brick elements and 2-node bar elements. The bar elements were tested for use with rigid cross sectional areas or constant element volumes. Using a rectilinear testing geometry, these models simulated six weeks of time under constant applied expansion forces. The testing found that computational speeds were greatly increased when solving with the static solution engine compared to the dynamic solution engine. The dynamic engine was unnecessary when inertial effects are negligible for such slow motion and lack of impact loads. Using the  $\gamma$ -modified creep equation, the 2-node bar element with rigid cross sectional area was able to closely replicate the creep strain curve of the 1-D model (Figs. 2-18 to 2-20). However, the simulated system expansion greatly diverged from 1-D model expected expansion (Figs. 2-21 to 2-23). This was due to ANSYS calculating each subsequent expansion step based on the previous width, not the initial width. Tests of the  $\gamma$ -modified creep model, using the brick elements for the suture, failed after less

than 40 seconds of simulated time (Fig. 2-25). This was due to the necking induced stress increase, coupled with the above strain expansion calculation (Fig. 2-24). From these simulation results it was concluded that the finite element analysis adapted creep model should not be recommended for use in a partial skull finite element analysis in its current form. Additional training of the creep model could be done in the future, utilizing the rectilinear testing geometry as a tool in further development to take into account both material deformation and calculation of  $t_{n+1}$  based on  $t_n$  (not  $t_0$  as the 1-D model is based). This may require the creep model to be reformulated as a time and strain hardening model, not just as time hardening as it currently exists.

### 4.3 Adaptation of 1-D Relaxation Model for Finite Element Analysis

Unlike adapting the creep model by modifying a pre-built subroutine, the stress relaxation model was adapted for finite element analysis by curve fitting a Prony series approximation to datasets generated by the 1-D relaxation model. Utilizing the ANSYS curve fitting utility, the 7-term Prony series expansion was curve fit to the supplied data set with the lowest regression residual (0.0089837) of the 3-, 5-, 7-, and 9-term expansions attempted. Solve time for the 7-term fit was also 34% faster than the 9-term fit. An assumed 5-second appliance activation period prevented the 1-D relaxation model from approaching an infinite stress asymptote at  $t=0$ . To account for this, the 7-term Prony model was curve fit to a dataset that was time shifted by -4.99 seconds. Time shifting the dataset produced in finite element analysis simulations peak stresses that were closer to the expected results from the 1-D model than the non-time shifted curve fit. Although the time shifted peak stress was lower than expected, this was caused by relaxation during the load step which is not accounted for in the original 1-D model. After calculating an initial Young's modulus input for the Prony model using the strain from the 1<sup>st</sup> activation and the derived  $\beta$ -term, the Prony model was tested for 29 sequential step-wise applied displacements. The Prony model was tested using the rectilinear testing geometry automatically meshed with 3-D brick elements. Non-linear geometry options were enabled and the static solution engine was used. This simulated full expansion procedure produced stress peaks that relaxed within 2-minutes of each peak (Fig. 2-30 (B)). The peak magnitude for subsequent appliance activations was reduced as the change in applied strain

was lower for incremental appliance activations (Fig. 2-30 (A)). It was concluded that the non-linear time dependency of the 1-D stress relaxation model was adapted adequately for finite element analysis use in ANSYS. Further research could be focused on incorporating the non-linear strain dependency of the 1-D model.

#### **4.4 Partial Cranium Modelling Utilizing Relaxation Model**

A partial cranium model was developed using ScanIP software with the +FE module (Simpleware Ltd. Exeter, UK) from patient CT data provided by Manuel Lagravere. The CT dataset was from an adolescent who had been a maxillary expansion patient. CT images taken prior to the patient receiving their bone-borne screw-type expansion appliance were chosen for this study to eliminate metal artifacts [ref] found in image sets that were taken with the appliances installed. The partial skull model, having incorporated the midpalatal suture and additional Craniofacial Sutures (craniofacial sutures), was tested under stepwise applied displacements, loaded in the same location as the patient's bone-borne appliance.

The effect of the non-linear stress relaxation model on maxillary expansion was evaluated by simulating the model for multiple cases with different material models for the various sutures. It was found that there was virtually no difference in the final displacement of the 1<sup>st</sup> molar and central incisor between the simulation case where the midpalatal suture volume was unconstrained and the case where the midpalatal suture volume had the relaxation model applied. This was as expected as the Prony approximation, as with the 1-D model it is based on, relaxes towards a negligible modulus of elasticity as time increases. The key differences are the tensile stresses within the suture in the 2-minutes following the appliance activation, and the effect it has of shortly causing a peak on the reaction load forces at the expansion appliance. By causing this increase in reaction force, it indicates that the adapted stress relaxation model does have a global effect on the partial skull finite element analysis model. The stress within the volume of the suture itself behaved as expected following the 5-second application of expansion.

Although the cases that applied low stiffness linear elastic properties to the craniofacial sutures diverged after only a handful of appliance activations, the results they generated are intriguing.

They showed that a reduction in the stiffness of these structures had a great effect on the overall movement of the dentition, and a vastly reduced appliance reaction force. Future research should look towards characterizing the material properties of the other craniofacial sutures, be they viscoelastic, orthotropic, shear resistant, or increasingly stiff in compression due to the proximity of adjoining bone structures [4], [5].

The effect of simulating the model with an ossified Intermaxillary Suture (intermaxillary suture) with the midpalatal suture assigned the relaxation model was investigated. It was found that this increased 1<sup>st</sup> molar motion while limiting the central incisor movement. This was in accordance with prior publications which noted a v-shaped expanded midpalatal suture as the anterior teeth had greater motion than the posterior teeth [3]. It was then concluded that the material properties of the intermaxillary suture are of equal importance to that of the midpalatal suture.

The partial skull model that was developed during this study was able to implement the stress relaxation material model in a large degree of freedom simulation with a reasonable computational duration. Utilizing the static solver engine and 10-cores of an Intel Xeon CPU running at 2.65GHz it was possible to simulate 8 days of time for a 211K element model within 8 hours. This is very reasonable in comparison to the several days it took the dynamic solver on a single core of an Intel i7 CPU running at 3.4 GHz to solve half an hour of simulated time.

#### **4.5 Overall Conclusions**

This study partially met its original project goal of implementing the tissue specific non-linear material models created by Romanyk et al. for the midpalatal suture in a 3-D finite element simulation environment. The  $\gamma$ -derived term was justified for use to modify the 1-D constitutive equations for a narrower initial suture width. The creep model, although adapted for finite element analysis, was unable to produce the expected suture expansion results. Although able to replicate the expected creep strain profile using the rigid cross sectional area 2-node bar elements, the expansion was exceptionally divergent due to the underlying assumptions of the original 1-D model. The time dependent non-linearity of the stress relaxation model was adequately approximated in finite element analysis utilizing a time shifted 7-term Prony series

expansion for the generalized Maxwell viscoelastic model. The strain dependent non-linearity was only approximated for averaged initial activation conditions using the variable  $\beta$  and was not an active variable during the course of the simulations. The analysis presented in this thesis determined that the static solution engine in ANSYS was appropriate for use with the two non-linear material models as the system can be assumed as pseudo-static due to lack of high accelerations or impact loads.

The adapted stress relaxation model was incorporated in a partial skull simulation and subjected to a clinically relevant stepwise expansion protocol. Displacement results made it apparent that the stress relaxation is unlikely to affect the final displacement of the teeth. However, the non-linear tissue model does affect their position in the two minutes following each activation as the suture relaxes. The reaction force results illustrated that the stress relaxation in the suture does have an effect on the compressive forces experienced by the expansion appliance.

#### **4.6 Future Work**

Much like any work of research there is an amount of development research that could potentially rectify the deficiencies of this study, and there is the opportunity to build upon this study's successes in the development of a predictive finite element analysis model for maxillary expansion.

Further development of the creep model for finite element analysis could utilize the rectilinear testing geometry testing geometry to refine the coefficients to train the existing model to better replicate in 3-D the expansion profile of the original 1-D model or the original experimental data. This platform could also be used to attempt determine coefficients to a model that hardens with strain and with time.

Incorporating the non-linear strain dependency of the original 1-D stress relaxation model into the approximated model for finite element analysis would be a good avenue to explore in future research. This would increase the accuracy of the model for different applied strains

throughout the simulation as well as reducing the amount of model setup required for future researchers or clinicians.

As observed in evaluating the displacement results and reaction forces in the partial skull model, it is recommended that additional tissue specific material properties be characterized for future skull simulations. Among these are craniofacial sutures such as the intermaxillary, frontozygomatic, zygomaticotemporal, zygomaticomaxillary, and nasal sutures. As previously alluded to, these material properties may differ in shear, compression, or tension due to the interdigitization of the bones and like the midpalatal suture may have non-linear properties as well. The reformation of the cranial bones during expansion may result in viscoelastic material responses such as stress relaxation. If the relaxation response of these bones could be characterized through experiments and mathematical modelling, it could be incorporated in any future models. This has previously been suggested by Romanyk et al.[6], and has been attempted using an arbitrary, non-tissue specific viscoelastic model by Ludwig et al.[7] This modification to the partial skull simulations could potentially reduce the unrealistically high reaction forces calculated during this study.

## 4.7 References

- [1] D. L. Romanyk, S. S. Liu, M. G. Lipsett, R. W. Toogood, M. O. Lagravère, P. W. Major, and J. P. Carey, "Towards a viscoelastic model for the unfused midpalatal suture: Development and validation using the midsagittal suture in New Zealand white Rabbits," *J. Biomech.*, vol. 46, no. 10, pp. 1618–1625, Jun. 2013.
- [2] D. L. Romanyk, S. S. Liu, R. Long, and J. P. Carey, "Considerations for determining relaxation constants from creep modeling of nonlinear suture tissue," *Int. J. Mech. Sci.*, vol. 85, pp. 179–186, Aug. 2014.
- [3] S. C. Jasinowski, B. D. Reddy, K. K. Louw, and A. Chinsamy, "Mechanics of cranial sutures using the finite element method," *J. Biomech.*, vol. 43, no. 16, pp. 3104–3111, Dec. 2010.
- [4] A. Maloul, J. Fialkov, D. Wagner, and C. M. Whyne, "Characterization of craniofacial sutures using the finite element method," *J. Biomech.*, vol. 47, no. 1, pp. 245–252, Jan. 2014.
- [5] S. S.-Y. Liu, L. A. Opperman, H.-M. Kyung, and P. H. Buschang, "Is there an optimal force level for sutural expansion?," *Am. J. Orthod. Dentofacial Orthop.*, vol. 139, no. 4, pp. 446–455, Apr. 2011.
- [6] D. L. Romanyk, C. R. Collins, M. O. Lagravere, R. W. Toogood, P. W. Major, and J. P. Carey, "Role of the midpalatal suture in FEA simulations of maxillary expansion treatment for adolescents: A review," *Int. Orthod.*, vol. 11, no. 2, pp. 119–138, Jun. 2013.
- [7] B. Ludwig, S. Baumgaertel, B. Zorkun, L. Bonitz, B. Glasl, B. Wilmes, and J. Lisson, "Application of a new viscoelastic finite element method model and analysis of miniscrew-supported hybrid hyrax treatment," *Am. J. Orthod. Dentofacial Orthop.*, vol. 143, no. 3, pp. 426–435, Mar. 2013.

## Bibliography

- Angell, EH. "Treatment of Irregularity of the Permanent or Adult Teeth. Part 1." *The Dental Cosmos* 1 (1860): 540–44.
- Angell, EH. "Treatment of Irregularity of the Permanent or Adult Teeth. Part 2." *The Dental Cosmos* 1 (1860): 540–44.
- Barrett, Julia F., and Nicholas Keat. "Artifacts in CT: Recognition and Avoidance." *RadioGraphics* 24, no. 6 (November 1, 2004): 1679–91. doi:10.1148/rg.246045065.
- Bathe, Klaus-Jürgen. *Finite Element Procedures*. Upper Saddle River, N.J. : Prentice Hall, c1996.
- Boresi, Arthur P. *Advanced Mechanics of Materials*. 6th ed. New York : John Wiley & Sons, c2003.
- Burrows, Annie M., Joan T. Richtsmeier, Mark P. Mooney, Tim D. Smith, H. Wolfgang Losken, and Michael I. Siegel. "Three-Dimensional Analysis of Craniofacial Form in a Familial Rabbit Model of Nonsyndromic Coronal Suture Synostosis Using Euclidean Distance Matrix Analysis." *The Cleft Palate-Craniofacial Journal* 36, no. 3 (May 1, 1999): 196–206. doi:10.1597/1545-1569(1999)036<0196:TAOCFI>2.3.CO;2.
- "Ch. 1.10: Compiling and Linking UPFs on Windows Systems." In *ANSYS® Academic Teaching Advanced, Release 14.5, Help System, Mechanical APDL Programmer's Reference II: Guide to User-Programmable Features*, n.d.
- "Ch. 2: Material Model Element Support." In *ANSYS® Academic Teaching Advanced, Release 14.5, Help System, Mechanical APDL Material Reference*, n.d.
- "Ch. 3.5.5: Creep." In *ANSYS® Academic Teaching Advanced, Release 14.5, Help System, Mechanical APDL Material Reference*, n.d.
- "Ch. 3.7.1: Viscoelastic Formulation." In *ANSYS® Academic Teaching Advanced, Release 14.5, Help System, Mechanical APDL Material Reference*. ANSYS, Inc., n.d.

“Ch. 5.2: Viscoelastic Material Curve Fitting.” In *ANSYS® Academic Teaching Advanced, Release 14.5, Help System, Mechanical APDL Material Reference*. ANSYS, Inc., n.d.

“Ch. 13.1: Element Shape Testing.” In *ANSYS® Academic Teaching Advanced, Release 14.5, Help System, Mechanical APDL Theory Reference*, n.d.

“Ch. 15.12.2: Convergence.” In *ANSYS® Academic Teaching Advanced, Release 14.5, Help System, Mechanical APDL Theory Reference*, n.d.

“Ch. 17.1: Static Analysis.” In *ANSYS® Academic Teaching Advanced, Release 14.5, Help System, Mechanical APDL Theory Reference*, n.d.

“Ch. 17.2: Transient Analysis.” In *ANSYS® Academic Teaching Advanced, Release 14.5, Help System, Mechanical APDL Theory Reference*, n.d.

Cielo, Christopher M., and Anil Gungor. “Treatment Options for Pediatric Obstructive Sleep Apnea.” *Current Problems in Pediatric and Adolescent Health Care, Updates on Obstructive Sleep Apnea Syndrome*, 46, no. 1 (January 2016): 27–33.  
doi:10.1016/j.cppeds.2015.10.006.

Culea, Laurențiu, and Cristina Bratu. “Stress Analysis of the Human Skull due to the Insertion of Rapid Palatal Expander with Finite Element Analysis (FEA).” *Key Engineering Materials* 399 (2009): 211–18. doi:10.4028/www.scientific.net/KEM.399.211.

Danz, Jan C., Bo M. Bibby, Christos Katsaros, and Andreas Stavropoulos. “Effects of Facial Tooth Movement on the Periodontium in Rats: A Comparison between Conventional and Low Force.” *Journal of Clinical Periodontology* 43, no. 3 (March 1, 2016): 229–37.  
doi:10.1111/jcpe.12505.

Fung, Y. C. *Biomechanics : Mechanical Properties of Living Tissues /*. 2nd ed. New York : Springer-Verlag, 1993.

Gamble, Jennifer, Manuel O. Lagravère, Paul W. Major, and Giseon Heo. “New Statistical Method to Analyze Three-Dimensional Landmark Configurations Obtained with Cone-

- Beam CT: Basic Features and Clinical Application for Rapid Maxillary Expansion." *Korean Journal of Radiology* 13, no. 2 (2012): 126–35. doi:10.3348/kjr.2012.13.2.126.
- Gautam, Pawan, Ashima Valiathan, and Raviraj Adhikari. "Stress and Displacement Patterns in the Craniofacial Skeleton with Rapid Maxillary Expansion: A Finite Element Method Study." *American Journal of Orthodontics and Dentofacial Orthopedics* 132, no. 1 (July 2007): 5.e1-5.e11. doi:10.1016/j.ajodo.2006.09.044.
- Holberg, Christof, Nikola Holberg, Katja Schwenzer, Andrea Wichelhaus, and Ingrid Rudzki-Janson. "Biomechanical Analysis of Maxillary Expansion in CLP Patients." *The Angle Orthodontist* 77, no. 2 (March 1, 2007): 280–87. doi:10.2319/0003-3219(2007)077[0280:BAOMEI]2.0.CO;2.
- Holberg, Christof, Luai Mahaini, and Ingrid Rudzki. "Analysis of Sutural Strain in Maxillary Protraction Therapy." *The Angle Orthodontist* 77, no. 4 (July 1, 2007): 586–94. doi:10.2319/090505-312.
- Işeri, H., A.E. Tekkaya, Ö. Öztan, and S. Bilgiç. "Biomechanical Effects of Rapid Maxillary Expansion on the Craniofacial Skeleton, Studied by the Finite Element Method." *European Journal of Orthodontics* 20, no. 4 (1998): 347–56.
- Jafari, Alireza, K. Sadashiva Shetty, and Mohan Kumar. "Study of Stress Distribution and Displacement of Various Craniofacial Structures Following Application of Transverse Orthopedic Forces—A Three-Dimensional FEM Study." *The Angle Orthodontist* 73, no. 1 (February 1, 2003): 12–20. doi:10.1043/0003-3219(2003)073<0012:SOSDAD>2.0.CO;2.
- Jasinowski, S. C., B. D. Reddy, K. K. Louw, and A. Chinsamy. "Mechanics of Cranial Sutures Using the Finite Element Method." *Journal of Biomechanics* 43, no. 16 (December 1, 2010): 3104–11. doi:10.1016/j.jbiomech.2010.08.007.
- Johnson, T. P. M., S. Socrate, and M. C. Boyce. "A Viscoelastic, Viscoplastic Model of Cortical Bone Valid at Low and High Strain Rates." *Acta Biomaterialia* 6, no. 10 (October 2010): 4073–80. doi:10.1016/j.actbio.2010.04.017.

- Knaup, Britta, Faruk Yildizhan, and Prof Dr Dr Heiner Wehrbein. "Age-Related Changes in the Midpalatal Suture." *Journal of Orofacial Orthopedics / Fortschritte Der Kieferorthopädie* 65, no. 6 (November 1, 2004): 467–74. doi:10.1007/s00056-004-0415-y.
- Lagravère, Manuel O., Jason P. Carey, Giseon Heo, Roger W. Toogood, and Paul W. Major. "Transverse, Vertical, and Anteroposterior Changes from Bone-Anchored Maxillary Expansion vs Traditional Rapid Maxillary Expansion: A Randomized Clinical Trial." *American Journal of Orthodontics and Dentofacial Orthopedics* 137, no. 3 (March 2010): 304–5. doi:10.1016/j.ajodo.2009.10.004.
- Lagravère, M. O., P. W. Major, and C. Flores-Mir. "Dental and Skeletal Changes Following Surgically Assisted Rapid Maxillary Expansion." *International Journal of Oral and Maxillofacial Surgery* 35, no. 6 (June 2006): 481–87. doi:10.1016/j.ijom.2006.01.025.
- Lee, Haofu, Kang Ting, Michael Nelson, Nichole Sun, and Sang-Jin Sung. "Maxillary Expansion in Customized Finite Element Method Models." *American Journal of Orthodontics and Dentofacial Orthopedics* 136, no. 3 (September 2009): 367–74. doi:10.1016/j.ajodo.2008.08.023.
- Liu, Sean Shih-Yao, Lynne A. Opperman, Hee-Moon Kyung, and Peter H. Buschang. "Is There an Optimal Force Level for Sutural Expansion?" *American Journal of Orthodontics and Dentofacial Orthopedics* 139, no. 4 (April 2011): 446–55. doi:10.1016/j.ajodo.2009.03.056.
- Liu, Sean Shih-Yao, Haisong Xu, Jun Sun, Elias Kontogiorgos, Patrick R. Whittington, Kenner G. Misner, Hee-Moon Kyung, Peter H. Buschang, and Lynne A. Opperman. "Recombinant Human Bone Morphogenetic Protein-2 Stimulates Bone Formation during Interfrontal Suture Expansion in Rabbits." *American Journal of Orthodontics and Dentofacial Orthopedics* 144, no. 2 (August 2013): 210–17. doi:10.1016/j.ajodo.2013.03.017.
- Ludwig, Björn, Sebastian Baumgaertel, Berna Zorkun, Lars Bonitz, Bettina Glasl, Benedict Wilmes, and Jörg Lisson. "Application of a New Viscoelastic Finite Element Method Model and Analysis of Miniscrew-Supported Hybrid Hyrax Treatment." *American Journal of*

*Orthodontics and Dentofacial Orthopedics* 143, no. 3 (March 2013): 426–35.  
doi:10.1016/j.ajodo.2012.07.019.

Maloul, Asmaa, Jeffrey Fialkov, Diane Wagner, and Cari M. Whyne. "Characterization of Craniofacial Sutures Using the Finite Element Method." *Journal of Biomechanics* 47, no. 1 (January 3, 2014): 245–52. doi:10.1016/j.jbiomech.2013.09.009.

Miroue, Michael Andrew. "The Human Facial Sutures: A Morphologic and Histologic Study of Age Changes from 20 to 95 Years." Master of Science in Dentistry, University of Washington, 1975.

Moin, Parviz. *Fundamentals of Engineering Numerical Analysis*. 2nd ed. New York : Cambridge University Press, 2010., 2010.

Moore, Keith L. *Clinically Oriented Anatomy*. 5th ed. Philadelphia : Lippincott Williams & Wilkins, c2006.

Persson, Maurits, and Birgit Thilander. "Palatal Suture Closure in Man from 15 to 35 Years of Age." *American Journal of Orthodontics* 72, no. 1 (July 1, 1977): 42–52. doi:10.1016/0002-9416(77)90123-3.

Provatidis, C. G., B. Georgiopoulos, A. Kotinas, and J. P. McDonald. "Evaluation of Craniofacial Effects during Rapid Maxillary Expansion through Combined in Vivo/in Vitro and Finite Element Studies." *The European Journal of Orthodontics* 30, no. 5 (October 1, 2008): 437–48. doi:10.1093/ejo/cjn046.

Provatidis, C., B. Georgiopoulos, A. Kotinas, and J. P. MacDonald. "In Vitro Validated Finite Element Method Model for a Human Skull and Related Craniofacial Effects during Rapid Maxillary Expansion." *Proceedings of the Institution of Mechanical Engineers, Part H: Journal of Engineering in Medicine* 220, no. 8 (August 1, 2006): 897–907.  
doi:10.1243/09544119JEIM92.

- Provatidis, C., B. Georgiopoulos, A. Kotinas, and J. P. McDonald. "On the FEM Modeling of Craniofacial Changes during Rapid Maxillary Expansion." *Medical Engineering & Physics* 29, no. 5 (June 2007): 566–79. doi:10.1016/j.medengphy.2006.03.007.
- Provatidis, C., B. Georgiopoulos, A. Kotinas, and J.P. McDonald. "In-Vitro Validation of a FEM Model for Craniofacial Effects during Rapid Maxillary Expansion," 68–73, 2003.
- Radhakrishnan, P., and J. J. Mao. "Nanomechanical Properties of Facial Sutures and Sutural Mineralization Front." *Journal of Dental Research* 83, no. 6 (June 1, 2004): 470–75. doi:10.1177/154405910408300607.
- Rice, David P., ed. *Craniofacial Sutures: Development, Disease and Treatment*. Vol. 12. *Frontiers of Oral Biology*. Basel; New York: Karger, 2008.
- Romanyk, D. L., M. O. Lagravere, R. W. Toogood, P. W. Major, and J. P. Carey. "Review of Maxillary Expansion Appliance Activation Methods: Engineering and Clinical Perspectives." *Journal of Dental Biomechanics* 1, no. 1 (January 1, 2010): 496906–496906. doi:10.4061/2010/496906.
- Romanyk, D. L., S. S. Liu, M. G. Lipsett, M. O. Lagravere, R. W. Toogood, P. W. Major, and J. P. Carey. "Incorporation of Stress-Dependency in the Modeling of Midpalatal Suture Behavior During Maxillary Expansion Treatment," June 26, 2013, V01BT55A002. doi:10.1115/SBC2013-14034.
- Romanyk, D. L., S. S. Liu, M. G. Lipsett, R. W. Toogood, M. O. Lagravère, P. W. Major, and J. P. Carey. "Towards a Viscoelastic Model for the Unfused Midpalatal Suture: Development and Validation Using the Midsagittal Suture in New Zealand White Rabbits." *Journal of Biomechanics* 46, no. 10 (June 21, 2013): 1618–25. doi:10.1016/j.jbiomech.2013.04.011.
- Romanyk, D. L., C. Shim, S. S. Liu, M. O. Lagravere, P. W. Major, and J. P. Carey. "Viscoelastic Response of the Midpalatal Suture during Maxillary Expansion Treatment." *Orthodontics & Craniofacial Research* 19, no. 1 (February 1, 2016): 28–35. doi:10.1111/ocr.12106.

Romanyk, Dan L., Caroline R. Collins, Manuel O. Lagravere, Roger W. Toogood, Paul W. Major, and Jason P. Carey. "Role of the Midpalatal Suture in FEA Simulations of Maxillary Expansion Treatment for Adolescents: A Review." *International Orthodontics* 11, no. 2 (June 2013): 119–38. doi:10.1016/j.ortho.2013.02.001.

Romanyk, Dan L., Sean S. Liu, Rong Long, and Jason P. Carey. "Considerations for Determining Relaxation Constants from Creep Modeling of Nonlinear Suture Tissue." *International Journal of Mechanical Sciences* 85 (August 2014): 179–86. doi:10.1016/j.ijmecsci.2014.05.022.

"ScanIP, +FE, +NURBS and +CAD Reference Guide." Simpleware Ltd., 2013.

Serpe, Larissa Carvalho Trojan, Las Casas, Estevam Barbosa De, Ana Cláudia Moreira Melo Toyofuku, Libardo Andrés González-Torres, Larissa Carvalho Trojan Serpe, Las Casas, Estevam Barbosa De, Ana Cláudia Moreira Melo Toyofuku, and Libardo Andrés González-Torres. "A Bilinear Elastic Constitutive Model Applied for Midpalatal Suture Behavior during Rapid Maxillary Expansion." *Research on Biomedical Engineering* 31, no. 4 (December 2015): 319–27. doi:10.1590/2446-4740.0637.

Serpe, L.C.T., L.A. González-Torres, R.L. Utsch, A.C.M. Melo, and Las Casas De. "Evaluation of the Mechanical Environment of the Median Palatine Suture during Rapid Maxillary Expansion," 63–68, 2014.

Serpe, L.C.T., L.A.G. Torres, Freitas Pinto De, A.C.M.M. Toyofuku, and Las Casas De. "Maxillary Biomechanical Study during Rapid Expansion Treatment with Simplified Model." *Journal of Medical Imaging and Health Informatics* 4, no. 1 (2014): 137–41. doi:10.1166/jmihi.2014.1233.

Thilander, Birgit, Sture Nyman, Thorkild Karring, and Ingvar Magnusson. "Bone Regeneration in Alveolar Bone Dehiscences Related to Orthodontic Tooth Movements." *The European Journal of Orthodontics* 5, no. 2 (May 1, 1983): 105–14. doi:10.1093/ejo/5.2.105.

Wang, Qian, Amanda L. Smith, David S. Strait, Barth W. Wright, Brian G. Richmond, Ian R. Grosse, Craig D. Byron, and Uriel Zapata. "The Global Impact of Sutures Assessed in a Finite Element Model of a Macaque Cranium." *The Anatomical Record: Advances in Integrative Anatomy and Evolutionary Biology* 293, no. 9 (September 1, 2010): 1477–91. doi:10.1002/ar.21203.

Wertz, Robert A. "Skeletal and Dental Changes Accompanying Rapid Midpalatal Suture Opening." *American Journal of Orthodontics* 58, no. 1 (July 1, 1970): 41–66. doi:10.1016/0002-9416(70)90127-2.

Wertz, Robert, and Michael Dreskin. "Midpalatal Suture Opening: A Normative Study." *American Journal of Orthodontics* 71, no. 4 (April 1, 1977): 367–81. doi:10.1016/0002-9416(77)90241-X.

"XV: N Commands - NSEL." In *ANSYS® Academic Teaching Advanced, Release 14.5, Help System, Mechanical APDL Command Reference*, n.d.

## Appendix A - APDL Code for Meshing and Testing RTG Models

This appendix contains example APDL code used for testing the adapted creep and relaxation models.

### A.1 Code for the RTG Model with a 2-Node Bar Element Suture – Creep Testing

```
!Change Working Directory to Specified Location
/cwd,'F:\WEPA-1 Backup\LINK 180 Tests with Gamma and AVG Coefficients\LINK
180 Tests (200g) - Rigid Cross Section'
!Clear Information in Directory Prior to Run
/clear
!Start preprocessing phase
/prep7

!*****
!Add Annotations
!Add Title and Subtitle to All Outputs
/title,Usercreep.f Suture Model -Link 180- Gamma and Avg Coeff
/stitle,1, 200 g Test - Rigid Cross Section
!Define Units to Annotate Results
/units,mpa

!*****
!Define Geometries

!##### Dimensional Parameters
!Suture Length (mm)
Lt=24.4
!Suture Thickness (mm)
tt=2.19
!Suture Width (mm)
wt=(9.2-2*4)/2
!Bone width (mm)
wb=1

!##### Applied Forces
springforce=200          !in grams
springforce=springforce*9.81/1000    !in newtons
*set,SPRINGFORCE_200,springforce/1000    !Newtons/Node

!*****
!Define Materials, Element Types, Real Constants, Etc.

!#####
!Material Type 1 (Linear Elastic Bone)
et,1,solid185
mp,dens,1,1000
```

```

mp,ex,1,20000          !Define Young's Modulus
mp,prxy,1,0.46         !Define Poisson's Ratio

#####
!Material Type 2 (UserCreep, using 50g coefficients)
et,2,link180
mp,dens,2,1000         !Define Density
mp,ex,2,1.27          !Define Young's Modulus
!mp,prxy,2,0.42       !Define Poisson's Ratio

!!!!!!!Keyoption 2 for Link180 will: 0)Enforce Incompressibility OR
1)Enforce rigid cross section
Keyopt,2,2,1
SECTYPE,,LINK
SECDATA,(Lt*tt)/1000

!Define Material Model
!tb,lab,mat numb,number of temps(default 1, max 1000),
!- number of data points/coefficients specified for a given temp (default 12
for implicit creep, max 1000),
!- tbopt (0 = explicit, 1-13 implicit creep equations, 100=usercreep),
eosopt, funcname

tb,creep,2,1,6,100     !material=2, nmtemp=1, npnts=4, tbopt=usercreep
!Define Temperature Point 1
tbtemp,100
*set,c1_200,1.12457
*set,c2_200,0.4912
*set,c3_200,0.4894
*set,c4_200,c1_200
*set,c5_200,c2_200
*set,c6_200,c3_200

!Define Coefficients at Previously Defined Temperature Point
tbdata,1,c1_200,c2_200,c3_200,c4_200,c5_200,c6_200          !tbdata,starting
location,c1,c2,c3,c4,c5,c6

##### Solid 1
!Generate Node List for Suture
N,1000,0,0,0
N,1010,0,0,tt
FILL
NGEN,100,10,1000,1010,,0,Lt/100,0
NGEN,2,1000,1000,1999,,wt,0,0

!Select 2nd material (50g suture) and element type to mesh
mat,2
type,2
e,1000,2000

```

```

EGEN,10,1,1
EGEN,100,10,1,10

NGEN,3,1000,2000,2999,,1,0,0

mat,1
type,1
e,2000,3000,3001,2001,2010,3010,3011,2011
EGEN,9,1,1001
EGEN,99,10,1001,1009
EGEN,2,1000,1001,1891

!*****
!finish preprocessing phase
finish

!enter processing phase
/solu

!*****
antype,static
outres,all,-100
nlgeo,on

!*****
!First Load Step, Apply Mechanical Loading
Rate,off
time,1.0e-8

!define symmetry boundary conditions
!select nodes for BCs
nsel,s,node,,1000,1999
d,all,ux,0
!reselect all nodes
nsel,all

!define applied forces/pressures
nsel,s,node,,4000,4999
D,ALL,UY,0
D,ALL,UZ,0
F,ALL,FX,SPRINGFORCE_200
!reselect all areas
nsel,all

solv

!*****
!Turning on Creep Calculations
rate,on

```

```

time,6*7*24*60*60      !Time in seconds, first term is number of weeks
!time,12*60*60
!time,1800
!crplim,0.1,1
!deltim,10,2,30
deltim,0.0001,0.0001,3600

!define symmetry boundary conditions
!select nodes for BCs
nselect,s,node,,1000,1999
d,all,ux,0
!reselect all nodes
nselect,all

!define applied forces/pressures
nselect,s,node,,4000,4999
D,ALL,UY,0
D,ALL,UZ,0
F,ALL,FX,SPRINGFORCE_200
!reselect all areas
nselect,all

solve

!exit processing phase
finish

!enter static post-processing phase
/post1

```

## A.2 Code for the RTG Model with a Brick Element Suture – Creep Testing

```

!Change Working Directory to Specified Location
/cwd,'F:\WEPA-1 Backup\UserCreep - 6 week trial - Avg Coeff - Static'
!Clear Information in Directory Prior to Run
/clear

!Start preprocessing phase
/prep7

!*****
!Add Annotations

!Add Title and Subtitle to All Outputs
/title,Usercreep.f Suture Model -6 Week - Avg Coeff - Static Solver
/stitle,UserCreep - MST Model 6 week Test

!Define Units to Annotate Results
/units,mpa

```

```

!*****
!Define Geometries
!##### Dimensional Parameters
!Suture Length (mm)
Lt=24.4/2
!Suture Thickness (mm)
tt=2.19
!Suture Width (mm)
wt=(9.2-2*4)/2
!Bone width (mm)
wb=2

!##### Applied Forces (Corrected for the reduced area)
springforce=50          !in grams
springforce=springforce*9.81/1000  !in newtons
*set,engseqv_50,springforce/(2*tt*Lt)    !in MPa

springforce=100        !in grams
springforce=springforce*9.81/1000  !in newtons
*set,engseqv_100,springforce/(2*tt*Lt)  !in MPa

springforce=200        !in grams
springforce=springforce*9.81/1000  !in newtons
*set,engseqv_200,springforce/(2*tt*Lt)  !in MPa
!##### Solid 1
!Volume 1 (Suture)
blc4,0,0,wt,Lt,tt
!Volume 2 (Bone)
blc4,wt,0,wb,Lt,tt
!Glue Volume Geometeries Togethet
vglue,1,2

!##### Solid 2
!Volume 3 (Suture)
blc4,0,Lt+1,wt,Lt,tt
!Volume 4 (Bone)
blc4,wt,Lt+1,wb,Lt,tt
!Glue Volume Geometeries Togethet
vglue,2,4

!##### Solid 3
!Volume 5 (Suture)
blc4,0,2*Lt+2,wt,Lt,tt
!Volume 6 (Bone)
blc4,wt,2*Lt+2,wb,Lt,tt
!Glue Volume Geometeries Togethet
vglue,4,6

```

```

!*****
!Define Materials, Element Types, Real Constants, Etc.

#####
!Material Type 1 (Linear Elastic Bone)
et,1,solid186
mp,dens,1,1000
mp,ex,1,20000          !Define Young's Modulus
mp,prxy,1,0.46        !Define Poisson's Ratio

#####
!Material Type 2 (UserCreep, using 50g coefficients)
et,2,solid186
mp,dens,2,1000        !Define Density
mp,ex,2,1.27          !Define Young's Modulus
mp,prxy,2,0.42        !Define Poisson's Ratio

!Define Material Model
!tb,lab,mat numb,number of temps(default 1, max 1000),
!- number of data points/coefficients specified for a given temp (default 12
for implicit creep, max 1000),
!- tbopt (0 = explicit, 1-13 implicit creep equations, 100=usercreep),
eosopt, funcname

tb,creep,2,1,6,100    !material=2, nmtemp=1, npnts=4, tbopt=usercreep
!Define Temperature Point 1
tbtemp,100
!*set,c1_50,1.0981
!*set,c2_50,0.5777
!*set,c3_50,0.5211
!*set,c4_50,c1_50
!*set,c5_50,c2_50
!*set,c6_50,c3_50

!Define Coefficients at Previously Defined Temperature Point
!tbdata,1,c1_50,c2_50,c3_50,c4_50,c5_50,c6_50          !tbdata,starting
location,c1,c2,c3,c4,c5,c6

#####
!Material Type 3 (UserCreep, using 100g coefficients)
et,3,solid186
mp,dens,3,1000        !Define Density
mp,ex,3,1.27          !Define Young's Modulus
mp,prxy,3,0.42        !Define Poisson's Ratio

!Define Material Model
!tb,lab,mat numb,number of temps(default 1, max 1000),
!- number of data points/coefficients specified for a given temp (default 12
for implicit creep, max 1000),

```

```

!- tbopt (0 = explicit, 1-13 implicit creep equations, 100=usercreep),
eosopt, funcname

tb,creep,3,1,6,100      !material=2, nmtemp=1, npnts=4, tbopt=usercreep

!Define Temperature Point 1
tbtemp,100
!*set,c1_100,1.1275
!*set,c2_100,0.5077
!*set,c3_100,0.4634
!*set,c4_100,c1_100
!*set,c5_100,c2_100
!*set,c6_100,c3_100

!Define Coefficients at Previously Defined Temperature Point
!tbdata,1,c1_100,c2_100,c3_100,c4_100,c5_100,c6_100      !tbdata,starting
location,c1,c2,c3,c4,c5,c6

#####
!Material Type 4 (UserCreep, using 200g coefficients)
et,4,solid186
mp,dens,4,1000      !Define Density
mp,ex,4,1.27      !Define Young's Modulus
mp,prxy,4,0.42      !Define Poisson's Ratio

!Define Material Model
!tb,lab,mat numb,number of temps(default 1, max 1000),
!- number of data points/coefficients specified for a given temp (default 12
for implicit creep, max 1000),
!- tbopt (0 = explicit, 1-13 implicit creep equations, 100=usercreep),
eosopt, funcname

tb,creep,4,1,6,100      !material=2, nmtemp=1, npnts=4, tbopt=usercreep

!Define Temperature Point 1
tbtemp,100
!*set,c1_200,1.1481
!*set,c2_200,0.3883
!*set,c3_200,0.4837
!*set,c4_200,c1_200
!*set,c5_200,c2_200
!*set,c6_200,c3_200

!Define Coefficients at Previously Defined Temperature Point
!tbdata,1,c1_200,c2_200,c3_200,c4_200,c5_200,c6_200      !tbdata,starting
location,c1,c2,c3,c4,c5,c6

#####
!*****

```

!Mesh The Geometries

!Select 1st material (bone) and element type to mesh

```
mat,1
type,1
vsel,s,,,3,3,1
esize,1
vmesh,all
vsel,all
```

```
mat,1
type,1
vsel,s,,,5,5,1
esize,1
vmesh,all
vsel,all
```

```
mat,1
type,1
vsel,s,,,7,7,1
esize,1
vmesh,all
vsel,all
```

!Select 2nd material (50g suture) and element type to mesh

```
mat,2
type,2
vsel,s,,,1,1,1
esize,0.2
vmesh,all
vsel,all
```

!Select 3rd material (100g suture) and element type to mesh

```
mat,3
type,3
vsel,s,,,2,2,1
esize,0.2
vmesh,all
vsel,all
```

!Select 2nd material (50g suture) and element type to mesh

```
mat,4
type,4
vsel,s,,,4,4,1
esize,0.2
vmesh,all
vsel,all
```

```

!*****

!finish preprocessing phase
finish

!enter processing phase
/solu

!*****
antype,static
outres,all,-500
nlgeo,on

!*****
!First Load Step, Apply Mechanical Loading
Rate,off
time,1.0e-8

!define boundary conditions
!select areas for BCs
asel,s,,5,5,1
da,all,symm
!reselect all areas
asel,all

!define boundary conditions
!select areas for BCs
asel,s,,11,11,1
da,all,symm
!reselect all areas
asel,all

!define boundary conditions
!select areas for BCs
asel,s,,22,22,1
da,all,symm
!reselect all areas
asel,all

!define applied forces/pressures
asel,s,,12,12,1
da,all,uy,0
da,all,uz,0
sfa,all,,pres,-engseqv_50
!reselect all areas
asel,all

!define applied forces/pressures

```

```

asel,s,,,23,23,1
da,all,uy,0
da,all,uz,0
sfa,all,,pres,-engseqv_100
!reselect all areas
asel,all

!define applied forces/pressures
asel,s,,,34,34,1
da,all,uy,0
da,all,uz,0
sfa,all,,pres,-engseqv_200
!reselect all areas
asel,all
solv

!*****
!Turning on Creep Calculations
rate,on
time,6*7*24*60*60      !Time in seconds, first term is number of weeks
!time,12*60*60
!time,1800
!crplim,0.1,1
!deltim,10,2,30
deltim,0.0001,0.0001,3600

!define boundary conditions
!select areas for BCs
asel,s,,,5,5,1
da,all,symm
!reselect all areas
asel,all

!define boundary conditions
!select areas for BCs
asel,s,,,11,11,1
da,all,symm
!reselect all areas
asel,all

!define boundary conditions
!select areas for BCs
asel,s,,,22,22,1
da,all,symm
!reselect all areas
asel,all

!define applied forces/pressures
asel,s,,,12,12,1

```

```

da,all,uy,0
da,all,uz,0
sfa,all,,pres,-engseqv_50
!rselect all areas
asel,all

!define applied forces/pressures
asel,s,,,23,23,1
da,all,uy,0
da,all,uz,0
sfa,all,,pres,-engseqv_100
!rselect all areas
asel,all

!define applied forces/pressures
asel,s,,,34,34,1
da,all,uy,0
da,all,uz,0
sfa,all,,pres,-engseqv_200
!rselect all areas
asel,all

solv

!exit processing phase
finish

!enter static post-processing phase
/post1

```

### **A.3 Code for the RTG Model with a Brick Element Suture – Relaxation Testing (Single Load Step)**

```

!Change Working Directory to Specified Location
/cwd,'C:\Users\fuhrer\Desktop\Prony - E0 tests\7Term Prony t5-5 Rom Fit\E0
eq. Rom@t5-5 x Beta x Gamma (div strain not modif by gamma) '
!Clear Information in Directory Prior to Run
/clear
!Start preprocessing phase
/prep7

!*****
!Add Annotations
!Add Title and Subtitle to All Outputs
/title,July 3 - Prony - E0 Romanyk at t5-5 Beta Gamma (div strain not modif)
/stitle,Prony Series Test
!Define Units to Annotate Results
/units,mpa

```

```

!*****!Define
Geometries
!##### Dimensional Parameters
!Suture Length (mm)
Lt=24.4
!Suture Thickness (mm)
tt=2.19
!Suture Width (mm)
wt=(9.72-2*4)/2
!Bone width (mm)
wb=4
!##### Solid 1
!Volume 1 (Suture)
blc4,0,0,wt,Lt,tt
!Volume 2 (Bone)
blc4,wt,0,wb,Lt,tt
!Glue Volume Geometeries Togethet
vglue,all

!*****
!Define Materials, Element Types, Real Constants, Etc.

!#####
!Material Type 1 (Linear Elastic Bone)
et,1,solid185
mp,dens,1,1000
mp,ex,1,20000          !Define Young's Modulus
mp,prxy,1,0.46        !Define Poisson's Ratio

!#####
!Material Type 2 (Prony Series Fit)
et,2,solid186
mp,dens,2,1000          !Define Density
mp,ex,2,18.74253       !Define Young's Modulus
mp,prxy,2,0.3          !Define Poisson's Ratio

!Time Shifted T>(5seconds-4.99) Prony Series Proximations
tb,prony,2,,7,SHEAR
!TB,LAB,MAT,NTEMP,NPTS,TBOPT,EOSOPT,FUNCNAME

!TBDATA,NSTART,C1,C2,C3,C4,C5,C6
!TBDATA,1,A1,T1,A2,T2,A3,T3
!TBDATA,7,A4,T4,A5,T5,A6,T6
!TBDATA,8,A7,T7,
TBDATA,1,0.3927,2.8,0.40143,10.376,0.14725,39.696
TBDATA,7,0.042999,149.81,0.011634,575.46,0.0030511,2310.1
TBDATA,13,0.00082323,11445

tb,prony,2,,7,BULK

```

```

!TB, LAB, MAT, NTEMP, NPTS, TBOPT, EOSOPT, FUNCNAME

!TBDATA, NSTART, C1, C2, C3, C4, C5, C6
!TBDATA, 1, A1, T1, A2, T2, A3, T3
!TBDATA, 7, A4, T4, A5, T5, A6, T6
!TBDATA, 8, A7, T7,

TBDATA, 1, 0.3927, 2.8, 0.40143, 10.376, 0.14725, 39.696
TBDATA, 7, 0.042999, 149.81, 0.011634, 575.46, 0.0030511, 2310.1
TBDATA, 13, 0.00082323, 11445

#####
!*****!Mesh
The Geometries
!Select 1st material (bone) and element type to mesh

mat,1
type,1
vsel,s,,,3
esize,1
vmesh,all
vsel,all

!Select 2nd material (50g suture) and element type to mesh
mat,2
type,2
vsel,s,,,1
esize,0.2
vmesh,all
vsel,all

!*****
!finish preprocessing phase
finish

!enter processing phase
/solu

!*****antype,
static
outres,all,all
nlgeo,on

!*****
!First Load Step, Apply Mechanical Loading
Rate,on
time,5
kbc,0 !ramped loading

```

```

!define boundary conditions
!select areas for BCs
asel,s,,,5,5,1
da,all,symm
!reselect all areas
asel,all

!define applied forces/pressures
asel,s,,,12,12,1
da,all,uy,0
da,all,uz,0
da,all,ux,0.125
!reselect all areas
asel,all

solv

!*****
time,1200      !Time in seconds, first term is number of weeks
deltim,0.0001,0.0001,60
kbc,0 !ramped loading

!define boundary conditions
!select areas for BCs
asel,s,,,5,5,1
da,all,symm
!reselect all areas
asel,all

!define applied forces/pressures
asel,s,,,12,12,1
da,all,uy,0
da,all,uz,0
da,all,ux,0.125
!reselect all areas
asel,all

solv

!exit processing phase
finish

!enter static post-processing phase
/post1

```









```
da,all,symm
!reselect all areas
asel,all

!define applied forces/pressures
asel,s,,,12,12,1
da,all,uy,0
da,all,uz,0
da,all,ux,hfscds*i
!reselect all areas
asel,all
```

```
SOLVE
save
```

```
*ENDDO
```

```
FINISH
```

```
/post26
```

## Appendix B - Attempt to Incorporate Strain Dependency into Prony Relaxation Model Using ANSYS Hyperelasticity Material Model

The original stress relaxation model developed by Romanyk et al. is a 1-D constitutive equation that is non-linearly dependent on time and is non-linearly dependent on the initial strain [1]. For ease of reference the  $\gamma$ -modified model is presented here in eq. (B-1).

$$\sigma_{\gamma}(\varepsilon_0, t_w) = 0.4894(0.2880(\gamma\varepsilon_0)t_w^{-0.4912})^{\frac{1}{0.4894}} \quad (\text{B-1})$$

In Chapter 2 this model was adapted for use in FEA utilizing a Prony series approximation of a data set generated by the  $\gamma$ -modified model. This Prony series approximation was able to replicate the time dependent non-linearity of the 1-D equation, however it was not able to incorporate the strain non-linearity. Partial skull simulations compensated for this by assigning an initial Young's Modulus based on the average initial strain in the suture. Individual elements were not able to automatically compensate for different initial strains, nor could this be recalculated for subsequent appliance activations. This appendix details an initial attempt to incorporate this strain dependency using hyperelastic curve fitting in ANSYS in conjunction with the Prony model.[2], [3]

### B.1 Method, Results, and Conclusions

The aim of this initial investigation was to evaluate the feasibility of replicating the strain dependency of the relaxation model through Hyperelastic curve fitting in ANSYS [4]. The 2<sup>nd</sup> order Mooney-Rivlin model was used for curve fitting (eq. (B-2)).

$$W = C_{10} * (\bar{I}_1 - 3) + C_{01} * (\bar{I}_2 - 3) + \frac{1}{d} (J - 1)^2 \quad (\text{B-2})$$

Stress versus strain data was generated utilizing MATLAB<sup>®</sup> code. This data set was generated for a time value,  $t$ , of 5 seconds (8.2672e-6 weeks). Initially two datasets were generated from two strain ranges shown in Table B-1. Curve fits were generated for a uniaxial test, which required engineering strain and engineering stress. As the degree of material necking could not be accommodated for using the original relaxation equation, theoretical stress and strain were supplied.

Table B-1: Strain Ranges and Approximate Curve Fit Residuals

Dataset	Strain Range		Equivalent Expansion Range (mm) Based on 1.72mm Original Width		Mooney-Rivlin Regression Residual
1	0.0581	4.6512	0.1	8	>40%
2	0.0291	0.1453	0.05	0.25	~1%

The resultant coefficients for Dataset 2 caused a numerical issue that prohibited testing of this dataset. The coefficients determined a non-positive initial elastic modulus as the deviatoric deformation constants were of the form  $C_{10} \leq C_{01}$ . The Dataset 1 coefficients were  $C_{10}=0.717228$  and  $C_{01}=0.160160$ .

### Response Function

A new feature to ANSYS 14.5 was the addition of a Hyperelastic Response function [2, Sec. 3.6.10] which allows for direct input of experimental stress and strain data. The uniaxial test profile was selected in ANSYS, and the stress strain data from Dataset 1 was input to ANSYS at runtime.

### Simulations

Both the Mooney-Rivlin and Response were tested in ANSYS utilizing a material test coupon geometry based upon the Type IV ASTM D638-14 standard (Fig. B-1). FEA geometry utilized a symmetry condition to reduce the overall length from 115mm to 57.5mm. Tests were simulated for 8 minutes of time and stretched the test coupon by a ramped displacement of 40 mm (20mm for the symmetry condition used to reduce the element count).

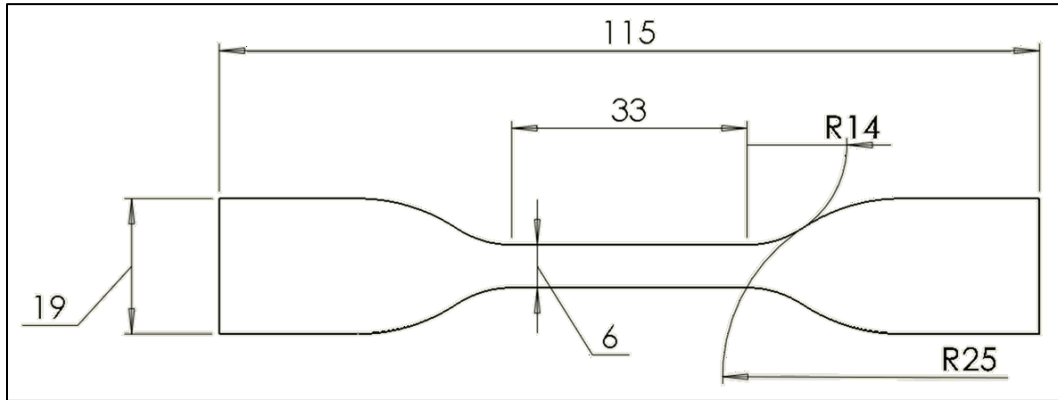


Fig. B-1: Specimen Geometry with Dimensions in mm; Thickness of 2mm

SOLID187 tetrahedral elements meshed the geometry with a 3.75mm mesh control size. As this model is not time dependent, results are presented in Fig. B-2 as stress versus strain results and are compared to the expected relationship as calculated from the  $\gamma$ -modified relaxation.

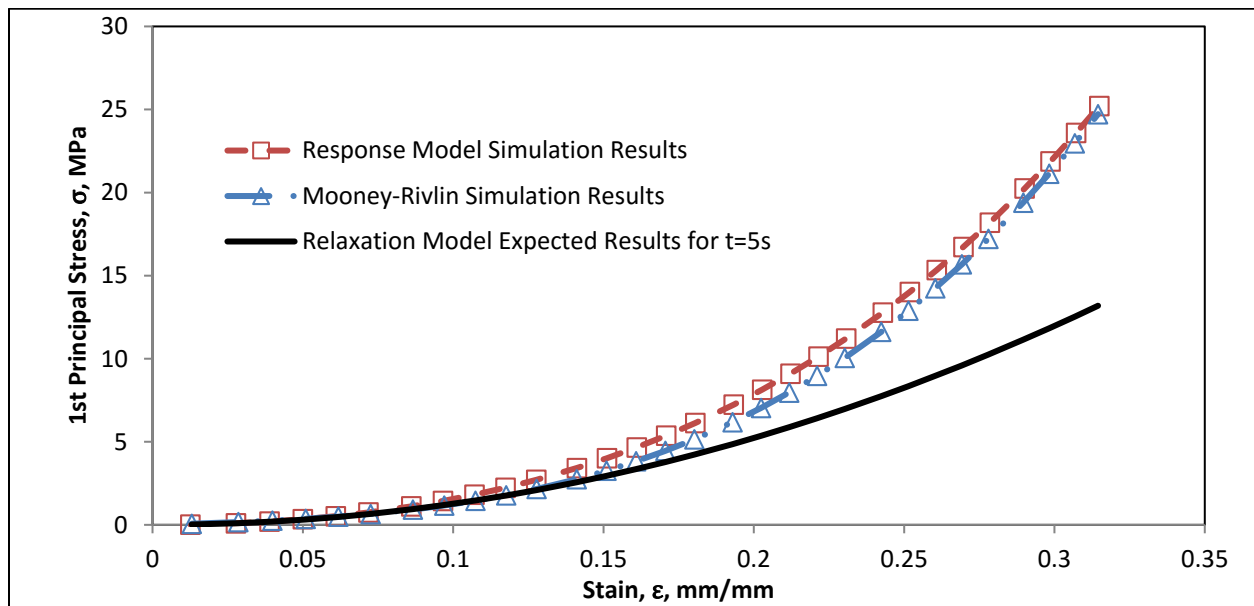


Fig. B-2: ANSYS Mooney-Rivlin and Response Function Results; 1<sup>st</sup> Principal Stress versus 1<sup>st</sup> Principal Strain

As can be seen from these results, the simulation stress strain curves for both models have a much higher stress than the expected model. As these are 1<sup>st</sup> principal stress and strain results, the reason for this discrepancy was not readily apparent. However, the window from 0-0.15 mm/mm does show a promising agreement with the anticipated behavior. At the time this model was tested it was anticipated that the full Dataset 1 strain range would be required for midpalatal suture simulations and was therefore judged inadequate. For the size of model

(1472 elements, 2681 nodes), the calculation time was considerable, approximately 15 minutes to solve for 8 minutes of simulated time.

A preliminary simulation confirmed that the model would converge utilizing the strain dependent non-linear Mooney-Rivlin curve fit in conjunction with the time non-linear Prony model curve fit. These results are not presented here. As the Hyperelastic model was judged inadequate at the time this was investigated, further tests were not completed. It is anticipated that the combination of this model and the Prony approximation of the time dependency would result in slight decreases in the stress peaks for the  $n > 1$  appliance activations.

## B.2 Future Work

This path of investigation could benefit from additional attention. This may require further investigation of adjusting the dataset windowing. Selecting 0mm/mm to 0.16mm/mm this the dataset range would likely be adequate as the full Prony relaxation simulations in Chapter 2 that were completed later have shown that the absolute mechanical strain is not key in peak stress calculations. Instead, the magnitude of change in mechanical strain is what affects the magnitude of peak stress. For 0.25 mm appliance activations, the maximum strain change magnitude is at the initial activation with a value of 0.145349 mm/mm. Additional testing of the Mooney-Rivlin fit should be done using the same rectilinear testing geometry as the used to test the Prony model to reduce any side effects of material necking during the validation simulations.

## B.3 References

- [1] D. L. Romanyk, S. S. Liu, R. Long, and J. P. Carey, "Considerations for determining relaxation constants from creep modeling of nonlinear suture tissue," *Int. J. Mech. Sci.*, vol. 85, pp. 179–186, Aug. 2014.
- [2] "Ch. 3.6: Hyperelasticity," in *ANSYS® Academic Teaching Advanced, Release 14.5, Help System, Mechanical APDL Material Reference*, .
- [3] "Ch. 6: Material Model Combinations," in *ANSYS® Academic Teaching Advanced, Release 14.5, Help System, Mechanical APDL Material Reference*, .

[4] "Ch. 5.1: Hyperelastic Material Curve Fitting," in *ANSYS® Academic Teaching Advanced, Release 14.5, Help System, Mechanical APDL Material Reference*, .

## Appendix C - APDL Code For Partial Skull Model Finite Element Trials

This appendix is comprised of the APDL Code used in this research project for preparing the partial skull model for simulations in ANSYS. This includes example code for loading the mesh and applying natural boundary conditions, applying material models and properties, manually separating the intermaxillary and midpalatal sutures, and the parameterized solution block.

### C.1 Loading Partial Skull Mesh and Creating Nodal Component Blocks

```
/CWD, 'C:\Users\fuhrer\Desktop\9 - Bone {Skull CFS IMS} Prony {MPS}'
/clear

      /prep7
      shpp, SILENT, ON      !Turns off the error checking for element shaping
                           (alternately could use silent to log warnings, but silence the warnings)

!BBBBBBBBBBBBBBBBBBBBBBBBBBBBBBBBBBBBBBBBBBBBBBBBBBBBBBBBBBBBBBBBBBBB
!BB Note, this input reading of the simpleware model must be BEFORE the
prep7 command BB
!BB (The input command exits prep7, so you need to reenter prep7
!BBBBBBBBBBBBBBBBBBBBBBBBBBBBBBBBBBBBBBBBBBBBBBBBBBBBBBBBBBBBBBBBBBBB
      /INPUT, 'Gator VI - 210_8k elements', 'ans', 'C:\Users\fuhrer\Desktop\9 -
Bone {Skull CFS IMS} Prony {MPS}',, 0
      /prep7
      /title, Bone {Skull CF Sutures IMS} - Prony {MPS} 29 Activations
!BBBBBBBBBBBBBBBBBBBBBBBBBBBBBBBBBBBBBBBBBBBBBBBBBBBBBBBBBBBBBBBBBBBB
!BB Loading Location Allowing Rotation of Load Point - Reduces Errors
!BBBBBBBBBBBBBBBBBBBBBBBBBBBBBBBBBBBBBBBBBBBBBBBBBBBBBBBBBBBBBBBBBBBB

      n, 100000, 51.522, 43.030, 23.598
      et, 3, link180
      type, 3
      mat, 10

      e, 7238, 100000
      e, 7239, 100000
      e, 10227, 100000
      e, 10651, 100000
      e, 10653, 100000
      e, 10747, 100000
      e, 10748, 100000
      e, 10930, 100000
      e, 11613, 100000
      e, 12571, 100000
      e, 31259, 100000
      e, 31337, 100000
      e, 31610, 100000
      e, 31611, 100000
```

```
e,31615,100000
e,31711,100000
e,31954,100000
e,31975,100000
e,31977,100000
e,31984,100000
e,39875,100000
e,40069,100000
e,40070,100000
e,42253,100000
e,43521,100000
e,43522,100000
e,43529,100000
e,43827,100000
e,45689,100000
e,45697,100000
e,46725,100000
e,48284,100000
e,52470,100000
```

```
!Define XMAX Node Set Components
  nsel,s,loc,x,65.730,65.731
  cm,NS_model_xmax,node
  NSEL,ALL
```

```
!Define Top of Cranium Node Set Components
  cs,11,cart,20204,37196,53559
  nsel,s,loc,z,-0.25,0.25
  CM,NS_Top_Of_Cranium,NODE
  nsel,all
```

```
!Define Back of Cranium Node Sets Components
  cs,12,cart,24386,13689,30044
  nsel,s,loc,z,-1,1
  CM,NS_Back_of_Cranium,NODE
  NSEL,ALL
```

```
csys,0 !return to the global coordinate system
```

```
/UNITS,MPA
!Get rid of all element lines and edges in Graphics Window
/EDGE,1,0,45
/GLINE,1,-1
/REPLOT
```

```
EPlot
/VIEW,1,, -1
```



```

cm,Temp1,elem

!!Create Temp Comp 2
esel,r,cent,z,38,60
esel,r,cent,y,0,32.3
cm,temp2,elem
cmsel,s,temp1,elem
cmsel,u,temp2,elem
esel,u,cent,z,45,60
cm,PT_JUST_MPS,elem
cmsel,s,PT_MPS_AND_IMS,ELEM
CMSEL,U,PT_JUST_MPS,ELEM
CM,PT_JUST_IMS,ELEM
esel,all
/color,cm,dgrey,pt_just_ims

```

## C.2 Application of Material Models and Properties

```

!%%%%%%%%%%%%%%%%%%%%%%%%%%%%%%%%%%%%%%%%%%%%%%%%%%%%%%%%%%%%%%%%%%%%%%%%
!%%      Change Mat Number for IMS Suture to Same as Nasal Sutures
!%%%%%%%%%%%%%%%%%%%%%%%%%%%%%%%%%%%%%%%%%%%%%%%%%%%%%%%%%%%%%%%%%%%%%%%%

```

```

cmsel,s,pt_just_ims,elem
mpchg,5,all
esel,all

```

```

!Get rid of all element lines and edges in Graphics Window
/EDGE,1,0,45
/GLINE,1,-1
/REPLOT

```

```

!%%%%%%%%%%%%%%%%%%%%%%%%%%%%%%%%%%%%%%%%%%%%%%%%%%%%%%%%%%%%%%%%%%%%%%%%
!%%      Verify the Material:Volume Relationships      %%
!%%%%%%%%%%%%%%%%%%%%%%%%%%%%%%%%%%%%%%%%%%%%%%%%%%%%%%%%%%%%%%%%%%%%%%%%

```

```

!material 2 is the bone (PT_COPY_OF_BONES)
!esel,s,mat,,2
!eplot
!esel,all
!material 3 is the zygomaticotemporal suture (PT_ZTS)
!esel,s,mat,,3
!eplot
!esel,all
!material 4 is the frontozygomatic suture (PT_FZS)
!esel,s,mat,,4
!eplot
!esel,all
!material 5 is the nasomaxillary suture (PT_NASAL_SUTURES)
!esel,s,mat,,5

```









```

                mp, dens, MATNM, 1000
                mp, ex, MATNM, 20000          !Define Young's Modulus (20,000 MPa, 20
GPa)
                mp, prxy, MATNM, 0.46        !Define Poisson's Ratio

```

```

#####
!Material For Frontozygomatic Suture
!Encode Material Number

```

```

    FZS=4
    matnm=fzs
    !$$$$$$$$$$$$$$$$$$$$$$$$$$$$$$$$$$$$$$$$$$$$$$$$$$$$$$$$$$$$
    !$$$$$$$$$$ Linear Elastic (Bone)  $$$$$$$$$$$
    !$$$$$$$$$$$$$$$$$$$$$$$$$$$$$$$$$$$$$$$$$$$$$$$$$$$$$$$$$$$$

```

```

                mp, dens, MATNM, 1000
                mp, ex, MATNM, 20000          !Define Young's Modulus (20,000 MPa, 20
GPa)
                mp, prxy, MATNM, 0.46        !Define Poisson's Ratio

```

```

#####
!Material For Nasomaxillary Suture AND IMS
!Encode Material Number

```

```

    NMS=5
    matnm=nms
    !$$$$$$$$$$$$$$$$$$$$$$$$$$$$$$$$$$$$$$$$$$$$$$$$$$$$$$$$$$$$
    !$$$$$$$$$$ Linear Elastic (Bone)  $$$$$$$$$$$
    !$$$$$$$$$$$$$$$$$$$$$$$$$$$$$$$$$$$$$$$$$$$$$$$$$$$$$$$$$$$$

```

```

                mp, dens, MATNM, 1000
                mp, ex, MATNM, 20000          !Define Young's Modulus (20,000 MPa, 20
GPa)
                mp, prxy, MATNM, 0.46        !Define Poisson's Ratio

```

```

#####
!Material Zygomaticomaxillary Suture
!Encode Material Number

```

```

    ZMS=6
    matnm=zms
    !$$$$$$$$$$$$$$$$$$$$$$$$$$$$$$$$$$$$$$$$$$$$$$$$$$$$$$$$$$$$
    !$$$$$$$$$$ Linear Elastic (Bone)  $$$$$$$$$$$
    !$$$$$$$$$$$$$$$$$$$$$$$$$$$$$$$$$$$$$$$$$$$$$$$$$$$$$$$$$$$$

```

```

                mp, dens, MATNM, 1000
                mp, ex, MATNM, 20000          !Define Young's Modulus (20,000 MPa, 20
GPa)
                mp, prxy, MATNM, 0.46        !Define Poisson's Ratio

```

```

#####
!Material For Mid Palatal Suture

```















## Appendix D - Alternate Partial Skull Meshing Method Using NURBS and HyperMesh

Of the components of the analysis presented in Chapter 3, the partial skull geometry and mesh as generated in SimpleWare's ScanIP and +FE modules is the centerpiece. Due to the edge smoothing that is inherent in Simpleware during the visualization and mesh generation there are discontinuities in the smoothness of the mesh. These occur at the intersections of the cranial bone and suture volumes as shown in Fig. 3-19. To attempt at rectifying this, an alternate method was looked at to segment the model and subsequently mesh it for FEA.

### D.1 Methods and Observations

The +NURBs module for Simpleware is a software module for Simpleware to create Non-Uniform Rational B-Spline (NURBS) surfaces from masked geometries. When this module and the Altair HyperMesh program became available for use, it was decided to utilize it to create a smooth meshed geometry. The new workflow from ScanIP to ANSYS is compared with the original workflow in Fig. D-1.

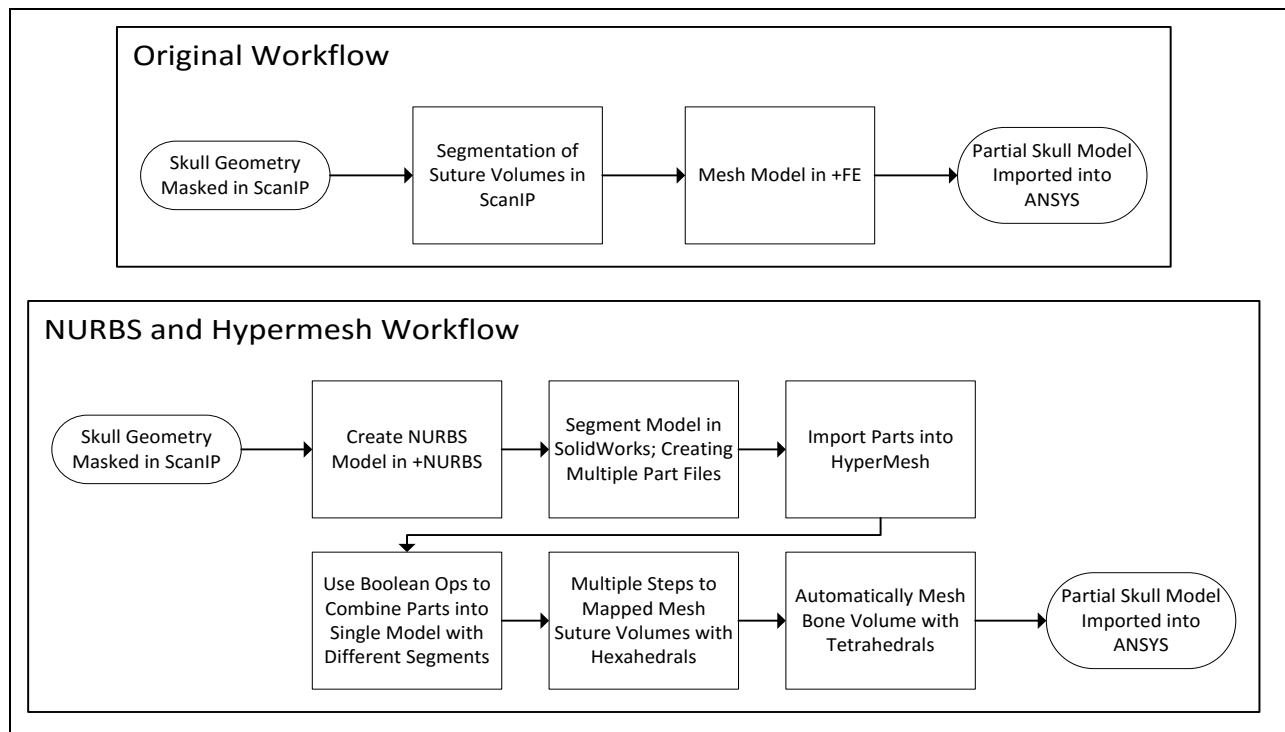
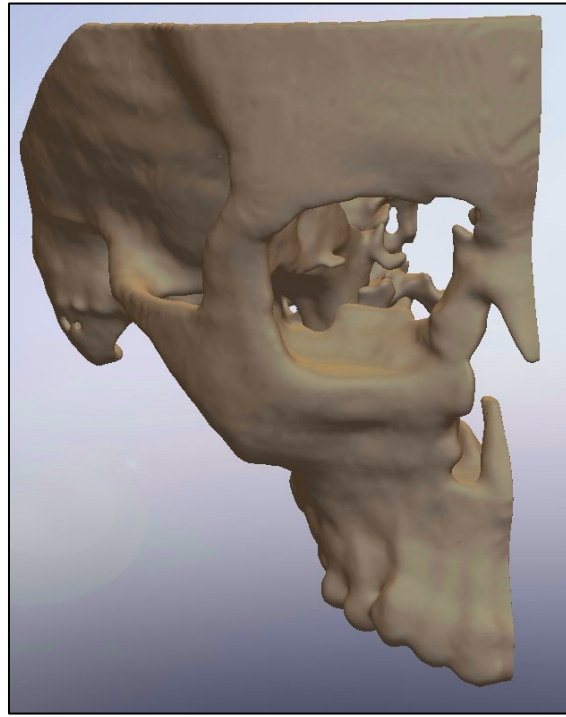


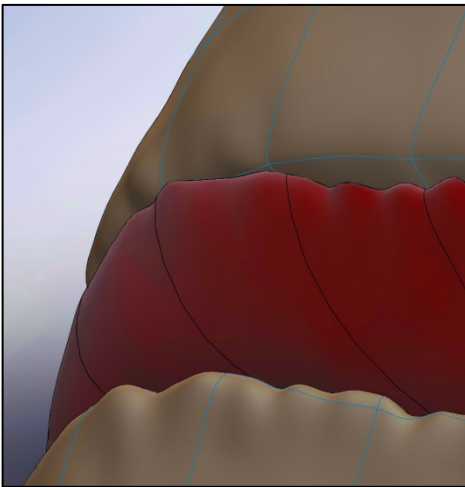
Fig. D-1: Specimen Geometry with Dimensions in mm; Thickness of 2mm

In utilizing this workflow, the  $\frac{1}{2}$  skull was generated in +NURBS to create the model in Fig. D-2 (A). This model does not have any ScanIP segmented sutures as the smoothing that plagued the original

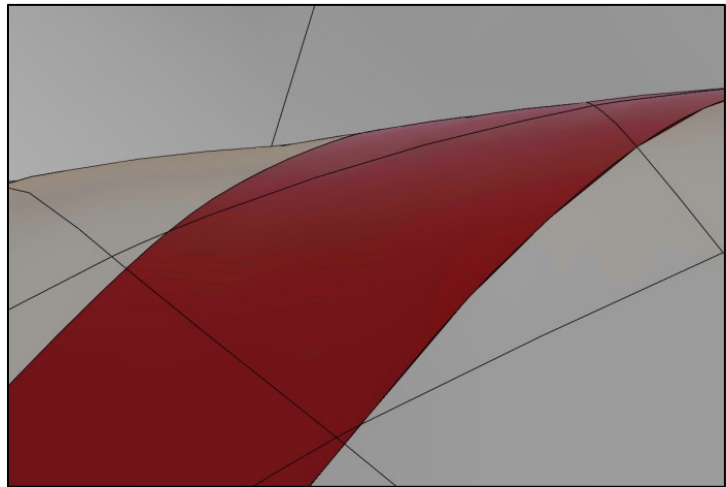
workflow is readily apparent in the close-up image in Fig. D-2 (B). This is in comparison to the smooth suture transition that resulted from the segmentation in SolidWorks (Fig. D-2 (C)).



(A) - Unsegmented NURBS Skull



(B) NURBS Segmented Suture

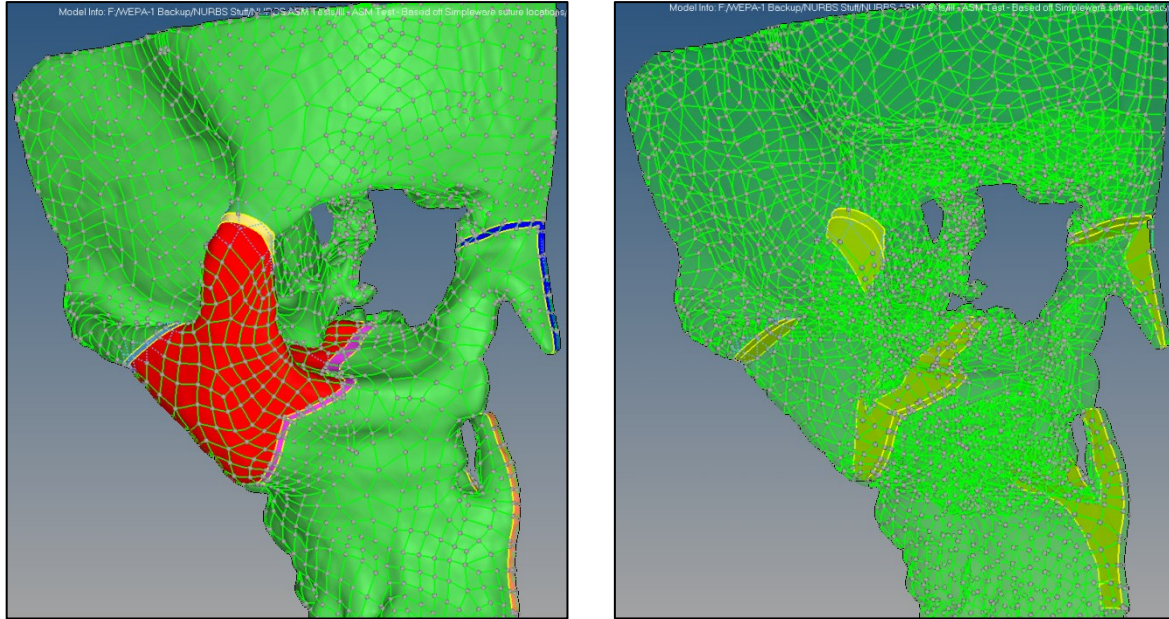


(C) SolidWorks Segmented Suture

Fig. D-2: NURBS Half Skull in SolidWorks

Once imported into HyperMesh as “.iges” manifold solids, the assembly needed to be combined into a single component comprised of separate solids (Fig. D-3 (A)). This was done to ensure that the mesh would be continuous and conformal at bone-suture volume intersects. The Boolean operation used was

the advanced A+B. It combined volumes “A” and “B” and then cut the final component along the separation line. This left a trimming plane between the two components (Fig. D-3 (B)). There was much difficulty in getting HyperMesh to create flat planes without facets, as the .iges suture files from SolidWorks were interpreted by HyperMesh to have non-conformal intersect faces.

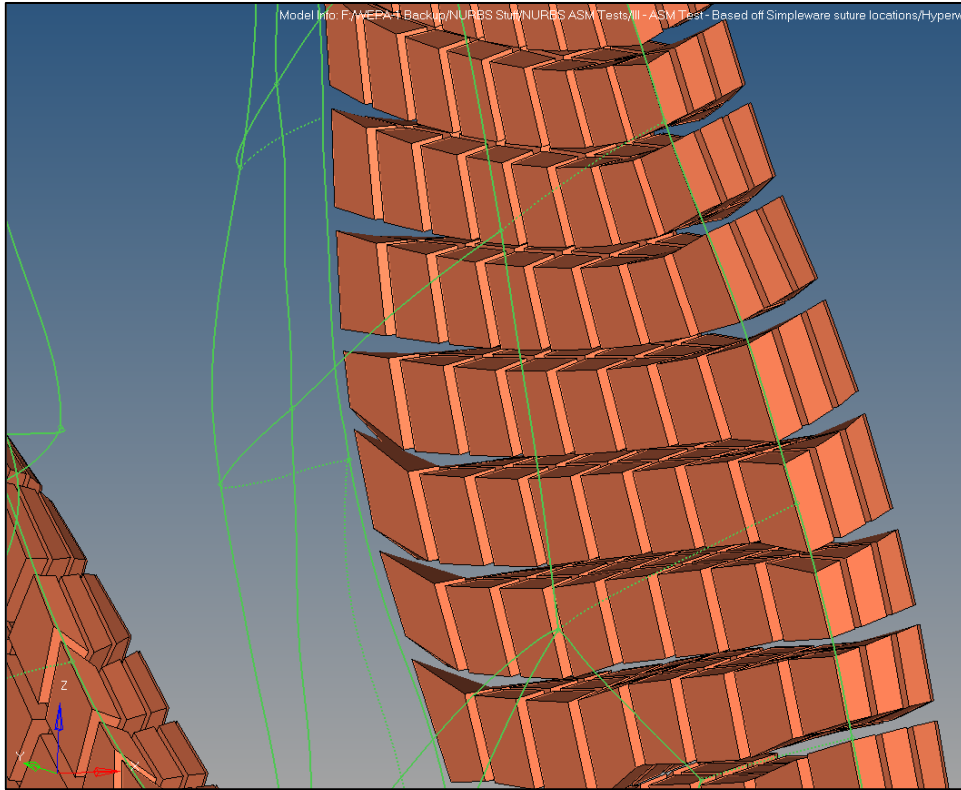


(A) Showing Various Components

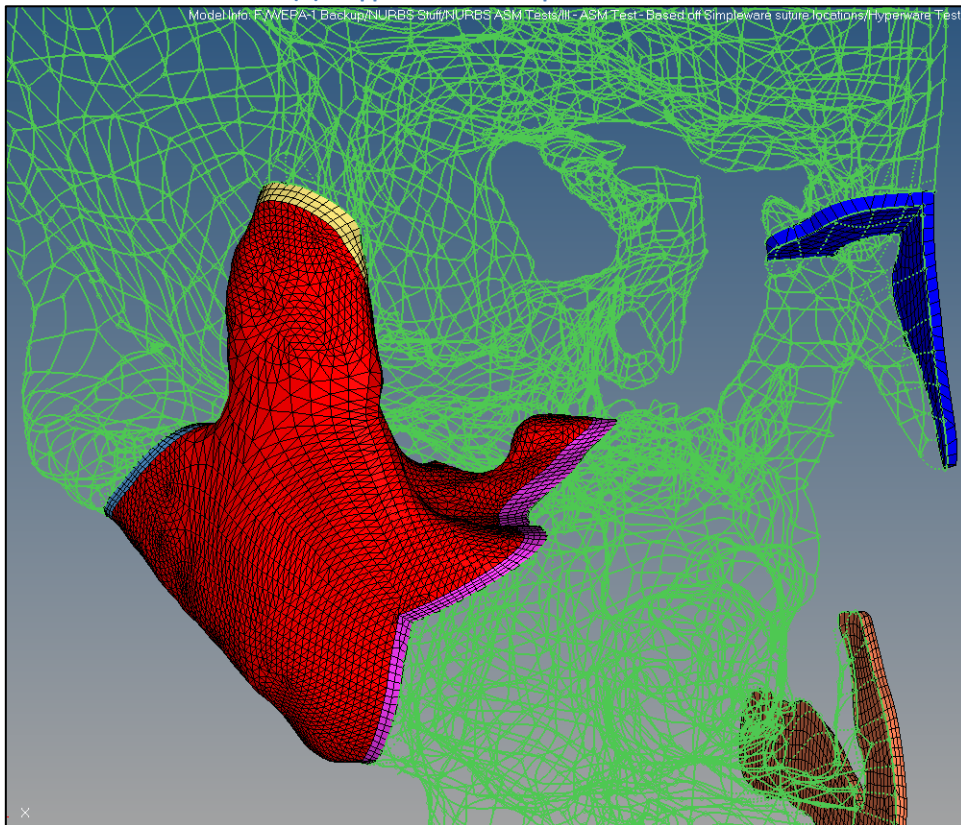
(B) Showing Trimming Planes in Yellow

Fig. D-3: HyperMesh Model

Following this the sutures were meshed using a semi-manual mapped meshing procedure using hexahedral elements. 0.3mm layers were used across the thickness of the sutures. This is shown in Fig. D-4 (A) for a portion of the midpalatal suture with separated elements to show the layering. Fig. D-4 (B) shows all of the mapped craniofacial sutures included in this study, as well as the automatically meshed zygomatic bone volume. It was found that HyperMesh was not able to mesh the remainder of the cranial bones. This was due to several factors such as complex geometry, the faceted faces between the remaining cranial geometry and sutures, and as well as the difficulty of conforming to the mesh that was created by the user for the sutures. The answer to this meshing problem was not readily apparent and as such this line of investigation was put to the side in favor of continued use of the mesh generated in SimpleWare +FE.



(A) Mapped Mesh of Midpalatal Suture



(B) Multiple Meshed Segments

Fig. D-4: Partially Meshed Geometry in HyperMesh

## D.2 Future Work

It could be advantageous to pursue this meshing method further to increase the mesh quality and the smoothness of the meshed geometry at the bone-suture intersects. In implementing the Prony relaxation model it would help increase the validity of results without increasing the mesh density. A mesh with a lower overall density would utilize less hard disk space in storing results and would likely be quicker in solving due to a fewer number of overall calculations per iteration. This could pay additional dividends if the Hyperelastic and Prony material models are investigated in conjunction in a partial skull model simulation for the sutures. If a fully viscoelastic model (sutures and bone) is developed in the future without access to a large amount of processing power, a smaller mesh will be advantageous due to reduced calculation time despite the lower spatial resolution.